Processing of High-Performance Fluoropolymers by Additive Manufacturing

Carlo Campanelli

Doctoral Thesis

Submitted to the University of Nottingham for the degree of Doctor of Philosophy

March 2019

Abstract

Polymers are used in different additive manufacturing (AM) techniques such as material jetting, material extrusion, binder jetting, vat photopolymerisation, sheet lamination, and powder bed fusion. Each technique has slightly different pros and cons but, in general, they are all suited for low-volume production, prototyping, complex geometry, bespoke parts, avoiding the losses of expensive materials (usually involved in traditional fabrication), rapid tooling/mould manufacture, and reverse engineering.

Only a small percentage of the available polymers on the market are suitable to be processed with AM techniques as particular material properties are required. The lack of a diversified portfolio of materials is one of the main limitations of AM, thus research in this field is essential for the advancement of the technology and to reduce the gap between AM and the traditional manufacturing industry. This PhD investigated the use of fluoropolymers in AM and identified powder bed fusion and material jetting as the most promising technologies to process these materials.

Fluoropolymers represent a particularly interesting family of polymers. PTFE, better known by the trademark Teflon, is the most famous and used fluoropolymer. Because of the particular characteristics of the C-F bond, fluoropolymers have many desirable properties such as biocompatibility, non-adhesiveness, wide service temperature (−260 °C - +260 °C), high chemical resistance, low dielectric constant (insulating), low refractive index, good transparency to UV, visible, and IR light, and high resistance to sunlight, flames, and weathering without the addition of fillers, plasticisers or stabilisers. These properties can be found in other materials but fluoropolymers are unique when two or more of these properties are required in the same application. The downside of all these amazing properties is that fluoropolymers are difficult to process. For example, because of its high crystallinity and viscosity (10^{10}-10^{12} Pa.s), PTFE is not melt processable like most thermoplastics polymers and requires special processes. The high chemical resistance makes them insoluble in most organic solvents at room temperature. The high temperatures required to process them cause a degradation of the polymer chain which generate corrosive by-products that require specific alloys to be used. The number of challenges further increases in AM as commercially available grades are tailored for more traditional processes such as injection moulding (pellets) and coating (fine powders). The investigation of fluoropolymers in AM is still very limited and mainly focused on one particular fluoropolymer, polyvinylidene fluoride (PVDF) and its copolymers, which has a relative low melting temperature (<180 °C) and piezoelectric properties.

Abstract

This PhD investigates three fluoropolymers: a terpolymer of tetrafluoroethylene, hexafluoropropylene and vinylidene fluoride (THV), polychlorotrifluoroethylene (PCTFE), and perfluoroalkoxy (PFA) with melting temperatures of 110 °C, 210 °C, and 304 °C, respectively. PCTFE and PFA were used in polymer powder bed fusion applications while THV was used in material jetting.

Several issues were faced and solved. The first challenge encountered was to find these fluoropolymers in a powder form with an ideal particle size distribution. This was not possible and particle sizes below the optimal values were used. Because of that, the powders were cohesive and did no flow well. Good flowability was achieved by testing several thermal treatments and additives such as fumed nano-silica and carbon black. The second issue was the high melting temperature of PCTFE and PFA which were too high for the powder bed fusion equipment used (EOS Formiga P100, maximum powder bed temperature of 182 °C). The isothermal crystallisation data of PCTFE and PFA confirmed that the ideal processing temperature was above 182 °C for both polymers. This led to a negative and a positive effect. The negative effect was a part warping after few tens of layers for PCTFE and part warping at the first layer for PFA. The positive effect was that the polymers did not age at the processing temperature and could be recycled without issues. Different scan strategies and the use of a build plate reduced considerably the warping. The third issue was the high molecular weight and consequent viscosity of the polymer melt. The melting and solidification of the polymers happened too quickly and the formed layers were porous. Higher laser powers reduced the porosity but also caused the decomposition of the polymer. A solution to this was to scan multiple times the same area with a lower laser power that did not cause decomposition. At this stage, single layers of laser sintered PFA were fabricated and found to be porous, flexible, with a fabric feeling to the touch, and with potential membrane applications.

THV was used in material jetting in different solvents and concentrations with two manufacturing systems: Dimatix and PICO Pμlse. The Dimatix was able to print very diluted formulations (1 wt%) and generate very thin uniform coatings and patterns down to 5-10 nm in thickness. The PICO Pμlse was able to print more concentrated formulation (10-20 wt%) into thicker films with higher throughput but lower resolution. The combination of the two printers could allow for both high throughput and resolution. The samples showed the potential to be used in the slow release of drugs.

Overall, this PhD showed that fluoropolymers have the potential to be used in AM in several applications and that they would benefit from high temperature systems and the collaboration of the powder suppliers to design polymer grades with properties tailored for AM (particle size, viscosity, etc.).

Acknowledgements

I would like to sincerely thank my supervisors Professors Christopher Tuck and Ricky Wildman. I am extremely appreciative for their guidance, support and patience in completing this PhD.

I thank all academic, technical, administrative and research members of the Centre for Additive Manufacturing for their help over the last few years.

I acknowledge funding from the EPSRC and Fluorocarbon.

I am especially grateful to Cohort 1 of the CDT in Additive Manufacturing and 3D Printing for their support and for making my time at the University of Nottingham an enjoyable experience.

Last but not the least, I would like to thank my family for supporting me throughout my PhD and life in general.

E quindi uscimmo a riveder le stelle.

If you are out to describe the truth, leave elegance to the tailor

- Albert Einstein

List of Publications

Conference Paper Published (First Author)

Processing of high performance fluoropolymers by laser sintering - 29th Annual International Solid Freeform Fabrication Symposium

Conference Paper to be submitted (First Author)

Characterisation of the surface topography evolution of an ink-jet printed transparent fluoroplastic with coherence scanning interferometry - 22nd International Conference on Metrology and Properties of Surfaces

Paper in preparation (First Author)

Material jetting, film formation, and mechanical properties of Tetrafluoroethylene - Hexafluoropropylene - Vinylidene Fluoride (THV)

Conference Presentations

Processing of fluoropolymers through Ink Jet Printing - IOP PGS Conference: Printing for the future 2018, Nottingham

Processing of high performance fluoropolymers by laser sintering - International Solid Freeform Fabrication Symposium, An Additive Manufacturing Conference, August 2018, Austin Texas.

Magazine column

Additively manufacturing fluoropolymers - TCT European Edition (Volume 26 Issue 5), August 2018

Table of Contents

Abstract i

Acknowledgements iii

List of Publications iv

Table of Contents v

List of Figures xi

List of Tables xxiv

List of Acronyms xxviii

1. Introduction 1

1.1 Context 1

1.2 Motivation, aim and objectives 3

1.3 Statement of novelty 5

1.4 Thesis structure 5

2 Literature review 7

2.1 Introduction 7

2.2 Powder bed fusion 7

2.2.1 Overview 7

2.2.2 Polymers for powder bed fusion 9

2.2.3 Material properties and processing parameters 9

2.2.4 Cohesive forces 13

2.3 Material Jetting 16

2.3.1 Overview 16

2.3.2 Printability assessment 18

2.3.3 Coffee ring effect 19

2.4 Fluoropolymers 21
2.4.1 Introduction 21
2.4.2 Fluoropolymers in additive manufacturing 25
2.4.3 Perfluoroalkoxy (PFA) – high temperature fluoropolymer 28
2.4.4 Polychlorotrifluoroethylene (PCTFE) – medium temperature fluoropolymer 29
2.4.5 THV – low temperature, soluble fluoropolymer 30
2.5 Gaps in research and statement of novelty 31
3 Methods and materials 33
3.1 Introduction 33
3.2 Materials 33
3.3 Methods 33
3.3.1 Powder bed fusion apparatus 33
3.3.2 Material Jetting apparatus 34
3.3.3 Powder mixing 35
3.3.4 Shape and surface morphology 35
3.3.5 Mass and density measurement 35
3.3.6 Differential Scanning Calorimetry (DSC) 35
3.3.7 Thermogravimetric Analysis (TGA) 36
3.3.8 Particle size distribution (PSD) 37
3.3.9 Fourier-transform infrared spectroscopy (FT-IR) 37
3.3.10 Dissolution of PCTFE 37
3.3.11 Thermal treatments of the PCTFE powder 38
3.3.12 FT4 powder flow rheometer 38
3.3.13 Surface tension and contact angle of the inks 39
3.3.14 Choice of solvents 39
3.3.15 Viscosity of the inks 39
3.3.16 Gel permeation chromatography (GPC) of THV 40

3.3.17 Ink preparation 40
3.3.18 E-beam crosslink of THV 40
3.3.19 THV coated glass slides 41
3.3.20 Coherence scanning interferometry (CSI) of the THV films 41
3.3.21 THV samples for tensile tests 42

4 Results – Powder bed fusion 43

4.1 Characterisation of the polymers 43
4.1.1 Introduction 43
4.1.2 Differential Scanning Calorimetry (DSC) 44
4.1.3 Thermogravimetric Analysis (TGA) 48
4.1.4 Particle size distribution (PSD) 50
4.1.5 Fourier-transform infrared spectroscopy (FT-IR) 52
4.1.6 Discussion – Characterisation of the polymers 56

4.2 Methods of improving the powder flow of PCTFE and PFA 57
4.2.1 Introduction 57
4.2.2 Individuating the source of the cohesion 57
4.2.3 Dissolution and precipitation of PCTFE 58
4.2.4 Additives 59
4.2.5 Static eliminator 60
4.2.6 Thermal treatments 60
4.2.7 FT4 Powder flow rheometer study 62
4.2.8 Discussion – Methods of improving the powder flow of PCTFE and PFA .. 66

4.3 Powder bed fusion of PCTFE 68
4.3.1 Introduction 68
4.3.2 Screening of the process parameters for neat PCTFE 68
4.3.3 PCTFE + 1 wt% carbon black 71
4.3.4 Discussion – Powder bed fusion of PCTFE 74

4.4 Powder bed fusion of PFA 76

4.4.1 Introduction 76
4.4.2 Screening and optimisation of the process parameters 76
4.4.3 Multiple layers and use of a substrate 91
4.4.4 Discussion – Powder bed fusion of PFA 96

5 Results – Material Jetting of THV 99

5.1 Ink characterisation 100
5.1.1 Surface tension, contact angle and density 100
5.1.2 Viscosity 103
5.1.3 Gel permeation chromatography (GPC) 107
5.1.4 Discussion – ink characterisation 108

5.2 Jetting with the Dimatix 110
5.2.1 Introduction 110
5.2.2 Ohnesorge and Z number 110
5.2.3 Droplet formation 111
5.2.4 Film formation of the THV 2.5 wt% MIBK-DMAc ink 113
5.2.5 Film formation of the THV 2 wt% in DMAc ink 113
5.2.6 Drop, line, and film formation of the THV 1 wt% in 50-50 v% MIBK-DMAc ink 114
5.2.7 Drop, line, and film formation of the THV 1 wt% MIBK ink 118
5.2.8 Discussion – Jetting with the Dimatix 135

5.3 Jetting with the PICO Pμlse 137
5.3.1 Introduction 137
5.3.2 THV 10% MIBK 137
5.3.3 THV 20% MIBK-Acetone 143
5.3.4 Discussion – Jetting with the PICO Pμlse 149

5.4 Water permeability investigation 150
5.4.1 Introduction 150
5.4.2 Results 150

5.4.3 Discussion 156

5.5 Peeling test 157

5.5.1 Introduction 157

5.5.2 Results and discussion 157

5.5.3 Summary 159

5.6 E-beam crosslinking 159

5.6.1 Introduction 159

5.6.2 Results and discussion 159

5.6.3 Summary 160

5.7 Mechanical tests 161

5.7.1 Introduction 161

5.7.2 Results and discussion 161

5.7.3 Summary 163

6 Discussion 164

6.1 Introduction 164

6.2 Characterisation of the polymers and improvement of the powder flow 164

6.3 Powder bed fusion of PCTFE and PFA 167

6.4 Material Jetting of THV 170

7 Conclusions 175

7.1 Introduction 175

7.2 Conclusions: powder bed fusion of PCTFE and PFA 175

7.3 Conclusions: material jetting of THV 176

8 Recommendations for future work 178

8.1 Introduction 178

8.2 Improvement of the raw materials 178

8.3 Improvement of the pPBF systems 178

8.4 Membrane applications 178
8.5 Heat treatments 179
8.6 Use of THV in powder bed fusion 179
8.7 Counter coffee ring effect 179
8.8 Wrinkle effect 179
8.9 E-Beam crosslinking 180
8.10 Drug release 180
8.11 Microfluidic devices 180
Bibliography 181
Appendix 197

List of Figures

Figure 1.1 – Left: a tool with optimised cooling channels design [21]. Right: schematic of the investment casting process [1]. 3

Figure 1.2 – 3D printed fuel nozzle by GE Aviation; 18-20 different parts merged in one single design [1], [8], [20]. 3

Figure 2.1- pPBF system schematic. Figure reproduced from [35]. 8

Figure 2.2 - Specific volume against temperature for (A) amorphous (B) partially crystalline, and (C) “fully” crystalline polymers. Image reproduced from [48]. 10

Figure 2.3- Melting and crystallisation characteristics for an idealized polymer DSC curve for pPBF [1], [50]..... 11

Figure 2.4 - Illustration of a cohesive and non-cohesive powder. Figure reproduced from [72]. 14

Figure 2.5 – Drop ejection by (a) continuous inkjet, (b) thermal drop-on-demand and (c) piezoelectric drop-on-demand. Figure reproduced from Derby [81]. 17

Figure 2.6 – Ejection mechanism of the PICO Pµlse. From left to right, opening and closing of the valve which causes the filling of the nozzle chamber and ejection of a drop. This cycle allows the ejection of a single drop of ink. The black and red arrows indicate the direction of the rod and ink flow, respectively. Figure reproduced from [92]. 18

Figure 2.7 - Illustration of the capillary flow (cause of the coffee ring effect) and inwards Marangoni flow. Figure reproduced from [101]. 19

Figure 2.8 - Height profile of a drop where coffee ring is (a) present and (b) absent. Reproduced from [102]. 20

Figure 2.9- PTFE chemical structure, the fluorine atoms are represented as yellow spheres [117] [118] 22

Figure 4.1 - DSC curves showing the melting and crystallisation temperatures of (a) PCTFE and (b) PFA. Heating/cooling rate of 20 °C/min. R01 and R02 are the first and second heating/cooling cycle, respectively. 44

Figure 4.2 - DSC curves of PCTFE (left side, a-c-e) and PFA (right side, b-d-f). Isothermal crystallization at different temperatures for the (a-b) neat powders and (c-d) powders with CB. (e-f) Plotted ln of the 1/2t crystallisation versus the reverse of the isothermal crystallisation temperature. 47

Figure 4.3- (Left) TGA of PCTFE kept at 201.55 °C for 5 hours. (Right) TGA of PCTFE and PFA at 10 °C/min and 20 °C/min, respectively. 49

Figure 4.4- Relationship between molecular weight and polymer physical properties. Figure reproduced from [45]. 49

Figure 4.5 - Left: SEM image of the PCTFE powder where only small particles of roughly 0.2-1 µm were observable. Right: PCTFE particle size distribution measured with a wet cell after 30 minutes of mixing and sonication. 50

Figure 4.6 - Left: SEM image of a PCTFE powder particle after 20 minutes at 250 °C. Right: SEM image of the neat PFA powder. 51

Figure 4.7 - Top: laser sintered PCTFE powder that was then ground. Bottom: Particle size distribution of the ground PCTFE laser sintered parts. 51

Figure 4.8 – Top: IR transmittance spectra of CB and PCTFE with and without 1wt% CB. Bottom: IR transmittance spectra of PFA with and without 0.2 and 0.4 wt% CB. 53

Figure 4.9 – Zoomed IR transmittance spectra of CB and PCTFE/PFA with and without the addition of CB. The red band indicate the wavelength of the CO_2 laser 54

Figure 4.10 - IR transmittance spectrum of THV. The red band indicate the wavelength of the CO_2 laser. 55

Figure 4.11- Left: PCTFE left on a glass slide after the evaporation of a PCTFE solution in fenchone. Right: SEM of PCTFE after the dissolution and precipitation test in eucalyptol. 59

Figure 4.12 - Left: PCTFE powder after 20 minutes at 250 °C. Right: surface of a cluster of small PCTFE particles before being sintered together. 62

Figure 4.13 - FT4 results. Top: CBD of the PCTFE powder for different heat treatment and additives. The red dashed line indicates the CBD of the virgin neat PCTFE powder. Values above the line indicate an improved CBD and lower cohesion. Bottom: SE of the PCTFE powder for different heat treatment and additives. The red dashed lines indicates the approximate level of cohesion. 63

Figure 4.14 - Left: neat PCTFE powder showing bad flowability. Right: PCTFE powder + 1 wt% CB showing improved flowability and absence of agglomerations. Test carried out at 30 °C..... 64

Figure 4.15 - FT4 results for the PFA powder for different mixtures. (a) Conditioned bulk density and (b) Specific Energy for the neat virgin/used powder and for the powder having 0.2 and 0.5 wt% CB. 65

Figure 4.16 - PFA powder flow. Left: good powder flow for the first layer. Right: poor powder flow for successive layers. Test carried out at 30 °C. 65

Figure 4.17 - Flow chart showing the development of the PCTFE powder with the EOS P100 68

Figure 4.18 - Hatching settings. X and Y are the directions of the laser scan while A stands for Alternating. Figure reproduced from [224]. 69

Figure 4.19 – (a) printing pattern and samples position. The numbers correspond to the printing parameters showed in the table above. (b) Representation of sample 13 and 14 which are made of 10 progressively shorter STL file overlapped. (c) Picture of the printed samples in the powder bed. 70

Figure 4.20 – (left) Laser sintered PCTFE samples still in the powder bed and SEM of the sample printed with 6 W (sample 16). 70

Figure 4.21 – Laser sintered 20 x 20 mm parts made with (left) PCTFE and (right) PCTFE 1 wt% CB. 71

Figure 4.22 - Laser sintered 20 x 20 mm parts made with PCTFE + 1 wt% CB. The parts were printed with different laser powers and number of scans. The coloured lines connect the parts which received the same amount of overall ED. Smoke was observed only for the 3 W parts. 72

Figure 4.23 - Laser sintered PCTFE + 1 wt% CB before and after 30 minutes at 250 °C. The density increased from ~ 35% to ~ 60%. 74

Figure 4.24 - Laser sintered PCTFE + 1 wt% CB. The top and bottom samples were made with a hatch spacing of 0.60 and 0.40 mm, respectively. Scan speeds of 5000/4000/3000/2000/1000/500 mm/s were used from left to right. Different track widths were observed. 74

Figure 4.25 - Flow chart showing the development of the PFA powder with the EOS P100 76

Figure 4.26 – Laser sintered PFA with a laser powder of (a-d) 18 W (b-e) 10 W, (c-f) 5 W. As the laser power decrease the parts become more porous and fragile. (a-b-c) SEM images of the samples. (d) Parts in the powder bed as printed and laser powers used. (e) 10 W sample wet with IPA. (f) 5 W sample cleaned of the excess loose powder with water and IPA. 77

Figure 4.27 - (top) Neat PFA and (bottom) PFA + 0.4 wt% CB printed with the same parameters. The red boxes show the samples which were strong enough to be picked up, the dotted arrows show the order of strength/sintering/warping. The red circles show the difference in warping, the neat PFA preferentially warped at the vertices while the PFA + 0.4 wt% CB warped at the edges. 78

Figure 4.28 - Laser sintered PFA 0.4 wt% CB. Single scan in the X direction at different laser powers. Smoke formation was observed starting at 16 W. 79

Figure 4.29 – Laser sintered PFA (a) without and (b) with carbon black highlighting the effect of the scan strategy and part orientation on sintering and warping. The

warping/sintering was stronger in areas corresponding to the hot spot (red area in (c), top right corner). The parts were first scanned in X direction (bottom to top) and then in the Y direction (right to left) as shown in (c). The parts at the bottom were scanned twice in the X direction and gave more uniform warping/colour. (d) Representation of the suggested position of the hot spots depending on the part orientation. The colour red indicates higher local temperatures. 81

Figure 4.30 - Laser sintered PFA 0.4 wt% CB using the Skin-core and Mesh 2D scan strategy. (a) Image of the scan pattern used, the green lines represent the laser path. (b) Printed parts at different laser powers and number of scans. 82

Figure 4.31 - Laser sintered PFA 0.4 wt% CB. Skin-core strategy to study the effect of a skin/contour produced with a lower ED. The lower ED caused the edges to be thinner, weaker, and more prone to be deformed by the residual thermal stresses. .. 83

Figure 4.32 - Laser sintered PFA 0.4 wt% CB. The same parameters were used for all the samples and scanned once in the X direction. The length of the samples (150, 100, 50, 20, 10, 5, 2.5 mm) influenced the warping behaviour and quality of the sintering. The shorter samples produced a light smoke during scanning due to higher local temperatures. 84

Figure 4.33 – (Left) Sorted and (right) unsorted scan strategy. Figures reproduced from [224] 84

Figure 4.34 - Laser sintered PFA 0.2 wt% CB. Parts of different sizes printed with multiple scans. eThe samples on the right side were printed (starting from the top) with 1-2-3-4-5-6-7 scans, Each consecutive scan increased warping and strength of the part. 85

Figure 4.35 - PFA 0.4 wt% CB. Preheating the powder bed with a low ED scan. The powder became darker after the scan. Where the powder bed was spread in a rougher layer this effect was decrease (top right corner). 86

Figure 4.36 - Laser sintered PFA 0.4 wt% CB. Because of the sorted scan strategy, the laser jumped from one section to the other and that fraction of a second was enough to create discontinuities (top and bottom of the neck of the dragon). 86

Figure 4.37 – Laser sintered PFA 0.4 wt% CB grids. Single scan in the X and Y direction with hatch spacings of 1.5-1-0.75-0.5 mm, left to right. The bottom SEM images show hatch spacings of the 1.5-0.75-0.5 mm grids..... 87

Figure 4.38 - Laser sintered PFA grids. Single and double scan track thickness in the X and Y direction with hatch spacings of 1.5-1-0.75 mm. Pre-scan means that the powder was pre-scanned with a weak ED before the grid was sintered. 88

Figure 4.39 - Laser sintered PFA 0.4 wt% CB. Rings of different thickness. 89

Figure 4.40 – Laser sintered PFA 0.2 wt% CB sheet/membrane (a) as printed and (c) after 3 hours at 260 °C. (b) Visible agglomerations of carbon black (black dots). (d) Drops of water on the membrane. (e) Membrane showing with good flexibility. 90

Figure 4.41 - Laser sintered PFA 0.2 wt% CB at different laser powers and number of scans. The red boxes show the samples that did not break when removed from the powder bed. The red "SS" indicates that smoke formation was observed. 91

Figure 4.42 - Laser sintered PFA 0.4 wt% CB. Brittle sample made of 8 layers. (a) Sample right after printing (in the powder bed). (b) The sample breaks during its removal from the powder bed..... 92

Figure 4.43 - Laser sintered PFA 0.2 wt% CB. 31 layers printed before running out of powder. The warping was minimised by printing concentric square patterns. Sample (a) right after printing and (b) after cooling to room temperature. (c)Sample after its removal from the powder bed (dimensions: 20 x 20 mm) 93

Figure 4.44 - Laser sintered PFA 0.4 wt% CB, 20 x 20 mm parts. Masking tape was used as build plate to reduce warping. 13 layers were printed before running out of powder..... 94

Figure 4.45 - Laser sintered PFA 0.2 wt% CB, 20 x 20 mm parts. (a) Parts printed on top of a PFA sheet used as build platform. The PFA sheet was taped on aluminium plate (b) Part printed on top of previously laser sintered PFA sheet. The PFA sheet was not taped down but just laid in the powder bed. 95

Figure 4.46 - Laser sintered PFA 0.2 wt% CB, 20 x 20 mm parts. (a) Laser sintered PFA sheet taped on an aluminium tape. The sheet touched the recoating blade and broke. (b) Part printed on top of a laser sintered PFA sheet glued on an aluminium plate. The part was easily removed by rubbing it (c). (d) Part printed with the same parameters but without the use of a support structure. The warping is more intense. 96

Figure 5.1 – Drop of a 1 wt% THV in MIBK solution (a) on a glass slide and (b) on a THV coated glass slide. Appearance during evaporation on a THV coated glass slide of a drop of (c) THV 1 wt% in MIBK and (d) THV 1 wt% in acetone. 101

Figure 5.2 – Viscosities at different temperatures and shear rates of several formulations with a THV loading of 1-5-10-20 wt%, (n = 3). Two geometries were used: cup and bobs (cb), parallel plate (pp). The figure highlights the effect of the Taylor-vortices at THV loadings of 5 and 10 wt% by comparing the cb and pp geometries (c-d)(e-f). 106

Figure 5.3 - Viscosity of several formulations at a shear rate of 100 s^{-1} (n = 3) with: (a-c-d) THV 1-5-10 wt% in MIBK, (b) THV 1 wt% in 50-50 v% MIBK-DMAc, (e) THV 20 wt% in 50-50 v% MIBK-acetone. (f) Viscosity trend at 22 °C for the different THV loadings reported in (a-c-d-e). The parallel plate geometry was used for all the measurements except for (e) where the cub and bobs geometry was used. 107

Figure 5.4 – (a) GPC graph and (b) molecular weight distribution of THV 221. ... 108

Figure 5.5 - Flow chart showing the development of the THV inks with the Dimatix 110

Figure 5.6 – Jetting of THV formulations with different concentrations, solvents, and waveforms. (a) THV 2.5 wt% in 50-50 v% MIBK-DMAc jetted with the standard Dimatix waveform. (b) THV 1wt% in MIBK jetted with the standard Dimatix waveform showed in (e). (c) THV 1wt% in MIBK drop at 1-9-14-20-29-49 µs after ejection. The drop was ejected with a custom-made waveform shown in (d). 112

Figure 5.7 – Film produced by jetting THV 2.5 wt% in 50-50 v% MIBK-DMAc. The film was not uniform and stick-slip motions and coffee ring effect were present. . 113

Figure 5.8 – Film produced by jetting THV 2 wt% in DMAC. The film was not uniform and coffee ring effect was present. 114

Figure 5.9 – THV 1 wt% in 50-50 v% MIBK-DMAc printed at a nozzle and substrate temperature of 28 °C. (a) Single drop. (b) 5 layers of a single line printed with a DS of 50 µm. 114

Figure 5.10 – THV 1 wt% in 50-50 v% MIBK-DMAc. 5 Layers of a 3 x 3 mm film printed with 1 nozzle with a DS of 35 µm at a nozzle and substrate temperature of 28 °C 115

Figure 5.11 – THV 1 wt% in 50-50 v% MIBK-DMAc printed with 16 nozzles and a nozzle and substrate temperature of 28 °C. (a) 99 layers of a 3 x 3 mm pattern printed with a DS of 10 µm. (b) 40 layers of a 3 x 3 mm pattern printed with a DS of 30 µm and a pause of 25 minutes after the first 20 layers. (c-d) 5 layers of a 5 x 0.6 mm pattern printed with a DS of 40 µm with a delay between layers of 0 and 20 seconds, respectively. 116

Figure 5.12 – THV 1 wt% in 50-50 MIBK-DMAc. Films of 5 layers with a drop spacing of 30 µm at (a) 28 °C, (b) 40 °C, (c-d-e-f) 50 °C. (d-e-f) Pore pattern of the film printed at 50 °C before and after being stretched with a needle tip. 117

Figure 5.13 – (a) Syringe deposition of a drop of THV 1 wt% in 50-50 MIBK-DMAc and its drying at (b) room temperature and (c) at 50 °C. The drop showed a coffee ring effect when dried at room temperature and a more homogenous film when dried at 50 °C. 118

Figure 5.14 – Jetted drops of THV 1 wt% in MIBK on a glass slide. Drops seen by (a) an optical microscope and (b) CSI. (c) Profile of the drops generated from the data acquired with the CSI. 119

Figure 5.15 – (a) CSI image and (b) profile of two layers of drops of THV 1 wt% in MIBK on a glass slide. 119

Figure 5.16 – THV 1% in MIBK. Lines printed on a glass slide with a nozzle and substrate temperature of 22 °C and a DS of (a-b) 60 µm, (c)120 µm, and (d) 140 µm.

The pictures were corrected in saturation, contrast, brightness, and sharpness to increase visibility of the tracks. The printed pattern is shown in (e). 121

Figure 5.17 – Printed THV 1 wt% in MIBK, single layer. (a) Non-uniform film made with a DS of 60 µm. (b) Zoomed section of (a). (c) Uniform film made with a DS of 75 µm. (d) SEM of (c) showing pores and agglomerations. (e) AFM and (f) CSI of (c) showing pores. Pictures (a-c) were corrected in saturation, contrast, and sharpness. Image (e) was corrected with 1st order flattening. 122

Figure 5.18 – Printed THV 1 wt% in MIBK, 5 layers with a DS of 75 µm. (a) Optical microscope image. (b) CSI 2D map. (c) CSI 3D map. (d) Horizontal CSI profile of the second line of "bumps" from the bottom. 123

Figure 5.19 – SEM images of printed THV 1 wt% in MIBK, 5 layers with a DS of 75 µm. Scale bars (a) 100 µm, (b) 10 µm. The film presents no porosity and more agglomerations compared to the 1-layer film in Figure 5.17c-d. 124

Figure 5.20 – (a) Agglomerations present on a 30-layer THV 1 wt% in MIBK film compared to (b) the drops formed by the dewetting of a film from the literature [245]. (c) Dewetting mechanism [245] and (d) possible growth stage observed in some of the printed THV films. 125

Figure 5.21 – SEM image showing the (black) agglomerations present in the jetted THV film (1 layer). The SEM image is acquired by scanning (from top to bottom) the sample with an electron beam. The black agglomerations were being moved (to the bottom) and discoloured over time by the scanning electron beam (white lines in the centre of the image). The other white elements were pores. 126

Figure 5.22 – Contaminations present when MIBK was deposited through a (a) green syringe, (b) white syringe, (c) standard Dimatix cartridge (DMC-11610) as printed and (d) after 20 min at 170 °C. 127

Figure 5.23 – 5-layer THV 1 wt% in MIBK film produced with (a) DMC-11610 (b) DMCLCP-11610. Because of the higher chemical resistance of the DMCLCP-11610, no agglomeration/contamination was visible. 128

Figure 5.24 – (a) CSI with height profile and (b-c) AFM (height and adhesion map) of a 1-layer THV 1 wt% in MIBK film printed with a DS of 75 µm without the contaminations coming from the DMC. The AFM images were corrected with a 1st order flattening. The film was uniform and had a thickness of roughly 10 nm with few defects in the nanometre range due to artefacts present on the glass slide. 129

Figure 5.25 - CSI of printed THV 1 wt% in MIBK. DS of 100 µm on the left column and 120 µm on the right column. From top to bottom, the number of layers printed were 2-5-10-20-50. 130

Figure 5.26 –CSI of printed THV 1 wt% in MIBK with a DS of 100 µm. The topography of the film mutated by going from (a) 5 layers to (b) 20 layers. 132

Figure 5.27 – (a) Plotted thickness of the centre and edge of isolated drops of THV 1 wt% in MIBK. (b) CSI of 10 layers and (c) 50 layers of isolated drops of THV 1 wt% in MIBK. 133

Figure 5.28 – Printed THV 1 wt% in MIBK on top of a THV coated glass slide. (a) Arrays of drops printed with a DS of 90 µm. (b) Checkboard design done by alternatively printing black and red patterns. The resolution was of 45 µm but because of the white gaps the actual DS was of 90 µm. (c) 4 layers printed with pattern (b). (d) CSI of two adjacent 100-layer parts printed with pattern (b). 134

Figure 5.29 – CSI of one-drop-thick grid patterns printed with a DS of 75 µm with (a) 2 layers, (b) 5 layers, and (c) 10 layers. 135

Figure 5.30 - Flow chart showing the development of the THV inks with the PICO Pulse 137

Figure 5.31 – Printed THV 10 wt% in MIBK with a nozzle temperature of 60 °C and a pressure of 0.5 bar 138

Figure 5.32 – Printed THV 10 wt% in MIBK with a nozzle temperature of 45 °C and pressure of 0.25 bar. (a) Array of drops. (b) Line printed with a DS of 500. (c-d) Film printed with a DS of 500. (d) Due to the unstable drop size the films had gaps in some positions. 139

Figure 5.33 - Printed THV 10 wt% in MIBK with a nozzle temperature of 30 °C, pressure of 1 bar, and DS of 500 µm. 1-2-3-layer (from left to right) of (a) drops, (b) lines, (c) films done with. 140

Figure 5.34 - Printed THV 10 wt% in MIBK with a nozzle temperature of 30 °C and pressure of 1 bar. CSI and profile of (a) 1-layer, (b) 2-layer, (c) 3-layer drop. 141

Figure 5.35 - Printed THV 10 wt% in MIBK with a nozzle temperature of 30 °C, pressure of 1 bar, and DS of 500 µm. CSI and profile of (a) 1-layer, (b) 2-layer, (c) 3-layer line. 142

Figure 5.36 – (a) 1-layer and (b) 2-layer lines printed with THV 10 wt% in MIBK at a nozzle temperature of 30 °C, pressure of 1 bar, and DS of 400 µm. 142

Figure 5.37 - Printed THV 10 wt% in MIBK with a nozzle temperature of 30 °C, pressure of 1 bar, and DS of 500 µm. CSI and profile of (a) 1- and (b) 2-layer films. 143

Figure 5.38 – Printed THV 20 wt% in 50-50 v% MIBK-acetone with a DS of 500 µm, nozzle temperature of 60 °C, and pressure of 2 bar. (a) Drop, (b) line, (c) film edge showing splashing. 144

Figure 5.39 – Drops, lines, and films made with THV 20 wt% in 50-50 v% MIBK-acetone printed with a nozzle temperature of 50 °C, pressure of 2 bar, and DS of (a) 1000, (b) 800 µm. The scale bar is 500 µm except in the drop in (a) where it is 200 µm. 145

Figure 5.40 - Drops, lines, and films made with THV 20 wt% in 50-50 v% MIBK-acetone printed with a DS of 600 µm, nozzle temperature of 50 °C, and pressure of 2 bar. (a) 1 layer, (b) 2 layers. The scale bar is 500 µm. 145

Figure 5.41 - Printed THV 20 wt% in 50-50 v% MIBK-acetone with a DS of 600 µm, nozzle temperature of 50 °C, and pressure of 2 bar. CSI and profile of 1-2-layer (a) drops, (b) lines, (c) films. 146

Figure 5.42 - Printed honeycomb made of THV 20 wt% in 50-50 v% MIBK-acetone with a DS of 600 µm, nozzle temperature of 50 °C, and pressure of 2 bar. (a) Picture and (b) CSI of a 1-layer honeycomb and (b) CSI of a 4-layer honeycomb. 148

Figure 5.43 – THV 10 wt% in MIBK was used to coat a water-soluble drug (opaque area) printed on a glass slide. Sample (a) before and (b) after being submerged in deionised water. The red box in (a) shows the drug while the orange box shows the protective THV layer. (c) Sample that was only partially submerged in water, the green box shows the part submerged in water. 150

Figure 5.44 – Optical microscope images with cross polarised light of the sample partially submerged in water. Edge of the drug (below a THV coating) showing the crystal structure of the drug (a) before and (b) right after being partially submerged in water, and (c) few days after being left to dry. (d) Dissolved drug due to a defect in the protective THV coating in the centre of the film (e-f) right after being partially submerged in water, and (c) few days after being left to dry. 152

Figure 5.45 – Optical microscope images of a water-soluble drug printed with the Dimatix on top of a THV coated glass slide and covered with 50 layers of a protective THV film. The layers were printed with a THV 1 wt% in MIBK ink. Sample (a-b) before and (b-c-e) after dissolution in water, the bright/blue spheres are drug crystals. (e) Visible holes in the protective THV layer. The drug was dissolved away to a non-uniform protective THV layer. 153

Figure 5.46 - Crystallisation process of the drug after (a) 35, (b) 40, (c) 48, and (d) 75 minutes from being removed from the water. The protective layer was made with 2 layers of THV 10 wt%. 154

Figure 5.47 – Optical microscope images of a water soluble drug printed with the Dimatix on top of a THV coated glass slide and covered with (a) 1, (b) 2, (c) 3 layers of protective THV film (THV 10 wt% in MIBK ink). After 3 hours in deionised water, the drug only dissolved in the portions of film disturbed by the wrinkle effect (left side). (d) Protective layer made of 1 layer of THV 20 wt% in 50-50 v% MIBK-acetone, the wrinkle effect was present but no visible dissolution happened after 6 hours in water..... 155

Figure 5.48 – Popped agglomeration/bubble of drug after being submerged in deionised water for 12 days. After popping the bubble, (a) a fluid came out of it and after the fluid dried (b-c) crystals were visible. This demonstrated that water got inside the bubble and that a degree of drug was still present. 156

Figure 5.49- Drug covered with 1 layer of THV 20 wt% in 50-50 v% MIBK-acetone. (a) Sample after being submerged in water for 12 days, no drug crystals were visible. (b) After 22 days from being removed from the water, the majority of the drug agglomeration crystallised..... 156

Figure 5.50 – THV films detached with the use of water. (a) Glass slide coated with 1 mL of THV 10% in MIBK with a syringe by drop casting. (b) 1-layer film of THV 20 wt% in 50-50 v% MIBK-acetone. (c) 2-layer film of THV 10 wt% in MIBK. (d) 10-layer film of THV 1 wt% in MIBK with a thickness of few tens of nanometres.... 158

Figure 5.51 – Electron beam irradiated THV coated glass slides. (a) 3 shots at 35 kV, the top side shows the THV film while the bottom shows the cracked glass slide surface. (b) 3 shots at 35 kV. (c) 1 shot 35kV. (d) Reference non-irradiated THV film. 160

Figure 5.52 - Tensile properties of THV samples printed with a DS of 600 and 800 µm. The samples were used as printed, after a thermal treatment in oven, and after being exposed to and E-beam. (a)Tensile strength at break and Yield stress. (b) Young's modulus maximum and minimum. (c) Elongation at break. (d) Stress strain curve of samples 221_1 (untreated), 222_1 (oven), and 219 (E-Beam). 163

List of Tables

Table 2.1- Carbon Bond Energies [119] 22

Table 2.2- Common monomers used in fluoropolymers and their boiling temperature. 23

Table 2.3- Common fluoropolymers and their processing and maximum service temperature 24

Table 2.4 - Chemical structure, melting temperature and service temperature range of PFA, PCTFE, and PFA. It should be noted that several grades of THV with different melting temperatures and service temperature ranges exist. In this PhD THV 221 was used. 25

Table 3.1 - Pico Pµlse fixed jetting parameters 34

Table 3.2 – Vapour pressure, surface tension, viscosity, and boiling point of several common solvents for THV. All the data refers to a temperature of 20 °C. *water is not a solvent for THV. 39

Table 3.3 - Average values of the change in thickness and weight of THV coated glass slides produced with 1 mL of a 10 wt% THV solution in MIBK after time and thermal treatments. The values refer to the THV film (n = 3) 41

Table 4.1 - Melting and crystallisation peaks of neat PCTFE and PCTFE + 1 wt% CB. R01 and R02 are the first and second heating/cooling cycle, respectively. (n=2). ... 45

Table 4.2 - Isothermal 1/2t crystallisation at different temperatures for the PCTFE and PFA powders with and without 1wt% CB. 45

Table 4.3 - Melting and crystallisation peaks of PFA with and without 0.2 wt% CB. R01 and R02 are the first and second heating/cooling cycle, respectively. 46

Table 4.4 – FT4 analysis of PCTFE. Conditioned bulk density (CBD), Specific Energy (SE), Stability Index (SI), and The Basic Flowability Energy (BFE) of PCTFE

powders with and without additives and after thermal treatments. NS = fumed nano-silica, CB = carbon black. (n=3) 63

Table 4.5 - Printing parameters for the neat PCTFE. Laser diameter 0.42 mm, hatch spacing 0.2 mm. 69

Table 4.6 – PCTFE 1 wt% CB pPBF experiments. N = normal, S = Support, A = Alternating. The total ED is the ED of a single scan multiplied by the number of scans. 73

Table 4.7 – PFA 0.4 wt% process map at 2000 mm/s, 0.2 mm hatch spacing, single layer. The numbers indicate the degree of warping: 0 – nothing happened, the printed part could not be seen or touched. 1 – the part was barely visible. 2 – the part was partially warped (only one side). 3 – the part warped in every direction. 4 – the part was fully sintered. Mixed numbers mean that the degree of warping changed on cooling. The bold numbers indicate the experiments carried out while the remaining numbers are deductions. 80

Table 4.8 – PFA 0.4 wt% process map at 2000 mm/s, 0.1 mm hatch spacing, single layer. The numbers indicate the degree of warping: 0 – nothing happened, the printed part could not be seen or touched. 1 – the part was barely visible. 2 – the part was partially warped (only one side). 3 – the part warped in every direction. 4 – the part was fully sintered. Mixed numbers mean that the degree of warping changed on cooling. The bold numbers indicate the experiments carried out while the remaining numbers are deductions. 80

Table 4.9 - Laser sintered PFA grids. Single and double scan track thickness in the X and Y direction with hatch spacings of 1.5-1-0.75 mm. The table also report the size of the gaps between the sintered tracks, and the % difference between the X and Y track. The values are reported in µm. 88

Table 5.1 – Surface energy (n = 6) and density (n = 3) measured at 23.6 °C of several THV formulations. 101

Table 5.2 – Contact angle of THV 1 wt% in acetone, THV 1 wt% in MIBK, and deionised water drops on a glass slide and THV coated glass slide at 20.5 °C (n = 6). 101

Table 5.3 – Wrinkle effect recap. Observations on the evaporation of several THV solution in different solvents and on different substrates..... 102

Table 5.4 – Viscosities at different temperatures of several THV solutions (n =3). The reported values are for shear rates of 100 s^{-1}. Two geometries were used: Cup and bobs (cb), parallel plate (pp). 105

Table 5.5 – Ohnesorge and Z number for several THV inks. 111

Table 5.6 – Line width of THV 1 wt% in MIBK on glass (n = 15). The width min. was introduced when the lines assumed a wavy shape. 120

Table 5.7 – Drop size and line width of printed THV 10 wt% in MIBK at different DS, pressure and nozzle temperature. 138

Table 5.8 – Thickness of printed THV 10 wt% in MIBK with a nozzle temperature of 30 °C, pressure of 1 bar, and DS of 500 µm. The higher edge was due to the coffee ring effect while the “shoulder” was the edge of the first layer drop as it spreads more. 140

Table 5.9 – Drop size and line width of printed THV 20% in 50-50 v% MIBK-Acetone at several pressures, temperatures and drop spacings (n = 15). The samples were printed with the Nordson EFD HPx High-Pressure Dispensing Tool. 144

Table 5.10 - Thickness of printed THV 20 wt% in 50-50 v% MIBK-acetone with a nozzle temperature of 50 °C, pressure of 2 bar, and DS of 600 µm. The coffee ring effect was practically absent. The shoulder was also absent as the drop size seemed to not change on the second layer. 147

Table 5.11 – Tensile properties of THV samples printed with a DS of 600 and 800 µm. The samples were tested as printed, after a thermal treatment in oven, and after being exposed to and E-beam. 162

Table 0.1- Thermal properties of PCTFE 197

Table 0.2- Typical Physical Properties of PCTFE..... 198

Table 0.3- Flow, apparent density, and ZST of NEOFLON (PCTFE)..... 199

Table 0.4- Electrical Properties of PCTFE..... 200

Table 0.5- Gas permeability of PCTFE and FEP 200

Table 0.6- 7 Days immersion test of PCTFE [150]..... 201

Table 0.7- Temperature necessary to solubilise PCTFE in different solvents 202

List of Acronyms

6-FTA	Hexfluoroisopropylidene Bisphthalic Acid
AM	Additive Manufacturing
ASTM	American Society for Testing and Materials International
BFE	Basic flowability energy
CAD	Computer-aided design
CBD	Conditioned bulk density
ChemP	Chemical Point
CIJ	Continuous inkjet
CTFE	Chlorotrifluoroethylene
D_{10}	10 % of the powder is below that specified size value
D_{50}	50 % of the powder is below that specified size value
D_{90}	90 % of the powder is below that specified size value
DMC	Dimatix cartridge
DoD	Drop-on-demand
DS	Drop spacing
DSC	Differential Scanning Calorimetry
E-beam	Electron beam
ECTFE	Ethylene-Chlorotrifluoroethylene
ETFE	Ethylene-Tetrafluoroethylene
EVE	Ester Vinyl Ether
EVE-OH	Ester Vinyl Ethers OH
FDM	Fused Deposition Modeling
FEP	Fluorinated Ethylene Propylene
FFKM	Perfluoroelastomer
FKM	Fluorocarbon elastomer
FRI	Flow rate index
FT4	FT4 Powder Rheometer System
FT-IR	Fourier transform infrared spectroscopy
HFIB	Hexafluoroisobutylene
HFP	Hexafluoropropylene
HFPO	Hexafluoropropylene Oxide
LS	Laser Sintering
MFA	Methylfluoroalkoxy resin

MJ	Material Jetting
P(VDF-TrFE)	Polyvinylidene fluoride trifluoroethylene
PA	Polyamide
PBF	Powder bed fusion
PCL	Polycaprolactone
PCTFE	Polychlorotrifluoroethylene
PDD	2,2-dimethyl-1,3-dioxole
PEEK	Poly(ether ether ketone)
PEK	Poly(ether ketone)
PEVE	Perfluoroethylvinyl Ether
PFA	Perfluoroalkoxy resin
PLA	Polylactide
PLLA	Poly-L-lactide
PMVE	Perfluoromethylvinyl Ether
pPBF	Polymer Powder Bed Fusion
PPVE	Perfluoropropylvinyl Ether
PTFE	Polytetrafluoroethylene
PVDF	Polyvinylidene fluoride
PVF	Polyvinyl fluoride
SBF	Simulated body fluid
SE	Specific energy
SEM	Scanning Electron Microscope
SLA	Vat Photopolymerisation
SLS	Selective Laser Sintering
TFE	Tetrafluoroethylene
Tg	Glass transition temperature
TGA	Thermogravimetric analysis
THE	Hexafluoropropylene-Tetrafluoroethylene-Ethylene
THV	Tetrafluoroethylene, Hexafluoropropene, Vinylidene fluoride terpolymer
Tm	Melting temperature
TrFE	Trifluoroethylene
VDF	Vinylidene Fluoride
VF	Vinyl Fluoride
ZST	Zero Strength Time

1. Introduction

1.1 Context

Additive Manufacturing (AM) is defined as a process that uses digital data (CAD) to fabricate a 3D object by selectively adding material layer by layer [1]. As reported by the American Society for Testing and Materials International (ASTM), 3D printers can be classified in 7 process categories [2]:

- binder jetting: "*an additive manufacturing process in which a liquid bonding agent is selectively deposited to join powder materials*".
- directed energy deposition: *"an additive manufacturing process in which focused thermal energy is used to fuse materials by melting as they are being deposited"*.
- material extrusion: "*an additive manufacturing process in which material is selectively dispensed through a nozzle or orifice*".
- material jetting: "*an additive manufacturing process in which droplets of build material are selectively deposited*".
- powder bed fusion: "*an additive manufacturing process in which thermal energy selectively fuses regions of a powder bed*".
- sheet lamination: "*an additive manufacturing process in which sheets of material are bonded to form an object*".
- vat photopolymerization: "*an additive manufacturing process in which liquid photopolymer in a vat is selectively cured by light-activated polymerization*".

AM saw its first commercialisation in the 1980s with a stereolithography printer designed by 3D Systems [1]. The first application of this technology involved the production of prototypes, hence the name "Rapid Prototyping". For many years, AM was limited to prototyping due to the low mechanical strength of the produced part. Currently, with limited post-processing operations, AM is capable of producing functional end-use parts presenting many advantages over traditional manufacturing [1] such as:

- Complex geometries, topology optimisation, light weight [3], [4]
- Personal / tailored applications (e.g. customised prosthetics and implants [5]–[7])
- Assembly reduction (reduced labour and capital infrastructure, Figure 1.2) [1], [8]
- Reduced development cost by 40-70% [9]
- Shorter lead-times by as much as 90% [9]
- Cheaper for low volume production due to zero tooling [10], [11]

- Functionally graded material (e.g. turbine blades with high mechanical properties and thermal performance in different locations [12])
- Often lower material waste
- Lower transportation cost of finished goods as they can be printed at the required location (as special equipment or tooling are no longer required) [13], [14]
- Create moulds for investment casting or the mould itself (Figure 1.1) [13], [14]

Nonetheless, AM is not without drawbacks:

- Poor surface finish [1]
- Lower dimensional accuracy compared to traditional manufacturing [1]
- Narrow material portfolio [15]
- Slow printing speed [1]

Future developments of AM:

- Cheaper, faster, more reliable, safer, versatile, and environmentally friendly [1]
- Wider material portfolio [15]
- Fully optimised multimaterial printers
- Eliminate the need for large warehouse (e.g. digital spare parts) and expensive tooling, leading to smaller and better distributed production facilities [1]

At the beginning of its era (1980s), AM was mainly used as a prototyping device, nevertheless it led to great economic benefits thanks to an enhanced visualization of the design and its flaws, flow testing, wind tunnel testing, and reduction of lead-time [1]. All these features produced a saving of thousands of dollars and months of prototyping for many companies [16]. The greatest drive for this technology has been given by the medical industry because of patient-tailored solutions and by the aerospace and automotive industries because of the complex geometric capabilities, light weights, and shorter lead-times. Some of the medical applications include: surgical and diagnostic aids (e.g. visualising and touching the vascular tracks inside a skull or organ [17], [18]), prosthetic development (e.g. custom made implants [5]–[7]), manufacturing (e.g. prosthetic hands and in-the-ear hearing aids [19]), and tissue engineering (e.g. scaffold and living cells to aid the recovery from an injury [7]) [1].
In 2015, GE Aviation started the production of a new compact fuel nozzle design by AM previously composed and assembled from 18-20 different parts (Figure 1.2). The useful life of the fuel nozzle is estimated to be five times longer while weighting 25% less and being more efficient [8], [20]. They recently produced their 30,000th fuel nozzle.

AM in the Automotive industry, while still too expensive for mass manufacturing, is widely used in low volume productions, prototyping, and in the racing sector (e.g. Formula 1, NASCAR) [1].

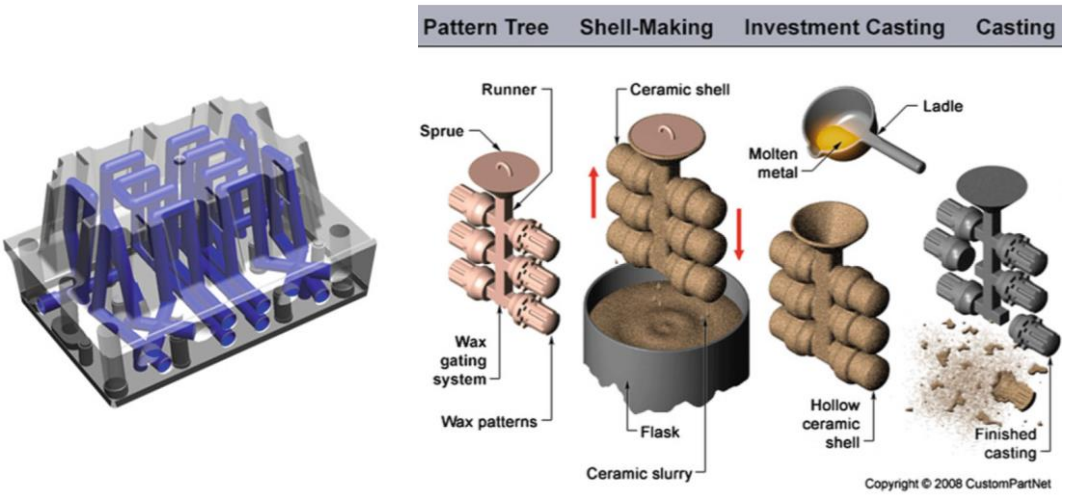


Figure 1.1 – Left: a tool with optimised cooling channels design [21]. *Right: schematic of the investment casting process* [1].



Figure 1.2 – 3D printed fuel nozzle by GE Aviation; 18-20 different parts merged in one single design [1], [8], [20].

1.2 Motivation, aim and objectives

AM has proven to be a capable manufacturing process with almost endless possibilities. Still, its potential is limited by the low number of processable materials, particularly in polymeric materials. Therefore, the aim of this PhD is to demonstrate the feasibility of using a previously unexplored material set (PCTFE, PFA, and THV) in AM through the use of the powder bed fusion (pPBF) and material jetting techniques (MJ). Other AM techniques such as vat photopolymerization, material extrusion, and binder jetting are available to process polymer. Nonetheless, vat photopolymerization require the use of UV curable monomers and the majority of the fluoropolymer monomers are gasses at room temperature, flammable, explosive, toxic, and very expensive. A way around this issue would be to disperse the chosen

fluoropolymer powder in a UV curable resin which would act as binder and be eliminated during the next sintering step. This specific route was investigated by 3M (section 2.4.2). Similarly, binder jetting would also require a binder that could be degraded and completely removed during the sintering step. Material extrusion is a promising technique thanks to its low entry cost and good quality of the produced parts. Nonetheless, a tailor-made system is needed to handle the corrosive and very toxic decomposition products of fluoropolymers. Decomposition should be avoided but it is always a possibility. Compared to material extrusion, pPBF allows for more complex geometries, better surface finish, nitrogen atmosphere, higher resolution, higher accuracy, and generally higher mechanical properties. Finally, MJ is the only AM technique capable of processing solutions/inks [1]. For these reasons pPBF and MJ were selected as the most appropriate AM techniques to process fluoropolymers.

Fluoropolymers have many outstanding properties such as wide service temperature, excellent chemical resistance, low gas permeability, low dielectric constant, low surface energy, and resistance to flames and sunlight. Because of all these properties they would be a significant addition to the 3D printing material portfolio. Among the many available fluoropolymers on the market, THV, PCTFE, and PFA have been chosen as the most interesting fluoropolymers to study as they cover a wide range of melting temperatures and properties. To show the feasibility of printing fluoropolymers with powder bed fusion and material jetting, the following objectives were identified for this PhD:

1. Investigate the properties of commercial powders to assess their potential use in powder bed fusion and material jetting with the use of several instruments and techniques
    - DSC, TGA, particle size distribution, FT4 powder rheometer, dissolution and precipitation, FT-IR, GPC, rheometer, drop shape analyser.
    - Use of additives and thermal treatments to improve the processability of the polymers in powder bed fusion and material jetting
2. Laser sintering of the PCTFE and PFA powders. Solve issues related to flowability and warping, optimise process parameters, and print functional parts.
3. Material jetting of THV. Use of two systems, Dimatix and PICO Pμlse, to print a wide variety of formulations made from several solvents and polymer loadings. Optimise the process parameters and print functional parts. Mechanical characterisation of the printed parts and investigation of possible applications.

1.3 Statement of novelty

This PhD has shown the possibility of both using PCTFE and PFA in pPBF and inkjet several THV formulations. Small parts, membranes and films were successfully produced with mechanical properties comparable to those of traditional manufacturing. Several techniques were adopted to improve the powder flow, bulk density, and minimise warping. Specifically, this thesis demonstrates novelty in the following areas;

1. Isothermal crystallisation and crystallisation activation energy of PCTFE and PFA with and without the addition of carbon black.
2. Use of a CO_2 laser to increase the particle size and flowability of powders. Sintering of the polymeric powder with a CO_2 laser and subsequent grinding.
3. Use of the FT4 powder rheometer to investigate the effect of carbon black, fumed nano-silica and thermal treatments on the flowability and conditioned bulk density of the PCTFE and PFA powders.
4. Printing of PFA membranes via pPBF.
5. Printing of small parts made of PCTFE via pPBF.
6. Printing of several formulations of THV via MJ and measurement of the mechanical properties.
7. Initial investigation on the permeability of THV for possible drug releasing applications.

1.4 Thesis structure

A description of the content of each chapter in the thesis is listed below.

Chapter 2: Literature review provides a review of the relevant studies on powder bed fusion and material jetting. The literature is split into three sections: powder bed fusion, material jetting, and fluoropolymers. The literature regarding the use of fluoropolymers in AM is very limited, general notions about the two printing techniques are also given. Finally, the chapter closes with a summary of the gaps in research found during the literature review and the novelty elements of the PhD.

Chapter 3: Methods and materials presents the established equipment, methods, and materials used in this study, this involves: characterisation of the raw material, powder modification, powder bed fusion, ink development, E-beam crosslink, and jetting. It also details the processes used to analyse the samples: porosity, determination of printed sample profiles, and mechanical tests.

Chapter 4: Powder bed fusion presents the work relating to the development and printing of the PCTFE and PFA powders. Firstly, results related to the analyses and improvement of the powders, then results related to the initial powder bed fusion of the powders and issues encountered, and finally detection of the limits of the technique/powders, possible countermeasures, and printing of thin membranes.

Chapter 5: Material jetting of THV presents the work relating to the development and printing of the THV inks. Firstly, results related to the development of the THV inks, then results related to the initial film printing, and finally investigation of the water permeability, effect of a pulsed electron beam on THV, and mechanical tests.

Chapter 6: Discussion discusses the findings of the PhD for each of the fluoropolymers and printers used. These findings will be compared to the literature surveyed, and used to highlight the novelty of this PhD.

Chapter 7: Conclusions highlights the main conclusions of this research, and identifies how the investigations in this study are novel.

Chapter 8: Recommendations for future work highlight areas where this PhD has not been able to fully investigate the process, and outline how this can be carried out.

2 Literature review

2.1 Introduction

This PhD's focus is the research and analysis of the polymer Powder Bed Fusion (pPBF) and Material Jetting (MJ) process for the creation of parts made of PCTFE, PFA, and THV. The literature was reviewed to understand the pPBF and MJ process, with a specific focus on the challenges which limit the range of processable materials. This literature review is separated into three sections; 1) the pPBF process, and 2) the MJ printing process, and 3) fluoropolymer materials. In the first section a brief background of the Powder bed fusion process, required material properties and main challenges are discussed. In the second section a brief background of the Material Jetting process, required material properties and main challenges are discussed. Finally, in the third section, fluoropolymer materials and their applications and properties are introduced. Their use in Additive Manufacturing is also reported, even though, to date, only few publications have been produced on the topic.

2.2 Powder bed fusion

2.2.1 Overview

Chapter 1.1 introduced AM and the seven process categories that it includes. This section will discuss the pPBF process (often referred to as Laser Sintering (LS)) as this was one of the two processes used in this PhD. This process is well described in literature today [22]–[25], only a brief overview of the process will be given here, while more focus is given to the relevant information in connection with the thesis topic.

In the pPBF process a heat source is used to selectively sinter and/or melt a powder bed (Figure 2.1) [1]. The powder inside the printing chamber is heated and kept at a temperature just below the melting point of the polymer while a laser selectively scans the surface of the powder bed to sinter the polymer in the desired position/shape. Next, the build platform drops a layer, the roller (or recoater blade) spreads another layer of powder, the laser scans the surface again and the cycle repeats until the whole part is printed [1]. Afterwards, the sealed build chamber is slowly cooled down to ambient temperature to avoid distortion, cracks and unwanted oxidation (the build chamber is kept under a nitrogen atmosphere). This step can take several hours, a much longer time compared to the ~ 15 minutes step in injection moulding [26]. The part is then removed from the build chamber and cleaned from the remaining loose powder. During the print, the unsintered powder works as support structure, no support structure is required and very complex geometries can be achieved.

It is worth pointing out that the term sintering is generally utilised when necking between the molten surfaces of adjacent particles of powdered material is achieved by means of heating without liquefaction [27]; while full melting can occur in laser sintering, the term is still used to distinguish this process from the process that uses metals (laser melting). During the process, no mechanical pressure is applied and the sintering relies only on temperature, gravity and capillary forces [22], [28], [29].

When compared to other 3D Printing techniques, powder bed fusion can process a wide variety of material such as metals, ceramics, and polymers [28], [30]. In the manufacturing of the latter, the most common thermal source are lasers, particularly the CO_2 laser which has a wavelength between 10.2 and 10.8 µm (925 and 980 cm^{-1}) [31]. It is important that the processed polymers absorb in this specific region of the infrared spectra and, usually, this is not a problem for most polymers as the C-H and C-C bonds have an acceptable absorption in the CO_2 laser wavelength [32], [33]. Additives can also be used to increase the absorbance of the powder in the wavelength of the thermal source.

The quality of the printed parts can be influenced by many factors such as the powder/material properties (density, porosity, powder flow, absorbance, thermal conduction, heat of fusion, degradation temperature/mechanism, processing window, particle size distribution), and printer settings (laser power/speed/spot size, hatch spacing, bed temperature, recoating system design, layer thickness [1], [22], [34]). Bourell et al. [23] summarised some of the issues that can be encountered in pPBF such as the increase in viscosity for some polymers with aging which can lead to porosity, the uneven bed temperatures due to convection motions in the nitrogen atmosphere, change in absorbance due to change in particle size, unmelted powder cores, low elongation at break, and smaller crystalline structures and lower polymer chain entanglements compared to injection mould.

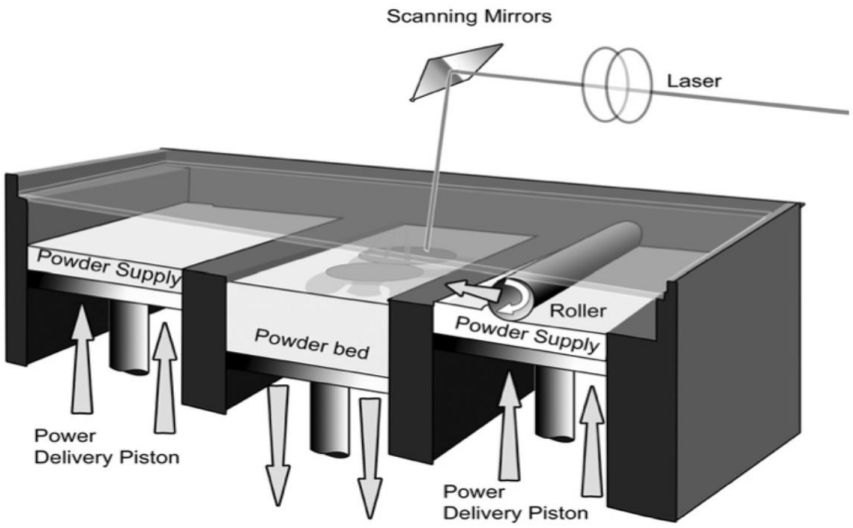


Figure 2.1- pPBF system schematic. Figure reproduced from [35].

2.2.2 Polymers for powder bed fusion

It is well-known that additive manufacturing (AM), and more specifically LS, has great potential but several limitations, one of which is the narrow material portfolio [15], [36]; of the tens of thousands of different polymers available for injection moulding, less than 30 of them are suitable for pPBF [22]. Furthermore, polyamide 12 made up ~ 95 % of the market in 2009 [9]. The main polymers used commercially in pPBF are listed below:

- PA12 (polyamide 12) [37]
- PA11 (polyamide 11) [38]
- PA612 (polyamide 612) [38]
- PA6 (polyamide 6) [38]
- PS (polystyrene) [39]
- PAEK (polyaryletherketone) [39], [40]
- PEBA (polyether block amide) [39]
- PP Polypropylene [37]
- PPS (polyphenylene sulfide) [41]
- TPU (thermoplastic polyurethane) [37]

Generally, small amounts of fillers can be used to increase mechanical and/or physical properties such as stiffness, heat and flame resistance, thermal conductivity, laser absorbance, bioactivity, and biodegradability [42]–[44].

2.2.3 Material properties and processing parameters

The narrow LS material portfolio is not just a coincidence. This limited number of materials is due to the specific proprieties required by the pPBF process, including precise particle size distribution (~45-90 µm [22]) to guarantee powder flow; relatively low melt viscosity to avoid porosity; absorbance in the wavelength of the specific heating element (e.g. CO_2 laser); and a wide processing window (i.e. the difference between melting and crystallisation temperature) to supress dimensional warping. The next sections will analyse these and other aspects in more depth.

2.2.3.1 Amorphous polymers

The polymer chains in amorphous materials are not organised in any particular structure, they do not have a defined melting point but they present a glass transition temperature (T_g) and show a gradual decrease in viscosity and density as the temperature increases [45]. Because of this, they exhibit more porous and less dense parts with a lower and more gradual shrinkage when compared to crystalline polymers [22], [34], [46], [47].

2.2.3.2 Semi-crystalline polymers and thermal properties

Semi-crystalline polymers possess both amorphous and crystalline regions. Because of the amorphous regions they possess a T_g and because of the crystalline regions (portion of polymer chains organised in a well-defined structure) they also present a well-defined melting and crystallisation temperature. In pPBF, having a sharp melting point and crystallisation temperature is favourable to improve dimensional stability and avoid warping, curling, and deformation [1].

During crystallisation (near the melting temperature, Tm) the specific volume of the polymer has a sharp decrease (shrinkage) due to a reorganisation of the polymer chains into crystalline regions (Figure 2.2) [48], [49]. An increase in crystallinity leads to an increase of density. The change in specific volume is proportional to the degree of crystallinity, amorphous polymers (no crystallinity) do not show any sharp change in specific volume, partially crystalline polymer show an intermediate change, and "fully" (as much crystallinity as possible) crystalline polymer show the biggest change. Therefore, it is important to have a good control of the crystallisation of the polymer during pPBF minimise warping and distortion. A low thermal expansion coefficient is also favourable as it would increase the part accuracy.

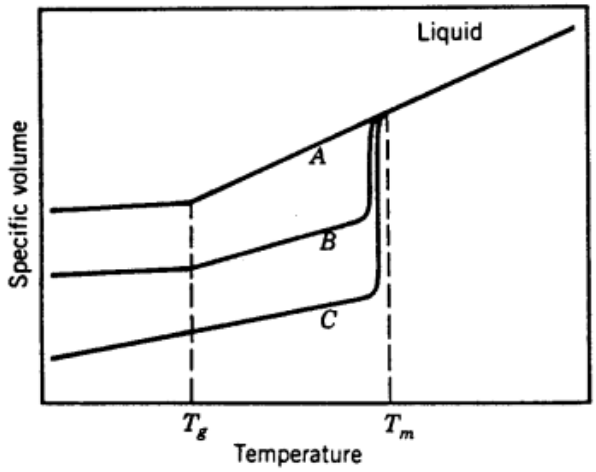


Figure 2.2 - Specific volume against temperature for (A) amorphous (B) partially crystalline, and (C) "fully" crystalline polymers. Image reproduced from [48].

The difference in temperature between melting and crystallisation point is usually referred as consolidation window, processing window, sintering window, or supercoiling window and it is believed to be essential for the success of a print (Figure 2.3) [1], [50], [51]. To obtain optimal results, the temperature of the powder bed should be kept in this window for the duration of the printing process as the printed parts will remain in a liquid state and crystallise only at the end of the process. This improves bonding between layers and prevents the warping and deformation caused by shrinkage which is in turn caused by a non-uniform crystallisation due to temperature gradients inside the powder bed [52], [53]. If the processing window is too

small the process is not robust as small variations in the processing temperature drastically affects the quality of the print, like in the case of ultra-high-molecular-weight polyethylene (UHMWPE) [54].

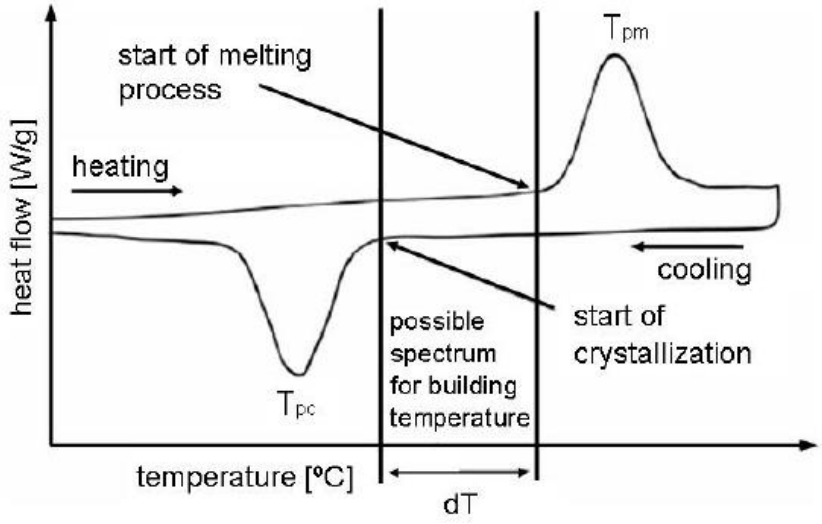


Figure 2.3- Melting and crystallisation characteristics for an idealized polymer DSC curve for pPBF [1], [50]

A wide processing window of roughly 30 °C [55] is, in fact, one of the reasons behind the success of Polyamide 12 in pPBF. In the case of CAPA 6501 polycaprolactone, the processing window was just 2 °C and small fluctuations in the processing temperature led to a failure due to curling or caking [56]. Nevertheless, some materials such as PEK [51], PEEK [57], thermoplastic elastomers (TPE) [25], and DURAFORM Flex grades [57] possess a very narrow processing window or none at all but can still be printed successfully. Furthermore, Wegner et al. [58] analysed PA 2200, Rolaserit PEGR, POM, PA 6, PBT, Rolaserit PP and concluded that a wide processing windows does not always guarantee a successful print. These conflicting results suggest that the influence of the processing window is material specific and a more in-depth investigation is needed to fully understand and predict it. An investigation on the warping behaviours in pPBF can be found in the literature [59].

A high heat of fusion (the heat of fusion indicate the amount of energy required by one gram of material to change its state from solid to liquid) is favourable as it improves the dimensional accuracy by reducing the amount of loose powder that partially sinters at the edges of the melt pools (as more energy is required to melt them.) [34]. Semi-crystalline polymers show superior mechanical properties, higher densities, and lower porosities when compared to amorphous polymers [34], [46], [47].

2.2.3.3 Powder bed temperature

As introduced in the previous section, small variations in the temperature of the powder bed can result in considerable changes in porosity, part density, and mechanical properties; higher temperatures (up to an optimal temperature) usually improve density and mechanical properties [60]. High powder bed temperatures also minimise the energy required by the laser to melt the powder, the temperature gradient, and thermal expansion between sintered and unsintered powder [47]. Shrinkage can also be reduced by pre-heating below T_m for semi-crystalline polymer and at/below T_g for amorphous polymer [22].

The ideal powder bed temperature is material-specific and range between 3 and 60 °C below the melting temperature for semi-crystalline polymers [22], [61]. The powder bed temperature may have other material-specific effects on the polymer powder such as decomposition or polymerisation. For example, PA12 powder is still reactive and, if kept at high temperatures long enough, the polymerisation between adjacent chains (polycondensation reactions) can take place leading to an increase in molecular weight, particle size, and mechanical properties, and decrease in powder flow and melt flow index (increase in viscosity) [55], [62]. Furthermore, the increase in viscosity and particle size leads to several issues such as orange peel (rough surface), lack of fusion, and reduced recyclability [51], [63], [64]. Thus, it is clear that an uneven powder bed temperature distribution can greatly affect the properties of the printed parts [22], [60]. Finally, the cooling rate is another important parameter as it can influence the presence of cracks, distortion, and part density (crystallinity) [34], [45], [65].

2.2.3.4 Laser parameters, layer thickness

As explained in the previous sections, lasers are the most common thermal source in pPBF. The Energy Density (ED) is the energy applied to the powder by the laser and is measured in W/mm^2. The ED is calculated with the following formula:

$$ED = \frac{laser\ power}{scan\ speed * hatch\ spacing} \qquad \textit{Equation 1}$$

Sometimes, a slightly different formula, where the hatch spacing is substituted with the laser spot size (diameter), is utilised:

$$ED = \frac{laser\ power}{scan\ \text{speed} * laser\ spot\ size} \qquad \textit{Equation 2}$$

Therefore, it is always important to specify how the ED is calculated. Nonetheless, while the ED can give an idea of the energy necessary to sinter a specific polymer, the same value of ED often gives different results when obtained by using different parameters (for example, a high laser power and high scan speed and a low laser power and low scan speed process can

have the same ED but give different melting behaviours). Furthermore, when the ideal ED for a specific polymer is calculated or discovered experimentally, it cannot be used as guideline or to compare different polymers. This is because properties such as the absorbance in the wavelength of the laser, powder bed temperature, particle size distribution, melt viscosity, and thermal properties (e.g. specific heat, heat of fusion) of the polymers play an important role in the sintering behaviour and energy required to achieve melting without decomposition. Furthermore, the absorbance of the laser is influenced by the particle size, packing of the powder bed and pore structure. In fact, as a rule of thumb, a material exhibits a higher absorptance in its powder form than in its dense form. Furthermore, bigger powder particles have a lower absorbance and the absorbance changes during sintering as the pore structure changes [66]–[68].

The laser scan pattern and speed is controlled by galvanometers and the maximum reachable speed is approximately 5000 mm/s [31]. The average laser spot size is roughly 300 µm and the suggested hatch spacing is between 1/3 and 1/6 of the laser spot size. The layer thickness is usually between 50 and 200 µm and, as a rule of thumb, it should be roughly three times bigger than the average powder particle size [1], [22], [69].

A possible scenario, while using the wrong process parameters, is an ED which is too high. The excessive amount of energy delivered to the powder could cause high polymer temperatures and degradation. Degradation can lead to the production of gases (often toxic) which can lead to porous parts (gasses trapped in the molten polymer), and to a decrease in molecular weight (Mw) which can lead to lower mechanical properties.

In the opposite scenario, several publications [34], [70] showed that a low ED can cause partial melting of the powder particles leaving unmolten cores. This effect was visible in the DSC analysis which showed 2 peaks (one for the melted particles and one for the unmolten cores). When the ED was increased, only one peak was visible, meaning that the cores of the powder particles were melted. It was suggested that, with the presence of unmolten particle cores, the printed parts could behave as a composite material. Depending on the strength of the interface between core and molten polymer, it could lead to higher or lower properties.

The laser parameters also influence the heating rate which can vary from ~ 1000 K/s to 22000 K/s [24], [71]. Because of the fast heating and cooling rates, it is often challenging for high viscosity polymers to achieve full melting and consolidation [62]. On the other hand, a lower viscosity leads to a higher shrinkage and lower part accuracy [28].

2.2.4 Cohesive forces

The cohesion between particles is the root cause of powder flow issues. Particles behave in a cohesive way when the interparticle attractive forces are larger than the weight of the particles.

In contrast, when the weight of the particles is larger than the interparticle attractive forces, the powder is said to be free flowing [72].

Figure 2.4 shows the behaviour of cohesive and non-cohesive powders. In non-cohesive powders, the force of gravity is strong enough to efficiently pack the particles leaving only random voids. In cohesive powders, the particles are so small that the force of gravity acting on each particle is weaker than the cohesive forces between particles. This leads to a bad packing (low bulk density) and structural voids (pockets of air) [72]. For this reason, generally, the powders used in pPBF have a particle size distribution between 45 and 90 µm [22].

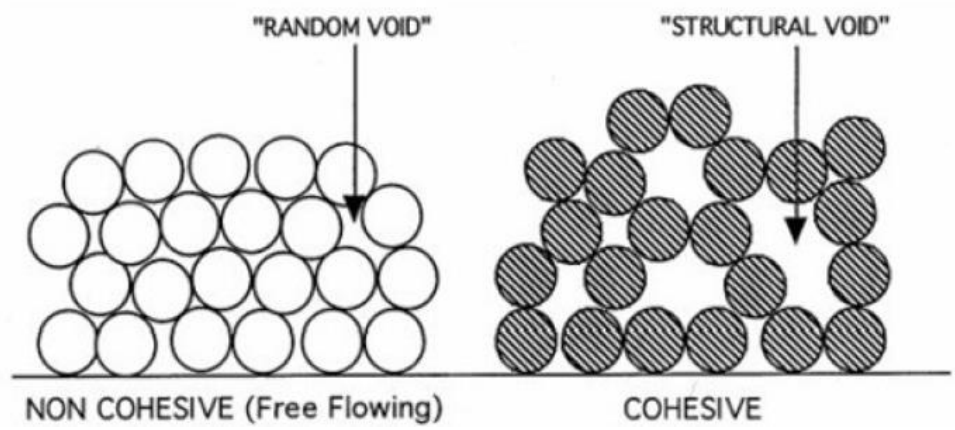


Figure 2.4 - Illustration of a cohesive and non-cohesive powder. Figure reproduced from [72].

The cohesion is caused by five forces: van der Waals forces, electrostatic forces, liquid bridges, solid bridges, and mechanical interlocking. The next sections explain in more depth each of these 5 forces, their nature and how they can be minimised.

2.2.4.1 Van der Waals forces

Van der Waals forces are always present and cannot be eliminated as they are an intrinsic property of the material. Materials with low surface energies (e.g. fluoropolymers) have weaker van der Waals forces [73]. The latter are proportional to the distance and surface contact between particles and can be decreased by increasing the distance and decreasing the surface contact between particles. This is usually done with the addition of a flowing agent - a material with a very small particle size, usually in the nanometres range, that position itself between the particles of the powder [73]. Because of their high surface area, most flowing agents absorb water faster than the cohesive powder and do not tend to became sticky. They can be organic or inorganic and one of the most used is fumed nano-silica [74], [75].

The van der Waals forces are considered to be made of three components: dipole-dipole interaction (Keesom), dipole-induced dipole interaction (Debye), and induce dipole-induced dipole (London) [76]. While the Keesom and Debye forces require the presence of at least one

dipole molecule, the London forces do not need a dipole, thus they are always present. The intensity of the London dispersion forces is proportional to the polarizability of the molecule (which is low for fluoropolymers) which depends on the total number of electrons and the distance over which they can move (higher distance, higher chances of a temporary dipole). Bigger molecules tend to have stronger London forces, hence higher boiling temperatures. Van der Waals forces are typically negligible at particle distances of 10-40 nm [76], [77]. An interesting example from nature, is the case of the spores of the puff-ball. The spores evolved to have small asperities on their surface to decrease the surface contact between spore particles and increase their separation. The decrease in cohesion allows the spores to be more easily dispersed in air [77].

2.2.4.2 Electrostatic forces

Electrostatic forces are similar in nature to the van der Waals forces but they operate at longer ranges and are caused by the presence of static charges. Static charges accumulate on the surface of a material due to triboelectric phenomena and they are a common issue for insulating materials (e.g. polymers) as they usually cannot discharge these charges even when grounded [73]. This issue is usually solved by increasing the conductivity of the material and grounding the equipment that comes in contact with the powder. Another option is to use a static eliminator (generally a metal bar with ion generating nozzles) that bombards the surface with positive and negative ions to neutralise the static charges from the surface of the particles and restore the electrical balance [78]. Generally, during the pPBF process the powder is constantly moved from one side of the chamber to the other. This can cause the accumulation of static charges on the surface of the particles and have a negative impact on the flowability of the powder and quality of the spread layer.

2.2.4.3 Liquid bridges

Liquid bridges, when present, exert the strongest force among the cohesive forces and are usually caused by water bridges between particles caused by the water adsorbed on the particles [76]. Liquid bridges can be avoided by decreasing the relative humidity. Nonetheless, the presence of a liquid veil above the particle could be beneficial in reducing the static electricity thanks to an increase in conductivity. Usually, liquid bridges are not an issue for most materials in pPBF as the powder bed is kept in a nitrogen atmosphere and at temperatures above 100 °C.

2.2.4.4 Solid bridges

Generally, a powder manifests solid bridges when the powder particles reach temperatures high enough to cause sintering. In extreme cases the entire powder bed can form a solid cake.

This is often observed in pPBF when the powder bed temperature is kept too close to the melting temperature of the polymer [22]. For some polymers this could even happen at temperatures just above their glass transition temperature. Solid bridges are initiated by everything that cause the particle to physically join such as the presence of solvent or solvent vapours.

2.2.4.5 Mechanical interlocking

The mechanical interlocking is governed by the shape of the particles. Irregular shaped particles tend to physically lock to one another and increase the cohesivity of the powder. A similar effect is also caused by rough surfaces [79]. Thus, smooth spherical particles have the best flowability and are preferred in pPBF. Several techniques have been developed to increase the sphericity and smoothness of pPBF powders (section 3.3.11).

2.3 Material Jetting

2.3.1 Overview

The other AM technique used in this PhD was Material Jetting (MJ). This process is well described in literature [80]–[82] and only a brief overview of the process is given here. The focus is kept to the relevant information in connection with the thesis topic. Similarly to pPBF, one of the major limitation of MJ is its narrow material portfolio due the specific material requirements such as solubility, viscosity, surface tension, molecular weight, and evaporation rate (section 2.3.2) [83]. MJ has been used in several applications such as thin-film transistor [84], resistors [85], antenna emitter [86], light emitting diodes [87], biodegradable microspheres [88], and microneedles [89]. One of the advantages of MJ over several other AM techniques is its ability to produce multi-material parts [83].

The MJ technology works very similarly to the traditional inkjet (ink printing) technology. Drops of solution/ink are ejected at precise coordinates and amounts to form a final product. In traditional inkjet, this often means printing a 2D document or image. In AM, this means printing 3D parts/structures by printing multiple layers. There are two main method of ejection: drop-on-demand (DoD) and continuous inkjet (CIJ). In DoD the drops are generated only when needed, in CIJ a stream of drops is continuously generated and directed/disposed into a gutter when not needed (Figure 2.5) [81]. DoD can be operated with a thermic or piezoelectric system. In the thermic system a small heating device heats the ink and generates a vapour bubble that pushes a drop out of the nozzle. In the piezoelectric system, which uses a piezoelectric actuator, an electric current is used to deform the piezoelectric element causing internal pressure waves that lead to the ejection of a drop of ink. The thermic system requires the inks to be thermally conductive and the high temperatures could have deleterious effects

on the ink. Nonetheless, this system is quite cheap and is still widely used in home desktop printers. In this PhD a Dimatix DMP-2830 printer with a piezoelectric DoD system was used. The speed of the ejected drops is usually between 5 and 8 m/s for DoD and > 10 m/s for CIJ [80].

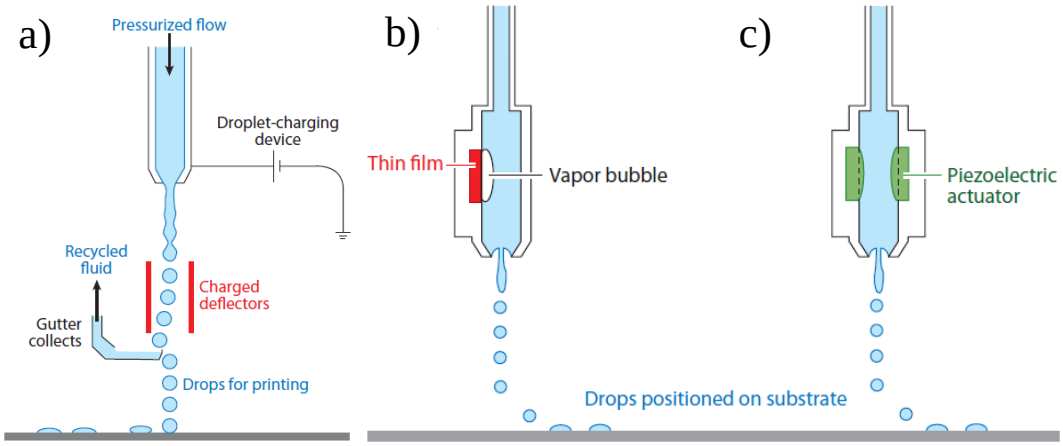


Figure 2.5 – Drop ejection by (a) continuous inkjet, (b) thermal drop-on-demand and (c) piezoelectric drop-on-demand. Figure reproduced from Derby [81].

The Dimatix Fluid Formulation Guidelines [90] states that the ideal viscosity range of the inks is between 10 and 12 mPa.s at operating temperatures. Viscosities up to 30 mPa.s are also printable but with limited performance. The suggested surface tension is between 28 and 33 dynes/cm (0.028 - 0.033 N/m). Surface tensions up to 70 dynes/cm are also printable but with limited performance. Evaporation at the nozzle/air interface of the jetting fluid should be avoided as it could lead to nozzle blockage. The addition of a humectant such as a glycol is usually suggested to lower evaporation. Finally, a pH within the range of 4 - 9 is recommended as different values may cause corrosion and damage the printhead.

For higher viscosity fluids, pneumatic and mechanical actuators can be used to produce DoD. The latter technique uses a jet valve which is actuated by an electrical modulated piezoelectric for high-speed and accurate dispensing. The printer uses a tuneable pressurised reservoir that pneumatically supplies the ink to the valve [91]. Figure 2.6 shows the ejection mechanism. First, the rod is in the closed position, blocking the flow of the ink out of the nozzle, then the rod is moved up in the opened position (Figure 2.6 a-b) by piezoelectric actuators. This creates a local negative pressure which fills the nozzle chamber with the ink. Finally, the rod goes back to the closed position (Figure 2.6 c-d) causing the ejection of a drop of ink. This cycle can be executed at frequencies as high as 1500 Hz. The closing speed and pulse time influence the volume, speed, and tail length of the ejected drop. The PICO Pµlse used in this PhD uses this jetting system.

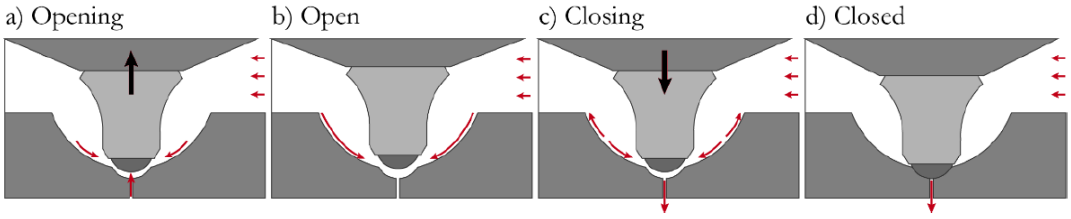


Figure 2.6 – Ejection mechanism of the PICO Pµlse. From left to right, opening and closing of the valve which causes the filling of the nozzle chamber and ejection of a drop. This cycle allows the ejection of a single drop of ink. The black and red arrows indicate the direction of the rod and ink flow, respectively. Figure reproduced from [92].

2.3.2 Printability assessment

In the jetting of low viscosity inks, a commonly used factor to assess the 'printability' of the ink is the Z number [1], [82] (reciprocal of the Ohnesorge number, Oh) which is calculated with the following equation:

$$Z\ number = \frac{1}{Oh} = \frac{\sqrt{\rho r \gamma}}{\mu} \qquad \textit{Equation 3}$$

Where ρ is the density of the ink, r is the characteristic length (usually taken as the nozzle diameter, 21.5 µm in the case of the Dimatix [90]), γ is the surface energy of the ink, and µ is the viscosity of the ink. The general rule of thumb is that if Z is between 1 and 10 the ink should have good printability. For values lower than 1, the ink is too viscous while for values above 10 the ink is too fluid [82]. Jang et al. [93] suggested that a more suitable range was $4 < Z < 14$. Other parameters useful to characterise the printability of viscoelastic fluids are the Weissenberg (Wi) number and Deborah (De) number [94] but they require the relaxation time of the polymer to be determined and are not as straightforward as the Z number [80]. Viscoelastic behaviours are usually encountered when the inks contain high molecular weight (Mw) polymers [95]–[97]. Haque et al. [98] calculated that with the typical strain rates encountered in material jetting ($> 5x10^{-4}\ s^{-1}$), polymers with a Mw higher than 5×10^4 g/mol were going to experience coil-stretch transitions. While they are in this coil-stretch state, the polymer chains become entangled and intermolecular interactions can arise, leading to a temporary increase in viscosity. When the external forces are removed the polymer chains contract to return to the more thermodynamically stable coil state [97]. When this happens, the ejected drops tend to exhibit long tails and difficulties in being ejected, even at low ink viscosities. Jetting can still be achieved but higher voltages and drop velocities are required [98]. Moreover, Haque et al. [98] showed that in the case of viscoelastic fluids, the solubility of a polymer in a solvent did not have a significant effect on the maximum printable concentration but that a lower solvent viscosity allowed more concentrated solutions to be printed. Furthermore, while the viscosity of Newtonian fluids does not change with the shear rate, the viscosity of non-Newtonian fluids changes with the shear rate, for some it increases (shear-thickening) and for some it decreases (shear-thinning) [80]. Polymer solutions are

usually shear-thinning. In MJ the fluids are usually exposed at high shear rates (~10^4 s^{-1}) for short period of times (5 - 250 µm) [80], [99]. The next section will introduce one of the main issues that can be encountered in MJ, the coffee ring effect.

2.3.3 Coffee ring effect

The coffee ring effect is a well-known and studied phenomena [100] and it refers to solutes or dispersed particles in a solution that accumulate preferentially at the edges of an evaporating drop/film. Its primary cause is the pinning of the edge of the evaporating drop and uneven evaporation rate (higher at the edges of the drop) which cause the formation of an outward capillary flow to replenish the evaporated solvent. This outward capillary flow causes the coffee ring effect. When the edges of the drop are pinned, the majority of the solute will be deposited at the same position (edge) (Figure 2.7).

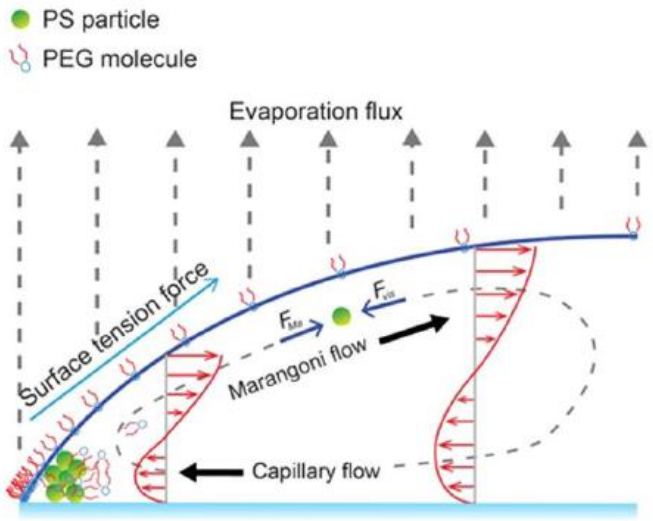


Figure 2.7 - Illustration of the capillary flow (cause of the coffee ring effect) and inwards Marangoni flow. Figure reproduced from [101].

The higher amount of solute at the edge causes the formation of a thicker ring and thinner centre (Figure 2.8a) [102]. When the coffee ring effect is absent the solute is homogenously distributed (Figure 2.8b) [102]. The coffee ring effect can be countered or suppressed in several ways.

The first way to counter the coffee ring effect is to create an inwards Marangoni flow (Figure 2.7). The latter is a flow of solution at the surface of a drop/film and is generated by surface tension gradients. The flow moves in the direction of the areas with the higher surface tension (from regions of low surface tension to regions of high surface tension). Therefore, and inwards Marangoni flow can be established by adding a solvent with a higher boiling point and lower surface tension (compared to the first solvent) [101]. During evaporation, at the

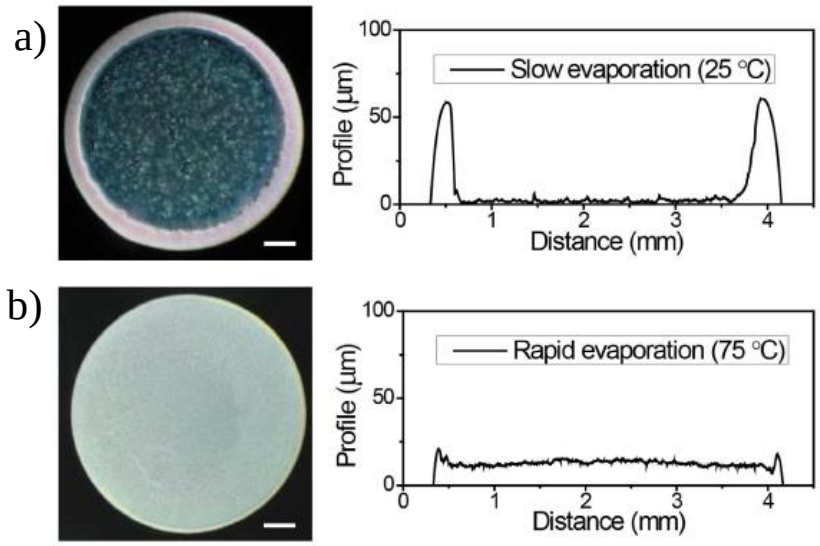


Figure 2.8 - Height profile of a drop where coffee ring is (a) present and (b) absent. Reproduced from [102].

edge of the drop/film, the more volatile solvent evaporates more quickly increasing the concentration of the high boiling solvent which also has a lower surface tension.

This creates a zone of lower surface tension at the edge and higher surface tension at the centre which creates an inward Marangoni flow. Surfactant could also be used to generate a similar effect. As the evaporation proceeds, the surfactants will accumulate at the edge creating an area with a lower surface tension (Figure 2.7) [101]. Temperature can also be used to obtain similar effects. A cold substrate was shown to lead to a stronger reduction in the evaporation rate at the edges compared to the centre of the drop/film, leading to a decrease of the coffee ring effect [103]. Furthermore, selectively increasing the temperature of the edge decreases the surface tension at the edge and establish an inwards Marangoni flow [104]. Nonetheless, the higher temperatures at the edges increase the evaporation rate at the edges and outward capillary flow (coffee ring effect). Consequently, the actual effect of the substrate temperature is quite controversial in the literature [102] [105].

The second way to counter the coffee ring effect is to stop the edges of the drop/film from pinning to the substrate. This can be done by using a substrate with a high receding contact angle [106], [107]. When the edge of the drop is not pinned the solute is more likely to be evenly distributed as the edges of the drop keep receding as more the evaporation progress (sometimes with a stick-slip motions [107]).

The third way to counter the coffee ring effect is to restrain the outward capillary flow. In the case of particles dispersed in a fluid, this can be done by changing the shape of the particles. While spherical particles, which flow and pack well, are more prone to give a strong coffee ring effect, ellipsoidal particles tend to jam and form an obstacle to the capillary flow [108].

A similar effect is observed when the viscosity of the solution is increased. The high viscosity slows down the diffusion and transport of the particles towards the edges [102].

The fourth way to counter the coffee ring effect is to change the evaporation profile of the drop/film. The coffee ring is in fact caused by the higher evaporation flux present at the edge of the drop. A mask could be used to modify the evaporation profile as showed by Harris et al. [109]. Saturating the environment with the solvent vapours was shown to slow down the evaporation rate and decrease the coffee ring effect by giving a more uniform evaporation profile to the drop [110]. In another work [102], it was shown that when high temperatures were used and the drop/film evaporated very quickly, the particles tended to accumulate at the air-liquid interface and not at the edge. This was caused by the quick descent of the interface which was faster than the particle diffusion.

2.4 Fluoropolymers

2.4.1 Introduction

Generally, fluoropolymers are made by the polymerization of tetrafluoroethylene (TFE) as homopolymer or as copolymer with other fluorinated or non-fluorinated monomers [111]. Table 2.2 reports a list of the most common monomers used to produce fluoropolymers, while Table 2.3 reports the main fluoropolymers grades commercially available.

Thanks to their outstanding properties such as wide continuous service temperatures, good release properties, biological inertness, low friction, low dielectric constant, low dissipation factor, and excellent resistance to chemicals, sunlight, flames and weathering without the addition of stabilizers, plasticiser or fillers, fluoropolymers have been widely used in all facets of human life from household to automotive, electrical and chemical industries, as well in medical devices and aircraft [112][113]. Partially fluorinated fluoropolymers such as PVDF, ETFE, ECTFE, and PCTFE have particularly good resistance to radiations and find application in the nuclear industry [113], [114]. For example, 20 megarads of radiation have little effect on the elongation at break and yield strength of PVDF, while 40 megarads causes a 40% drop in the elongation at break and an increase in yield strength [113]. While any one of these properties can be found in other materials, fluoropolymers are matchless when two or more of these properties are needed in the same application [111].

Typical applications include: gaskets, valve and pipe liners, wire and cable insulation, connectors, seals, food processing equipment covering, cookware coatings, cardiovascular grafts, heart patches, ligament replacement, and process surfaces [113]. Fluoropolymers gain their peculiar properties from the strong C-F bond (~480 kJ/mol, the strongest known single bond in organic chemistry (Table 2.1) [115]), which also increases the C-C bond strength by roughly 100 kJ/mol compared to that found in hydrocarbons (~360 kJ/mol) [116]. This

increase in bond energy is due to the high electronegativity of the fluorine atoms. In fact, the fluorine atoms, with their larger size (compared to hydrogen), shield the carbon backbone of the polymer, increasing its chemical resistance (Figure 2.9). The combination of strong bond energies, size, and electronegativity of fluorine atoms is the basis for the properties of fluoropolymers [117] [118]. The great thermal stability of fluoropolymers allows most of them to be easily recycled and processed multiple times without degradation. Furthermore, the high density of the polymer makes for facile separation from other polymers and the absence of additives increases the lifetime of the end products (plasticizer can evaporate and fillers could cause recycling problems) [111].

Polytetrafluoroethylene (Figure 2.9), also known with the trademark Teflon, is one of the most used fluoropolymers; the symmetrical arrangement of the atoms in the chain results in a lack of polarity and therefore in an exceptional electrical performance with a low dielectric constant and dissipation factor that remain consistent over a wide temperature range [111].

Table 2.1- Carbon Bond Energies [119]

Bond	Bond Energy (Kcal/mol)
C–F	116
C–H	99
C–O	84
C–C	83
C–Cl	78
C–Br	66
C–I	57

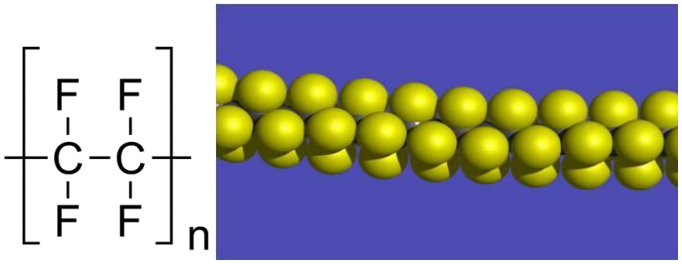


Figure 2.9- PTFE chemical structure, the fluorine atoms are represented as yellow spheres [117] [118]

The steric hindrance of the fluorine atoms makes the PTFE chains rigid (rod-like, Figure 2.9) and limit chain entanglement. The weak interactions between chains due to the lack of polarity and chain righty cause PTFE to suffer from cold flow (tendency of the PTFE chains/rods to slip one over the other when loads are applied even at low temperatures). The rod-like structure of the PTFE chains also leads to a great degree of order and crystallinity (up to 92-98% for virgin PTFE that has never been melted [120]).

The high molecular weight, degree of crystallinity, and rigid helical chain structure of PTFE lead the polymer to have a very high melting point of 335 °C with an upper continuous use temperature of 260 °C [111]. Some fluoropolymers such as polychlorotrifluoroethylene (PCTFE) can also be used at cryogenic temperature down to -251 °C [111]. Additionally, the excellent resistance to sunlight, flames, and weathering without the addition of stabilizers,

plasticizer or fillers [111] make them ideal for applications where assuring the absence of contaminants is crucial (e.g. chemical analysis).

With the exception of polytetrafluoroethylene (PTFE) and polyvinyl fluoride (PVF), all fluoropolymers are melt-processable into sheets, films, profiles, and mouldings using traditional manufacturing methods [112]. However, due to the large use of PTFE and its inability to be melted, special processes have been developed. PTFE powder is compressed, sintered and milled in its final shape. Therefore, complex geometries are not achievable and the wasted material can reach 50% of the final mass of the object. Moreover, the waste cannot be recycled via traditional methods, leading to both an economic loss and an environmental problem [111]. Additive manufacturing could drastically reduce these problems.

Table 2.2- Common monomers used in fluoropolymers and their boiling temperature.

Compound	**Formula**	Boiling Temperature at 1 atm (°C)
Ethylene	$CH_2=CH_2$	-104 [121]
Tetrafluoroethylene (TFE)	$CF_2=CF_2$	-75.6 [122]
Chlorotrifluoroethylene (CTFE)	$CF_2=CClF$	-27 [123]
Vinylidene Fluoride (VDF)	$CH_2=CF_2$	-83 [124]
Vinyl Fluoride (VF)	$CFH=CH_2$	-72 [125]
Propene	$CH_3CH=CH_2$	-47.7 [126]
Hexafluoropropylene (HFP)	$CF_3CF=CF_2$	-29.4 [127]
Hexafluoroisobutylene (HFIB)	$CF_3C(CH_2)CF_3$	14.5 [127]
Hexafluoropropylene Oxide (HFPO)	CF_3CFOCF_2	-27 [127]
Hexfluoroisopropylidene Bisphthalic Acid (6-FTA)	$C_6H_3(COOH)_2C(CF_3)_2C_6H_3(COOH)_2$	244(T_m) [127]
Perfluoromethylvinyl Ether (PMVE)	$CF_3OCF=CF_2$	-23 [127]
Perfluoroethylvinyl Ether (PEVE)	$CF_3CF_2OCF=CF_2$	7.4 [127]
Perfluoropropylvinyl Ether (PPVE)	$CF_3CF_2CF_2OCF=CF_2$	35 [127]
Ester Vinyl Ether (EVE)	$CH_3OOCCF_2CF_2OCF(CF_3)CF_2OCF=CF_2$	151 [127]
Ester Vinyl Ethers OH (EVE-OH)	$CF_2=CFOCF_2CF(CF3)OCF_2CF_2CH_2OH$	105 [127]

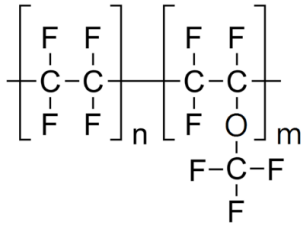
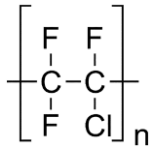
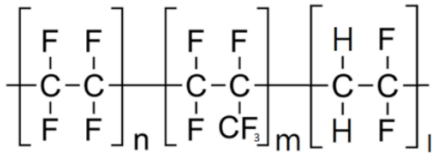
Table 2.3- Common fluoropolymers and their processing and maximum service temperature

Fluoropolymer	**Monomers**	Processing T. (°C)	Max. Service T. (°C)
Polytetrafluoroethylene (PTFE)	$CF_2=CF_2$	325-380 [128][112]	260 [112]
TEFLON AF	$CF_2=CF_2$ + PDD	260-340 [112]	260-500 [128]
Polychlorotrifluoroethylene (PCTFE)	$CF_2=CClF$	210-215 [128]	200 [45]
Polyvinylidene fluoride (PVDF)	$CH_2=CF_2$	170-230 [128] [112]	120-150 [112][45]
Polyvinyl fluoride (PVF)	$CFH=CH_2$	204-249 [119][112]	125 [45]
Fluorinated Ethylene Propylene (FEP)	$CF_2=CF_2$ + $CF_3CF=CF_2$	255-360 [128] [112]	204 [112]
Methylfluoroalkoxy resin (MFA)	$CF_2=CF_2$ + $CF_3OCF=CF_2$	305 [128]	
Perfluoroalkoxy resin (PFA)	$CF_2=CF_2$ + $CF_3CF_2CF_2OCF=CF_2$	300-445 [112]	260 [112]
Ethylene-Tetrafluoroethylene (ETFE)	$CH_2=CH_2$ + $CF_2=CF_2$	265-310 [128] [112]	150-177 [112]
Ethylene-Chlorotrifluoroethylene (ECTFE)	$CH_2=CH_2$ + $CF_2=CClF$	235-300 [128] [112]	171 [112]
Polychlorotrifluoroethylene (PCTFE)	$CF_2=CClF$	201-265 [112]	120-177 [112]
Perfluoroelastomer (FFKM)	/	/	200-315 [112]
Fluorocarbon elastomer (FKM)	/	/	215 [112]
Tetrafluoroethylene, Hexafluoropropylene, Vinylidene Fluoride (THV)	(TFE + HFP + VDF) $CF_2=CF_2$ + $CF_3CF=CF_2$ + $CH_2=CF_2$	120-225°C [112]	70-130 [129]
Hexafluoropropylene, Tetrafluoroethylene, Ethylene (HTE)	(TFE + HFP + Ethylene) $CF_2=CF_2$ + $CF_3CF=CF_2$ + $CH_2=CH_2$	180-210 [112]	/

The fluoropolymers used in this PhD are Polychlorotrifluoroethylene (PCTFE), Perfluoroalkoxy (PFA) and a terpolymer of Tetrafluoroethylene, Hexafluoropropylene and Vinylidene fluoride (THV). Their chemical structure, melting temperature, and service

temperature range are reported in Table 2.4. PFA, PCTFE, and THV were chosen because they cover a wide range of properties of processability. Their melting temperature is 305, 210, and 115 °C, respectively. PFA and PCTFE are not soluble in common organic solvents while THV has a lower crystallinity and is soluble in common organic solvents such as acetone. Further details on these fluoropolymers are given in the next sections. PTFE would have also been an interesting material to study thanks to its excellent properties, diffuse use in commercial applications and relatively low cost (9 $/kg against the 70 $/kg for PFA [130]). Nonetheless, its high chemical resistance and inability to be melt processed preclude its use in most AM techniques.

Table 2.4 - Chemical structure, melting temperature and service temperature range of PFA, PCTFE, and PFA. It should be noted that several grades of THV with different melting temperatures and service temperature ranges exist. In this PhD THV 221 was used.

PFA		Melting temperature = 304 °C Service temp. range = −196 to 260 °C
PCTFE		Melting temperature = 210 °C Service temp. range = −240 to 180 °C
THV		Melting temperature = 115 °C Service temp. range = −40 to 93 °C

2.4.2 Fluoropolymers in additive manufacturing

In the literature, very few publications discuss the use of fluoropolymers in AM. Furthermore, the focus is mainly on polyvinylidene fluoride (PVDF) and its copolymers because of its relatively low melting temperature, solubility, and piezoelectric properties (ability to convert mechanical or thermal energy into electricity and vice versa [131]).

PVDF was successfully used in a particular fused deposition modelling system (FDM) called electric poling-assisted additive manufacturing (EPAM) [132], [133]. During the printing, molten PVDF was mechanically stressed in-situ by the leading nozzle and electrically poled by an high electric field at the same time [132]. This process allowed the printing of cheap piezoelectric devices that could be used in smart materials such as sensing, actuation, energy harvesting and pump devices [132].

In other publications, material jetting was investigated. Zhang et al. [134] conducted the first attempt in jetting P(VDF-TrFE) with a Microfab jetting system. They studied the effect of several solvents on the printed drops and found that a combination of a low boiling temperature good solvent and a high boiling temperature poor solvent was the ideal combination to minimise the coffee ring effect. Nonetheless, the high boiling temperature solvent required long times in oven to be completely removed. They used a 0.5 wt% P(VDF-TrFE) ink and the produced drops had size of ~22 µm and thickness of ~1 µm. Bhansali et al. [96] tried to inkjet a P(VDF–TrFE) solution in dimethylformamide (DMF) with a Microfab Jetlab II but they did not succeed in their intent. They found that jetting was not possible even at concentrations as low as 0.1 wt%. They suggested that this was due to the high Mw of the polymer and it behaving like a viscoelastic fluid. Thuau et al. [135] jetted 1 wt% P(VDF-TrFE) in 50:50 cyclopentanone/DMSO mixture with a single nozzle system (Microfab Jetlab4) . The ink had a viscosity of 5.4 mPa/s and a surface energy of 35.6 mN/m. One and 12 layers had a thickness of ~170 nm and 2 µm, respectively. By sandwiching a P(VDF–TrFE) layer between two silver layers, they produced a piezoelectric generator and transducer. Pabst et al. [136], [137] used a Dimatix Nova 256/80 to inkjet piezoelectric polymer actuators based on a 2 wt% solution of P(VDF-TrFE) in cyclopentanone with a VDF:TrTFE ratio of 70:30 wt%. Printing one hundred layers led to a thickness of 9 µm after a 24 hours temper in a convection oven at 130 °C (step required to remove the solvent). Such long evaporation step makes the process unsuitable for the production of thicker/bigger parts. They produced a micropump with pump rates up to 130 µL/min. Similarly to the previous publication [96], Haque et al. [98] saw that the P(VDF–TrFE) wt% in the inks was limited by the high Mw of the polymer and only 0.5 wt% solution could be reliably printed. The use of low viscosity solvents allowed the use of higher P(VDF–TrFE) loadings. Overall, the jetting of fluoropolymers in the literature was limited to low concentration inks of P(VDF–TrFE) copolymer and the use of high boiling temperature solvents often limited the throughput of the inkjet process, requiring time consuming oven drying steps.

PVDF was also used in a home-made pPBF system to produce small scaffolds (~ 1.5 x 1.5 x 1, values taken from a picture with a ruler, they did not specify if the units were inches or centimetres) aimed at bone regeneration applications [138]. The biocompatibility was proven feasible through immersions in simulated body fluid (SBF) for 14 days and by culturing MG63 cells [138]. The ideal Energy Density to sinter PVDF (calculated using Equation 2) was found to be 1.56 J/mm^2, lower and higher ED led to an increase in porosity due to incomplete fusion and formation of decomposition gasses, respectively. The dimensions of the tensile samples were not reported but they showed a tensile strength of 45.31 ± 0.52 MPa which was in line with the values obtained through traditional manufacturing [139], [140]. It would have been interesting knowing the particle size distribution of the PVDF powder but it was not reported

[138]. Shuai et al. [141] continued the study of Huang et al. [138] by using the same pPBF system and by adding 58s bioactive glass to the PVDF powder. Similarly to [138] they focused on the bioactivity of the composite and did not describe in depth the laser sintering process and parameters. The addition of 58s bioactive glass showed an increased MG-63 cell growth, especially in the first few days. The cell density of all the scaffolds made from neat PVDF and PVDF with 10-20-30 wt% 58s bioactive roughly reached the same value after 7 days. In a further study, Shuai et al. [142] added nanodiamonds to the PVDF powder. This time the particle size of the nanodiamonds and PVDF were reported and were of 5-10 nm and ~250 nm, respectively. The PVDF particle size was much smaller than the standard (~45-90 µm, section 2.2.3) but no mention to the powder flowability was given in the paper. The powders were mixed by making and dispersing and sonicating the powders in a 30 ml beaker with 15 mL absolute ethyl alcohol. Afterwards, the dispersion was added to a planetary high-energy ball mill to improve mixing. The mixture prepared had 0.5-1-2-3 wt% of nanodiamonds. They used the same pPBF system used in the previous studies [138], [141] and a layer thickness of 0.1-0.2 mm (which is too vague). The dimensions of the tensile samples were not reported but the increase in tensile strength reached its maximum with the addition of 1 wt% nanodiamonds. The tensile strength increased by 23.01% (59.61 MPa). The nanodiamonds started to agglomerate at concentrations above 1 wt% and lead to lower tensile strengths. In a further study Huang [143] added MgO whiskers to the PVDF powder. The PVDF powder had a particle size of roughly 350 nm while the MgO whiskers had a width and length of roughly 2.5 and 15 µm. Several mixtures, up to 5 wt% in MgO, were prepared similarly to [142]. The same home-made pPBF system cited above was used and the printing parameters were not reported. The addition of MgO whiskers increased the tensile strength and elongation at break, reaching maximum values at a concentration of 2 wt%. Overall, the use of fluoropolymers in pPBF is limited to few papers produced by the same group of people and focused on PVDF. Furthermore, the papers were focused on the biological properties of PVDF, little to no consideration was given to the pPBF process and many essential process parameters, necessary for the reproduction of the studies, were missing.

Finally, 3M recently announced a way to 3D Print PTFE through SLA with promising initial results such as similar density and yield strength, and better surface finish compared to traditional manufacturing [144]. A photocurable resin is used to bind the PTFE powder particles together in the desired shape. The resin is then removed during a post sintering step. A tensile strength at break of 23 MPa and elongation at break of 240 % were obtained [144]. These values were lower than those obtained with traditional manufacturing (20-35 MPa and 300-550 % [120]).

The fluoropolymers investigated in this PhD and introduced in the next sections possess either higher chemical and thermal resistance or better processability and throughput compared to the fluoropolymer used so far in the literature.

2.4.3 Perfluoroalkoxy (PFA) – high temperature fluoropolymer

When PTFE is copolymerised with perfluoro(propyl vinylether) (PPVE) a perfluoroalkoxy (PFA) is obtained. The addition of PPVE introduce branching groups in the otherwise linear polymer chain structure of PTFE. The presence of theses pendant groups disturbs the packing of the PTFE rods leading to a decrease in crystallinity and melting temperature. Furthermore, the branching acts as an obstacle to cold flow (creep) and just 1% of PPVE is enough to cause these change in properties [112]. Because of this low percentage, low steric strain at the branching point, and high strength of the C-O bond, PFA has the same maximum service temperature of PTFE and a melting temperature of 305-310 °C, which is 20 °C below that of PTFE [112], [145]. The mechanical properties at high temperatures of PFA are equal or superior to those of PTFE. Moreover, PFA coatings do not suffer from microporosity as PTFE [112]. The melt viscosity of PTFE is over one million times higher than that of PFA [140]. Depending on the cooling rate, PFA crystallinity and specific gravity ranges from 48% to 60% and from 2.12 to 2.17 [112], [146]. PFA has three second-order transitions at -100, -30 and 90 °C [146].PFA ages at high temperatures due to cross-linking caused by the reactive end groups like –COF and $–CH_2OH$ [112]. The crosslinking makes PFA stronger but also more brittle. PFA has high clarity and adsorbs ~10% in the IR region, 13-20% in the visible region, and 20-45% in the UV region [112], [145]. The crystallinity of PFA range from 65% to 75% as polymerised and around 58% when cooled slowly from the melt [145]. The limiting oxygen index is over 95% and the polymer is self-extinguishing [145].

PFA is used in demanding applications where high service temperatures and high chemical resistances are required. PFA can be filled with carbon to create a semi-conductive polymer useful for electric heat tracing applications; when the temperature rises, PFA expands, the distance between carbon particles increases, and the conductivity decreases [111]. PFA is also used to transport chemicals and work in pure environment as it virtually inert to all chemicals and solvents. Nonetheless, PFA can be attacked by elemental fluorine and alkali metals at elevated temperatures and pressures [145]. It is often more convenient to produce something pure rather than purifying it through refining steps. The use of PFA also guarantees the accuracy and repeatability of measurements [111] (thanks to its chemical inertness and absence of fillers/additives that could contaminate the sample).

The most common ways to process PFA are via: injection moulding, extrusion, rotomolding/rotolining, and transfer moulding. In injection moulding the resin is melted and slowly injected into a mould cavity. Extrusion is similar to injection moulding but it produces

long continuous shapes. In Rotomolding/rotolining the resin is positioned inside of a mould which is then heated to 350-360°C and simultaneously rotated on two perpendicular axes to create an internal coating. Finally, in transfer moulding, the resin is melted above its melting point and forced into a fitting at high pressure [111].

2.4.4 Polychlorotrifluoroethylene (PCTFE) – medium temperature fluoropolymer

Polychlorotrifluoroethylene (PCTFE) is the homopolymer of chlorotrifluoroethylene (CTFE, formula: CF_2=CClF). The structure of PCTFE is very similar to that of PTFE (CF_2=CF_2). While they share many properties (e.g. same helical configuration of the polymer chains), they differ in that one fluorine atom is replaced with a chlorine atom. As chlorine atoms are bigger than fluorine atoms, it takes 16.8 monomer units to complete a helix turn, while PTFE assume a 13/6 configuration (6 turns every 13 CF_2 units) [120], [147]. The crystal structure is pseudohexagonal with lattice parameters of a = 0.644 nm and c = 4.15 nm [140]. Due to the nature of fluorine atoms and lack of polarity caused by the symmetrical structure, PTFE suffer from cold flow - the PTFE rods (Figure 2.9) tends to slip one over the other. In the case of PCTFE, the chlorine atom disturbs the symmetry of the chain structure and the acquired polarity increases the interactions between chains preventing cold flow. Furthermore, the chlorine atoms disturb and lower the crystallinity of the polymer making it melt-processable. Nevertheless, the high melt viscosity of the polymer (~$1x10^8$ Pa.s [148]) requires high processing temperatures to lower the viscosity (to allow its use in traditional processes such as injection moulding), leading to an increase in cost and risk of degrading the polymer [149]. PCTFE has a melting point and crystallisation temperature of roughly 213 °C [150] and 178.5 °C [120] respectively; it has a wide service temperature range, down to -250 °C and up to 180 °C [149]. Furthermore, PCTFE is non-flammable (limiting oxygen index = 100% [120], [151]), inert toward all inorganic and most organic chemicals [120], [149], one of the best gas barrier materials (even at low temperature) [152], optically clear (up to 4 mm in thickness) [120], has zero moisture absorption [120], and excellent resistance to ultraviolet and X-ray radiation [120]. The crystallinity of the polymer ranges between 30% and 70% with a theoretical fully amorphous density of 2.077 g/cm^3 and fully crystalline density of 2.187 g/cm^3; the crystallinity of a particular grade/sample can be extracted from its density [140], [145], [153], [154]. All these remarkable properties make it an ideal material for many applications, from aerospace to pharmacy. Nonetheless, its high viscosity, processing temperature, and insolubility in common organic solvents make the processing of PCTFE challenging. The physical, thermal, chemical, and electrical properties of PCTFE can be found in the appendix.

PCTFE is a homopolymer and it is produced by the free-radical reaction of its monomer (CTFE). The latter is a colourless gas at room temperature (1 bar), fairly toxic (rat LC_{50} 4000

ppm for 4 hours [155]), flammable and explosive [120]. Its reactivity is similar to that of other olefins and it can be polymerised in emulsion [156], suspension[157], solution [158], and bulk [159]. In the industrial bulk polymerisation, the reaction takes 168 hours to reach a conversion of 40% and the control of the reaction temperature is very challenging [120]. CTFE is stable in degassed water but slowly hydrolyses in the presence of oxygen [160]. Liquid CTFE and oxygen react in a wide range of temperature to form several oxygenated compounds such as peroxides. CTFE is more stable (less reactive) than tetrafluoroethylene (TFE) and can be shipped without the use of inhibitors as long as no oxygen is present [120]. The reaction between oxygen and liquid CTFE has been exploited in a patent to form peroxides which decompose to produce free radicals and start the polymerisation [160], [161]. UV-light and gamma ray radiation also initiate the reaction [120]. These properties could be useful in several AM techniques.

2.4.5 THV – low temperature, soluble fluoropolymer

With the exception of PTFE and polyvinyl fluoride (PVF), all fluoropolymers are melt processable [112] and only a few are soluble in common solvents at room temperature, including THV, PVDF, Teflon AF, and CYTOP.

THV is available in several grades but only THV 221 is soluble in conventional solvents. THV 221 is a random terpolymer of 51.4% tetrafluoroethylene (TFE), 10.4% Hexafluoropropene (HFP), and 38.2% vinylidene fluoride (VDF) [162]. THV is one of the latest fluoropolymers to be commercialised (1996) and the work published on this material is still limited [163]. Despite the relatively low melting temperature of 115 °C, the decomposition temperature is around 410 °C [162], [164]. The service temperature ranges from -40 to 93 ºC [165]. The properties of THV include high transparency, good bondability, high flexibility and flex life, low refractive index as well as efficient electron beam cross-linking [114]. Electron beam cross-linking improves the chemical resistance and increases the temperature resistance of the polymer to temperatures >150 °C [114]. Beside the fact that THV can be crosslinked with an electron beam, almost no information is available in the literature about the cross-linking process or properties of the irradiated THV.

Most THV applications gravitate around multilayer parts, where a thin layer is used as protective coating or to provide enhanced barrier properties to other layers [114]. Ok et al. have published several works on the film formation of THV by drop casting and electrospinning using acetone and ethyl acetate as good solvent, ethanol and chloroform as antisolvent, and additives such as Kaolinite and Montmorillonite. They were able to achieve water contact angles as high as 145° [162], [166], [167]. Patent US20080118541A1 [168] stated that fluoropolymers are widely used in medical applications thanks to their outstanding biocompatibility and low drug permeability. Unlike most fluoropolymers, THV has a low

crystallinity which allows for a faster drug release and higher elongation at break (lower tendency for the film to crack). Because of these properties, Pacetti [168] patented the use of THV in medical devices such as coronary stents. THV can also be used in microfluidic devices thanks to its transparency, thermal resistance, and chemical resistance. King et al. [169] tested microfluidic devices made of Dyneon THV 500, polydimethylsiloxane (PDMS), Norland Optical Adhesive 81 (NOA81), and a (non-defined) 3D printed material (printed with an Objet Connex350TM). The tests were conducted in a Belousov–Zhabotinsky reaction medium and THV showed no swelling and overall good performance. Begolo et al. [170] successfully produced and tested a droplet microfluidic device made of two THV 500 sides bonded together with a thin film of THV 220. Slim et al. [171], recognising the interest for THV in microfluidic chip applications, functionalised the surface of THV through a two-step strategy consisting of a local reduction of THV to alkyne group and a successive click reaction with azidebearing ligand. In a previous publication, Perréard et al. [172] functionalised the surface of THV with a three-step strategy. Both publications used the same THV grade but did not specify which one. Nonetheless, judging from the stated melting temperature of 165 °C, the used grade was not THV 221. PFA capillaries are often used in microfluidic applications but the commercially available sizes does not allow for miniaturisation [170]. At this regard, material jetting can be useful thanks to its high resolution and precision. The smallest achievable resolution depends on the drop size which is normally around 50 µm [173]. Further information on the jetting mechanism, drop formation, resolution, and required fluid properties are reported in section 2.3. The literature about the jetting of fluoropolymers is quite limited and it is mainly focused on polyvinylidene fluoride–trifluoroethylene P(VDF-TrFE) and its piezoelectric properties as explained in section 2.4.2 [96], [98], [135]–[137].

2.5 Gaps in research and statement of novelty

From reviewing the literature, it is clear that the research area of fluoropolymers in AM is still mostly unexplored. A possible cause for this may be due to the difficulty in processing these materials [120], [140] and lack of grades tailored for AM. Today, only a small number of polymers are commercially available and can be successfully produced via AM [83]. This is especially true for pPBF where polyamide and few other polymers are the main materials used (PA12, PA11, PA612, PA6, PS, PAEK, PEBA, PP, PPS, TPU [37]–[41]). None of these polymers possess the outstanding combination of properties that fluoropolymers hold such as wide service temperature, non-stick ability, and excellent resistance to chemicals, sunlight, flames and weathering without the addition of stabilizers, plasticiser or fillers (section 2.4). The introduction of fluoropolymers in AM would expand the use of AM into new applications and processes. To date, the use of fluoropolymers in pPBF is limited to PVDF [138], [141]–[143]. All the research done on this material was conducted by the same group of people and

focused on the biological properties of small scaffolds (~ 1.5 x 1.5 x 1 cm). Little to no consideration was given to the pPBF process and many essential process parameters, necessary for the reproduction of the studies, were missing.

In this PhD, several parameters and techniques used to print PCTFE and PFA were investigated and described in depth. Regarding MJ, the use of fluoropolymers in this technique is limited to P(VDF–TrFE). Furthermore, P(VDF–TrFE) was used only at low concentrations (< 3 wt%) and, the high boiling temperature of the solvents used, often required a time and energy consuming oven drying steps which limited the throughput of the process [96], [98], [135]–[137]. In this PhD several solvents and solutions with THV loadings up to 20 wt% and drying times down to a few seconds were successfully jetted. The fluoropolymers investigated in this PhD either possess higher chemical and thermal resistance or better processability and throughput compared to the fluoropolymers used so far in the literature. Small parts, membranes and films with mechanical properties comparable to those of traditional manufacturing were successfully produced. Several techniques to improve the powder flow, bulk density, and minimise warping were adopted and described in depth. Specifically, this thesis demonstrates novelty in the following areas:

1. Isothermal crystallisation and crystallisation activation energy of PCTFE and PFA with and without the addition of carbon black.
2. Use of a CO_2 laser to increase the particle size and flowability of powders.
3. Use of the FT4 powder rheometer to investigate the effect of carbon black, fumed nano-silica, and thermal treatments on the flowability and conditioned bulk density of the PCTFE and PFA powders.
4. Printing of PFA membranes via pPBF.
5. Printing of small parts made of PCTFE via pPBF.
6. Printing of several formulations of THV via MJ and measurement of the mechanical properties.
7. Initial investigation on the permeability of THV for possible drug releasing applications.

3 Methods and materials

3.1 Introduction

The following sections present the established equipment, methods, and materials used in this study. This involves: characterisation of the raw material, powder modification, laser sintering, ink development, E-beam crosslinking, and jetting. It also details the processes used to analyse the samples: porosity, determination of printed sample profiles, and mechanical tests.

3.2 Materials

PCTFE powder (Chemical Point UG), PFA ACX-31S powder (Daikin), THV 221 aggregate (3M) were used. PCTFE had a melt flow index (MFI) of 0.97 g/10min (as stated by the supplier) and an average particle size below 1 µm. PCTFE had a Zero Strength Time (ZST) of 128 seconds. The ZST is correlated to the molecular weight. PCTFE is not easily dissolved, making the measurement of the molecular weight challenging. Therefore, the molecular weight is usually given as a measurement of the ZST (a mechanical test, ASTM D1430 [174]), higher ZST corresponds to higher molecular weights. PFA had a melt flow index of 25 g/10min (ASTM D3307, as reported by the supplier) and an average particle size of 24 µm. MONARCH 800 Carbon Black (nanoparticles) and CAB-O-SIL Untreated Fumed Silica (nanoparticles) (both from Cabot Corporation) were used as flowing agents. The pPBF system was used with PCTFE, PCTFE + 1 wt% CB, PFA, PFA + 0.2 wt%, and PFA + 0.4wt%.

Eucalyptol for synthesis (1,8 Cineole) (Merck), L-Fenchone ≥98% (Sigma Aldrich), 4-Methyl-2-pentanone (MIBK) ≥99.5% for analysis (Acros Organics), N,N-Dimethylacetamide 99% (DMAc) (Sigma Aldrich), and Acetone ≥99.8% (VWR) were used as solvents. The solvents were used as received.

Two types of syringes were used. The Braun Inject syringes which were made of polypropylene/polyethylene, latex-free, and silicone oil-free (the syringes were green in colour) [175]. The BD Plastipak which were made of polypropylene/polycarbonate, latex-free, and with a medical grade silicone oil (< 0.25 mg/cm^2) (the syringes were white in colour) [176].

3.3 Methods

3.3.1 Powder bed fusion apparatus

A commercially available pPBF system (EOS Formiga P100) was used. This machine used a CO_2 laser which operated at a wavelength between 10.2 µm and 10.8 µm (925 and 980 cm^{-1})

with a spot size of 420 µm and a nominal laser power of 30 W. The maximum scan velocity was 5000 mm/s while the working volume was 200 x 250 x 350 mm. The maximum powder bed temperature was 182 °C (this is the powder bed temperature used in the experiments, unless explicitly stated otherwise). The layers were deposited with a doctor blade. The energy density (ED) was calculated with Equation 1. The powders used were: PCTFE, PCTFE + 1 wt% CB, PFA, PFA + 0.2 wt% CB, and PFA + 0.4 wt% CB.

3.3.2 Material Jetting apparatus

One of the two printers used in this study was the Fujifilm Dimatix DMP-2830 [177]. The printer was used with two different types of 10 pL cartridges (DMC): DMC-11610 and DMCLCP-11610. The difference between the two cartridges was in the chemical resistance of the component coming in contact with the fluids to be printed. The DMC-11610 was made of chemically resistant epoxy, peroxide treated EPDM, Polypropylene, silicon, and silicon dioxide. DMCLCP-11610 was made of chemically resistant epoxy, Kalrez, liquid crystal polymer, silicon, silicon dioxide [178]. Both cartridges had 16 nozzles linearly spaced at 254 microns and nozzle diameter of ~ 21.5 µm [178]. The cartridges were filled with 2 mL of ink. The second printer used was the Nordson EFD PICO Pµlse [91]. The printer had a single interchangeable nozzle with diameters ranging from 50 to 600 µm. In this study a nozzle diameter of 150 µm was used. The printing inks can be pressurised at pressures up to 49 bar (700 psi). The maximum nozzle temperature was roughly 100 °C. The maximum dispensing frequencies was 1500 Hz. A wide range of fluids with low to high viscosities could be printed. The valve was controlled through the PICO Toµch valve controller [179]. The settings used are reported in Table 3.1

Table 3.1 - Pico Pµlse fixed jetting parameters

Parameter	Value
Close Volts	120 volts
Stroke	75%
Open	0.25 ms
Close	0.20 ms
Valve Mode	Timed
Pulse	0.27 ms
Cycle	10 ms
Count	1
Frequency	200 Hz

3.3.3 Powder mixing

Powders and additives were mixed in polypropylene containers roughly 1 kg at a time. The mixing was done with stainless steel blades at ~1000 RPM for several hours.

3.3.4 Shape and surface morphology

The shape and surface morphology of the samples were investigated using a Hitachi TM3030 Tabletop Microscope (SEM) [180] at 15 keV in Charge-up Reduction Mode. This mode allowed the analysis of non-conductive samples which were mounted on a conductive double-sided adhesive tape. No sputter coating was required if the Charge-up Reduction Mode was used. Nonetheless, dwelling too much time on the same spot or using high magnifications induced polymer melting. The powders, solution and printed object were also observed with a NIKON Eclipse LV 100 ND having 5x, 10x, 20x, 50x, and 100x objectives, in reflected and transmitted light [181].

3.3.5 Mass and density measurement

The density of the printed parts was calculated by measuring the volume and weight of the parts. The weight was measured with a Kern ABT 100-5m scale. The volume of the parts was calculated by measuring the dimensions of the parts with a calliper and a micrometre. The density of each ink was calculated by weighing 1 mL of solution on a Kern ABT 100-5m scale. Each measurement of density was repeated 3 times.

3.3.6 Differential Scanning Calorimetry (DSC)

The thermal characterization was conducted with a DSC 8000 (PerkinElmer). The samples were weighed with a Kern ABT 100-5m scale and aluminium pans were used. The neat PCTFE sample weighed 8.2 mg while the PCTFE sample with 1 wt% carbon black (CB) weighed 8.6 mg. The neat PFA sample weighed 7.4 mg while the PFA sample with 0.2 wt% carbon black weighed 8.6 mg. The same samples were utilized for the isothermal crystallization experiments. The crystallization and melting temperature were obtained with a heating/cooling rate of 20 °C/min over a range of 0-230 °C and 0-330 °C for PCTFE and PFA, respectively. The PCTFE isothermal crystallization was measured by holding the temperature at 230 °C for 3 minutes with subsequent cooling at 40 °C/min to 180 °C and by finally holding the temperature at 180 °C for roughly 20-25 minutes. At this point the sample was heated back to 230 °C with a rate of 100 °C/min and all the previous steps repeated. At each repeat, the holding temperature was changed to 182-184-186-190 °C for both neat PCTFE and PCTFE with 1 wt% CB. Similarly, the PFA isothermal crystallization was measured by holding the temperature at 330 °C for 2 minutes with subsequent cooling at 40 °C/min to 276 °C and held

for roughly 20-25 minutes. At this point the sample was heated back to 330 °C with a rate of 100 °C/min and all the previous steps repeated at 276-278-280-282-284-286-288 °C for the neat PFA powder and 284-286-288-290-292-294 °C for the PFA with 0.2 wt% CB. Higher temperatures were used for PFA 0.2 wt% CB because at lower temperatures the crystallization was happening too quickly. All the reported values were obtained from calculations within the PerkinElmer Pyris software v11.1.0.0488. The crystallization activation energy was calculated by plotting the natural logarithm of the isothermal crystallization peak time (time passed from the reaching of the isothermal temperature to the crystallization peak) against the reverse of the temperature in Kelvin multiplied by 1000. The DSC scans were repeated twice for the determination of the melting and crystallization temperatures (at 20 °C/min) and once for the determination of the isothermal crystallization. There is a general misconception that the isothermal crystallisation should be measured using high cooling rates and, usually, rates above 20 °C/min are required only for polymers that crystallise quickly such as polypropylene (PP) [182], [183]. The crystallisation activation energy was calculated with a special form of the Arrhenius equation [184]:

$$ln\,[\Delta t] = \frac{E}{RT} + c \qquad \textit{Equation 4}$$

Where Δt is the isothermal crystallization peak time (time passed from the reaching of the isothermal temperature to the crystallization peak), E is the activation energy, R is the gas constant (8.314 J/mol.K), and T is the absolute temperature. The crystallization activation energy was calculated by plotting the natural logarithm of Δt against the reverse of the temperature in Kelvin multiplied by 1000 [184]. The slope of the linear least squares regression is the activation energy (when multiplied by the gas constant). For a more complete approach of the activation energy, the Sestak-Berggren equation [185], [186] could be used but it has been shown to give comparable results to the Arrhenius equation [183]:

$$\frac{d\alpha}{dt} = Z\,\alpha^m\,(1-\alpha)^n\,exp\,[\frac{E}{RT}] \qquad \textit{Equation 5}$$

Where dα/dt is the rate of the reaction, Z is the Arrhenius pre-exponential factor, α is the fraction reacted, (1- α) is the fraction left unreacted, *m* is the reaction order for the induction period, and *n* is the reaction order for the crystallisation reaction.

3.3.7 Thermogravimetric Analysis (TGA)

The thermogravimetric characterization was conducted with a TGA 4000 (PerkinElmer). The weight of the PCTFE sample was of 7.080 mg. The sample was heated to 200 °C at 20 °C/min and the temperature held for 5 hours. The instrument overshot and the actual hold temperature was of 201.55 °C. This temperature is ~ 20 °C above the maximum processing temperature and was chosen to have a margin of safety. Furthermore, as showed by the DSC in section

4.1.2, the ideal processing temperature to delay the crystallisation of the polymer was above 190 °C. The full decomposition of PCTFE and PFA were not studied due to the lack of an extraction system and high toxicity of the decomposition products of fluoropolymers. Therefore, only the start of the decomposition was observed for PCTFE and PFA before stopping the experiment. The weight of the PTFE sample was 3.071 mg and the experiment was carried out with a heating rate of 10 °C/min. The weight of the PFA sample was 13.267 mg and the experiment was carried out with a heating rate of 20 °C/min. A baseline was used for the PFA experiment.

3.3.8 Particle size distribution (PSD)

The particle size distribution was obtained using a Mastersizer 3000 (Malvern, UK) with the Hydro EV accessory for wet analyses and the Aero S accessory for dry analyses. Particles were assumed non-spherical for the PFA powder and spherical for the PCTFE powder based on the SEM images. Refractive index and absorption index were assigned values of 1.43 and 0.002 for both polymers [187], [188]. In the wet analyses, deionized water was used as a dispersant, and a refractive index of 1.330 was employed. The reported particle size distribution values were obtained from calculations within the Mastersizer software and are reported as D_{10}, D_{50}, and D_{90}. D_{90} means that 90% of the particles are below that value, D_{50} means that 50% of the particles are below that value, D_{10} means that 10% of the particles are below that value.

3.3.9 Fourier-transform infrared spectroscopy (FT-IR)

The infrared spectroscopy was conducted with a Frontier MIR/FIR Spectrometer (PerkinElmer). The samples were analysed in the powder form. The force gauge used was between 120 and 140. Five spectra in the 700-4000 cm^{-1} range were acquired for each sample. The samples analysed were PCTFE, PCTFE + 1 wt% CB, PFA, PFA + 0.2 wt% CB, PFA + 0.4 wt% CB, THV, and neat carbon black. The IR spectrometer was used to determine the absorbance of the powders in the wavelength of the CO_2 laser which is between 925 and 980 cm^{-1} (10.2 - 10.8 µm) [31].

3.3.10 Dissolution of PCTFE

By following the instructions from the patent [189], 10 wt% solutions were tested in fenchone and eucalyptol with the aim of changing particle size distribution through dissolution and precipitation. Other solvents are available (Appendix Table 0.6 and Table 0.7) but they are toxic, and require high temperature and often high pressures (to increase the boiling temperature of the solvents). Supercritical CO_2 at 100 °C was also tested using an existing

system present in the Chemistry Building. A colleague, Sam Irving, operated the supercritical CO_2 reactor.

3.3.11 Thermal treatments of the PCTFE powder

Samples were prepared by filling 250 mL beakers with roughly 40 g of PCTFE powder. Each sample was then subject to a different thermal treatment in an oven. The thermal treatments consisted of 4 hours at 200 °C, 205 °C, and 210 °C, and 23 hours at 210 °C. Afterwards, the powders were ground with a pestle and mortar. A similar process to increase the bulk density of PEEK powder up to 17% by reducing the specific surface of the particles (smoother particles) was patented by EOS [190]. Schmidt et al. [191] used a heated downer reactor to smooth polymeric particles that were injected in the reactor as an aerosol to minimise contacts between particles and reactor walls. The residence time in the reactor necessary to achieve smooth particles depended on the viscosity of the polymer. They suggested to use a conditioning temperature 20 °C above the glass transition and that the higher the melt viscosity, the higher the conditioning temperature should be.

3.3.12 FT4 powder flow rheometer

The flowability of the powders and conditioned bulk density (CBD) were measured with an FT4 powder rheometer (Freeman Technology). The tests were done using 25 mL glass containers and the Stability & Variable Flow Rate Method. This method measures several parameters but the ones reported here are the Basic Flowability Energy (BFE), Stability Index (SI), Specific Energy (SE), and CBD. The BFE is the energy (mJ) needed to displace a conditioned and stabilised powder at a given flow pattern and flow rate – typically -5° helix downwards and 100 mm/s blade tip speed. This flow pattern is a downward anti-clockwise motion of the blade, generating a compressive, relatively high stress flow mode in the powder. The SI is the factor by which the flow energy requirement changes during repeat testing (seven measurements are made and the SI is the ratio between the BFE of the seventh and first measurement). The SE is normalized against mass and measured in mJ/g. SE is used to determine the flowability of a powder in a low stress environment and it is particularly sensitive to cohesion, particles shape and surface texture. Generally, values below 5 mJ/g are associated with low cohesion, while values above 10 mJ/g are associated with high cohesion [192]. The measured bulk density is called conditioned because the instrument executes a conditioning cycle to remove external influences and increase repeatability. The conditioning establishes a low stress, homogeneous packing state. The majority of the measurements were repeated 3 times but some of measurements were done only once because of the high repeatability of the measurements. By way of comparison Ziegelmeier et al. [193], [194] tested

the quality of the data obtained with the FT4 to a Revolution Powder Analyzer and the Hausner Ratio and showed that all the methods gave similar results.

3.3.13 Surface tension and contact angle of the inks

The surface tension and contact angle of the prepared inks were measured by pendant and sessile drop shape analysis (Krüss DSA100S). 1 mL syringes with flat tip needles and diameter of 1.250 mm were used for both tests. The surface tension and contact angle were computationally calculated. Measurements were taken in different days at room temperatures of 23.6 °C for the surface energies and 20.5 °C for the contact angles. Six repeats were done for each measurement.

3.3.14 Choice of solvents

Common solvents used to dissolve THV 221 are acetone, ethyl acetate, methyl ethyl ketone (MEK), methyl isobutyl ketone (MIBK), tetrahydrofuran (THF), and dimethylacetamide (DMAc) [168], [195]. MIBK was elected as main solvent because of its ideal vapour pressure which would allow fast evaporation of the ink but not so fast that the nozzles of the printer would clog. MIBK was also relatively cheap and safe [196]. To modify the drying speed of the MIBK inks for specific applications, dimethylacetamide (DMAc) and acetone were added to the MIBK ink at a 1:1 ratio by volume. The addition of DMAc slowed down the evaporation of the ink due to its lower vapour pressure, while the addition of acetone speeded up the evaporation of the ink due to its higher vapour pressure (Table 3.2).

*Table 3.2 – Vapour pressure, surface tension, viscosity, and boiling point of several common solvents for THV. All the data refers to a temperature of 20 °C. *water is not a solvent for THV.*

Solvent	Vapour pressure (mmHg)	Surface tension (mN/m)	Viscosity (mPa.s)	Boiling T (°C)
Acetone [197]	184.5	23.32	0.36	56.29
Ethyl Ac. [197]	73	23.75	0.45	77.11
MIBK [197]	16	23.64	0.58	117.4
Water* [197]	17.54	72.8	1	100
DMAc [198]	1.33	33.8	1.02	166

3.3.15 Viscosity of the inks

The shear viscosity of the formulated inks was assessed using a Malvern Kinexus Pro with a cup and bob geometry and a 40 mm parallel plate geometry. The latter was used with a vapour trap and a plate gap of 200 μm. The cup and bob geometry was initially used because it is a geometry ideal for solutions with a high evaporation rates. Nonetheless, this geometry was not

accurate at high shear rates (> 100 s^{-1}) as the high speeds and centrifugal forces generated Taylor-vortices which caused the measured viscosity to increase [199]. All the viscosities were measured with the parallel plate geometry except for THV 20 wt% in 50-50 v% MIBK-acetone, its high evaporation rate made the data from the parallel plate not reliable. The shear rate swept between 10 s^{-1} to 1000 s^{-1} at 22-28-35-45-60 °C. 22 and 28 °C were chosen because the laboratory room temperature was usually around 22 °C and the minimum programmable temperature of the Dimatix printer was 28 °C. The rheometer often had difficulties in reaching a steady state for shear rates lower than 100 s^{-1}, with consequent wide standard deviations. The ink used were THV 1 wt% in 50-50 v% MIBK-DMAc, THV 1-5-10 wt% in MIBK, and THV 20 wt% in 50-50 v% MIBK-acetone. Three repeats were done for all the inks except for THV 20 wt% in 50-50 v% MIBK-acetone which was repeated only twice because of the high evaporation rate of the ink.

3.3.16 Gel permeation chromatography (GPC) of THV

The molecular weight of THV 221 was calculated by gel permeation chromatography (Agilent 1260 Infinity II). The used column was MIXED-C with a range of 200 – 2,000,000 Daltons. The polymer solution was prepared by dissolving 5 mg of THV in 2 mL of HPLC-grade tetrahydrofuran (THF). The dn/dc was calculated using the refractive index of THV (1.363) THF (1.404) with the following formula:

$$dn/dc = \frac{\text{THV RI} - \text{THF RI}}{\text{THV density} - \text{THV concentration in the pure solvent}} \qquad \textit{Equation 6}$$

The density of THV 221 was 1.93 g/mL while the THV concentration in the pure solvent was 0 g/mL. The dn/dc was calculated to be -0.21.

3.3.17 Ink preparation

Solvents and polymers were weighed on a Kern ABT 100-5m scale. Afterwards, the solutions were mixed in 20 mL vials with a magnetic stirrer for several hours at room temperature and left at rest for at least 24 hours. The polymer loadings are reported in weight % while the mixture of solvents are reported in volume %.

3.3.18 E-beam crosslink of THV

The samples were crosslinked with a pulsed electron beam irradiation system (Sodi-tech PF32A). This system is typically used to modify the mechanical properties and appearance of the surfaces of metals and ceramics. A characteristic use of the system was showed by Murray et al. [200] which used the exact same setup to repair the cracks on the surface of an austenitic

steel part that had been cut with an electrical discharge machining (EDM). Further information about the pulsed electron beam irradiation technology can be found in the literature [201]–[203].

The fixed parameters used to crosslink the THV samples were: diameter of the electron beam = 60 mm, anode voltage = 5 kV, pulse length = 0.8 - 3 µs [203], argon pressure = 0.05 Pa, and irradiation distance = 300 mm. The variable parameters were: number of shots = 1, 3, 5 and cathode voltage = 30 kV (energy density = 12 J/cm^2), 35 kV (energy density = 19.5 J/cm^2). In a first test glass THV coated glass slides were used. See section 3.3.19 for the preparation of the coated glass slides. In a second test THV strips of ~ 30 x 5 mm were printed with the PICO Pµlse and THV 10 wt% at a nozzle temperature of 50 °C, pressure of 1.5 bar, drop spacing of 800 µm, 8 layers. The strips were then exposed to the E-beam, 1 shot at 35 kV, and submerged in MIBK. The thickness of the films was ~ 155 µm.

3.3.19 THV coated glass slides

The glass slides were coated with 1 mL of THV 10 wt% in MIBK by drop casting with a syringe, dried at room temperature, and conditioned for 20 minutes at 170 °C. The thickness of the films was ~ 27 µm. Table 3.3 reports the thickness and weight of the THV films as printed, one week after, 36 days after, after 2 hours at 80 °C, after 40 minutes at 170 °C, and after another 9 days. The films lost ~1.7 mg of solvent over one week and ~0.2 mg of water after thermal treatments.

Table 3.3 - Average values of the change in thickness and weight of THV coated glass slides produced with 1 mL of a 10 wt% THV solution in MIBK after time and thermal treatments. The values refer to the THV film (n = 3)

Time	Thickness (µm)	Weight (mg)	Loss (mg)
few hours at room T	27	96.2	
1 week after	27	94.5	1.7
36 days after	27	94.4	0.1
2h at 80°C	/	94.2	0.2
40 min at 170°C	26	94.2	0
9 days after	26	94.4	-0.2

3.3.20 Coherence scanning interferometry (CSI) of the THV films

A ZYGO NewView 8300 coherence scanning interferometry (CSI) system was used to acquire high resolution images and profiles of the THV parts. The system was kept in a temperature-controlled environment at 20 ± 1 °C, isolated from noise and dust, and it was well suited to measuring samples with low reflectance such as the thin THV films. Recent

advancement in the technology, which allowed higher sensitivities and noise reduction, made the CSI system suitable for the analysis of certain AM parts [204]. Resolution lower than one nanometre was achieved. The data obtained via CSI was analysed and processed with the Mountains 7 Surface Imaging, Analysis and Metrology software. The instrument and data processing were conducted by Carlos Alberto Gomez at the University of Nottingham.

3.3.21 THV samples for tensile tests

The tensile tests were printed two at a time on the same glass slide with the PICO Pµlse using a 20 wt% THV solution in 50-50 v% MIBK-acetone. The sample were strips of 70 x 8 mm printed using between 4 and 10 layers (the change in number of layers was due to changes in drop spacing or errors encountered during the printing process such as running out of ink or nozzle failure). A total of 19 samples were printed with a nozzle temperature of 50 °C and a pressure of 1.5 bar (while using the Nordson EFD HPx High-Pressure Dispensing Tool which increase the actual pressure used by ~7 times). 11 samples were printed with a DS of 800 µm while the remaining 8 samples were printed with a DS of 600 µm. 4 samples from each set were subject to a heat treatment in oven at 170 °C for 40 minutes. 3 samples from the 800 µm DS set were exposed to an electron beam (1 shot, 35 KeV) in a similar manner as explained in the section 3.3.18.

The tensile tests were performed on an Instron 3369 tensile system (Instron Ltd, Bucks, UK) at a temperature of 18 °C with a rate of testing of 50 mm/min and a length (distance between jaws) of 45 mm. Because of the standard clamps utilised and/or small thickness and properties of the THV films, the films slipped 0.75 cm from each jaw (regardless of the tightness of the jaws) so that the actual length used in all the calculations was of 60 mm and not 45 mm. The stress-strain curve did not show Hookean (linear) behaviour therefore the Young's modulus could not be calculated with precision. To have an approximate value of the Young's module two values were taken at different points. The maximum value of the Young's modules was taken from 14 points (from second 0.4 to second 1.7) while the minimum value was taken from 34 points (from second 0.4 to second 3.7). The first 4 points (from second 0 to second 0.3) were not used to avoid "artefacts caused by a take up of slack and alignment or seating of the specimen" [205].

4 Results – Powder bed fusion

It is well known that Additive Manufacturing has great potential but several limitations, one of which is the narrow material portfolio. Of the thousands of different polymers available for injection moulding, less than 30 of them are suitable for being pPBF [22]. Furthermore, polyamide 12 made up ~ 95 % of the market in 2009 [9]. This limited number of materials is due to the specific requirements for powder-based AM, such as: precise particle size distribution (~45-90 µm) to guarantee good powder flow; relatively low viscosity to avoid porosity; absorbance in the wavelength of the specific heating element (e.g. CO2 laser); and a wide processing window (i.e. the difference between melting and crystallisation temperature) to supress dimensional warping. Fluoropolymers have outstanding properties (section 2.4.1) and have not yet been properly used in AM (section 2.4.2).

The PCTFE and PFA powders used in this study were not designed for additive manufacturing. This chapter investigates:

- The properties of the powders to assess their potential use in a pPBF process
    - Ways of improving the properties of the powders
- The laser sintering of the powders
    - Ways of improving the process

4.1 Characterisation of the polymers

4.1.1 Introduction

This section investigates and characterises the PFA and PCTFE powders for their use in pPBF using the following methods and techniques:

- DSC
    - Melting and crystallisation
    - Isothermal crystallisation
    - Activation energy of crystallisation
- TGA
    - Stability of the powders
- Particle size distribution
- FT4 powder rheometer
    - Neat powders
    - Additives: carbon black and fumed nano-silica
    - Thermal treatments
    - Static eliminator

- Dissolution and precipitation of PCTFE
- FT-IR

4.1.2 Differential Scanning Calorimetry (DSC)

This section investigates the crystallisation, melting temperature, isothermal crystallisation and activation energy of crystallisation of the PFA and PCTFE powders with and without carbon black. The methodology can be found in section 3.3.6. The choice of using PCTFE + 1 wt% CB and PFA + 0.2 wt% CB was based on the FT4 results (good powder flow) (section 4.2.7). CB was chosen over fumed nano-silica because it showed a higher improvement in powder flow (section 4.2.7). The melting and crystallisation behaviours of a polymer have a great influence on the processability of a material and they are important properties to characterise (section 2.2).

The DSC curves for the PCTFE powder showed the presence of a wide processing window of 40 °C between the melting peak (210.72 ± 0.15 °C) and the crystallization peak (170.43 ± 0.32 °C) (Figure 4.1a, Table 4.1). For comparison, PA12 has a broad processing window of 38 °C [62]. The presence of 1 wt% CB did not visibly affect the melting temperature (210.94 ± 0.01 °C) but it did shift the crystallization peak to a higher temperature (173.09 ± 0.01 °C) (Figure 4.1a). During the second heating and cooling cycle (R02) the melting peaks were narrower and shifted at slightly higher temperatures for both neat and with CB powders. The crystallisation peak shifted at slightly lower temperature for both neat and with CB powders.

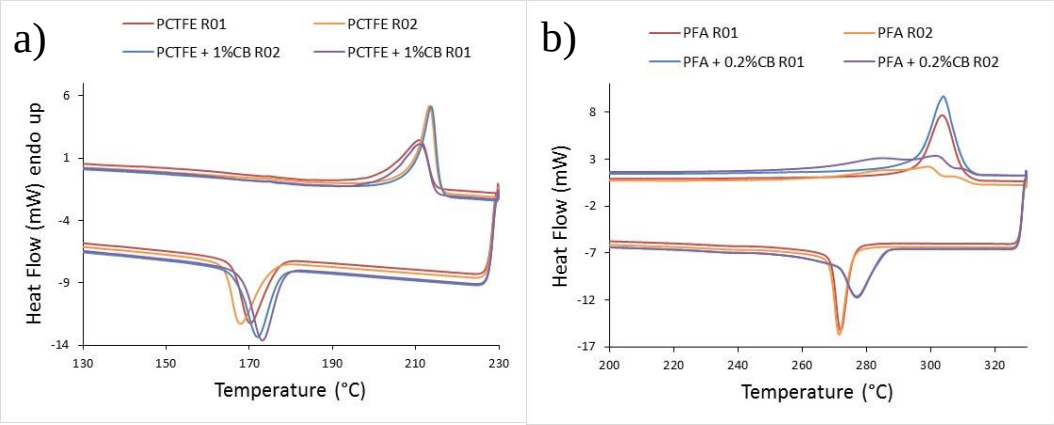


Figure 4.1 - DSC curves showing the melting and crystallisation temperatures of (a) PCTFE and (b) PFA. Heating/cooling rate of 20 °C/min. R01 and R02 are the first and second heating/cooling cycle, respectively.

Table 4.1 - Melting and crystallisation peaks of neat PCTFE and PCTFE + 1 wt% CB. R01 and R02 are the first and second heating/cooling cycle, respectively. (n=2).

			Peak (°C)	stdev	Onset (°C)	stdev
R01	**PCTFE**	**Melting**	210.72	0.15	201.48	0.37
		Crystallisation	170.43	0.32	177.06	0.46
	PCTFE 1% CB	**Melting**	210.94	0.01	202.22	0.63
		Crystallisation	173.09	0.01	178.13	0.06
R02	**PCTFE**	**Melting**	213.22	0.06	208.98	0.11
		Crystallisation	168.04	0.25	175.11	0.55
	PCTFE 1% CB	**Melting**	213.56	0.14	209.27	0.18
		Crystallisation	171.94	0.00	177.17	0.01

The isothermal crystallization in Figure 4.2a-c and Table 4.2 shows that the crystallization was happening relatively quickly, even at 10-20 °C above the crystallization temperature. As expected, the crystallization peaks decreased in height and increased in width as the isothermal temperature increased. Under isothermal conditions, the presence of 1 wt% CB increased the crystallization speed by roughly 52%. The activation energy of the crystallization was not affected by the presence of 1 wt% CB, as showed in Figure 4.2e. The activation energy equation for PCTFE and PCTFE + 1 wt% CB were y = -47.495x + 104.79 and y = -47.048x + 103.38, respectively. The gradients of these equations multiplied by the gas constant gave activation energies of 394.9 and 391.2 kJ/mol, respectively. Overall, these results suggest that a powder bed temperature above 190 °C is required: at that temperature, the 1/2t crystallisation (time to reach 50% of the crystallization) was 11.47 and 6.92 minutes when PCTFE was used without and with CB, respectively.

Table 4.2 - Isothermal 1/2t crystallisation at different temperatures for the PCTFE and PFA powders with and without 1wt% CB.

	PCTFE		**PFA**			
	Neat	**1 wt% CB**	**Neat**		**0.2 wt% CB**	
Temperature (°C)	**1/2t (min)**	**1/2t (min)**	**Temperature (°C)**	**1/2t (min)**	**Temperature (°C)**	**1/2t (min)**
180	1.154	0.742	276.36	0.431	278.43	0.070
182	1.644	1.093	278.42	0.728	282.41	0.071
184	2.375	1.651	280.40	1.117	284.41	0.258
186	3.697	2.53	282.30	2.044	286.42	0.495
190	11.47	6.924	284.30	3.441	288.43	0.799
193		16.747	286.35	5.526	290.39	1.400
			288.35	7.399	292.38	2.080
					294.38	3.742

The DSC curves for the PFA powder also showed the presence of a relatively wide processing window of 32 °C between the melting peak (304.10 ± 0.57 °C) and the crystallization peak (271.93 ± 0.17 °C) (Figure 4.1b). The presence of 0.2 wt% CB did not visibly affect the melting temperature (304.13 ± 0.13 °C) but it did shift the crystallization peak to a higher temperature (276.96 ± 0.09 °C) (Figure 4.1b). During the second heating and cooling cycle (R02) the melting peaks were much wider and shifted at lower temperatures for both neat and with CB powders. The crystallisation peaks were mostly unchanged for both powders.

Table 4.3 - Melting and crystallisation peaks of PFA with and without 0.2 wt% CB. R01 and R02 are the first and second heating/cooling cycle, respectively.

			Peak (°C)	stdev	Onset (°C)	stdev
R01	**PFA**	**Melting**	304.10	0.57	296.29	0.47
		Crystallisation	271.92	0.17	275.81	0.03
	PFA 0.2% CB	**Melting**	304.13	0.13	296.14	0.11
		Crystallisation	276.96	0.09	285.18	0.08
R02	**PFA**	**Melting**	299.47	0.42	280.90	1.70
		Crystallisation	271.47	0.15	275.45	0.01
	PFA 0.2% CB	**Melting**	301.73	0.11	283.48	0.21
		Crystallisation	277.08	0.09	285.32	0.45

The isothermal crystallization in Figure 4.2b-d and Table 4.2 for the neat PFA shows that the crystallization was happening relatively quickly, even at 20 °C above the crystallization temperature. At equal temperatures, the presence of 0.2 wt% CB increases the crystallization speed by roughly 10 times. The activation energy of the crystallization was slightly affected by the presence of 0.2 % CB, as shown in Figure 4.2b-d. The activation energy equations for PFA and PFA + 0.2 wt% CB were y = -75.881x + 137.26 and y = -82.849x + 147.3, respectively, corresponding to activation energies of 630.9 and 688.8 kJ/mol, respectively. In summary, these results suggest that a powder bed temperature above 288 °C is required for PFA: at that temperature, the 1/2t crystallisation was 7.39 and 0.79 minutes when PFA was used without and with CB, respectively.

Similar results were found by Silverman et al. [206] when they investigated the effect of tungsten disulphide inorganic nanotubes (INT-WS2) on the crystallisation behaviour and kinetics of poly(3-hydroxybutyrate-co-3-hydroxyvalerate) (PHBV). They showed that increasing loadings of nanotubes accelerated the crystallisation and shifted the crystallisation at much higher temperatures. They also used a hot stage microscope and polarised light to observe the growth of the spherulites with time; they saw that the growing rate and density was much higher when the nanotubes were used. The crystal growth rate was sixteen times

faster when 1 wt% of nanotubes was used. Similarly, Wudy et al. [207] reported an increase in crystallisation temperature when glass beads where added to PA12. Drummer et al. [208] used isothermal crystallisation analyses to determine the activation energy of polyamide 12 (PA12), polyoxymethylene (POM), high density polyethylene (PE-HD), polypropylene (PP) and polyetherketone (PEEK HP-3, EOS GmbH). They showed that PA12 and PP had the lowest slope and activation energy meaning that fluctuations in powder bed temperature would have a lower impact on the crystallisation speed. For comparison, the isothermal crystallisation of Nylon can be found in the publication by Neugebauer et al. [52].

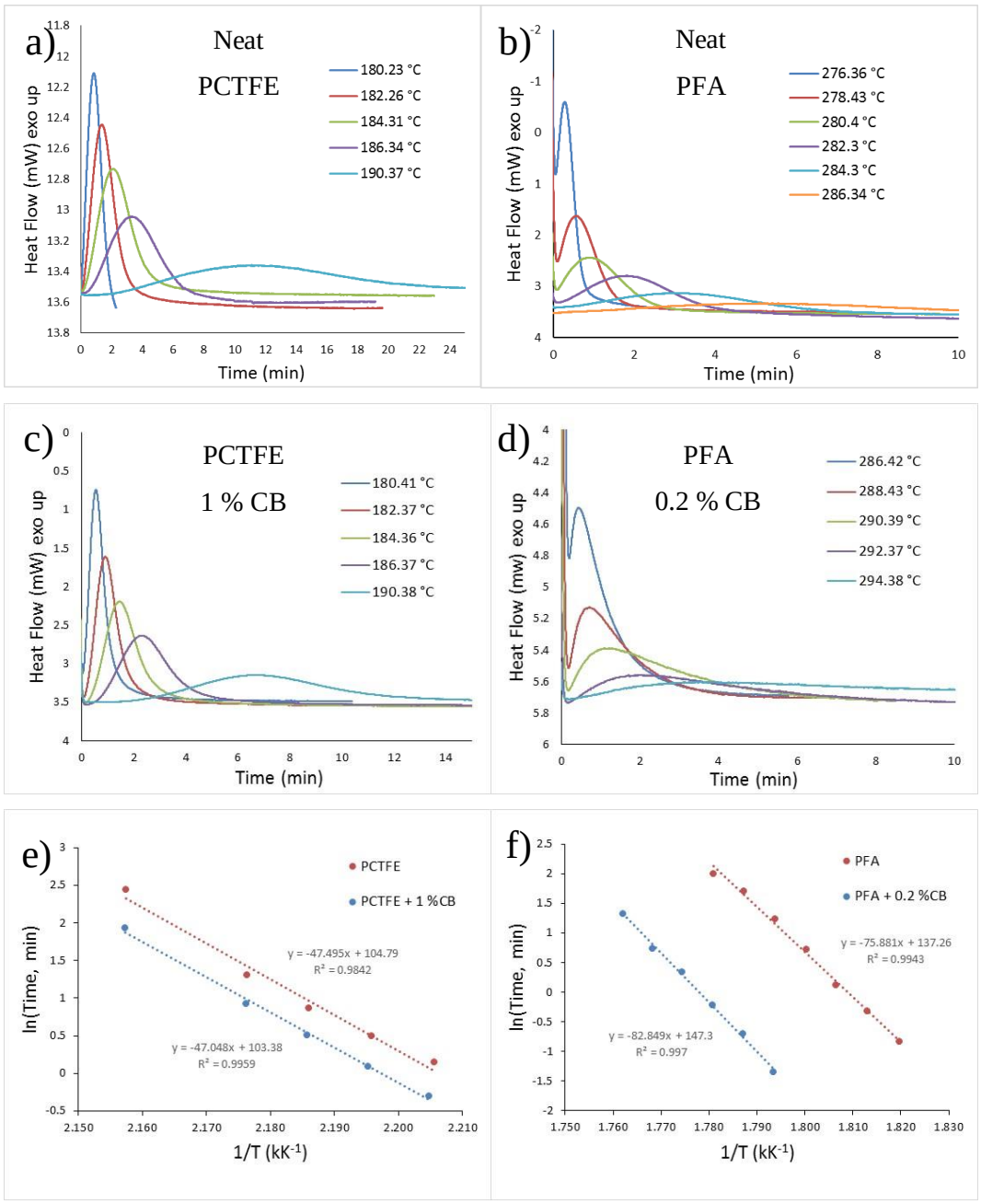


Figure 4.2 - DSC curves of PCTFE (left side, a-c-e) and PFA (right side, b-d-f). Isothermal crystallization at different temperatures for the (a-b) neat powders and (c-d) powders with CB. (e-f) Plotted ln of the 1/2t crystallisation versus the reverse of the isothermal crystallisation temperature.

4.1.2.1 DSC Conclusions

The thermal characterization of the PCTFE powder showed the presence of a wide processing window of 40 °C between the melting peak (210.72 ± 0.15 °C) and the crystallization peak (170.43 ± 0.32 °C). The PFA powder also showed a wide processing window of 32 °C between the melting peak (304.10 ± 0.57 °C) and the crystallization peak (271.93 ± 0.17 °C). For comparison, PA12 has a broad processing window of 38 °C [62].

Furthermore, the DSC showed how the presence of carbon black (CB) increased the crystallization temperature, and consequently the crystallization speed from the melt polymers. This would increase the minimum powder bed temperature that is required to delay crystallisation and avoid warping. PCTFE likely requires a powder bed temperature above 190 °C: at that temperature, the 1/2t crystallisation was 6.92 and 11.47 minutes when PCTFE was used with and without CB, respectively. Similarly, PFA likely requires a powder bed temperature above 288 °C: at that temperature the c1/2t crystallisation was 0.79 and 7.39 minutes when PFA was used with and without CB, respectively. After the addition of CB, the activation energy of crystallisation was almost unchanged for PCTFE (394.9 and 391.2 kJ/mol) and slightly increased for PFA (630.9 and 688.8 kJ/mol).

4.1.3 Thermogravimetric Analysis (TGA)

This section investigates the stability and decomposition of PCTFE, PFA, and THV. The methodology can be found in section 3.3.7.

The aim of the experiment was to ensure that the PCTFE and PFA powder would not decompose at the powder bed temperatures used during the experiments (~ 182 °C). Figure 4.3 shows that no significant decomposition took place after 5 hours at 201.55 °C for PCTFE; the weight decreased by just 0.17% (roughly 0.013 mg over 7.080 mg). The increase in weight seen at the start of the analysis was likely due to buoyancy effects [209]. Several sources in the literature confirmed the thermal stability of PCTFE which did not show any significant decomposition after 3h at 250 °C [149]. PCTFE decomposition starts slowly at 300 °C and accelerate at 400°C as showed in Figure 4.3 and confirmed by the literature [120], [149], [150]. The main decomposition product is CTFE monomer with traces of $C_2F_2Cl_2$, C_3F_5Cl, and $C_2F_3Cl_3$ [149]. PFA decomposition starts slowly at 400 °C as showed in Figure 4.3 and confirmed by the literature [210]. After 2 years at 285 °C PFA showed no sign of decomposition [145]. THV 221, despite the relatively low melting temperature of ~ 115 °C, decomposes around 410 °C [162], [164].

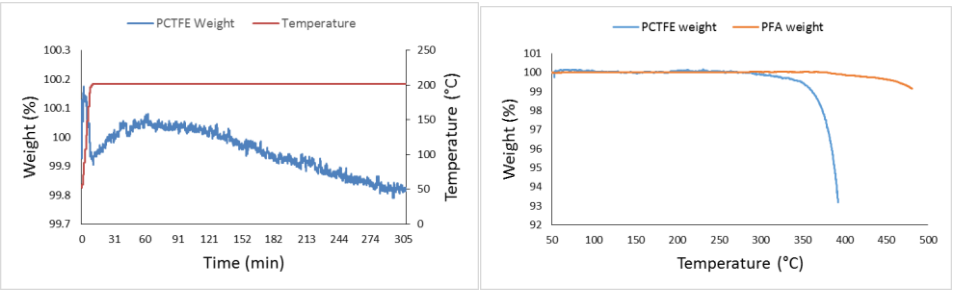


Figure 4.3- (Left) TGA of PCTFE kept at 201.55 °C for 5 hours. (Right) TGA of PCTFE and PFA at 10 °C/min and 20 °C/min, respectively.

4.1.3.1 TGA Conclusions

The start of the PCTFE and PFA decomposition (300 and 400 °C, respectively) agreed with the literature. PCTFE did not show any significant decomposition after 5 hours at 201.55 °C. These results confirmed that PCTFE and PFA could be processed safely at the powder bed temperatures used in pPBF (182 °C) without the production of harmful decomposition product and decrease in Mw. Furthermore, thermal degradation is expected to happen during extrusion and compression moulding of PCTFE, inducing the Zero Strength Time (of a generic PCTFE grade) to drop from 350 to roughly 200 and 300 seconds [211], respectively. Hence, pPBF could allow the production of parts with higher ZST/molecular weight with potentially higher physical properties compared to traditional manufacturing. Figure 4.4 shows the relationship between molecular weight and polymer physical properties [45]; a trade-off, called commercial polymer range, is often put in place as the viscosity, which increases with the molecular weight, escalates the processing cost. Nonetheless, using high molecular weight and high viscosity polymers is also challenging in pPBF (high porosity [25]).

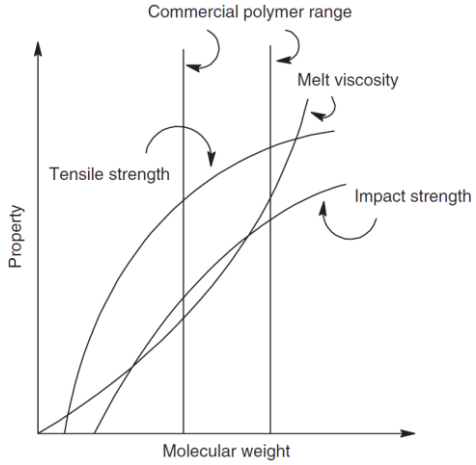


Figure 4.4- Relationship between molecular weight and polymer physical properties. Figure reproduced from [45].

4.1.4 Particle size distribution (PSD)

This section investigates the particle size distribution of the PCTFE and PFA powders and change in particles size due to thermal treatments. The methodology can be found in section 3.3.8. The particle size distribution has a great influence on the powder flowability and it an important value to characterise (section 2.2).

The average particle size quoted for the PCTFE powder was 150 µm but this value was found to be misleading. Initial dry analyses of the particle size distribution by volume gave results already different to those stated by the supplier: D_{10} 1.39 µm, D_{50} 21.6 µm, D_{90} 158 µm. Nonetheless, the powder was too cohesive for that particle size range. SEM imaging showed that all the particles in the powder were roughly below 1 µm in size (Figure 4.5). Therefore, the dry analysis could not break the powder agglomerations effectively. To solve this issue, wet analyses were conducted. The wet analysis showed two peaks, the first at 0.4 µm (real size) and the second at 20 µm (agglomerations) (Figure 4.5). The presence of the two peaks is likely due to the fact that the dispersing medium (water) was not ideal for PCTFE. The size of the second peak decreased with more mixing and sonication time suggesting that the dispersion improved with more time and mixing. Finally, the SEM imaging agreed with the peak at 0.4 µm (Figure 4.5).

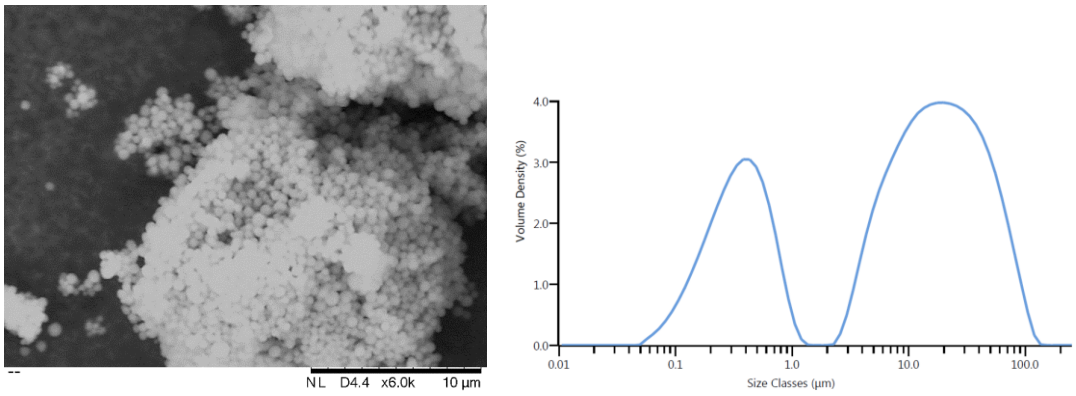


Figure 4.5 - Left: SEM image of the PCTFE powder where only small particles of roughly 0.2-1 µm were observable. Right: PCTFE particle size distribution measured with a wet cell after 30 minutes of mixing and sonication.

The PFA powder had a particle size distribution by volume of D_{10} 8.03 µm, D_{50} 24.9 µm, D_{90} 51.2 µm. These values agreed with the values provided by the supplier and the SEM imaging (Figure 4.6 right). The particle size distribution by number was D_{10} 0.932 µm, D_{50} 1.30 µm, D_{90} 4.07 µm, showing that the majority of the particle were small and thus leading to possible cohesive behaviours.

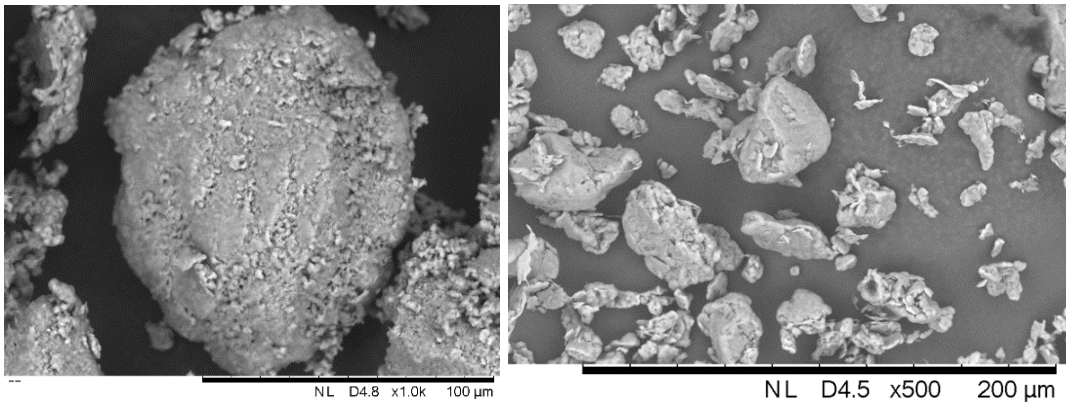


Figure 4.6 - Left: SEM image of a PCTFE powder particle after 20 minutes at 250 °C. Right: SEM image of the neat PFA powder.

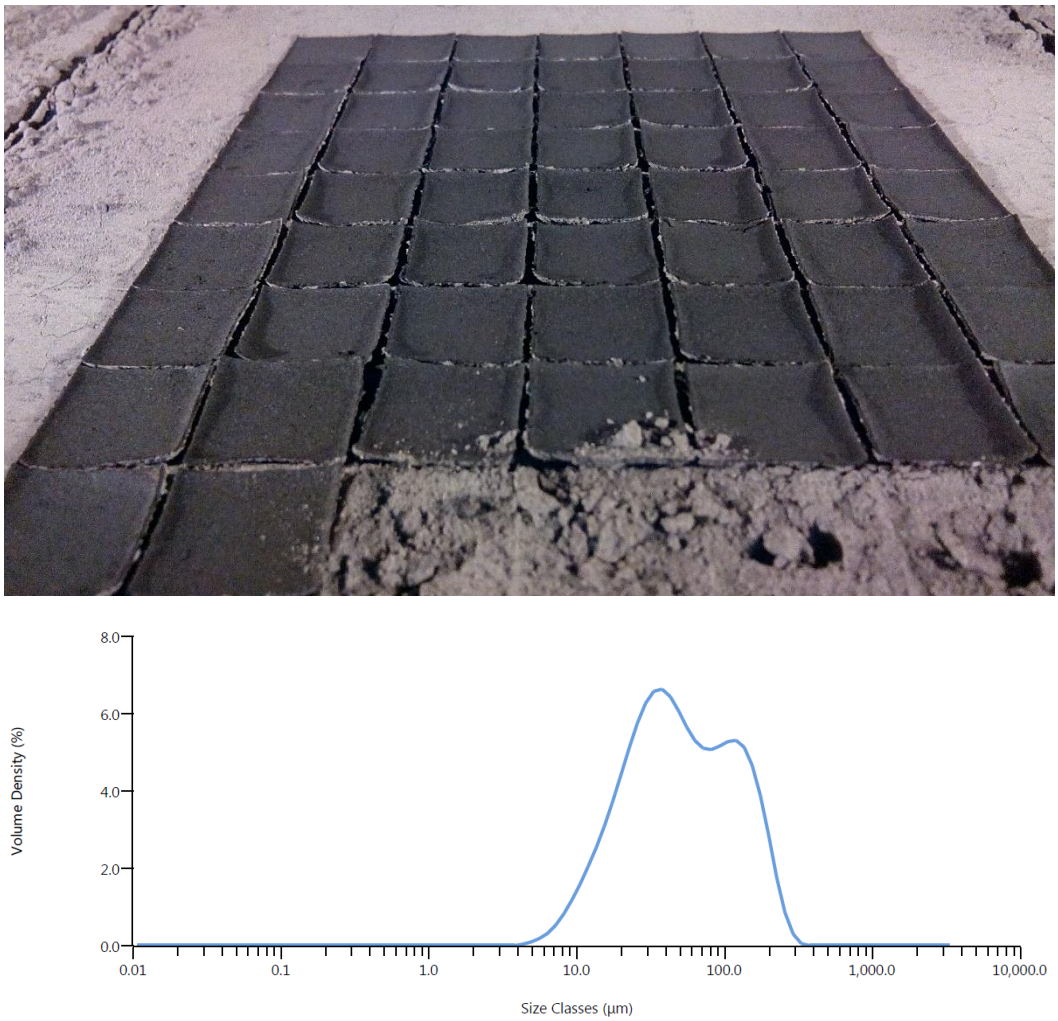


Figure 4.7 - Top: laser sintered PCTFE powder that was then ground. Bottom: Particle size distribution of the ground PCTFE laser sintered parts.

In a further test the PCTFE powder with 1 wt% CB was laser sintered in the EOS P100 and then ground back to powder (this is possible because the parts were very porous and fragile)

(Figure 4.7). The parameters used were: 2 scans, laser power 2W, scan velocity 2000 mm/s, hatch spacing 0.05 mm. The powder so produced showed an increase in particle size into an acceptable range: D_{10} 16.2 µm, D_{50} 48.1 µm, D_{90} 153 µm. The particles looked similar to those produced by grinding a powder heated for 20 minutes at 250 °C (Figure 4.6 left) and to the virgin PFA particles (Figure 4.6 right). This suggested that the use of a laser/oven could be used to effectively increase the particle size. More details on the thermal treatments and flowability of the powders are given in section 4.2.

From the literature, the ideal particle size was found to be between 45 and 90 µm [22], [51] but sometimes, a small amount of small particles could improve packing density as they fill the gaps between the bigger particles. Nonetheless, this is not always the case [193].

4.1.4.1 PSD Conclusions

The PCTFE powder had a particle size smaller than 1 µm which was much smaller than the size quoted from the supplier (~ 150 µm). The dry analysis gave an incorrect particle size distribution as it was not capable of breaking the agglomeration apart. The wet analysis gave two peaks, one for the well dispersed powder and one for the agglomerations. Finally, it was shown that particle size could be increased with a thermal treatment in an oven or with a laser.

The PFA powder had an average particle size of ~ 25 µm which was in agreement with the size quoted by the supplier and the SEM imaging.

Because of the low particle size distribution, PCTFE and PFA are not free flowing powders. To improve the flowability and allow their use in pPBF several techniques and additives were used (section 4.2).

4.1.5 Fourier-transform infrared spectroscopy (FT-IR)

This section investigates the IR absorbance of PCTFE, PFA, and carbon black. The methodology can be found in section 3.3.9. As discussed in section 2.2, the pPBF uses a CO_2 laser to sinter the polymer powder. Powders with a high absorbance in the wavelength of the CO_2 laser require lower laser powers (lower ED) to melt or decompose.

The PCTFE IR spectrum (Figure 4.8) was in agreement with the spectrum found in literature [212], [213]. The spectrum showed high absorbance at the CO_2 laser wavelength due to the C-Cl stretching at 937 and 972 cm^{-1} [149], [214]. Carbon black had a great absorbance in the entire IR range measured (Figure 4.8). The addition of 1 wt% CB to the PCTFE powder shifted the entire PCTFE spectrum to a lower transmittance (higher absorbance). Zoomed sections of the spectra are shown in Figure 4.9. Because of its broad absorption range, CB is often used to increase the absorption in several processes that uses different heating sources such as high speed sintering [215] and laser diode [216], [217].

PFA showed a low absorbance in the wavelength of the CO_2 laser. Similarly to PCTFE, the addition of CB increased the overall absorbance (Figure 4.8, Figure 4.9). Compared to PFA, THV showed a slightly higher absorbance in the wavelength of the CO_2 laser because of the presence of C-H bonds [143], [218] (Figure 4.10).

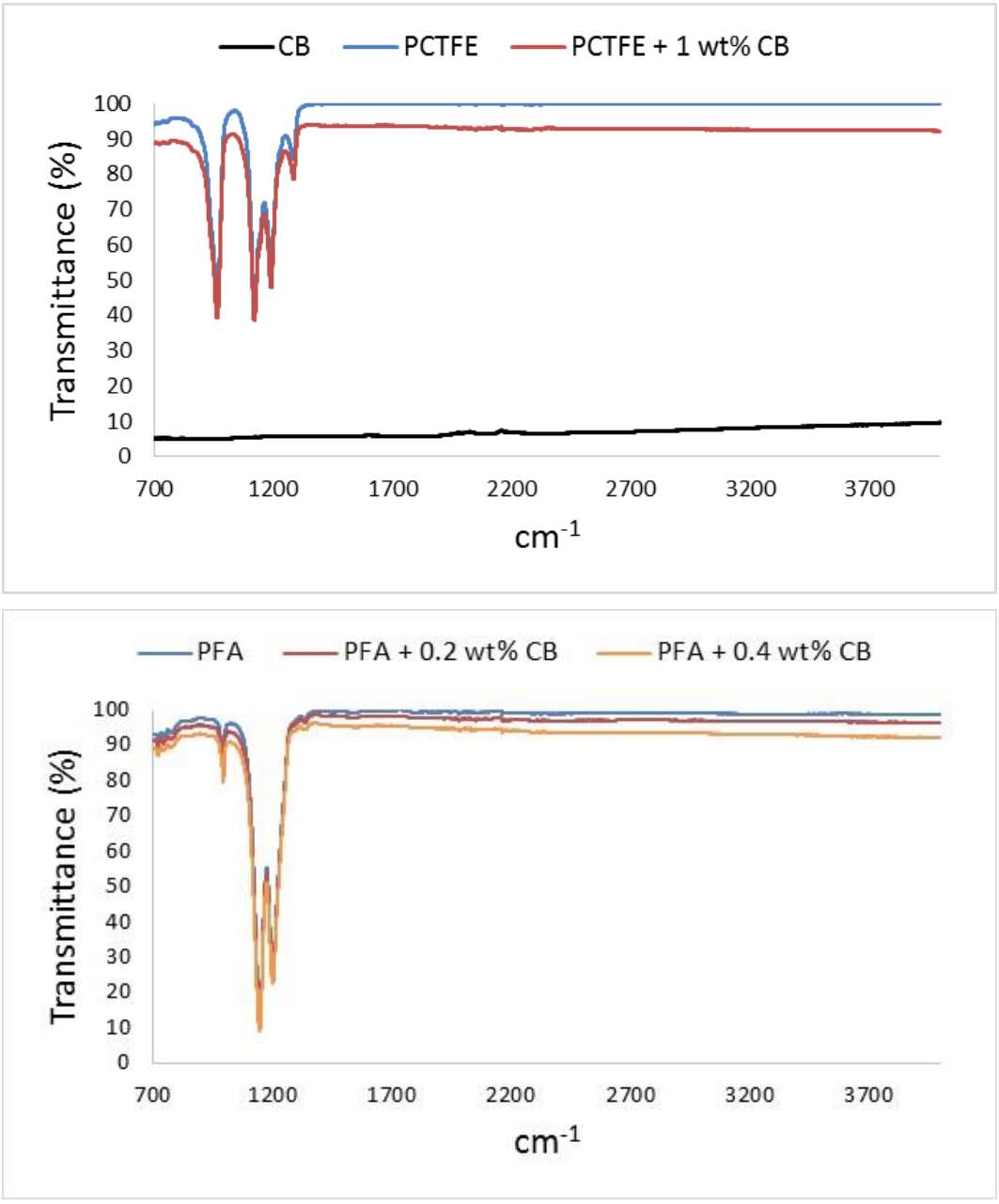


Figure 4.8 – Top: IR transmittance spectra of CB and PCTFE with and without 1wt% CB. Bottom: IR transmittance spectra of PFA with and without 0.2 and 0.4 wt% CB.

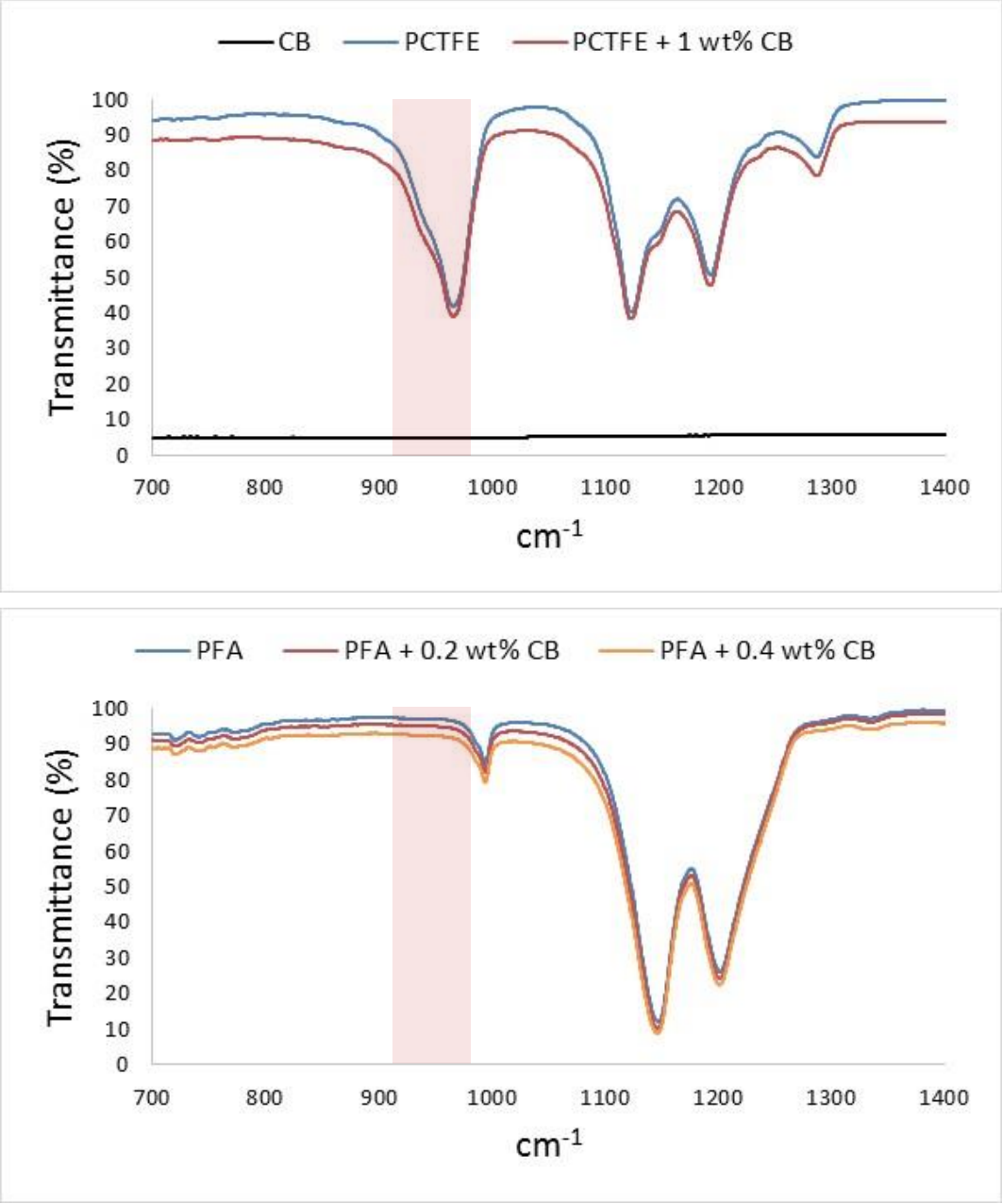


Figure 4.9 – Zoomed IR transmittance spectra of CB and PCTFE/PFA with and without the addition of CB. The red band indicate the wavelength of the CO_2 laser

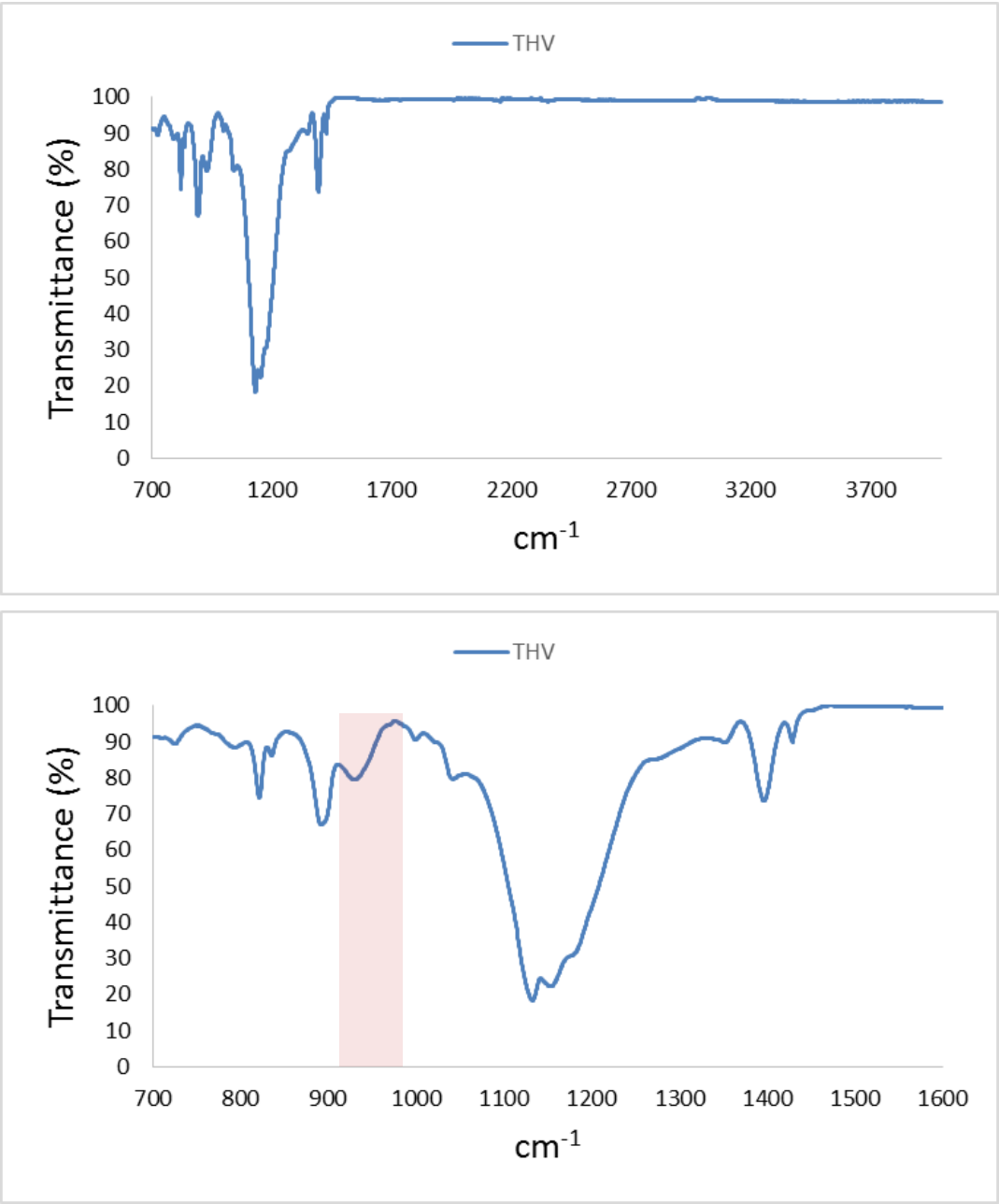


Figure 4.10 - IR transmittance spectrum of THV. The red band indicate the wavelength of the CO_2 laser

4.1.5.1 FT-IR Conclusions

The IR spectra showed that PCTFE had a great absorbance in the wavelength of the CO_2 laser, while PFA had a low absorbance and THV had a slightly higher absorbance than PFA. CB had a great absorbance in the entire IR region measured and its addition to the polymer powders increased the overall absorbance.

4.1.6 Discussion – Characterisation of the polymers

The thermal characterization of the PCTFE and PFA powder showed how the presence of carbon black (CB) increased the crystallization temperature, and consequently the crystallization speed from the melt polymers. Therefore, increasing the minimum powder bed temperature required to avoid warping. This aspect (the influence of additives on crystallisation) is often overlooked in the literature for pPBF and only few papers investigated it [206], [207]. It appears that the isothermal crystallisation and activation energy of crystallisation of PFA and PCTFE with and without CB have never been published before. This PhD showed that PCTFE likely required a powder bed temperature above 190 °C as, at that temperature, the 1/2t crystallisation was 6.92 and 11.47 minutes when PCTFE was used with and without 1 wt% CB. Similarly, PFA likely required a powder bed temperature above 288 °C: at that temperature, the 1/2t crystallisation was less than 10 minutes for both neat PFA and PFA with 0.2 wt% CB. The activation energy of crystallisation for PCTFE and PFA was 394.9 and 630.9 kJ/mol, respectively (Figure 4.2e-f). After the addition of CB, the activation energy of crystallisation was almost unchanged for PCTFE and slightly increased for PFA. A similar study was conducted by Drummer et al. [208]. They used isothermal crystallisation analyses to determine the activation energy of polyamide 12 (PA12), polyoxymethylene (POM), high density polyethylene (PE-HD), polypropylene (PP) and polyetherketone (PEEK HP-3, EOS GmbH). They showed that PA12 and PP had the lowest slope and activation energy meaning that fluctuations in powder bed temperature would have a lower impact on the crystallisation speed.

The TGA analyses showed that no significant decomposition took place after 5 hours at 201.55 °C for PCTFE (Figure 4.3). Several sources in the literature confirmed the thermal stability of PCTFE which did not show any significant decomposition after 3 hours at 250 °C [149]. PCTFE decomposition started slowly at 300 °C and accelerated at 400°C (Figure 4.3). These values were confirmed by the literature [120], [149], [150]. The main decomposition products of PCTFE are CTFE monomers with traces of $C_2F_2Cl_2$, C_3F_5Cl, and $C_2F_3Cl_3$ [149]. The PFA decomposition started slowly at 400 °C (Figure 4.3) and was confirmed by the literature [210]. After 2 years at 285 °C PFA showed no sign of decomposition [145]. These results confirmed that PCTFE and PFA could be processed safely, without the production of harmful decomposition products and a decrease in Mw, at the powder bed temperatures used in pPBF (182 °C). Furthermore, thermal degradation is actually expected to happen during extrusion and compression moulding of PCTFE, inducing the Zero Strength Time (of a generic PCTFE grade) to drop from 350 to roughly 200 and 300 seconds [211], respectively. Hence, pPBF could allow the production of parts with higher ZST (molecular weight) with potentially higher mechanical properties compared to traditional manufacturing. Nonetheless, using high

molecular weight and high viscosity polymers is also challenging in pPBF (high porosity [25], [51], [63], [64]).

The pPBF system used in this PhD was equipped with a CO_2 laser (heating source) and it was important that the processed polymers absorbed at the wavelength of the CO_2 laser. Generally, this is not a problem for most polymers as the C-H and C-C bonds have an acceptable absorption in the CO_2 laser wavelength [32], [33]. The PCTFE IR spectrum showed high absorbance at the CO_2 laser wavelength due to the C-Cl stretching at 937 and 972 cm^{-1} [149], [214] (Figure 4.9). Carbon black had a great absorbance in the entire IR range measured (Figure 4.8). The addition of 1 wt% CB to the PCTFE powder shifted the entire PCTFE spectrum to a lower transmittance (higher absorbance). Because of its broad absorption range, CB is often used to increase the absorption in several processes that use different heating sources such as lamps (High Speed Sintering) [215] and laser diode (Sintratec) [216], [217]. PFA showed a low absorbance in the wavelength of the CO_2 laser. Similarly to PCTFE, the addition of CB increased the overall absorbance. Compared to PFA, THV showed a slightly higher absorbance in the wavelength of the CO_2 laser because of the presence of C-H bonds [143], [218].

4.2 Methods of improving the powder flow of PCTFE and PFA

4.2.1 Introduction

While section 2.2.4 reports and explains the possible sources of cohesion, this section reports the experiments carried out to minimise cohesion and maximise flowability. Experiments include:

- Dissolution and precipitation
- Additives
    - Carbon black (CB)
    - Fumed nano-silica (NS)
- Static eliminator
- Thermal treatments through:
    - Different temperatures and residence times in oven
    - Use of a CO_2 laser

4.2.2 Individuating the source of the cohesion

As explained in more depth in section 2.2.4, cohesion is usually caused by five forces/factors: liquid bridges, solid bridges, mechanical interlocking, van der Waals forces, and electrostatic forces [73].

In the case of using PCTFE and PFA powders in pPBF, liquid bridges could be ruled out as fluoropolymers (especially PCTFE) have near zero moisture absorption and the processing temperatures were above 100 °C. Solid bridges could also be discarded as their formation would happen only when the powder was hit by the laser. The high melting temperatures and viscosities of the polymers prevent the powder from caking at the processing temperature (182 °C). Mechanical interlocking was possible for the PFA powder as the particles had irregular shapes. Mechanical interlocking was unlikely for PCTFE as the particles were spherical. Van der Waals forces are always present and cannot be eliminated. Nonetheless, because of the low polarizability of fluoropolymers, they show low van der Waals forces [163], [219], a property reflected in their non-stick ability. Electrostatic charges are present due to the insulating properties of fluoropolymers. In summary, the cohesion in the PCTFE and PFA powder was mainly due to van der Waals and electrostatic forces.

Van der Waals forces can be reduced by increasing the distance between particles by adding small particles in the nanometre range (flowing agents). Increasing the particle size with a thermal treatment could also decrease cohesion by increasing the force of gravity acting upon each particle and decreasing the contact surface between particles. Electrostatic charges can be decreased or eliminated by ensuring that the instrument is grounded and by increasing the conductivity of the powder by adding conductive particles or increasing the humidity level. Another possibility is to use a static eliminator that eliminates the charges present on the powder particles by bombarding them with both positive and negative ions. These ideas are investigated in the next sections.

4.2.3 Dissolution and precipitation of PCTFE

An EOS patent [220] showed that it was possible to modify the particle size distribution of a powder through dissolution and precipitation. Because of its high chemical resistance, PCTFE is insoluble in most solvents. As stated in a patent [189], PCTFE can form ~ 10 wt% solutions in cineol (better known as eucalyptol), fenchone, and camphor at ~ 160 °C. This section investigates the solubility of PCTFE in eucalyptol, fenchone, and supercritical CO_2.The methodology can be found in section 3.3.10.

The PCTFE powder appeared to be insoluble in supercritical CO_2 at 100 °C while only a minimal portion dissolved in fenchone after several hours at 185 °C. While using a syringe, 10 drops of the PCTFE-fenchone solution were deposited on the same spot on a glass slide at 185 °C obtaining a small precipitate (Figure 4.11 left).

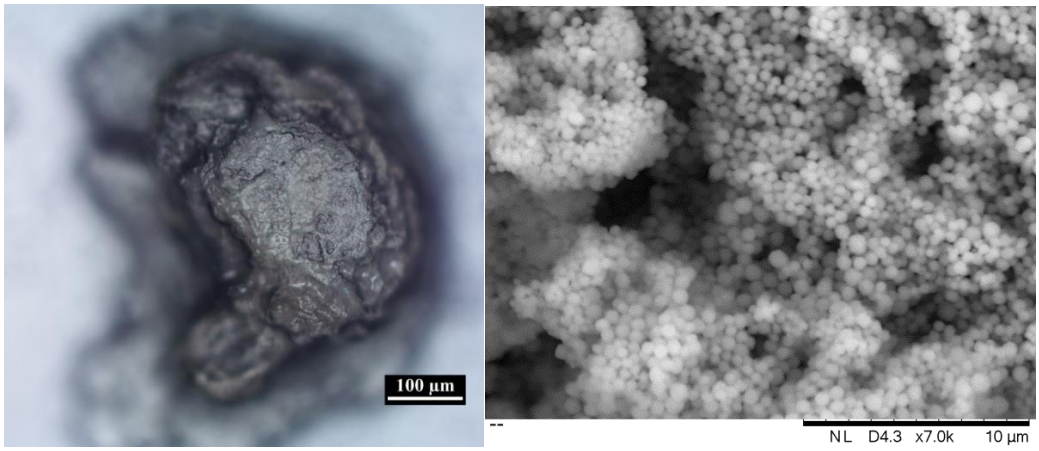


Figure 4.11- Left: PCTFE left on a glass slide after the evaporation of a PCTFE solution in fenchone. Right: SEM of PCTFE after the dissolution and precipitation test in eucalyptol.

In another experiment, a 10 wt% mixture of PCTFE powder and eucalyptol was prepared. The mixture, cloudy at room temperature, became clear at 160 °C suggesting dissolution. After 90 minutes at 160 °C the solution became slightly yellow. While cooling at 5 °C/min, the solution was still clear at 100 °C, started to become cloudy around 85 °C, and became cloudy at 65 °C. The solution was then evaporated at room temperature in the course of several days and analysed at the SEM (Figure 4.11 right). The powder looked very similar to the virgin powder (Figure 4.5) suggesting that no dissolution took place; the initial change during heating from cloudy to clear could be explained by the fact that PCTFE becomes clear at high temperatures as observed in another analysis. Overall, eucalyptol and fenchone seemed to have a small effect on the polymer and 10 wt% solutions (as stated in the patent [189]) were not obtainable. Thus, the scale up of a dissolution and precipitating system was not feasible with those solvents. The disagreement between the experiments and the patent could be explained by the fact that the paper was submitted in the 1958, just few years after the first commercialisation of PCTFE. It could be possible that the early syntheses of PCTFE were different from the modern ones (e.g. lower molecular weight).

4.2.3.1 Conclusions

The dissolution tests did not achieve the expected results. The solubility of PCTFE in fenchone and eucalyptol was much lower than the one stated in the patent [189]. This did not allow for the scale up of the process, making dissolution and precipitation an unfeasible solution to obtain powders with an ideal size for the pPBF process.

4.2.4 Additives

Van der Waals and electrostatic forces were the main contributors to the cohesiveness of the PCTFE powder and thus the main issue to solve to achieve good powder flow. Two different

flowing agents were used to achieve said goal: fumed nano-silica and carbon black. Several wt% were investigated. The FT4 powder rheometer was utilised to characterise the powders and the results reported in section 4.2.7 (carbon black performed better than fumed nano-silica).

4.2.5 Static eliminator

Static charges accumulate on the surface of a material due to triboelectric phenomena and are a common issue for insulating materials as they usually cannot discharge these charges even when grounded. A static eliminator (generally a metal bar with ion generating nozzles) bombards a surface with positive and negative ions to neutralise static electricity charges from the surface and restore the electrical balance [78]. For this purpose, a static eliminator was used on the PCTFE powder before and after being deposited inside of the EOS P100. No discernible improvement in flowability was observed. The FT4 powder rheometer was also utilised to characterise the powders and the results reported in section 4.2.7 (no significant change was measured).

4.2.6 Thermal treatments

This section investigates the effect of thermal treatments on the PCTFE powder. The methodology can be found in section 3.3.11.

The cohesiveness of PCTFE was mainly given by its small particle size distribution (0.2 – 1 µm), thus a thermal treatment could increase the particle size by sintering together the small particles. Four 1 mL vials were filled with 0.5 mL of PCTFE powder and left in the oven at 250 °C for 5/10/15/20 minutes.

- 5 minutes – the powder cake broke apart just by tapping the vial and the SEM did not show any sign of sintering.
- 10 minutes – the powder cake broke apart quite easily and the SEM did not show any sign of sintering.
- 15 minutes – the powder cake broke apart quite easily with a spatula and the SEM might have shown some initial sign of sintering.
- 20 minutes – the powder cake shrunk and was much harder to break apart with a spatula; less powder stuck to the spatula. The SEM showed good melting and many particles between 50 and 200 µm. These big particles were once agglomerations of many small particles as showed in Figure 4.12 and Figure 4.6.

To obtain enough powder to run an FT4 test, a 250 mL beaker with 100 mL of PCTFE powder was thermally treated. Nonetheless, with the increase in sample volume, the difference in conductivity between powder and glass created complications; the powder in contact with the

glass reached the oven temperature more quickly and started to sinter earlier than the bulk of the powder. This led to a less uniform sintering and longer sintering times:

- 60 minutes at 250 °C – the bulk powder was unchanged while the powder at the bottom (in contact with the base of the beaker which was in contact with the oven grid) started to sinter and shrink.
- 90 minutes at 250 °C – the entire powder bulk shrunk towards the centre of the beaker (not in contact with the glass walls anymore) forming a hard cake having the shape of the beaker with softer powder in the centre. Nonetheless, when ground in a disk mill, an almost free flowing powder was obtained. The SEM showed a wide particle size distribution (from few microns to 500 µm) due to the non-uniform sintering step.
- 10 minutes at 300 °C – The sintering was excessive.

To minimise the effect of the thermal gradients, further experiments were carried out at lower temperatures but longer residence times:

- 4h at 200 and 205 °C – the SEM revealed no observable change but the FT4 showed an improving trend as the temperature increased (section 4.2.7).
- 4h at 200 and 210 °C – the SEM revealed the first sign of slight sintering. The powder also seemed to stick less to the spoon.
- 23h at 210 °C – the SEM revealed a beginning of sintering. The FT4 results continued the positive trend of the previous experiments. Figure 4.13 in section 4.2.7 shows the bulk density trend at increasing temperature and residence time in the oven. An increasing bulk density indicates a decrease in cohesiveness and better packing.

A similar process to increase the bulk density of PEEK powder up to 17% by reducing the specific surface of the particles (smoother particles) was patented by EOS [190]. Schmidt et al. [191] used a heated downer reactor to smooth polymeric particles that were injected in the reactor as an aerosol to minimise contacts between particles and reactor walls. The residence time in the reactor necessary to achieve smooth particles depended on the viscosity of the polymer. They suggested to use a conditioning temperature 20 °C above the glass transition and that the higher the melt viscosity, the higher the conditioning temperature should be.

A thermal treatment was also carried in the EOS P100 by sintering several layers of powder (parameters: 2 scans, 2W laser power, 2000 mm/s scan speed, 0.05 mm hatch spacing) and subsequently grinding them with mortar and pestle. The SEM showed similarities between the powder sintered in the oven and the powder sintered in the EOS P100, while the FT4 analysis (section 4.2.7) showed a great improvement in flowability. This great improvement was also due to the presence of CB. Therefore, as the powders sintered in the oven and EOS P100 looked similar in the SEM, it could be possible to reach similar results through a thermal conditioning step in the oven and addition of CB.

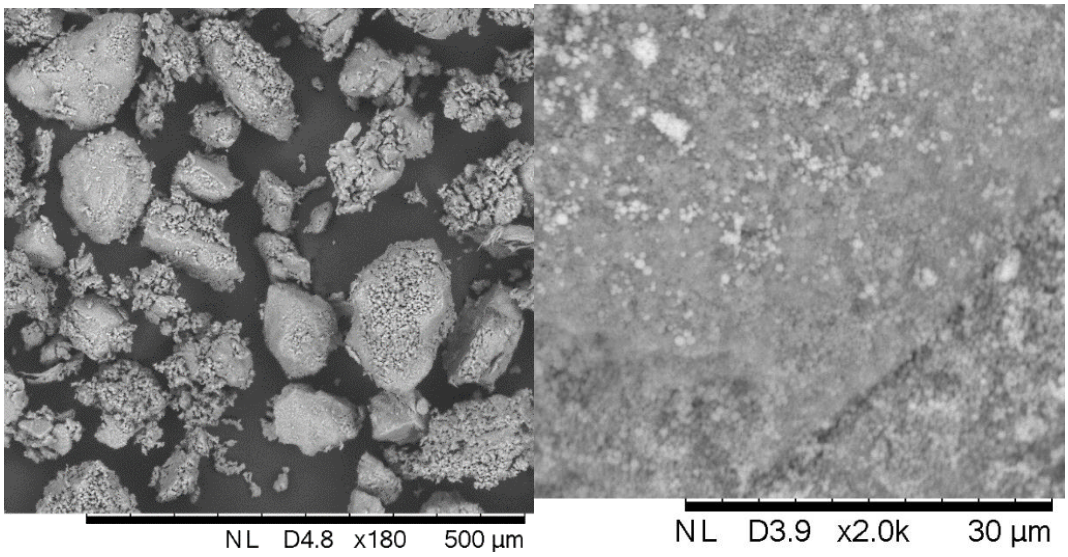


Figure 4.12 - Left: PCTFE powder after 20 minutes at 250 °C. Right: surface of a cluster of small PCTFE particles before being sintered together.

4.2.6.1 Conclusions

Thermal treatments showed promise in increasing the particle size by either using an oven or a CO_2 laser. Nonetheless, a uniform temperature throughout the powder during the process is required for a better control over the particle size distribution. This could be achieved by sintering the powder inside of PTFE bottles/containers which have similar thermal conductivity and will not melt or interact with the powder at the sintering temperatures utilised.

4.2.7 FT4 Powder flow rheometer study

This section investigates the flowability of the PCTFE and PFA powders with and without carbon black and nano-silica and after thermal treatments. The methodology can be found in section 3.3.12.

The conditioned bulk density (CBD) results for the PCTFE powder are reported in Table 4.4 and Figure 4.13. The CBD of the virgin powder was 0.51 g/mL, 23.8% of the absolute density (2.13 g/mL), while the specific energy (SE) was 11.83 mJ/g. The use of a static eliminator did not visibly improve the CBD or SE. The thermal conditioning at 200-205-210 °C for 4h and 210 °C for 23h progressively improved the CBD to 0.54-0.57-0.60-0.62 g/mL, respectively. The SE showed a more marked decrease at 210 °C for 23h. The use of fumed nano-silica (NS) had a negative effect on the CBD, which decreased to 0.42 g/mL for 2 wt% NS; the SE also decreased to 8.2 mJ/g.

Table 4.4 – FT4 analysis of PCTFE. Conditioned bulk density (CBD), Specific Energy (SE), Stability Index (SI), and The Basic Flowability Energy (BFE) of PCTFE powders with and without additives and after thermal treatments. NS = fumed nano-silica, CB = carbon black. (n=3)

	CBD (g/mL)	stdev	SE (mJ/g)	stdev	BFE (mJ)	stdev	SI	stdev
virgin	0.51	0.01	11.83	0.23	90.5	1.6	1.42	0.12
static eliminator	0.52	/	11.95	/	79.3	/	1.49	/
200 °C, 4h	0.54	0.01	10.77	0.18	71.1	0.00	1.39	0.04
205 °C, 4h	0.57	0.01	10.89	0.39	73.8	4.31	1.30	0.04
210 °C, 4h	0.60	0.01	10.33	0.79	81.2	3.04	1.11	0.00
210 °C, 23h	0.62	0.01	9.46	0.41	86.1	5.23	1.04	0.08
2 wt% NS	0.42	/	8.20	/	46.4	/	1.38	/
0.55% CB + 0.43% NS	0.53	/	5.85	/	46.6	/	1.35	/
0.55 wt% CB	0.56	0.01	5.50	0.06	46.1	1.92	1.24	0.04
1 wt% CB	0.59	/	3.69	/	34.4	/	1.12	/
2 wt% CB	0.59	/	3.35	/	35.8	/	1.12	/
3 wt% CB	0.57	/	3.50	/	32.5	/	1.08	/
sintered	0.82	0.00	4.55	0.07	267	13	0.94	0.03

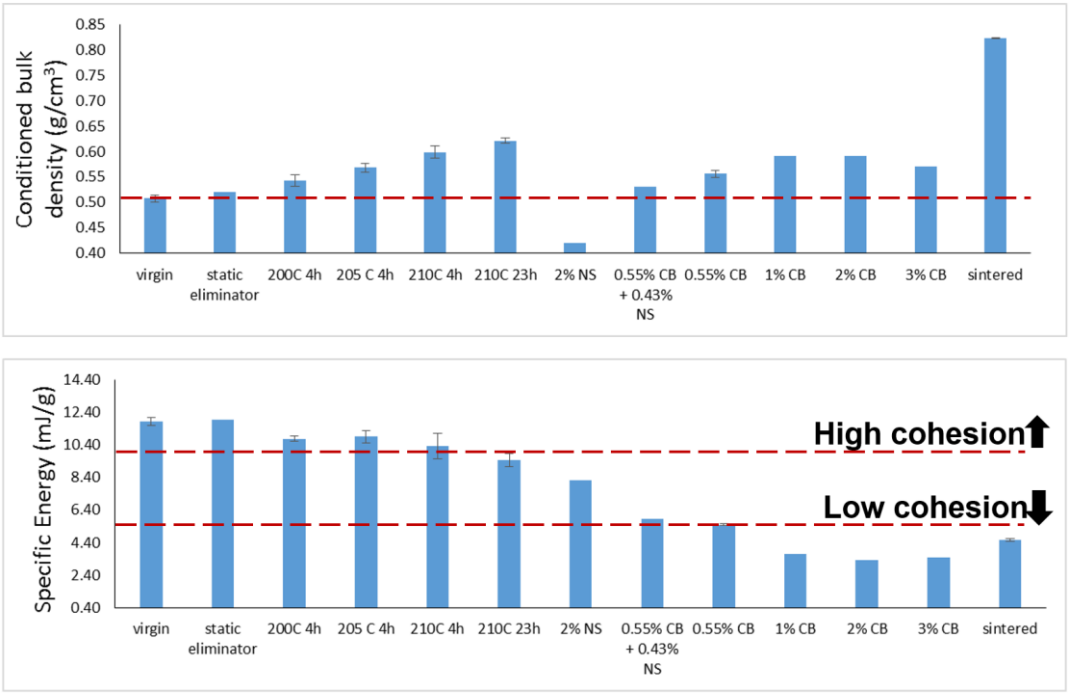


Figure 4.13 - FT4 results. Top: CBD of the PCTFE powder for different heat treatment and additives. The red dashed line indicates the CBD of the virgin neat PCTFE powder. Values above the line indicate an improved CBD and lower cohesion. Bottom: SE of the PCTFE powder for different heat treatment and additives. The red dashed lines indicates the approximate level of cohesion.

The addition of carbon black (CB) showed an improvement to the CBD and SE. The CBD increased to 0.56-0.59-0.59-0.57 g/mL and the SE decreased to 5.50-3.69-3.35-3.50 mJ/g for 0.55-1-2-3 wt% CB, respectively. The improvements seemed to peak at 2 wt% CB after which they declined, indicating that this is the concentration with optimal coverage of the polymer particles. CB performed better than NS possibly because CB is a conductive material and could also decrease the cohesion between particles caused by static charges [75].

A further test was to laser sinter the PCTFE 1 wt% CB powder in the EOS P100 and then grind it. The parameters used were: 2 scans, laser power 2W, scan velocity 2000 mm/s, hatch spacing 0.05 mm. The powder produced showed a great improvement in CBD (0.82 g/mL, 38.6%) and a low SE (4.55 g/mL). This improvement was due to the increase in particle size. The FT4 findings were confirmed by experimental observations. Figure 4.14 shows how the PCTFE powder was cohesive and not capable of forming a smooth layer inside of the EOS P100. With the addition of 1 wt% CB, the powder was able to form smooth repeatable layers (Figure 4.14). Even though 2 wt% CB showed the best flowability in the FT4 study, 1 wt% CB was used to minimize possible negative effects on the properties of the final parts.

The SI of the tested powders get closer to unity with thermal conditioning and CB suggesting a more stable powder. The BFE decreases with the addition of CB and NS due to the decrease of the cohesive forces between the powder particles. The BFE increases in the case of the sintered powder due to an increase in particle size and bulk density (decrease of pockets of air, more energy is required to move the same volume of powder).



Figure 4.14 - Left: neat PCTFE powder showing bad flowability. Right: PCTFE powder + 1 wt% CB showing improved flowability and absence of agglomerations. Test carried out at 30 °C.

A similar study was done for the PFA powder (Figure 4.15). The virgin powder had a CBD of 0.80 g/mL, 37.3% of the absolute density (2.15 g/mL) and SE of 10.07 mJ/g. The neat PFA powder performed better than the neat PCTFE powder due to the larger particle size distribution of PFA. The used powder (17 uses/cycles) did not show any visible change to the CBD or SE. The addition of carbon black showed an improvement to the CBD and SE. The

CBD increased to 0.89 and 0.90 g/mL (41.9%) while the SE decreased to 5.52 and 3.57 mJ/g for 0.2 and 0.5 wt%, CB, respectively.

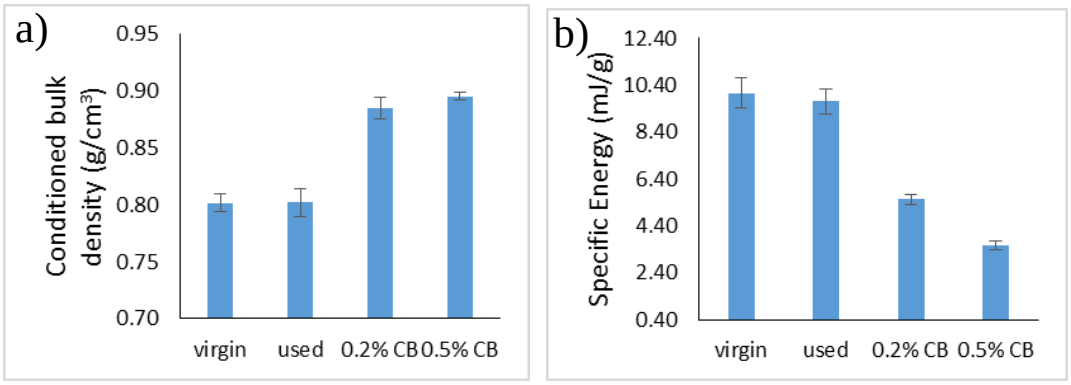


Figure 4.15 - FT4 results for the PFA powder for different mixtures. (a) Conditioned bulk density and (b) Specific Energy for the neat virgin/used powder and for the powder having 0.2 and 0.5 wt% CB.

While using the PFA powder in the EOS P100, it was observed that the powder could form a smooth layer but only on the first layer (Figure 4.16). Nevertheless, the spreading of successive layers failed due to the cohesiveness of the powder. In fact, even when the powder seemed to be spreading well, nothing was being spread onto a layer until the powder bed decreased by roughly 7 layers (0.7 mm) and the powder was deposited all at once (Figure 4.16 right). Similar to the PCTFE powder, this issue was resolved with the addition of 0.4 wt% CB. A lower CB loading was required for PFA compared to PCTFE because of the larger particle size distribution of PFA as shown in section 4.1.4. Under the SEM, the PFA powder looked similar to the thermally-treated PCTFE powder (Figure 4.6). This suggested that the PFA powder may have been produced in a similar manner and that thermal treatments could be an effective way to increase the particle size and improve flowability.



Figure 4.16 - PFA powder flow. Left: good powder flow for the first layer. Right: poor powder flow for successive layers. Test carried out at 30 °C.

4.2.7.1 FT4 Conclusions

The effect of two thermal treatments and two additives were assessed with the FT4. The first heat treatment method consisted of heating the PCTFE powder at temperatures above 200 °C for several hours. The longer the residence time and the higher the temperature, the greater the improvement in flowability. The second heat treatment method consisted of using the CO_2 laser of the EOS P100 to sinter a layer of powder and subsequently grind the produced parts. The newly obtained powder showed an increase in particle size (D_{10} 16.2 µm, D_{50} 48.1 µm, D_{90} 153 µm, section 4.1.4) and a remarkable increase in conditioned bulk density to 0.82 g/mL from the 0.51 g/mL of the virgin powder, 37.3% and 23.8% of the absolute density, respectively. The PFA had a larger particle size distribution and, under the SEM, the powder particles looked similar to the thermally-treated PCTFE particles. This suggests that the PFA powder may have been produced in a similar way: with a thermal treatment step.
The first additive tested was fumed nano-silica which decreased the CBD but improved the overall flowability. The second additive was carbon black which improved both CBD and flowability. CB performed better than NS possibly because CB is a conductive material and could also decrease the cohesion between particles caused by static charges [75]. Despite the larger particle size distribution, the PFA powder still required the use of CB to have good flowability but in a smaller amount compared to PCTFE: just 0.5 wt% instead of 1 wt%. Loadings as low as 0.2 wt% showed satisfactory flowing properties (Figure 4.15b). Finally, no visible changes were observed between the virgin and used powder.

4.2.8 Discussion – Methods of improving the powder flow of PCTFE and PFA

The PCTFE had a particularly small particle size distribution (<1 µm) and required a flowing agent to spread correctly in the EOS P100. This particle size was much smaller than the current standard of ~45-90 µm [22]. Nonetheless, there were examples in the literature where powders with a particle size smaller than 1 µm were used [142], [143] and printed successfully. However, these publications did not investigate or explain the flowability characteristics of the powder. In this PhD an in-depth study of the flowability of the powders that showed how a sub-optimal powder size could be made acceptable with the use of flowing agents [73]–[75] and thermal treatment was conducted. The effect of two additives and two thermal treatments were assessed with the FT4 powder rheometer [221]. By way of comparison, Ziegelmeier et al. [193], [194] tested the quality of the data obtained with the FT4 to a Revolution Powder Analyzer and the Hausner Ratio and showed that all the methods gave similar results. Carbon black was the additive that showed the best improvement in flowability. Even though 2 wt% CB showed the best flowability in the FT4 study (Table 4.4), 1 wt% CB was used to minimize possible negative effects on the properties of the final parts. Another flowing agent utilized

was fumed nano-silica (NS) but it did not perform as well as CB. When mixed with the PCTFE powder, NS gave a lower CBD and higher SE (lower flowability) compared to CB. CB performed better than NS possibly because CB is a conductive material and could also decrease the cohesion between particles caused by static charges [75]. NS is usually the principal material of reference when flowability issues are encountered in pPBF [191], [222], [223]. The results of this PhD showed that CB may provide a better solution to the flowability issues in powders for pPBF. Despite the larger particle size distribution, the PFA powder still required the use of CB to have good flowability but in a smaller amount compared to PCTFE: just 0.5 wt% instead of 1 wt%. Moreover, loadings as low as 0.2 wt% showed satisfactory flowing properties.

The effect of two thermal treatments were also assessed with the FT4 powder rheometer. The first heat treatment method consisted of heating the PCTFE powder at temperatures above 200 °C for several hours. The longer the residence time and the higher the temperature, the greater the improvement in flowability (Table 4.4). This was likely due to an increasing number of particles sintered together which increased the particle size and decreased cohesion (Figure 4.5 and Figure 4.6). A similar process to increase the bulk density of PEEK powder up to 17% by reducing the specific surface of the particles (smoother particles) was patented by EOS [190]. Schmidt et al. [191] used a heated downer reactor to smooth polymeric particles that were injected in the reactor as an aerosol to minimise contacts between particles and reactor walls. The residence time in the reactor necessary to achieve smooth particles depended on the viscosity of the polymer.

The second heat treatment method consisted of using the CO_2 laser of the EOS P100 to sinter a layer of powder and subsequently grind the produced parts. The newly obtained powder showed an increase in particle size and a remarkable increase in conditioned bulk density to 0.82 g/mL from the 0.51 g/mL of the virgin powder, 37.3% and 23.8% of the absolute density, respectively. It is believed that this is the first time that a CO_2 laser was used to increase the particle size and improve the flowability of a polymeric powder. With a tailor-made system, this may become a suitable and scalable process to optimise particle size and flow. The PFA powder had a larger particle size distribution and, under the SEM, the powder particles looked similar to the thermally-treated PCTFE particles (Figure 4.6). This suggested that the PFA powder may have been produced in a similar way: with a thermal treatment step. Finally, no visible changes were observed between the virgin and used (17 uses/cycles) PFA powder (Figure 4.15), suggesting that no sintering was happening between the particles of the powder at the used powder bed temperatures (182 °C). This fact, added to the high thermal resistance of fluoropolymer, would mean that the PCTFE and PFA powder could be recycled numerous times without incurring issues such as changes in viscosity and particle size [55], [62].

4.3 Powder bed fusion of PCTFE

4.3.1 Introduction

This section reports the experiments carried out with the PCTFE powder and EOS P100 which are reported in the following flow chart:

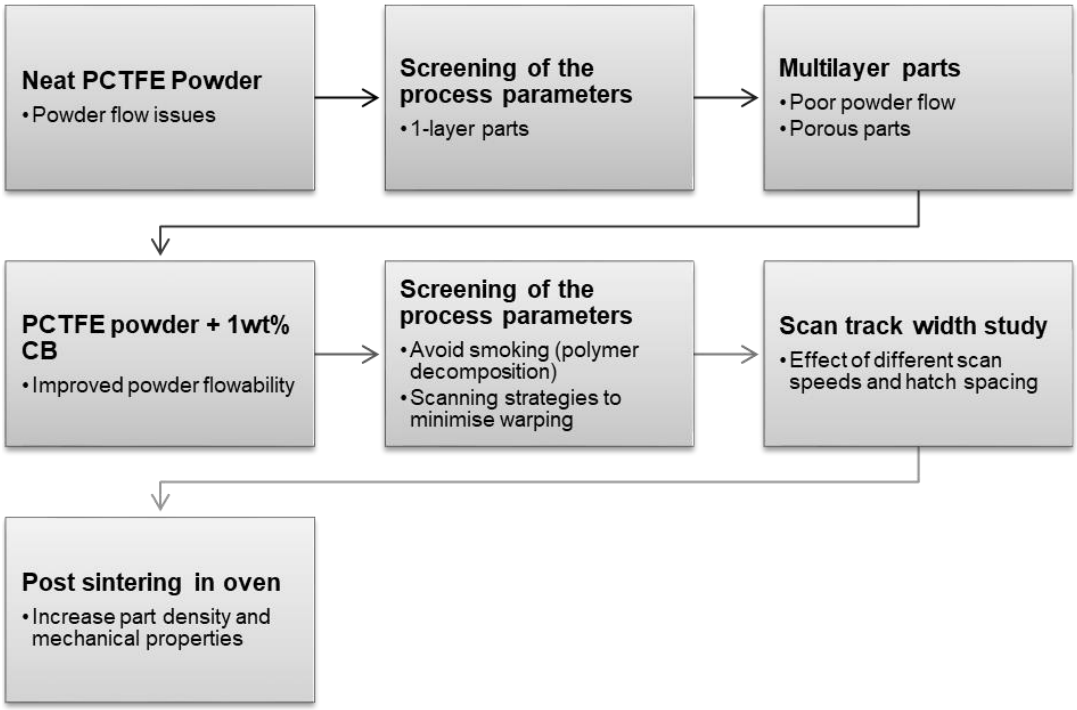


Figure 4.17 - Flow chart showing the development of the PCTFE powder with the EOS P100

4.3.2 Screening of the process parameters for neat PCTFE

As an initial test, the PCTFE powder was used as received without the addition of additives. A screening of the process parameters was conducted to obtain an outline of ideal conditions. To find the ideal energy density (ED) groups of 3 square samples were sintered using different printing parameters. The printing parameters are reported in Table 4.5 while the used pattern is shown in Figure 4.19a. The samples were made of 1 layer, only in this occasion the powder layer was spread manually. The dimensions of the square samples were 20 x 20 mm while the two red lines (samples 13-14) were 20 x 150 mm. A new sintering technique, referred to as "multi-scan", was also tested to solve a software limitation regarding the maximum number of scans per layer. In fact, the software only allowed 2 scans per sample, one in the X direction and one in Y direction as shown in Figure 4.18 [224]. To bypass this software limitation, an object could be duplicated multiple times and overlapped on the same position fooling the software into scanning the same area more than twice. This idea was tested with samples 9-10-11-12-13-14. Figure 4.19b shows the 10 overlapped rectangles used to print sample 13 and

14, where each rectangle was 15 mm shorter than the previous one. This new technique would allow increased control over the ED. The test was successful and multiple scans (>2) were possible on the same sample. Nonetheless, all the samples produced a certain amount of smoke reflecting the high absorption in the wavelength of the laser as discussed in section 4.1.5, indicating that lower ED should be used.

Table 4.5 - Printing parameters for the neat PCTFE. Laser diameter 0.42 mm, hatch spacing 0.2 mm.

Sample No.	Blade type	Layer (mm)	Scans per layer	Total ED (J/mm^2)	ED* (J/mm^2) spacing Eq.1	Laser Power (W)	Scan speed (mm/s)
1	curved	0.1	2	0.050	0.025	10	2000
2	curved	0.1	2	0.076	0.038	15	2000
3	curved	0.1	2	0.1	0.050	20	2000
4	curved	0.1	2	0.126	0.063	25	2000
5	curved	0.1	2	0.126	0.063	25.1	2000
6	curved	0.1	2	0.2	0.100	20	1000
7	curved	0.1	2	0.250	0.125	25	1000
8	curved	0.1	2	0.252	0.126	25.1	1000
9	curved	0.1	6	0.15	0.025	25.1	5000
10	curved	0.1	6	0.186	0.031	25	4000
11	curved	0.1	6	0.252	0.042	25	3000
12	curved	0.1	6	0.3	0.050	25	2500
13	curved	0.1	10	0.2	0.020	16	4000
14	curved	0.1	10	0.31	0.031	25	4000
15	flat	0.1	2	0.016	0.008	3	2000
16	flat	0.1	2	0.03	0.015	6	2000
17	flat	0.1	2	0.04	0.020	8	2000

* the ED refers to a single scan

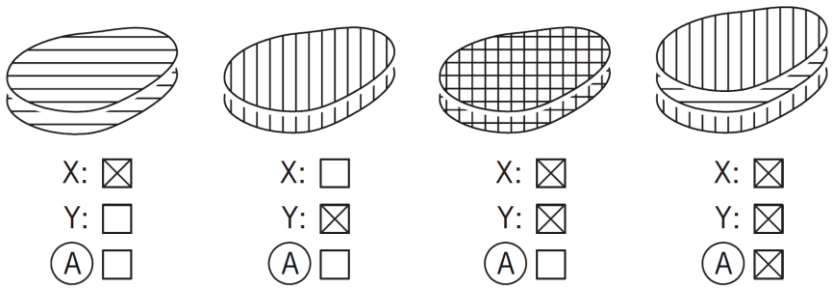


Figure 4.18 - Hatching settings. X and Y are the directions of the laser scan while A stands for Alternating. Figure reproduced from [224].

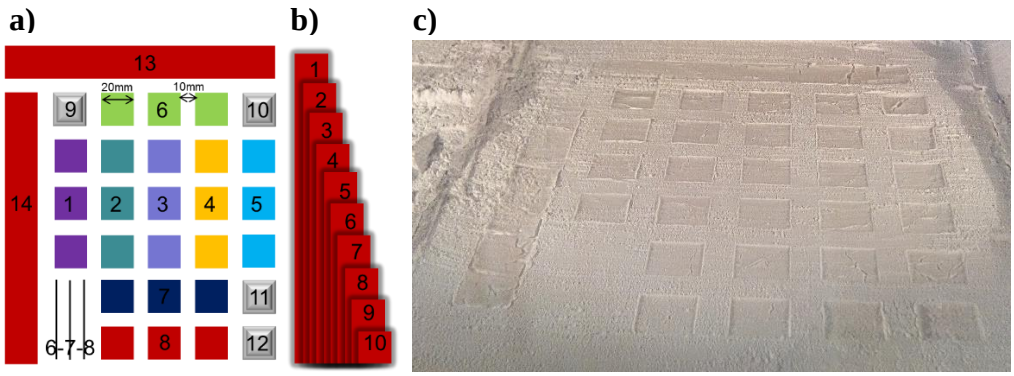


Figure 4.19 – (a) printing pattern and samples position. The numbers correspond to the printing parameters showed in the table above. (b) Representation of sample 13 and 14 which are made of 10 progressively shorter STL file overlapped. (c) Picture of the printed samples in the powder bed.

Figure 4.20 shows 4 20 x 20 mm samples printed with the following parameters: 3-6-8-10 W laser power, 2 scans per layer (one in the X direction, one in the Y direction), 26 layers, 2000 mm/s scan speed, 0.2 mm hatch spacing, 0.1 mm layer thickness, 178 °C powder bed temperature. Figure 4.20 shows on the left a very rough and uneven powder bed and on the right the SEM image of the sample printed with a laser power of 6 W. Figure 4.21 (left) shows the same sample after being removed from the powder bed. The samples were porous and brittle. It was observed that EDs around 0.015 J/mm^2 produced a white smoke indicating decomposition of the polymer.

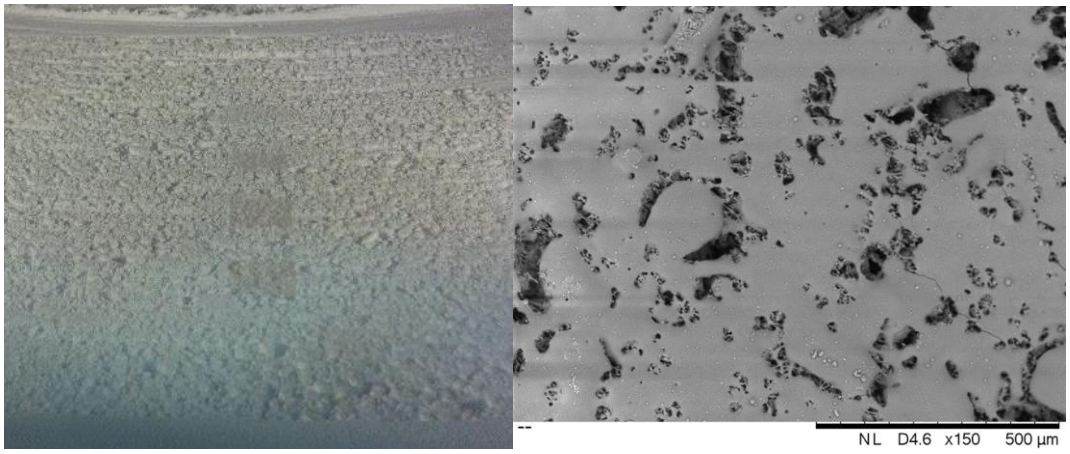


Figure 4.20 – (left) Laser sintered PCTFE samples still in the powder bed and SEM of the sample printed with 6 W (sample 16).



Figure 4.21 – Laser sintered 20 x 20 mm parts made with (left) PCTFE and (right) PCTFE 1 wt% CB.

4.3.3 PCTFE + 1 wt% carbon black

As seen in section 4.2.7, the powder flow increased greatly with the addition of CB. Spreading consecutive even layers was now possible. Nonetheless, it was observed that the quality of the spread layer decreased when the blade was moving/spreading big quantities of powder. The best results were achieved when the blade spread the minimum amount of powder required to form a single layer. It could be possible that when a small amount of powder is spread the powder agglomerates are more easily broken apart and "pushed" under the blade. It is then important to consider the amount of powder on the blade while assessing the powder flow in the machine.

The presence of CB was also likely to have an effect on the sintering behaviour of the powder as it strongly absorbed in the wavelength of the laser (section 4.1.5). A small process map experiment was planned (Figure 4.22) after taking into consideration the knowledge gained in the experiments with the neat powder. 12 samples were printed with a laser power of 1-2-3 W and 2-3-4-6 scans at a scan speed of 2000 mm/s, hatch spacing of 0.2 mm, 1 layer, and powder bed temperature of 182 °C. It was found that the 3 W laser (0.008 J/mm^2) caused the formation of a small amount of smoke for all the scans used while 1-2 W did not cause smoke formation despite the total energy received (considering multiple scans) by the powder was the same. This was due to the cooling of parts between consecutive scans. The parts that received the same total ED are connected by coloured lines in Figure 4.22. At first, the laser sintered parts did not show warping but after ~ 5 minutes warping was clear on the 3-4-6 scan components.

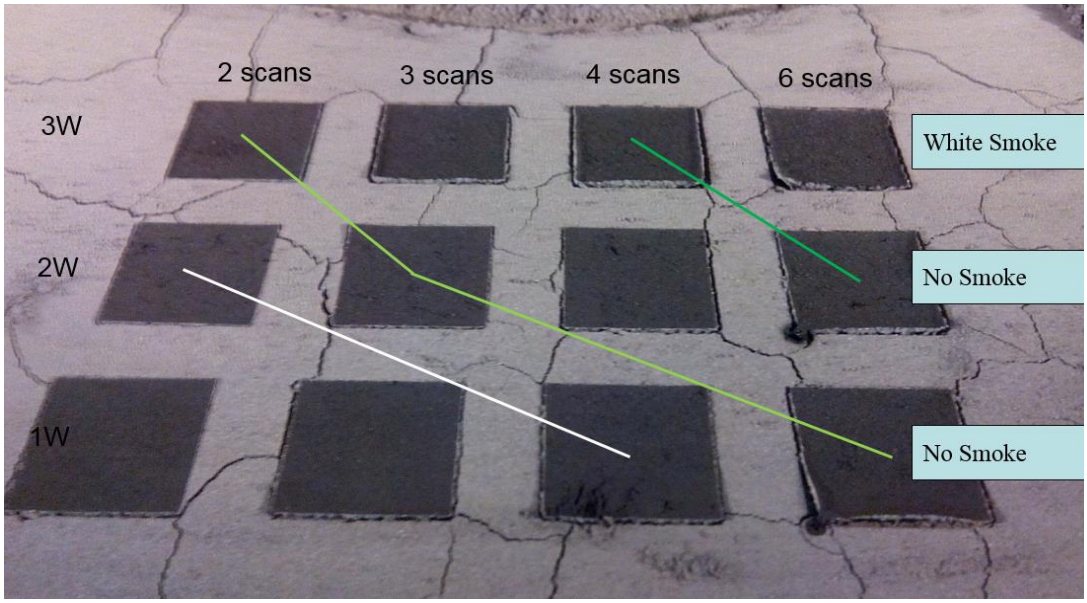


Figure 4.22 - Laser sintered 20 x 20 mm parts made with PCTFE + 1 wt% CB. The parts were printed with different laser powers and number of scans. The coloured lines connect the parts which received the same amount of overall ED. Smoke was observed only for the 3 W parts.

Table 4.6 shows the pPBF experiments conducted on the PCTFE 1 wt% CB powder to minimise warping. The processing of PCTFE was in fact limited by the warping of the parts (Figure 4.21 right) due to the relatively low powder bed temperature of 182 °C, too close to the crystallization temperature. Therefore, experiments were carried out to pinpoint the optimal laser parameters and scan strategies to minimize warping. As in the previous experiment it was observed that a 3 W laser caused light smoke, laser powers of 1 and 2 W were used for the remaining experiments. The experiments were evaluated by counting the number of layers printed before catastrophic failure (the part touching the recoating blade). It was observed that:

- The number of layers before the parts would warp enough to touch the recoating blade decreased at higher scan numbers (the other parameters were kept constant) due to the higher degree of sintering as confirmed by SEM imaging.
- The Support (S) scan strategy consisted of scanning the surrounding powder with a low energy density scan before scanning the actual part. The number of layers printed before warping almost tripled compared to a Normal (N) scan with the same laser parameters, going from 4 to 11 layers. While the additional scanning was not strong enough to considerably sinter the powder, it might have mitigated the warping by providing a fixed boundary condition that acted counter to the bending moments (shrinkage) that were generated and/or by increasing the local powder temperature (longer crystallisation times). The same technique was also successfully used with the PFA powder in section 4.4.3 (Figure 4.43).

- The Alternating (A) scan strategy introduced a waiting time between scans which caused the parts to cool down between successive scans. This decreased the amount of warping but it was likely caused by an overall lower degree of sintering.
- The combination of Alternating and Support (A + S) scan strategy did not seem to introduce any major improvements.

Table 4.6 – PCTFE 1 wt% CB pPBF experiments. N = normal, S = Support, A = Alternating. The total ED is the ED of a single scan multiplied by the number of scans.

Type	Total ED (J/mm^2)	Number of scans per layer	Laser Power (W)	Scan Speed (mm/s)	Hatch Spacing (mm)	Layer Thickness (mm)	Number of layers before failing	Note
N	0.008	1	3	2000	0.2	0.05	N/A	Light smoke
N	0.008	3	1	2000	0.2	0.05	22	
N	0.010	2	2	2000	0.2	0.05	20+	Ran out of powder
N	0.015	3	2	2000	0.2	0.05	15	
N	0.020	4	2	2000	0.2	0.05	9	
N	0.030	6	2	2000	0.2	0.05	4	
S	0.030	6	2	2000	0.2	0.05	11	
A	0.030	6	2	2000	0.2	0.05	16	
A	0.030	12	1	2000	0.2	0.05	18	
A+S	0.030	12	1	2000	0.2	0.05	19	No improvements
N	0.020	2	1	2000	0.05	0.05	11	Warps from layer 1

In a further test, parts were laser sintered with the following parameters: 2 W laser power, 3 scans, 2000 mm/s scan speed, 0.2 mm hatch spacing, 0.05 mm layer thickness, 15 layers. One of the parts was then subject to an oven post-sintering step of 30 minutes at 250 °C. This temperature was chosen because, from previous experiments (section 4.2.6), 23 hours at 210 °C (melting temperature) did not cause any visible sintering while 20 minutes at 250 °C caused the powder to cake. The thermal treatment increased the density of the printed part from ~ 35% to ~ 60% (Figure 4.23). The parts were no longer brittle and could be bent to angles greater than 90° without fracture. Further increases in densities may be achieved with longer residence times or higher temperatures.

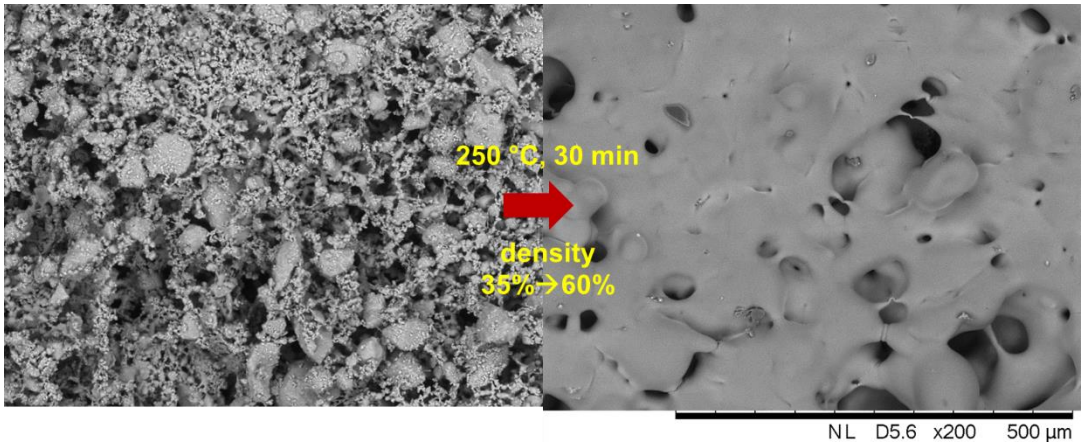


Figure 4.23 - Laser sintered PCTFE + 1 wt% CB before and after 30 minutes at 250 °C. The density increased from ~ 35% to ~ 60%.

Figure 4.24 shows a test carried out to observe the change in track width of a single-track scan. The laser spot diameter of the CO_2 laser used was 0.42 mm [31], thus hatch spacings of 0.40 mm and 0.60 mm were used with a laser power of 1 W and scan speeds of 5000/4000/3000/2000/1000/500 mm/s. This test was carried out to assess if a laser spot diameter of 0.42 meant that this value was also the minimum track width. It was found that the track width increased at lower scan speeds and it was possible to see and count all the scan lines in every sample except at 1000 and 500 mm/s with a hatching of 0.40 mm. This was due to the fact that at low scan speeds the heat from the laser had more time to diffuse through the powder and sinter a wider region. Another consequence of higher scan speeds was the decrease in depth of the melt pool [225], [226]. Therefore, track widths smaller than the laser spot diameter are achievable.

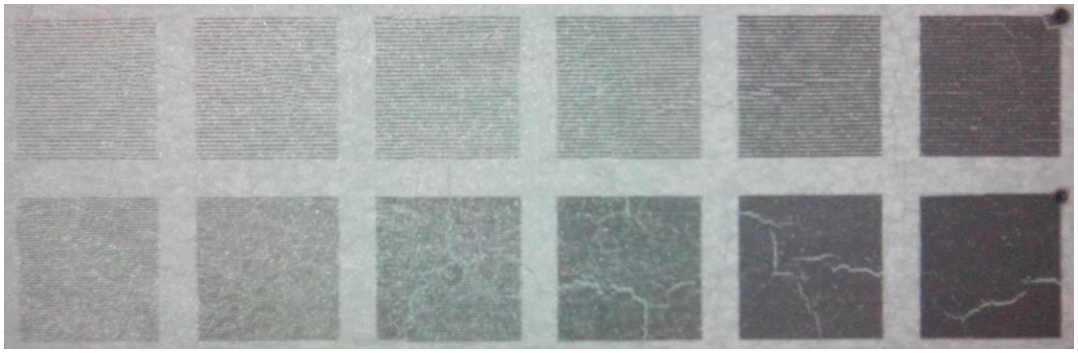


Figure 4.24 - Laser sintered PCTFE + 1 wt% CB. The top and bottom samples were made with a hatch spacing of 0.60 and 0.40 mm, respectively. Scan speeds of 5000/4000/3000/2000/1000/500 mm/s were used from left to right. Different track widths were observed.

4.3.4 Discussion – Powder bed fusion of PCTFE

It is well-known that additive manufacturing (AM), and more specifically LS, has great potential but several limitations, one of which is the narrow material portfolio [15], [36]. This

is especially true for pPBF where polyamide and few other polymers are the main materials used (PA12, PA11, PA612, PA6, PS, PAEK, PEBA, PP, PPS, TPU [37]–[41]). Furthermore, PA12 made up ~ 95 % of the market in 2009 [9]. None of these polymers possess the outstanding combination of properties that fluoropolymers hold (section 2.4).

Today, the use of fluoropolymers in pPBF is limited to PVDF [138], [141]–[143]. All the research done on this material was conducted by the same group of people and focused on the biological properties of small scaffolds (~ 1.5 x 1.5 x 1 cm). Little to no consideration was given to the pPBF process and many essential process parameters, necessary for the reproduction of the studies, were missing. In this PhD, several parameters and techniques used to print PCTFE and PFA were investigated and described in depth.

The sintered PCTFE parts showed a tendency to warp after 10-20 layers depending on the parameters and scan strategies utilized (Table 4.6). This was caused by the powder bed temperature (~182 °C) being too close to the crystallization temperature of the polymer (170 °C) and low powder bulk density [22], [61]. The presence of CB increased the absorbance of the CO_2 laser as evidenced by how the powder started smoking at lower energy densities (0.008 J/mm^2). No smoke was observed at 0.008 J/mm^2 without CB. Optimized scanning strategy led to a marked increase in printable layers before parts would warp enough to touch the recoating blade. The reduced warping was likely due to a lower degree of sintering when a delay was introduced between scans on the same layer and due to a support effect from the surrounding powder when the part and surrounding powder were exposed to a low energy scan before scanning the actual part. The printed parts were brittle but a post sintering step at 250 °C for 30 minutes increased the strength of the parts and density from ~35% to ~60% (Figure 4.23). Higher densities may be achieved with longer residence time and/or higher temperatures in the oven.

4.4 Powder bed fusion of PFA

4.4.1 Introduction

This section reports the experiments carried out with the PFA powder and EOS P100 system which are reported in the following flow chart:

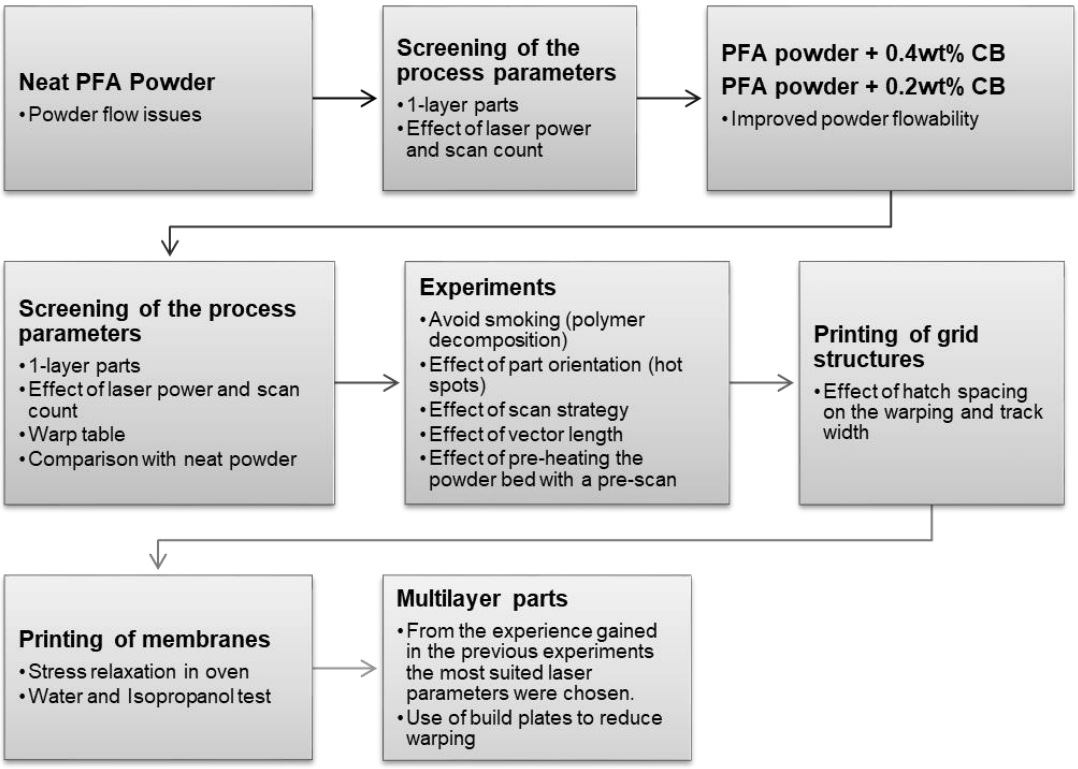


Figure 4.25 - Flow chart showing the development of the PFA powder with the EOS P100

4.4.2 Screening and optimisation of the process parameters

The sintering of a single layer of the PFA powder revealed that the amount of warping was proportional to the degree of sintering and energy density (ED) except when the polymer was fully melted (Figure 4.26). This was likely due to the relatively high viscosity of the polymer and fast heating/cooling rates characteristic of the pPBF process which limited the flow of the molten polymer. These factors did not allow for the formation of a complete molten layer unless high EDs (with consequent decomposition) would be used. All the following experiments used a powder bed temperature of 182 °C and were single layer, unless explicitly stated otherwise. Figure 4.26 shows how the degree of sintering decreased at lower laser powers (lower EDs). The parameters used to produce the 20 x 20 mm parts were 26W, 18 W (Figure 4.26a), 10W (Figure 4.26b), 5 W (Figure 4.26c), 2 scans, 2000 mm/s scan speed, 0.1 mm hatch spacing. When the samples were cleaned with isopropanol they appeared translucent (Figure 4.26e). When a laser power of 18 and 26 W was utilized it caused smoking.

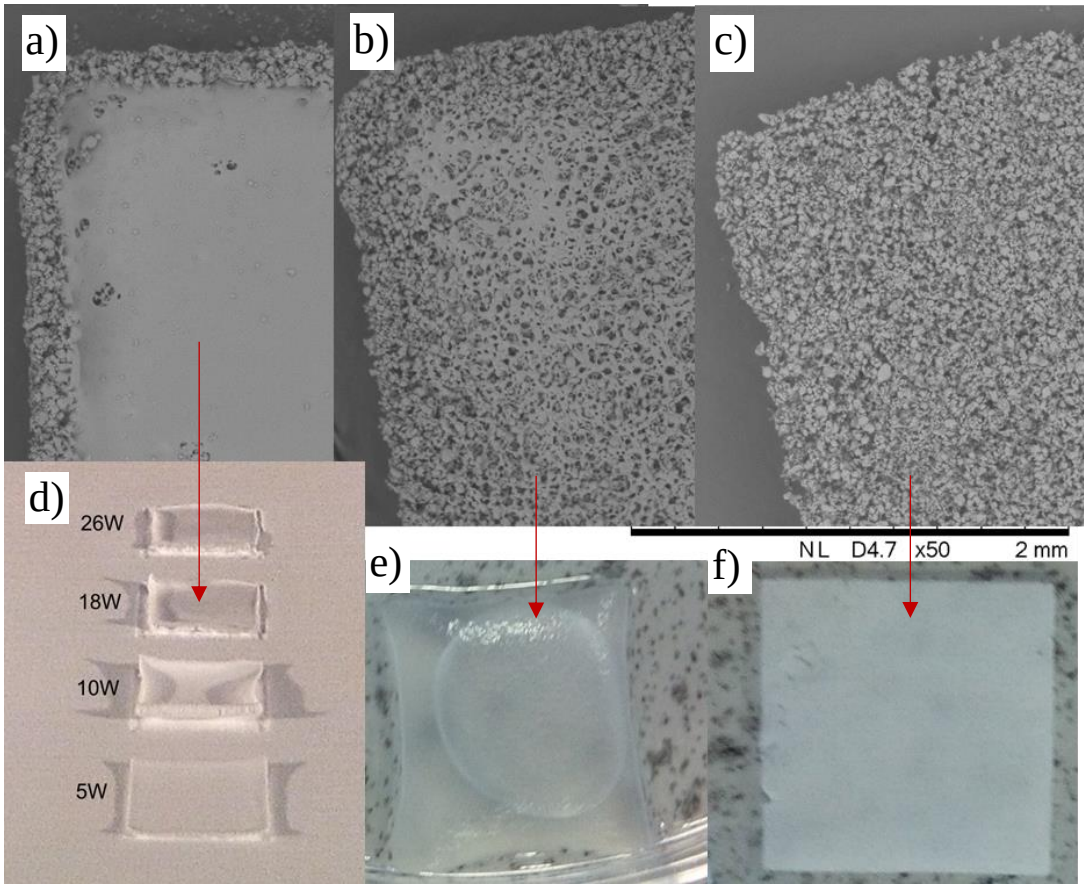


Figure 4.26 – Laser sintered PFA with a laser powder of (a-d) 18 W (b-e) 10 W, (c-f) 5 W. As the laser power decrease the parts become more porous and fragile. (a-b-c) SEM images of the samples. (d) Parts in the powder bed as printed and laser powers used. (e) 10 W sample wet with IPA. (f) 5 W sample cleaned of the excess loose powder with water and IPA.

As seen in section 4.2.7 the powder flow increased greatly with the addition of CB. Spreading consecutive even layers was now possible. Nonetheless, it was observed that the quality of the spread layer decreased when the blade was moving/spreading big quantities of powder. The best results were achieved when the blade spread the minimum amount of powder required to form a single layer. It is then important to consider the amount of powder on the blade while assessing the powder flow in the machine.

Figure 4.27 shows neat PFA and PFA 0.4 wt% CB samples printed with the same parameters. Parameters utilised: 3-4-5-6-7 W laser power, 2-4-8 scans (X-Y), 2000 mm/s scan speed, 0.2 mm hatch spacing. The first column was scanned twice (once in the X and once in the Y direction), the second column was scanned 4 times (X-Y-X-Y scan pattern), the third column was scanned 8 times (X-Y-X-Y-X-Y-X-Y scan pattern). The laser power was gradually increased from top to bottom and was 4-5-6-7 W for the first 2 columns and 3-4-5-6 W for the third column. A lower laser power was used for the last column as it was scanned 8 times and the delivered energy would have been too high otherwise. The test showed that the presence of carbon black made it easier to detect/observe the parts printed with lower EDs and that the

level of sintering could have been followed by the change in colour/shade. A darker region corresponded to a higher level of sintering and part strength. In both neat PFA and PFA 0.4 wt% CB the warping is more pronounced with the increase of sintering. Neat PFA warped predominately at the vertices of the squares while PFA 0.4 wt% CB warped predominately at the centre of the sides (see red circles in Figure 4.27).

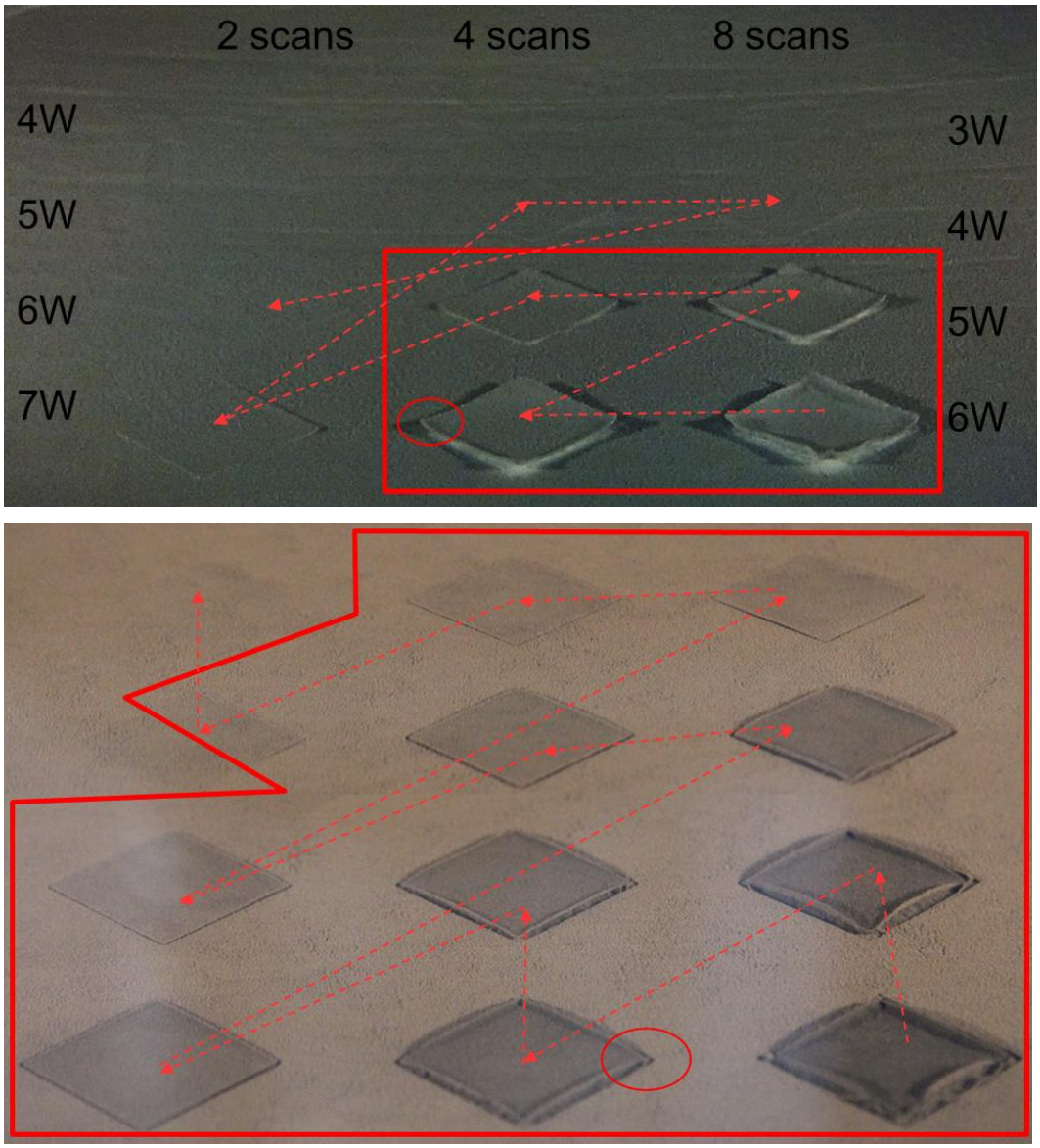


Figure 4.27 - (top) Neat PFA and (bottom) PFA + 0.4 wt% CB printed with the same parameters. The red boxes show the samples which were strong enough to be picked up, the dotted arrows show the order of strength/sintering/warping. The red circles show the difference in warping, the neat PFA preferentially warped at the vertices while the PFA + 0.4 wt% CB warped at the edges.

This could be due to the increase in absorbance and thermal conductivity and different heating/cooling mechanisms given by the addition of carbon black. The two red boxes in Figure 4.27 show the samples which were strong enough to be picked up. The majority of the samples done with the PFA with CB could be picked up confirming the higher absorption of the laser due to the presence of CB. The sample produced with 2 W and 2 scans were sintered

only in top right corner. The reason for this was the presence of a hot spot which will be discussed in more detail later on (Figure 4.29). The dotted arrows in Figure 4.27 shows the order of strength/sintering/warping for the different parameters used. The orders were similar for both neat PFA and PFA with CB but, in the latter, the 8 scans parts tended to warp more. Further investigations are needed to better understand these phenomena.

Next, a test to identify the laser power and ED that would produce smoking/decomposition for PFA 0.4 wt% CB was carried out (Figure 4.28). Parameters used: from 10 to 19 W laser power, single scan in the X direction, 2000 mm/s scan speed, 0.2 mm hatch spacing. During the experiment the 19 W (0.048 J/mm^2) showed the formation of smoke. After carefully watching the recorded video of the experiment, the samples showed a faint first hint of smoke at 16 W (0.040 J/mm^2) which became increasingly more evident at 17 W and 18 W. Recording the experiments proven to be very important to the understanding of the process as several details were only visible after carefully watching the videos numerous times in slow-motion or frame by frame.

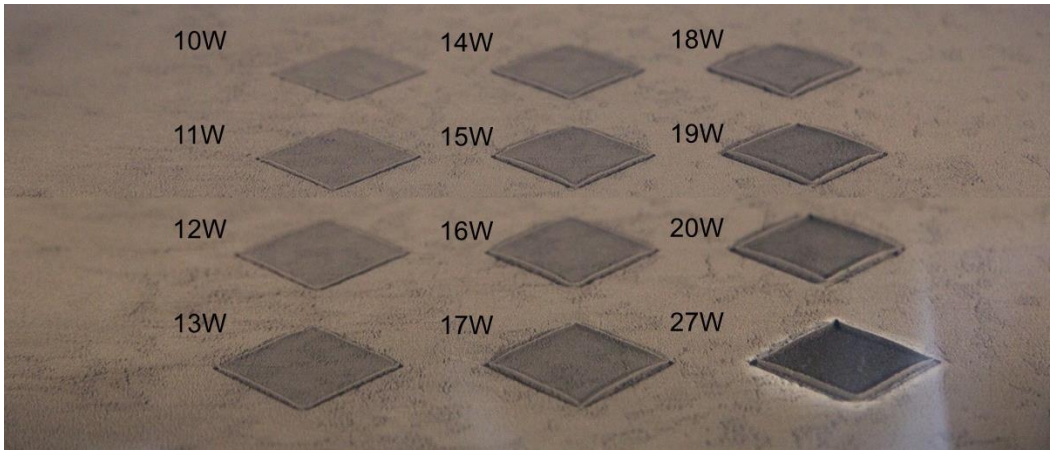


Figure 4.28 - Laser sintered PFA 0.4 wt% CB. Single scan in the X direction at different laser powers. Smoke formation was observed starting at 16 W.

Table 4.7 and Table 4.8 show the PFA 0.4 wt% CB process map for variable laser powers, variable number of scans, 2000 mm/s scan speed, and hatch spacing of 0.2 and 0.1 mm. The bold numbers indicate the experiments carried out while the rest were deductions. No number was assigned where either no experiment was carried out or a deduction was not possible. The numbers indicate the degree of warping:

- 0 – nothing happened, the printed part could not be seen or touched
- 1 – the part was barely visible
- 2 – the part was partially warped (only one side)
- 3 – the part warped in every direction
- 4 – the part was fully sintered
- mixed numbers mean that the degree of warping changed on cooling

Table 4.7 – PFA 0.4 wt% process map at 2000 mm/s, 0.2 mm hatch spacing, single layer. The numbers indicate the degree of warping: 0 – nothing happened, the printed part could not be seen or touched. 1 – the part was barely visible. 2 – the part was partially warped (only one side). 3 – the part warped in every direction. 4 – the part was fully sintered. Mixed numbers mean that the degree of warping changed on cooling. The bold numbers indicate the experiments carried out while the remaining numbers are deductions.

	Number of scans (0.2 mm hatch spacing)										
Laser power (W)		1	2	3	4	5	6	7	8	9	10
	1	0	0	0	0	0	0	0	0	0	0
	2	0	0	0	0	0	**0**	0	0	0	**0**
	3	0	0	0	0	0	**0**	0	**0**		
	4	0	0	0	**0**		**0-1**	0-1	**0-1**		
	5	0	**0**		**1**		**2**		**3**	3	4
	6	0	**0-1**		**2-3**		**3**	3	**4**	4	4
	7		**1-2**		**3**		**3**	3	4	4	4
	8						**4**	4	4	4	4
	9						**4**	4	4	4	4
	10						**4**	4	4	4	4
	11						**4**	4	4	4	4

Table 4.8 – PFA 0.4 wt% process map at 2000 mm/s, 0.1 mm hatch spacing, single layer. The numbers indicate the degree of warping: 0 – nothing happened, the printed part could not be seen or touched. 1 – the part was barely visible. 2 – the part was partially warped (only one side). 3 – the part warped in every direction. 4 – the part was fully sintered. Mixed numbers mean that the degree of warping changed on cooling. The bold numbers indicate the experiments carried out while the remaining numbers are deductions.

	Number of scans (0.1 hatch spacing)												
Laser power (W)		1	2	3	4	5	6	7	8	9	10	11	12
	1	0	**0**										
	2	0	**0**				**1**						**3**
	3		**2**		**3**	3	3	3	**4**	4	4	4	4
	4		**2**		3	3	3	3	4	4	4	4	4
	5		**3**	3	3	3	4	4	4	4	4	4	4
	6		3	3	3	3	4	4	4	4	4	4	4
	7		3	3	3	3	4	4	4	4	4	4	4
	8		3	3	3	3	4	4	4	4	4	4	4
	9		3	4	4	4	4	4	4	4	4	4	4
	10		**3**	4	4	4	4	4	4	4	4	4	4

On one hand, working between 0 and 1 assured that the parts would not hit the recoating blade and be dislodged while printing multiple layers. On the other hand, the parts were brittle and barely sintered. The test showed that a hatch spacing of 0.1 had a narrower processing window

(range of parameters that leads to a successful print) compared to a hatch spacing of 0.2 mm (Table 4.7 and Table 4.8), meaning that a small change in the parameters would cause the printing process to fail.

The orientation of the part was also important as shown in Figure 4.29; the parts were scanned twice with the same parameters, once in the X direction (from bottom to top) and once in Y direction (from right to left). This meant that at the end of the first scan (X), right before the second scan would start, the last area exposed to the laser was the top side (Figure 4.29c). As the top side had less time to cool down, it was at a higher temperature during the Y scan, generating a hot spot (Figure 4.29d). A higher temperature meant more sintering, which meant more warping (as observed in Figure 4.26 and from other experiments). When the sample was rotated by 45° the last part to be scanned in the first scan (X) was positioned in the middle of the next scan (Y), giving more uniform temperature distribution and warping. Nevertheless, the top right side still showed the presence of a smaller hot spot. The warping could be followed by looking at the shadows cast by the parts. When carbon black was used, the areas with a higher degree of sintering appeared darker (Figure 4.29b top parts). When more than two scans were used, two hot spots and preferential warping in opposite positions were present, one in the top right corner and one in the bottom left corner. When 2 scans in the X direction were used the parts showed uniform warping and colour (Figure 4.29b bottom parts). Other examples of how the scan strategy can affect the warping can be found in the literature [227], [228].

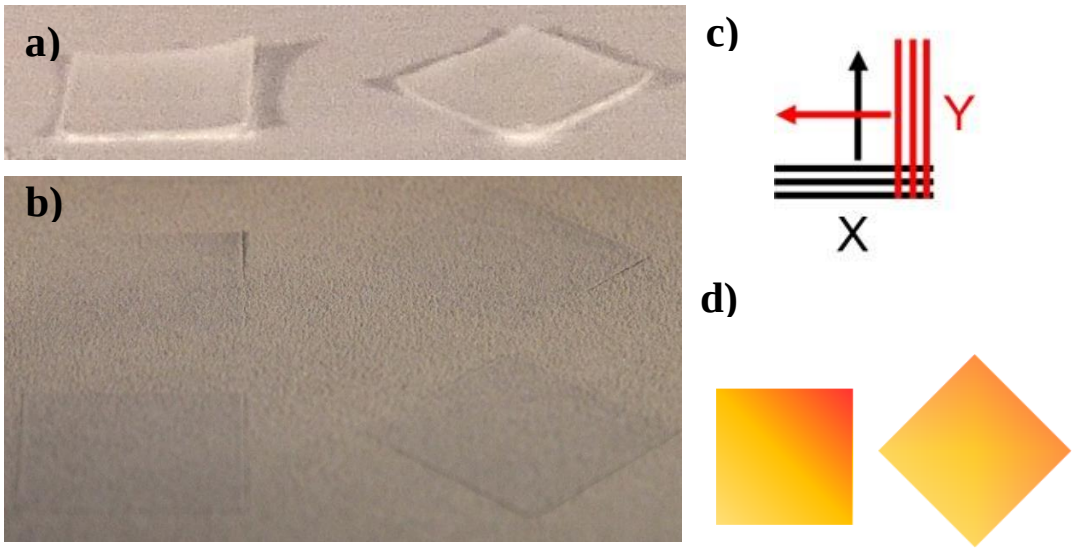


Figure 4.29 – Laser sintered PFA (a) without and (b) with carbon black highlighting the effect of the scan strategy and part orientation on sintering and warping. The warping/sintering was stronger in areas corresponding to the hot spot (red area in (c), top right corner). The parts were first scanned in X direction (bottom to top) and then in the Y direction (right to left) as shown in (c). The parts at the bottom were scanned twice in the X direction and gave more uniform warping/colour. (d) Representation of the suggested position of the hot spots depending on the part orientation. The colour red indicates higher local temperatures.

Figure 4.30 shows an experiment carried out to study the effect of the "Skincore" and "Mesh 2D" scanning strategies available in the Formiga P100 Desktop-PSW 3.3 software. The Skincore strategy allowed to select 4 different parameters: pre-scan, skin-scan, core-scan, post-scan. The part was divided in 2 sections, the skin (contour) and the core (central area). In this experiment the pre-scan and post scan were not used. The parameters used for the skin/contour scan (2 mm thick) were as in the previous experiments and showed in Figure 4.30. The core-scan was done with the same parameters but with a Mesh 2D pattern which had a grid pattern (Figure 4.30a). Each (green) grid segment was only scanned once in the direction of the segment and not twice as in the skin-scan. When multiple scans were used it was observed that the parts started to warp between scans and in each successive scan the laser "pushed down" the warped area but the successive warping was stronger than the previous one. This could be due the re-melting and stress relaxation caused by the laser in each consecutive scan. Nonetheless, each consecutive scan increased the degree of sintering and warping. Darker regions were also visible where the grid segments of the Mesh 2D met (in the centre). These areas receive in fact twice as much ED because of the overlap of the grid segments. This detail should be kept in mind when using the Mesh 2D pattern as it creates hot spots, different part properties and possible degradation.

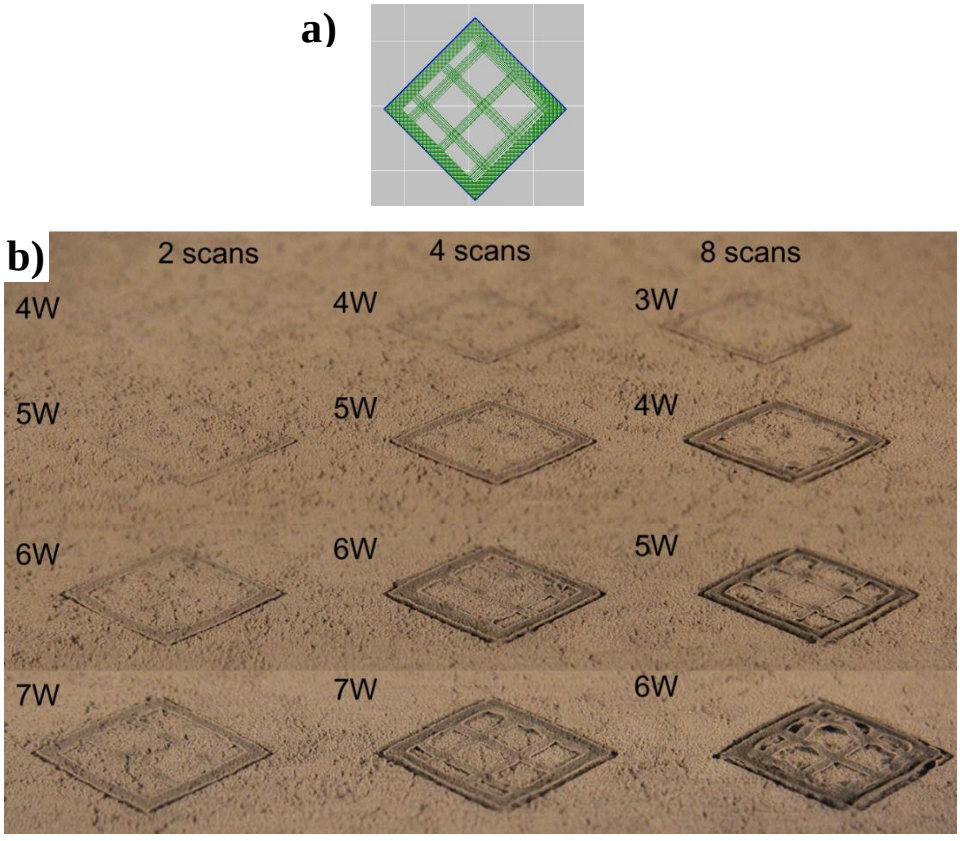


Figure 4.30 - Laser sintered PFA 0.4 wt% CB using the Skin-core and Mesh 2D scan strategy. (a) Image of the scan pattern used, the green lines represent the laser path. (b) Printed parts at different laser powers and number of scans.

Figure 4.31 shows a test carried out to observe the influence of a contour scanned with a lower ED compared to the ED of the core. Similarly to the previous experiments, the Skincore scan strategy was used. The contours (2 mm thick) were produced with the following parameters for all the samples: 2 scans, 6 W laser power, 2000 mm/s scan speed, 0.2 mm hatch spacing. The cores were produced with the same parameters used for the core-scan in the previous experiments and showed in Figure 4.31. In the previous experiments it was observed that the warping predominately happened at the edges/contour and that higher ED led to greater warping. Scanning the contour with a lower ED could initially seem like a possible way to reduce the warping. Nonetheless, the observed results suggested the opposite. The warping was much greater when the contour was produced with a lower ED. The lower ED caused the contour to have a lower degree of sintering, be thinner, and weaker. Therefore, the contour was more prone to be deformed by the residual thermal stresses from the central region. The 2 scans, 6 W sample had its contour and core printed with the same parameters but their shades were different. This indicated that the size of the scan length has an effect on the final part. Shorter scan lengths, such as in the contour, reached higher local temperatures as the laser came back to the same spot more quickly during the scanning process. More details on the effect of the vector length will be given in the next experiment. Catchpole et al. [229] conducted a similar study on the effect of scan strategies in metal powder bed fusion.

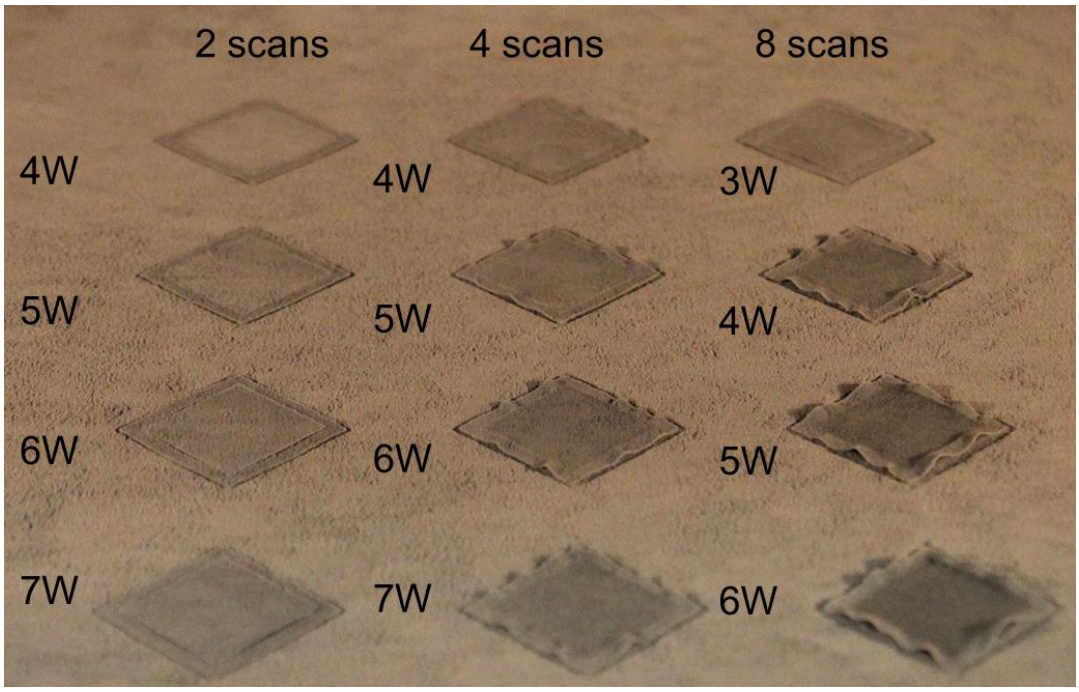


Figure 4.31 - Laser sintered PFA 0.4 wt% CB. Skin-core strategy to study the effect of a skin/contour produced with a lower ED. The lower ED caused the edges to be thinner, weaker, and more prone to be deformed by the residual thermal stresses.

Figure 4.32 shows how the scan length (150, 100, 50, 20, 10, 5, 2.5 mm) influenced the properties of the printed parts. All the parts were printed with the same parameters: 1 scan in

the X direction, 18 W laser power, 2000 mm/s scan speed, 0.2 mm hatch spacing. When the samples were longer than 100 mm the warping started to appear in the bottom centre of the sample too, instead of just at the contour. The bottom part of the sample was where the scan of the part began and the first to cool down. Samples of 20 mm and less produced a light smoke when scanned, showing that higher local temperatures were reached. This was caused by the laser coming back to the same spot more quickly during the scan of short samples/vectors, which gave the part less time to cool down. Figure 4.33 shows two examples of scan patterns: sorted and unsorted. In this example, the sorted scan has different vector lengths while the unsorted scan has the same vector length for the entire sample. It is, therefore, important to keep in consideration the changes in scan lengths in a part when designing it, as this could lead to different sintering rates and possible decomposition. Wegner et al. [71] observed similar results showing that the heating rates were not affected by the ED but they greatly increased with shorter vector lengths while the maximum melt temperature increased with higher EDs and shorter vector lengths.



Figure 4.32 - Laser sintered PFA 0.4 wt% CB. The same parameters were used for all the samples and scanned once in the X direction. The length of the samples (150, 100, 50, 20, 10, 5, 2.5 mm) influenced the warping behaviour and quality of the sintering. The shorter samples produced a light smoke during scanning due to higher local temperatures.

In another experiment 20 x 20 mm and 40 x 40 mm parts were scanned with the following parameters: 2 scans in the X direction, 5 W laser power, 2000 mm/s scan speed, 0.2 mm hatch spacing. The 20 x 20 mm parts were very fragile and broke as they were removed from the powder bed. The 40 x 40 mm parts showed no discernible sintering and no parts were formed. This showed again the effect of the scan length.

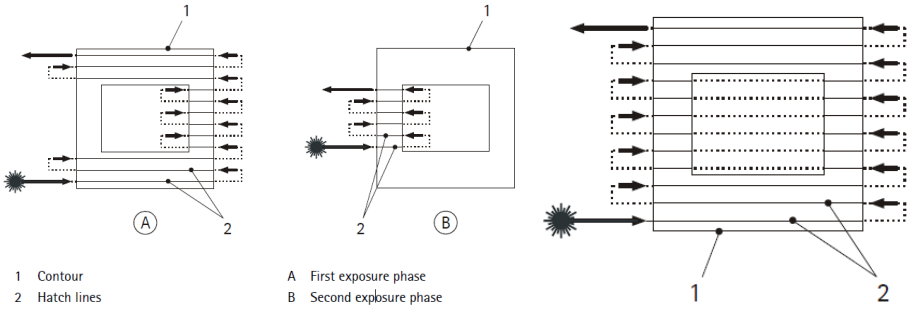


Figure 4.33 – (Left) Sorted and (right) unsorted scan strategy. Figures reproduced from [224]

Figure 4.34 shows in the top left area a 100 x 100 mm part printed with the following parameters: 5 scans in the X direction, 17 W laser power, 2000 mm/s scan speed, 0.2 mm hatch spacing. The parameters for the bottom 100 x 100 mm part were: 10 scans alternating X and Y direction, 20 W laser power, 2000 mm/s scan speed, 0.75 mm hatch spacing. The series of 20 x 20 mm squares on the right side were printed with an increasing number of scans in the X direction: 1-2-3-4-5-6-7 scans (from top to bottom), 15 W laser power, 2000 mm/s scan speed, 0.2 mm hatch spacing.

The top left sample showed progressive shrinkage, warping, and change in colour/shade with each consecutive scan. The warping and shrinkage were very limited on the top side of the part (as the scan is done from bottom to top). The bottom left sample was printed with a wider hatch spacing and formed a grid-like structure. The shrinkage was uniform in every direction and warping limited. More information on this will be given in a successive experiment (Figure 4.37). The parts on the left showed a gradual increase in warping and strength with each additional scan. From 2 scans on the parts produced a light smoke and, from 5 scans on, the parts were very strong and flexible.

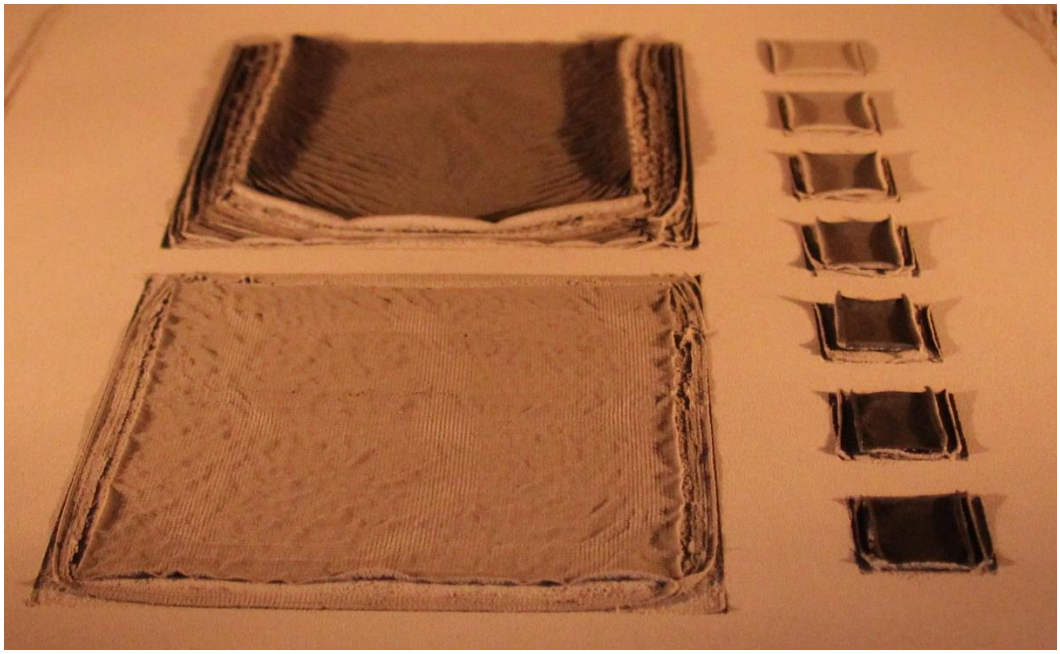


Figure 4.34 - Laser sintered PFA 0.2 wt% CB. Parts of different sizes printed with multiple scans. eThe samples on the right side were printed (starting from the top) with 1-2-3-4-5-6-7 scans, Each consecutive scan increased warping and strength of the part.

Figure 4.35 shows a test carried out to assess the feasibility to use a low ED scan to pre-heat the powder bed. The EOS P100 measures and report in real time the powder bed temperature with an Optris CT pyrometer which measures the average temperature in a ~ 80 x 80 mm area located in the front centre of the powder bed. Therefore, it should have been possible to follow the local increase in temperature caused by the low ED scan. Nonetheless, the pyrometer had a spectral response between 8 and 14 µm and the measurements were influenced by the

presence of the CO_2 laser (wavelength ~ 10.6 µm) during the scanning process. Consequently, the measurements collected during the scan of the powder bed were not reliable. This effect was confirmed by a sudden drop of temperature soon after the completion of the scan. The powder showed a change in colour after one and more scans but no significant sintering. When the powder bed was rougher the change in colour was reduced (Figure 4.35, top right corner). It is possible that the laser was having an effect just on the surface of the particles.

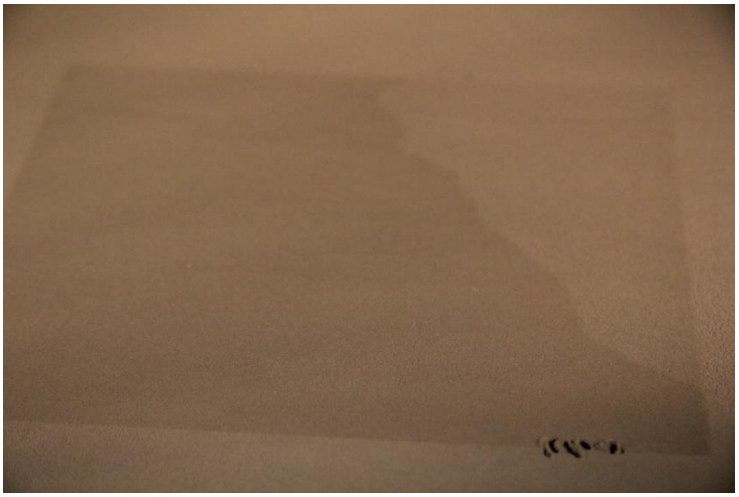


Figure 4.35 - PFA 0.4 wt% CB. Preheating the powder bed with a low ED scan. The powder became darker after the scan. Where the powder bed was spread in a rougher layer this effect was decrease (top right corner).

Sometimes, while using the same patterns (square/rectangle), some details/mechanisms could go unobserved. For this reason, more complex shapes were used (Figure 4.36). The figure shows how the sorted scan strategy caused discontinuities in the top and bottom part of the neck of the dragon. In fact, in the sorted scan strategy the part is broken down into several sections which are scanned at different times (Figure 4.33). That fraction of a second while the laser jumped from one section to the other was enough to create discontinuities (see top and bottom of the neck of the dragon). Furthermore, the same issue observed in Figure 4.32 was also observed here, the thin/short contour ring around the dragon produced a light smoke because of the shorter vector length which led to higher local temperatures and decomposition.

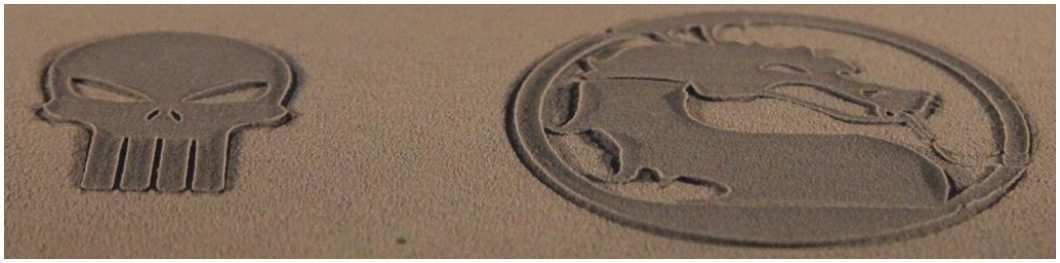


Figure 4.36 - Laser sintered PFA 0.4 wt% CB. Because of the sorted scan strategy, the laser jumped from one section to the other and that fraction of a second was enough to create discontinuities (top and bottom of the neck of the dragon).

Another experiment is shown in Figure 4.37, where 20 x 20 mm parts were printed at different hatch spacings (1.5-1-0.75-0.5 mm), 20 W laser power, 2000 mm/s, 1 scan in the X direction, 1 scan in the Y direction, and single layer. The SEM showed the presence of gaps for hatch spacings of 1.5-1-0.75 mm while only few gaps were visible for 0.5 mm (nonetheless, it was possible to see the grid pattern with the naked eye, see Figure 4.37). The track width (~ 350 µm) was roughly the same in the X and Y direction with a hatch spacing of 1.5 mm, but the Y track was thicker (~ 400 µm) when a hatch spacing of 0.75 mm was used. This was because the Y scan was done after the X scan, which increased the temperature of the powder in the surrounding area (thus, it was like processing at a higher powder bed temperature). When the hatch spacing was wider than 0.5 mm, the parts showed more homogenous shrinkage and no warping.

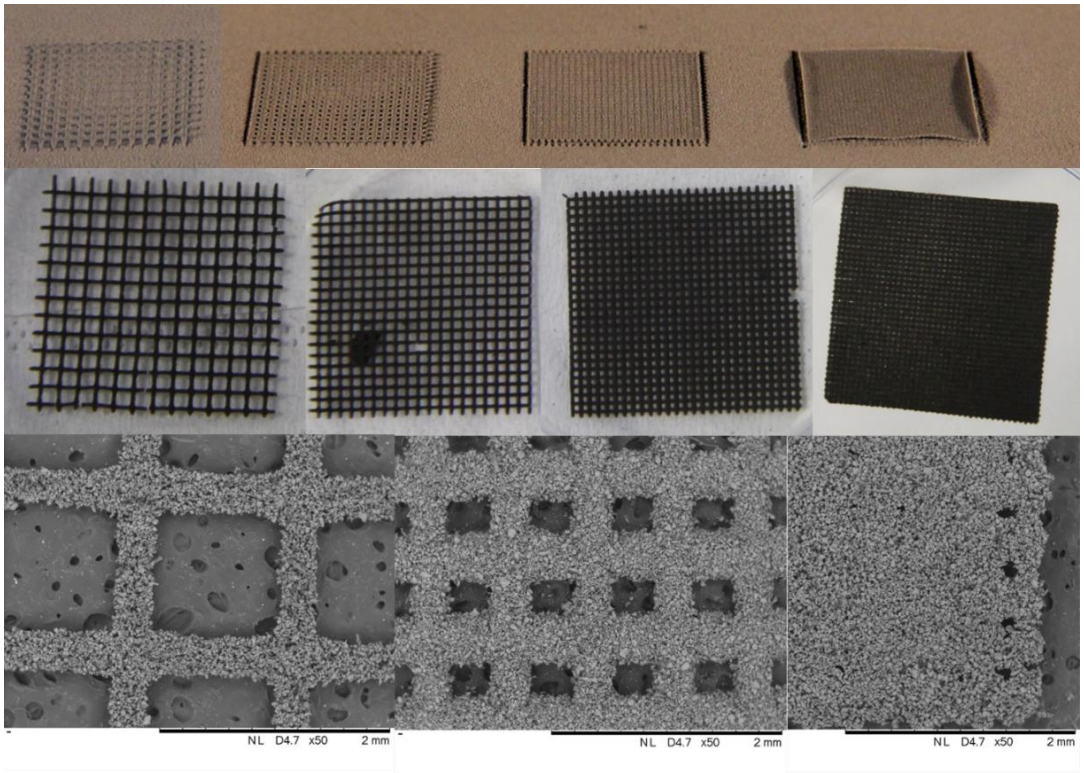


Figure 4.37 – Laser sintered PFA 0.4 wt% CB grids. Single scan in the X and Y direction with hatch spacings of 1.5-1-0.75-0.5 mm, left to right. The bottom SEM images show hatch spacings of the 1.5-0.75-0.5 mm grids.

The thickness of the X and Y scan track are reported in Table 4.9 and Figure 4.38. The table also report the size of the gap between the sintered tracks and the % difference between the X and Y track. The results showed that when the hatch spacing was 1.5 mm, the thickness of the X and Y track were approximately the same. As the hatch spacing was reduced to 1 mm and 0.75 mm the Y track got progressively thicker, 351 ± 18 and 401 ± 17, respectively. Next, the 1 mm hatch spacing was printed in 3 different ways: 1 scan, 1 scan with a low ED pre-scan (5 W, 2 scans in the X direction), and with 2 scans. The Y thickness progressively increased from

351 ± 18 (1 scan) to 406 ± 17 (pre-scan) and 437 ± 23 (2 scans) as showed in Figure 4.38. The X thickness also progressively increased from 316 ± 14 (1 scan) to 340 ± 22 (pre-scan) and 382 ± 18 (2 scans). The pre-scan experiment showed an increase in the thickness of the tracks confirming that a pre-scan does temporary increase the temperature of the powder bed.

Table 4.9 - Laser sintered PFA grids. Single and double scan track thickness in the X and Y direction with hatch spacings of 1.5-1-0.75 mm. The table also report the size of the gaps between the sintered tracks, and the % difference between the X and Y track. The values are reported in µm.

	X	Y	gap X	gap Y	diff %
1.5 mm, 1 scan	335	345	1082	1045	3
stdev	17	7	18	23	
1 mm, 1 scan	316	351	626	581	11
stdev	14	18	19	19	
1 mm, 1 scan, pre-scan	340	406	594	524	19
stdev	22	17	22	14	
1 mm, 2 scans	382	437	567	501	15
stdev	18	23	22	27	
0.75 mm, 1 scan	353	401	330	258	14
stdev	12	17	10	12	

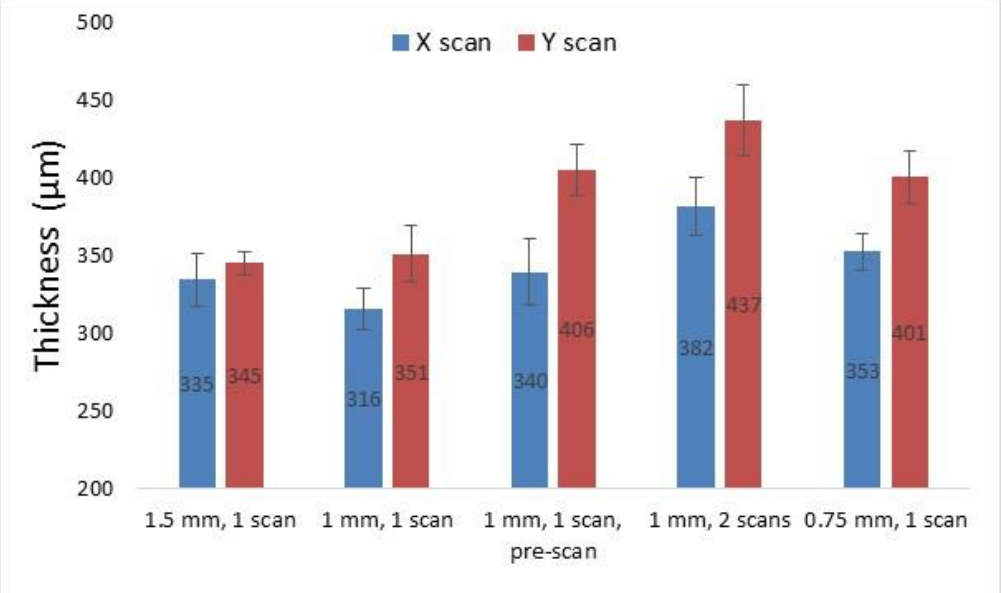


Figure 4.38 - Laser sintered PFA grids. Single and double scan track thickness in the X and Y direction with hatch spacings of 1.5-1-0.75 mm. Pre-scan means that the powder was pre-scanned with a weak ED before the grid was sintered.

Figure 4.39 shows two rings printed with a thickness of one and two scan track, respectively. The parameters used were: 1 scan (only contour), 20 W laser power, 2000 mm/s scan speed, no hatch spacing.

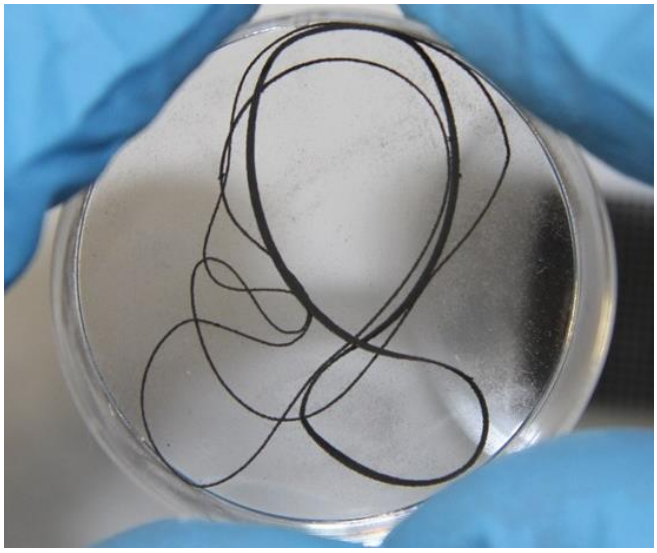


Figure 4.39 - Laser sintered PFA 0.4 wt% CB. Rings of different thickness.

A lower CB loading was also tested. PFA with 0.2 wt% CB showed a smooth layer formation similar to that of 0.4 wt% CB. With this formulation, a single layer 100 x 100 mm sheet/membrane with a thickness of ~150 µm and porosity of ~ 60% was printed (Figure 4.40a). The parameters utilized were: single scan in the X direction; 18 W laser power, 2000 mm/s scan speed; and 0.2 mm hatch spacing. The sheet warped soon after printing, as seen in Figure 4.40a. After a thermal treatment of 3 hours at 260 °C (260 °C is the maximum service temperature of PFA) to relieve the residual stresses, the film became flat (Figure 4.40c). To the touch, the sheet had a fabric feeling and was extremely flexible (Figure 4.40e). By lifting and looking through the sheet, CB agglomerates were visible (Figure 4.40b). These agglomerations were due to sub-optimal mixing. The sheet was porous but water drops had high contact angles and could not penetrate it (Figure 4.40d). On the other hand, isopropanol, which has a lower surface tension than water, went through the membrane. A drop of water mixed with a small amount of isopropanol also went through the membrane. The porosity of the membrane may be tuned by changing the process parameters or with a post-sintering in oven.

In the literature, researchers have just recently started to assess the quality of laser sintered polyamide membranes [230]. Low et al [231] published a review about the production of membranes in AM. They report that the main limitations of AM to produce membranes are the production speed, build size, resolution, and material portfolio. Some techniques such as two-photon polymerisation have high resolution but slow speed, small size, and high cost while other AM techniques are faster but with lower resolutions.

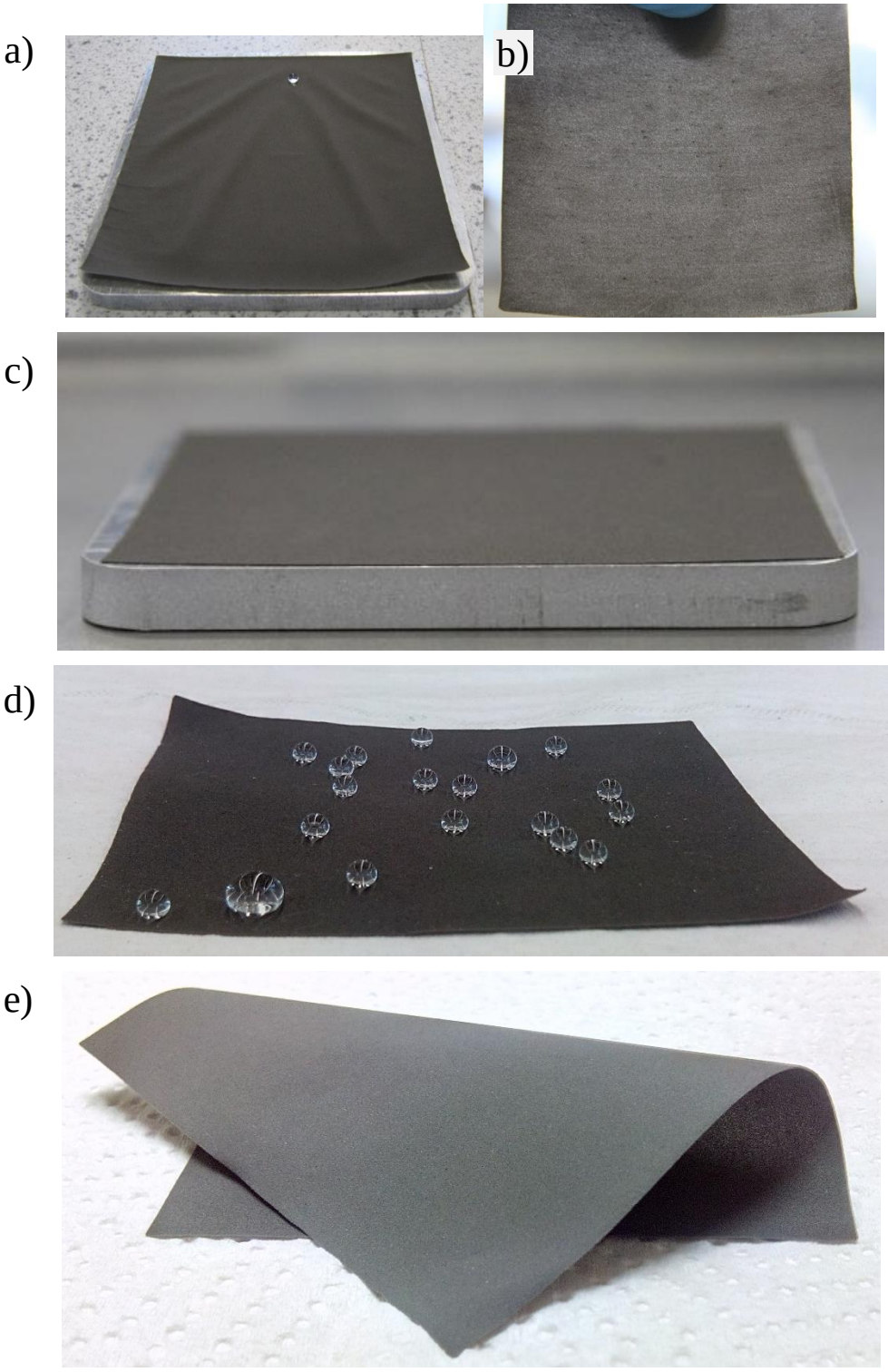


Figure 4.40 – Laser sintered PFA 0.2 wt% CB sheet/membrane (a) as printed and (c) after 3 hours at 260 °C. (b) Visible agglomerations of carbon black (black dots). (d) Drops of water on the membrane. (e) Membrane showing with good flexibility.

Finally, Figure 4.41 shows 20 x 20 mm samples printed with PFA + 0.2 wt% CB at different laser powers and number of scans at a fixed scan speed and hatch spacing of 2000 mm/s and 0.2 mm. The red boxes show the sample that did not break when removed from the powder bed while the "SS" show the sample that produced smoke (19 W, 1 scan). The samples

scanned once were done with laser powers between 10 and 19 W while the samples scanned multiple times were done with laser powers between 4 and 9 W.

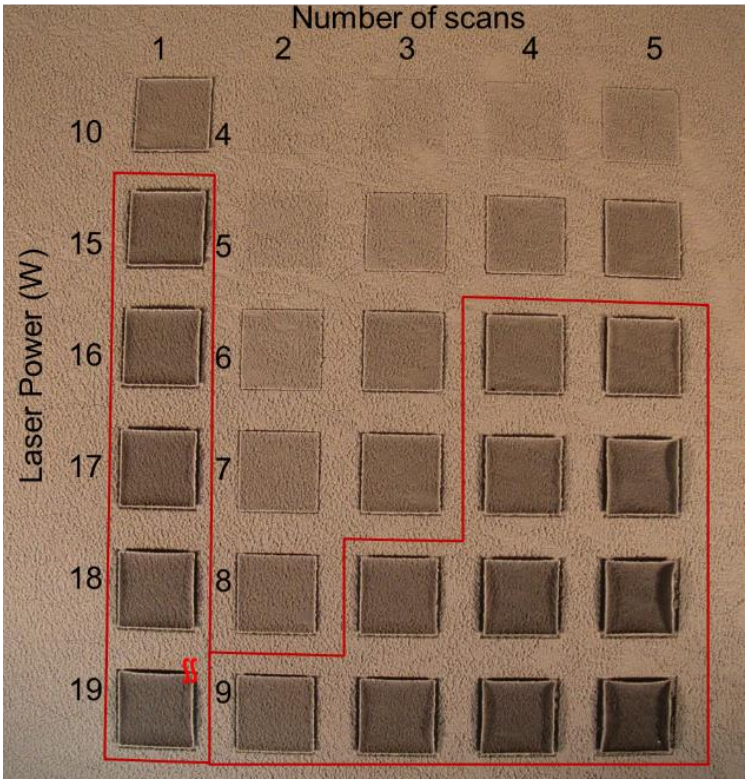


Figure 4.41 - Laser sintered PFA 0.2 wt% CB at different laser powers and number of scans. The red boxes show the samples that did not break when removed from the powder bed. The red "SS" indicates that smoke formation was observed.

4.4.3 Multiple layers and use of a substrate

From the experience gained from the previous experiments, printing multiple layers was attempted with the following parameters: 4 scans, 3 W laser power, 2000 mm/s scan speed, 0.2 mm hatch spacing, and 0.1 mm layer thickness. These parameters were chosen to minimise warping. As showed in Figure 4.27 and Table 4.7, 4 scans with a 3 W laser did not show any significant warping. The print was successful and 8 layers were printed before running out of powder (Figure 4.42a). Nonetheless, the sample was brittle and broke while being picked up from the powder bed. Poor bonding and delamination were evident between layers (Figure 4.42b). The low ED employed to avoid warping was accompanied by poor sintering and interlayer bonding.

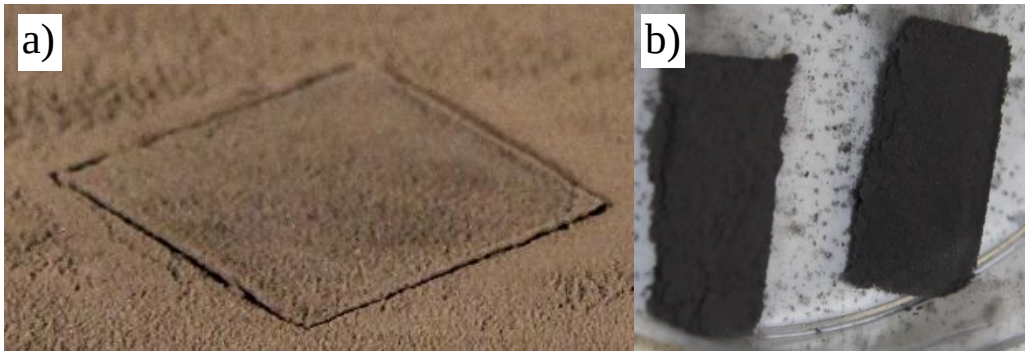


Figure 4.42 - Laser sintered PFA 0.4 wt% CB. Brittle sample made of 8 layers. (a) Sample right after printing (in the powder bed). (b) The sample breaks during its removal from the powder bed.

To improve on the previous experiment, multiple layers were printed with the following parameters: 1 scan, 5 W laser power, 2000 mm/s scan speed, 0.2 mm hatch spacing, 0.1 mm layer thickness., This time, the printed pattern was made of concentric squares of size 20 x 20, 40 x 40, 60 x 60, 80 x 80 mm (Figure 4.43), hence the 20 x 20 mm square was scanned 4 times. The order of printing was from the biggest square to the smallest square. Each square was printed with the same parameters. The 1(4) scan, 5 W laser power parameters were chosen because they gave a higher degree of sintering (and warping) compared to 4 scans 3 W laser power parameters (used in the previous experiment) as showed in Figure 4.27 and Table 4.7. The aim of the concentric squares was to limit warping while obtaining a 20 x 20 mm part. This was similar to the Support scan strategy used in the PCTFE experiments (Table 4.6). The test was a success and 31 layers were printed without warping before running out of powder. The other square patterns did not receive enough ED to sinter but the increase in local powder bed temperature and light “anchoring” offered by the external squares allowed the central square to limit its warping. After repeating the experiments, 50 layers were printed before running out of powder. The samples were stronger than the previous experiment, but they were still brittle and showed delamination (Figure 4.43c). When the 20 x 20 mm square was printed with the same parameters (4 scans, 5 W laser power) but without the other concentric squares it failed due to warping.

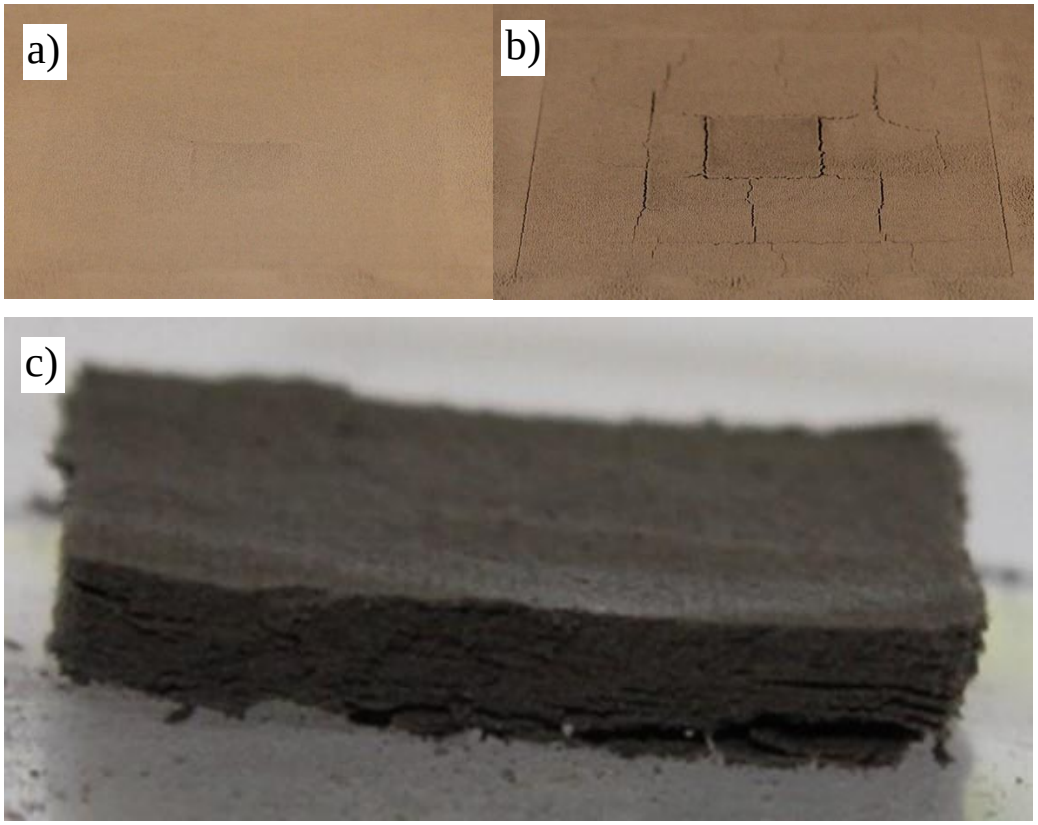


Figure 4.43 - Laser sintered PFA 0.2 wt% CB. 31 layers printed before running out of powder. The warping was minimised by printing concentric square patterns. Sample (a) right after printing and (b) after cooling to room temperature. (c)Sample after its removal from the powder bed (dimensions: 20 x 20 mm)

Warping was the main failure mechanism at this stage; thus, an aluminium plate (100 x 100 x 8 mm) covered in blue masking tape was introduced in the centre of the build chamber and used as build plate. The rationale was that during the sintering of the first layer, the melted powder would stick to the masking tape decreasing or eliminating the warping [232]. The technique gave good results and 3 layers were printed with only minor warping before running out of powder (Figure 4.44). The minor warping was due to the weak bonding between tape and polymer. The parameters used were: 14-16-15-17 W laser power (clockwise order from top left), 1 scan. 2000 mm/s scan speed, 0.2 mm hatch spacing, 0.1 mm layer thickness, and 13 layers. These parameters were used as they showed good part strength and limited warping (Figure 4.28). A similar issue and approach was reported by Niino et al. [233] when they processed PEEK at 200 °C instead of the usual > 350 °C. To avoid warping they anchored the in-process parts to a rigid PEEK plate 12 mm thick and obtained densities up to 96 %.

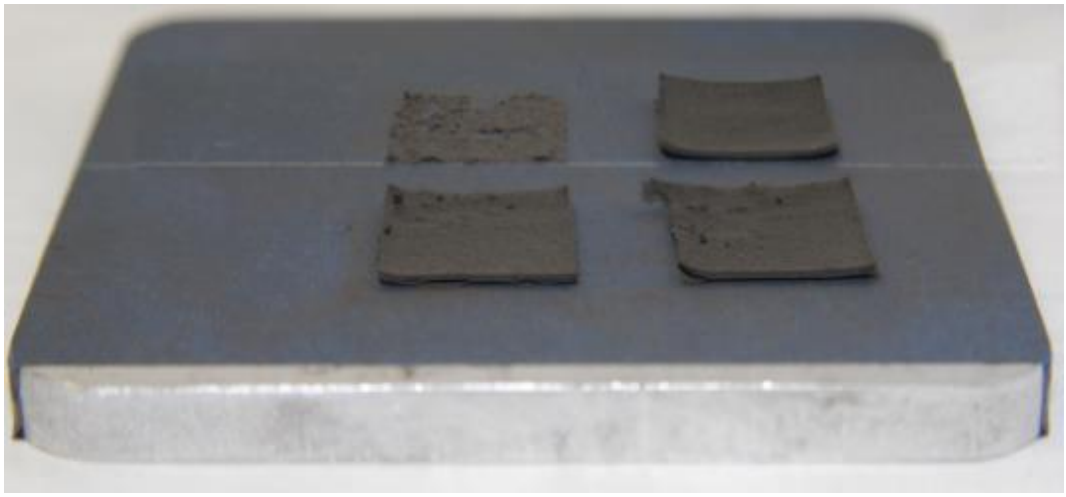


Figure 4.44 - Laser sintered PFA 0.4 wt% CB, 20 x 20 mm parts. Masking tape was used as build plate to reduce warping. 13 layers were printed before running out of powder.

PFA and ETFE sheets were also tested as build plate. The parameters used were: 6 scans at 8 W, 1 scan at 18 W, 4 scans at 8 W, with 2000 mm/s scan speed, 0.2 mm hatch spacing, 0.1 mm layer thickness, room temperature powder bed temperature. The pre-scans were used to increase the local powder temperature as no heating was being used in this experiment while the post scans were used to increase sintering while avoiding decomposition. No heating was being used as the EOS P100 was not designed to be used with modified/external build plates and thus it was very difficult to obtain a thin even layer while keeping the modified build plate in a fixed position. Several manual operations were required, thus, working at room temperature was necessary.

The adhesion of the printed parts to the PFA and ETFE sheets did not improve considerably and the sheets tended to warp when exposed to the laser (Figure 4.45a). The poor bonding was likely due to the well-known poor bondability of fluoropolymers and low powder bed temperature (room temperature was in fact the temperature used for this and the following experiments). The warping of the PFA and ETFE sheets was caused by their low rigidity and limited thickness (< 3 mm). Furthermore, the printed parts could be easily rubbed off the surface of the sheets.

In further tests PFA sheets previously printed (Figure 4.40) were used as build plates. The same parameters were used as in the previous experiment were used. The sintered PFA sheet was just laid on top of the powder bed and powder was spread on top of it. After printing, the entire sheet warped (Figure 4.45b). The sheet was then laid on a stainless-steel plate and fixed with kapton tape to contain warping. The tape did not stick well to the PFA sheet and the sheet broke after it got caught by the recoating blade (Figure 4.46a). Finally, the sheet was glued with a standard glue stick to the stainless-steel plate and one layer printed on it (Figure 4.46b). This time, neither the sheet nor the printed part warped. Nonetheless, the printed part could be

easily rubbed off showing poor bonding with the substrate (Figure 4.46c). Figure 4.46d shows how much the part would warp without the use of build plates.

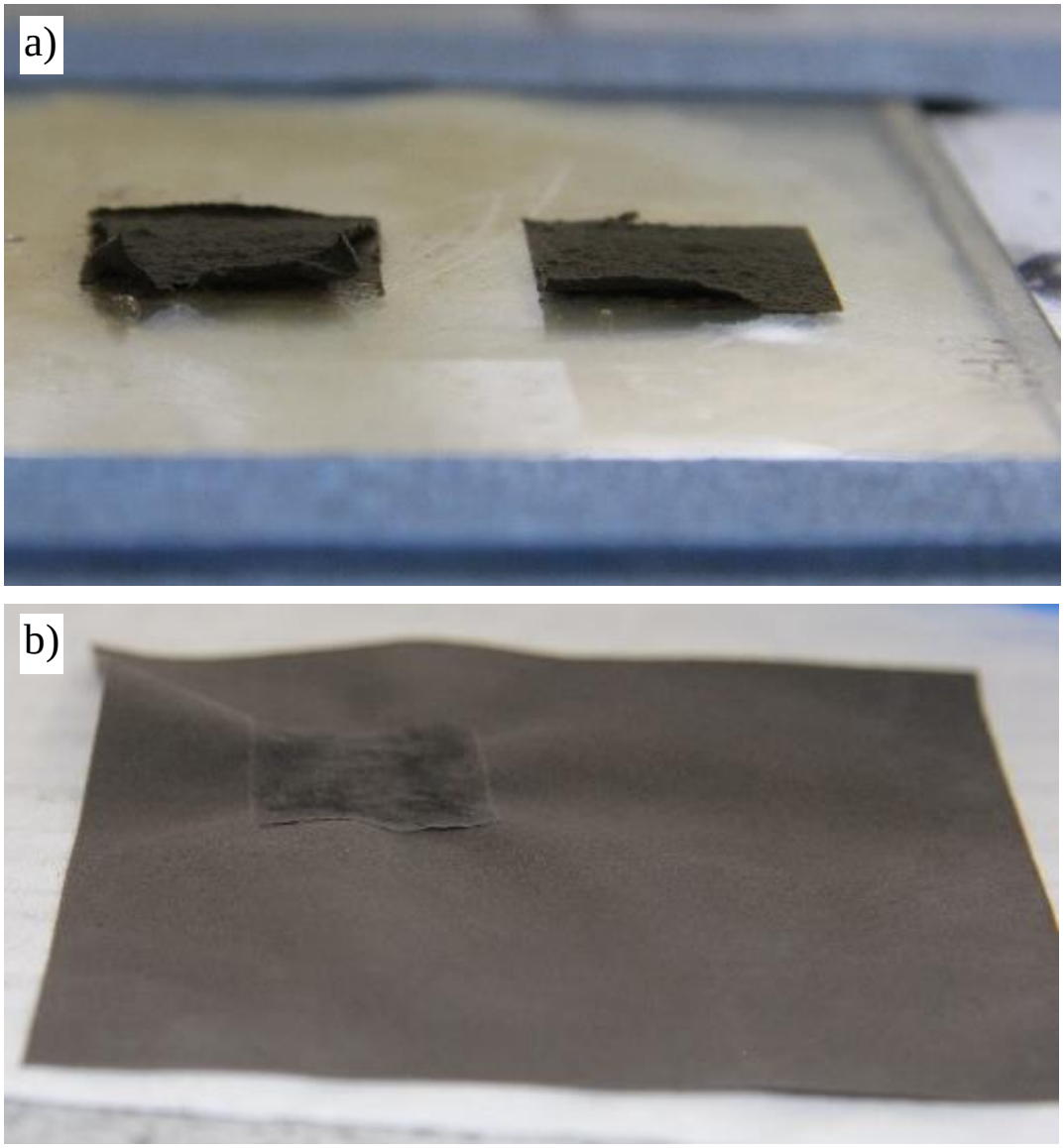


Figure 4.45 - Laser sintered PFA 0.2 wt% CB, 20 x 20 mm parts. (a) Parts printed on top of a PFA sheet used as build platform. The PFA sheet was taped on aluminium plate (b) Part printed on top of previously laser sintered PFA sheet. The PFA sheet was not taped down but just laid in the powder bed.

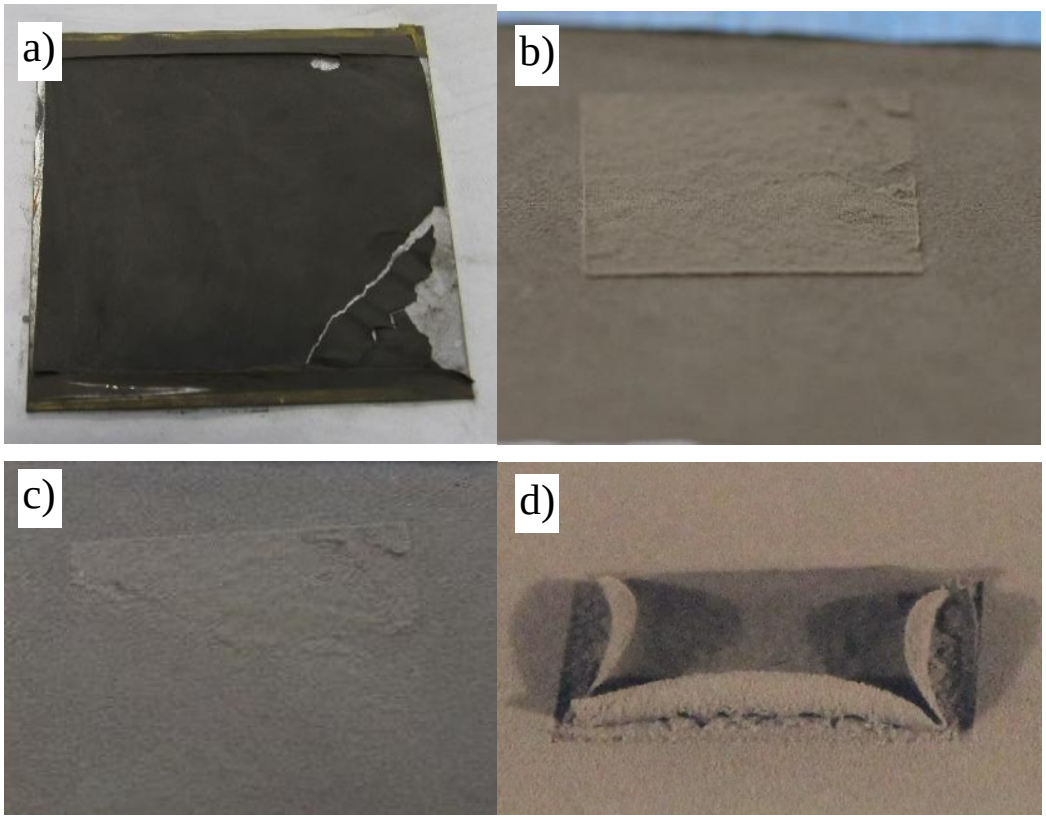


Figure 4.46 - Laser sintered PFA 0.2 wt% CB, 20 x 20 mm parts. (a) Laser sintered PFA sheet taped on an aluminium tape. The sheet touched the recoating blade and broke. (b) Part printed on top of a laser sintered PFA sheet glued on an aluminium plate. The part was easily removed by rubbing it (c). (d) Part printed with the same parameters but without the use of a support structure. The warping is more intense.

4.4.4 Discussion – Powder bed fusion of PFA

Following the discussion about the use of PCTFE in pPBF (section 4.3.4), this section adds PFA to the discussion.

Neat PFA was used in the initial screening of the process parameters. It was observed that the amount of warping was proportional to the degree of sintering and energy density except when the polymer was fully melted (Figure 4.26). This tendency to instantly warp was due to the wide thermal jump between the crystallization temperature (271.93 °C) and powder bed temperature (182 °C). 0.4 wt% CB was then added to the powder and the same process parameters were used to have a comparison with the neat PFA (Figure 4.27). The strength of the samples increased with the addition of CB confirming the increase in absorbance in the wavelength of the CO_2 laser (section 4.1.5). Different warping behaviours, likely to a different heating/cooling mechanism, were also observed when PFA was laser sintered with and without CB (Figure 4.27). The samples were found to produce smoke when EDs of 0.040 J/mm^2 were used. Several printing parameters were investigated to produce two process maps showing the degree of warping of several sets of parameters (Table 4.7 and Table 4.8). The

test showed that a hatch spacing of 0.1 had a much narrower optimal processing window compared to a hatch spacing of 0.2 mm, meaning that a small change in the parameters would cause the printing process to fail. The orientation of the parts was found to have an effect on the final properties of the parts [227], [228]. When two scans were used, 1 in X direction and 1 in Y direction, a hotspot on the top right corner was created. This effect could be partially countered by rotating the samples by 45° or by scanning twice only in the X (or Y) direction (Figure 4.29).

The EOS P100 software allowed the used of two special scan strategies, "Skincore" and "Mesh 2D" [224]. The Mesh 2D scan was used to create grids inside of a 2 mm square contour and showed a flaw in its design as one section of it was scanned twice, leading to possible polymer degradation (Figure 4.30). The Skincore scan was used to study the effect of a low ED contour with a high ED core (Figure 4.31). It was found that the warping at the contour of the sample was stronger (with a low ED contour) because the now weaker (more porous [138]) contour was more prone to be deformed by the residual thermal stresses. The vector length also had an effect on the part properties. Lower vector lengths showed the production of smoke and hence decomposition as the parts were reaching higher local temperatures (Figure 4.32). This was caused by the laser coming back to the same spot more quickly during the scan of short samples/vectors, which gives the part less time to cool down. Wegner et al. [71] observed similar results with PA powders. Furthermore, these observations were also confirmed by the fact that while using the same parameters to print two parts of different size, only the smaller part showed detectible sintering. Consecutive scans of a part on the same layer could be used to increase the sintering and strength of the parts to the detriment of geometrical accuracy due to warping and shrinking (Figure 4.34). The sorted scan strategy caused discontinuities in samples with complex geometries due to the laser jumping from one section to the other (Figure 4.36). To the best of my knowledge, these implications have never been discussed in the literature of pPBF. Furthermore, there is a tendency in the literature for pPBF to only use very basic scanning strategies such 1 or 2 X-Y scans without exploring other solutions [22][234]. This might be due to the software limitation of commercial pPBF systems, usually designed and optimised to print a limited number of commercial polymers and not for research purposes. On this note, another diffuse issue with commercial pPBF system is the big building chambers [31], designed to increase throughput but inconvenient when testing new powders and formulations (as high quantitative of powder are required, often more than 10 kg for powder composition).

Warping was absent when grid structures with a hatch spacing above 0.75 mm were produced (Figure 4.37). The grids shrank uniformly in all directions. The Y track width increased with decreasing hatch spacing as the local powder temperature was being increased by the previous X scan. The track width was also increased by a low ED pre-scan or by scanning the grid twice

(Figure 4.38). All these different techniques will also be useful in the development of other challenging polymers in AM. These observations were also possible because of the difficulties in processing PCTFE and PFA and their narrow processing window. Small changes in parameters that would go unnoticed in commercial pPBF powder grade like PA 12 (because of PA 12 wide and robust processing window [235]) become very noticeable in PCTFE and PFA. Nonetheless, these effects still happen in powders like PA 12 and may have an influence on the final properties of the parts. Therefore, challenging polymers have the advantage of being sensitive to any small changes in processing parameters and highlighting all the effects that the parameters have on the polymer powder and final parts. This makes challenging polymers interesting case studies.

Thin, flexible, porous, hydrophobic membranes were also produced. Water droplets did not go through the membrane but isopropanol droplets (because of their lower surface tension) went through it. The membranes did warp after printing but a heat treatment at 260 °C flattened them (Figure 4.40). This suggested that a powder bed temperature of 260 °C could avoid warping. By looking through the thin membranes, carbon black agglomerations were visible, hence this could also be a method to assess the quality/performance of different mixing methods. The density, porosity and pore size of the membranes may be tuned by changing the laser parameters or with a post-sintering step in an oven. In the literature, researchers just started to assess the quality of laser sintered polyamide membranes [230], [231].

Multiple layer parts were possible but the produced parts were very brittle. Slightly stronger parts of 50 layers were produced by pre-scanning a wider area of the powder bed (Figure 4.43). The warping was also mitigated by using blue masking tape on a build plate [232]. 13 layers were printed before running out of powder which meant that more layers could have been printed (Figure 4.44). With the same parameters and without the use of a build plate, the parts would have warped at the first layer. PFA and ETFE sheets were also used as build platform but with poor results due to several technical issues (section 4.4.3). A similar approach was reported by Niino et al. [233] when they processed PEEK at 200 °C instead of the usual > 350 °C. To avoid warping they anchored the in-process parts to a rigid 12 mm thick PEEK plate and obtained densities up to 96 %.

Overall, PCTFE and PFA showed potential for pPBF and can already be used to produce thin membranes and small parts. A process that uses a relatively low powder bed temperature can bring considerable economic advantages both on equipment investment [236] and power consumption. In fact, 35% of the consumed energy is used by the chamber heaters [237]. Nonetheless, systems with higher powder bed temperatures and/or support structures might be required to print bigger and more complex parts made of PCTFE and PFA.

5 Results – Material Jetting of THV

Similarly to pPBF, one of the major limitation of MJ is its narrow material portfolio due the specific material requirements such as solubility, viscosity, surface tension, molecular weight, and evaporation rate (section 2.3.2) [83]. MJ has been used in several applications such as thin-film transistors [84], resistors [85], antenna emitter [86], light emitting diodes [87], biodegradable microspheres [88], and microneedles [89]. One of the advantages of MJ over several other AM techniques is its ability to produce multi-material parts [83].

The polymer chosen for this study was THV which is a terpolymer of Tetrafluoroethylene, Hexafluoropropylene and Vinylidene fluoride. The properties of THV include high transparency, good bondability, high flexibility and flex life, low refractive index as well as efficient electron beam cross-linking [114]. Most THV applications gravitate around multilayer parts, where a thin layer is used as protective coating or to provide enhanced barrier properties to other layers (section 2.4.5) [114].

In this chapter, a Fujifilm Dimatix DMP-2830 and a PICO Pµlse (section 2.3.1) were used to print low and high polymer loadings (1-20 wt%) with the use of several solvents such as methyl isobutyl ketone (MIBK), Dimethylacetamide (DMAc), and acetone. The Dimatix was capable of processing low polymer loadings and had a relatively high resolution of 50-100 µm. The PICO Pµlse was capable of processing higher polymer loadings, had a lower resolution of ~ 1000 µm, and higher throughput compared to the Dimatix.

This chapter:

- Assesses the use of THV in material jetting
    - Identifies the most suitable solvents
    - Characterises several formulations/inks
        - Viscosity
        - Surface Tension
        - Contact angle
        - Density
        - Z number
        - Molecular weight
    - Outlines the use of the Dimatix to assess the printing behaviour of the several prepared formulations.
        - Identify the best formulation
        - Optimise printing parameters
        - Print functional complex parts
    - Outlines the use of PICO Pµlse to assess the printing behaviour of high polymer loading formulations.

        - Identify the best formulation
        - Optimise printing parameters
        - Print functional complex parts
- Characterises the printed parts
    - Use of several analytical instrument to evaluate the quality of the prints
    - Mechanical tests of the printed parts and how they compare with traditional manufacturing

Several issues such as wrinkling, coffee ring effects, and the presence of contamination were encountered. Films and multilayer components of thicknesses from a few nanometres to hundreds of microns were successfully printed with complex geometries and excellent mechanical properties.

5.1 Ink characterisation

This section discusses the data required to calculate the Z number and characterise the inks such as surface tension, contact angle, density, wrinkle effect, viscosity, and molecular weight. For the choice of solvent see section 3.3.14)

5.1.1 Surface tension, contact angle and density

This section investigates the surface tension, contact angle and density of several THV inks/formulations. The methodology can be found in section 3.3.13.

The density, surface tension, and contact angle of several THV inks are reported in Table 5.1 and Table 5.2. As expected, the density of the inks increased with the polymer wt% while the formulation containing DMAc had a higher surface energy.

The THV 1 wt% solution in MIBK had contact angles of 17.8° and 59.7° on a glass slide and a THV coated glass slide, respectively. The THV 1 wt% solution in acetone had contact angles of 43.7° and 51.8° on a glass slide and a THV coated glass slide, respectively. Deionised water had contact angles of 41.3° and 105.8° on a glass slide and a THV coated glass slide, respectively. The THV coated glass slides were prepared as described in section 3.3.19. As expected, the contact angle of the formulations increased on a THV coated glass slide. The contact angles of the acetone and MIBK formulations were quite different on a glass slide but almost the same on a THV coated glass slide.

Table 5.1 – Surface energy (n = 6) and density (n = 3) measured at 23.6 °C of several THV formulations.

Solvent	Concentration of THV [%]	Surface energy [mN/m]	Stdev	Density [g/mL]	Stdev
50-50 MIBK/DMAc	1	27.84	0.08	0.9351	0.0052
MIBK	1	22.66	0.22	0.8011	0.0030
MIBK	5	24.08	0.16	0.8291	0.0034
MIBK	10	24.40	0.13	0.8464	0.0075

Table 5.2 – Contact angle of THV 1 wt% in acetone, THV 1 wt% in MIBK, and deionised water drops on a glass slide and THV coated glass slide at 20.5 °C (n = 6).

Contact angle on	THV 1 wt% acetone	Stdev	THV 1wt % MIBK	Stdev	Water	Stdev
Glass	43.7	2.7	17.8	1.6	41.3	1.7
THV	61.8	4.4	59.7	0.6	105.8	0.8

5.1.1.1 Wrinkle effect

During the measurement of the contact angle of the 1 wt% THV-MIBK solution an unusual phenomenon was observed. At first, the polymer seemed to form a skin on the drop surface (Figure 5.1b) and suddenly expand violently due the evaporation of the underlying solvent (Figure 5.1c), followed by a slow deflation. This phenomenon will be referred as "wrinkle effect" from now on.

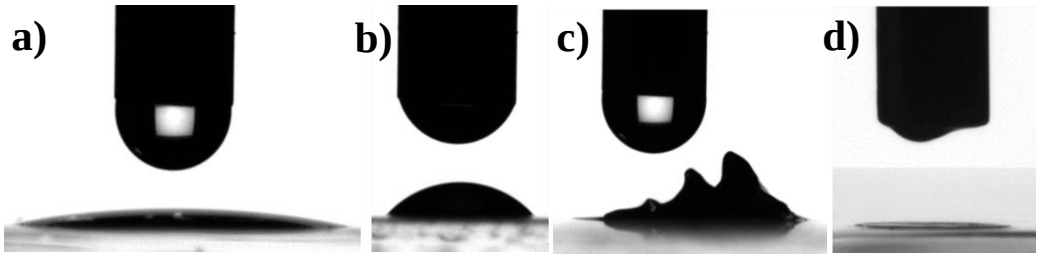


Figure 5.1 – Drop of a 1 wt% THV in MIBK solution (a) on a glass slide and (b) on a THV coated glass slide. Appearance during evaporation on a THV coated glass slide of a drop of (c) THV 1 wt% in MIBK and (d) THV 1 wt% in acetone.

The formation of a skin on the surface of a drop of polymer solution is usually linked to the high molecular weight of the polymer [238] and high evaporation rate of the solvent [102], [239]. In a specific experiment (Figure 5.1c), the dosing needle with a drop of solution was resting above the left side of a drying drop. During the drying process, 3 peaks of growing heights the further they were from the centre of the above drop appeared. This could be due to the fact the the above drop locally saturated the enviroment with solvent vapours and slowed

down the evaporation rate near it, leaving the right side of the drying drop with a higher evaporation rate and higher peaks/polymer displacement.

Table 5.3 – Wrinkle effect recap. Observations on the evaporation of several THV solution in different solvents and on different substrates.

Solution	Substrate and solvent affinity	Result
Drop of THV 1 wt % in MIBK	Glass substrate, modest solvent	flat
Drop of THV 1 wt % in MIBK	THV substrate, modest solvent	wrinkle
Drop of pure MIBK	THV substrate, modest solvent, no polymer in ink	wrinkle
Drop of THV 1 wt% in MIBK-DMAc	THV substrate, modest solvent, lower evaporation rate	flat
Drop of THV 1 wt% in Acetone	THV substrate, good solvent, higher evaporation rate	flat

Other experiments also showed the formation of bubbles which, in some cases, burst suggesting that solvent vapours were being generated inside of the underlying polymer film. Furthermore, the rapid expansion of the polymer was often initiated and more severe at the contour of the drop, where the evaporation rate was higher. Nontheless, these phenomena were only observed when a drop of the 1 wt% THV in MIBK ink was deposited on a THV coated glass slide and not when the same drop was deposited on a glass slide, suggesting that the THV substrate was causing the effect. This hypothesis was further supported by the fact that the wrinkle effect was also present when a drop of pure MIBK (no polymer in it) was deposited on a THV film, suggesting that the presence/formation of a polymer skin on the drop surface was unlikely. This could be explained by a combination of MIBK being a modest solvent for THV and having a relatively high evaporation rate: MIBK swells the polymer but then evaporates before full dissolution could happen, causing a sudden and violent expansion of the polymer film. Acetone is a better solvent for THV than MIBK (faster dissolution rate) and THV 1 wt% in acetone did not show the wrinkle effect despite the higher vapour pressure (higher evaporation rate) (Figure 5.1). THV 1 wt% in 50-50 v% MIBK-DMAc also did not show the wrinkle effect as DMAc (lower vapour pressure and modest solvent for THV) slowed down the evaparation rate. Therefore, it is suggested that this phenomena was caused not by the formation of a skin on top of the polymer drop but by the swelling of the underling THV film followed by a quick solvent evaporation. This behaviour was inhibited when a good solvent or slower evaporation rate solvent were employed. These observation are summarised in Table 5.3. The wrinkle effect was also observed during the water permeability investigation, further details are reported in section 5.4.2. A solvent is defined as a good solvent for a specific polymer when the interactions between solvent and polymer chains are more energetically

favourable (lower internal energy) than the interactions between polymer chains (and monomeric units of the chain itself). If the opposite case is true, the solvent is defined as a poor solvent for that specific polymer. In the case the solvent-polymer interactions and polymer-polymer interactions are identical the solvent is defined as a theta solvent [240]. This work and other publications refer to solvents having solvent-monomer interactions between those of theta solvents and good solvents as modest/fair solvents [241].

A similar but not identical phenomenon to the wrinkle effect was observed by Spangle et al. [241] during the spin coating of several polymers with different molecular weights and polydispersity in good, fair and poor solvents with high and low volatilities. They observed that when films were made with two solvents with similar volatilities, but different affinity for the polymer, the film made with the poor solvent was wavy and not uniform. However, when two good solvents with different volatilities were tested, the solvent with higher volatility gave a wavy and not uniform film. This effect was more visible at lower concentration and disappeared above ~ 20 wt%, concentration slightly above the calculated critical entanglement concentration (17 wt%). They hypothesised that either the high viscosity or entanglement due to the increase in polymer loading were impeding the flow of the solution preventing the formation of the waves. As will be showed in section 5.3 and 5.3.4, the wrinkle effect decreased at higher polymer loadings, while it increased for thick and dry THV films.

In summary, MIBK showed an unusual drying mechanism referred to as “wrinkle effect”. When pure MIBK was deposited on top of a THV film, it deformed the surface forming wavy patterns. This behaviour was likely due to the relative quick evaporation rate of MIBK and its being a modest solvent for THV. The wrinkle effect was in fact not visible when a good solvent or a modest slow evaporating solvent were used.

5.1.2 Viscosity

This section investigates the viscosity of several THV inks/formulations. The methodology can be found in section 3.3.15.

The measured viscosities are reported in Table 5.4, Figure 5.2, and Figure 5.3. While using the cup and bob (cb) geometry the influence of Taylor-vortices on viscosity increased at lower viscosities and were more visible in the 5 wt% solution compared to the 10 wt% in MIBK (Figure 5.2c-e). The Taylor-vortices were negligible in the 20 wt% ink (Figure 5.2g). Nonetheless, the values of the viscosities for the cup and bob and parallel plate (pp) were similar at a shear rate of 100 s^{-1} (Table 5.4). The value of viscosity for inkjet applications is usually taken at 100 s^{-1} as standard rheometers can’t reach the actual shear rates of jetting and the change in viscosity is usually negligible as showed in Figure 5.2a-b-d-f. The viscosity of the inks roughly increased of 10-100-1000 times going from 1 to 5-10-20 wt%, respectively (Figure 5.3f). Figure 5.3a-e show the decrease of viscosity at higher temperature at a shear

rate of 100 s^{-1}. During the preparations of the inks, it was observed that the inks prepared with acetone had a visibly lower viscosity and dissolved the THV in considerably less time.

In summary, the viscosity of the inks roughly increased 10-100-1000 times by going from 1 to 5-10-20 wt%. The cup and bob geometry was initially used because it was a geometry ideal for solutions with high evaporation rates. However, this geometry was not accurate at high shear rates (> 100 s^{-1}) because of the formation of Taylor-vortices which caused the measured viscosity to increase. Nonetheless, the parallel plate geometry measurements showed that the viscosity values obtained at a shear rate of 100 s^{-1} were comparable with those obtained with a cup and bob geometry. As expected, the viscosity decreased at higher temperatures. It is believed that the viscosity and viscosity trends of THV solution have never been reported in literature before, making this work an important initial step in the diffusion of this material (section 2.4.5) into more fields/applications.

Table 5.4 – Viscosities at different temperatures of several THV solutions (n =3). The reported values are for shear rates of 100 s^{-1}. Two geometries were used: Cup and bobs (cb), parallel plate (pp).

Formulation	22°C		28°C		35°C		45°C		60°C	
	Viscosity (mPa.s)	**Stdev**	**Viscosity (mPa.s)**	**Stdev**	**Viscosity (mPa.s)**	**Stdev**	**Viscosity (mPa.s)**	**Stdev**	**Viscosity (mPa.s)**	**Stdev**
THV 1% in 50-50 MIBK-DMAC, pp	1.417	0.008	1.376	0.010	1.207	0.016				
THV 1% in MIBK, pp	**0.933**	0.002	0.899	0.003	0.812	0.003				
THV 5% in MIBK, pp	**7.392**	0.171	6.503	0.110	5.987	0.091	5.057	0.149		
THV 10% in MIBK, pp	**73.310**	2.763	58.707	0.212	44.713	1.124	36.137	1.207	27.153	0.967
THV 20% in 50-50 v% MIBK-acetone, pp	Not reliable	Not reliable	Not reliable	Not reliable	3019	706	Not reliable	Not reliable	Not reliable	Not reliable
THV 5% in MIBK, cb	7.958	0.065	7.110	0.224	6.131	0.145				
THV 10% in MIBK, cb	69.63	1.03	81.94	3.25	52.95	1.59				
THV 20% in 50-50 v% MIBK-acetone, cb	**1088.0**	21.0			848.8	40.4	680.1	19.4	463.5	2.4

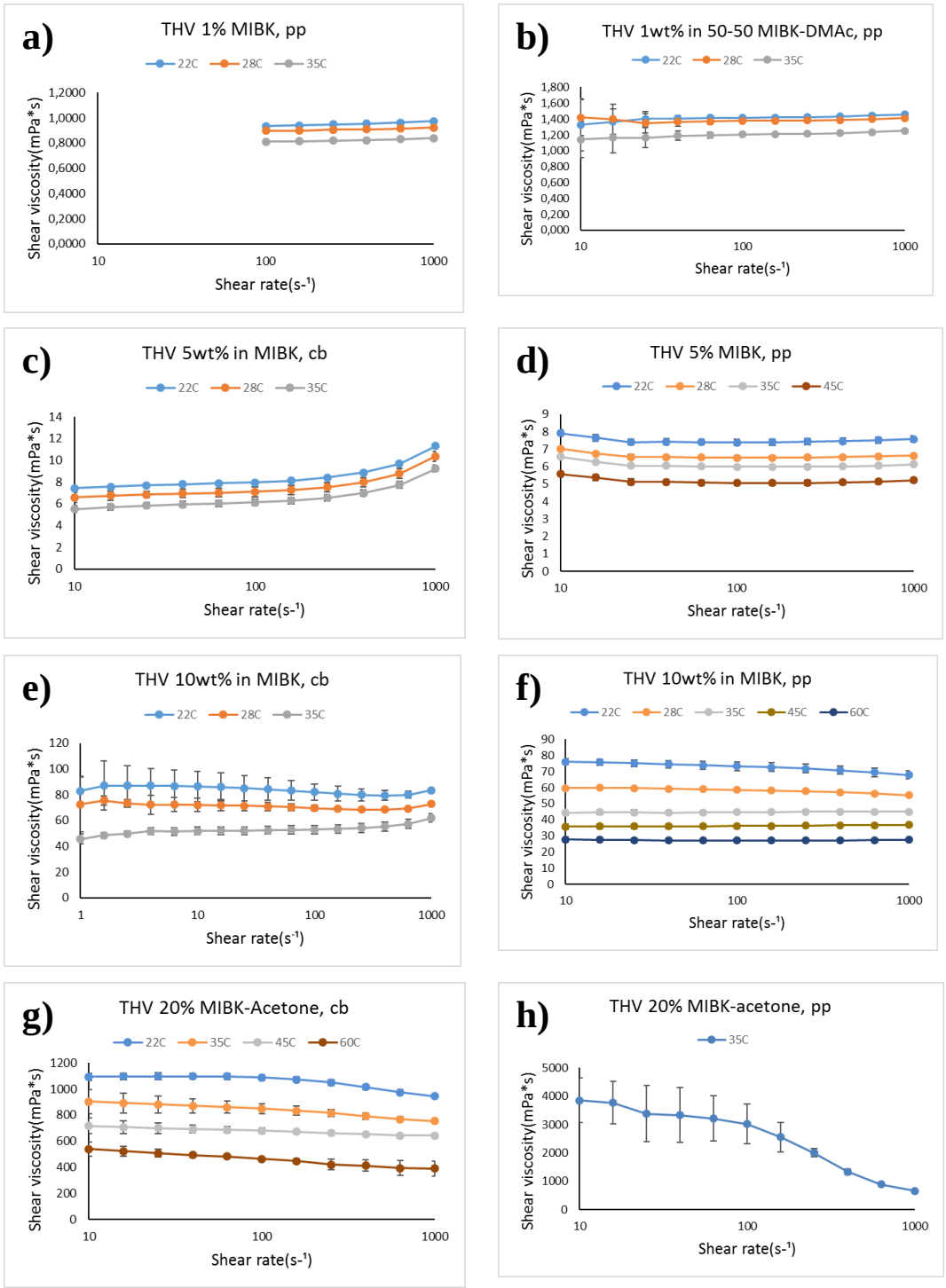


Figure 5.2 – Viscosities at different temperatures and shear rates of several formulations with a THV loading of 1-5-10-20 wt%, (n = 3). Two geometries were used: cup and bobs (cb), parallel plate (pp). The figure highlights the effect of the Taylor-vortices at THV loadings of 5 and 10 wt% by comparing the cb and pp geometries (c-d)(e-f).

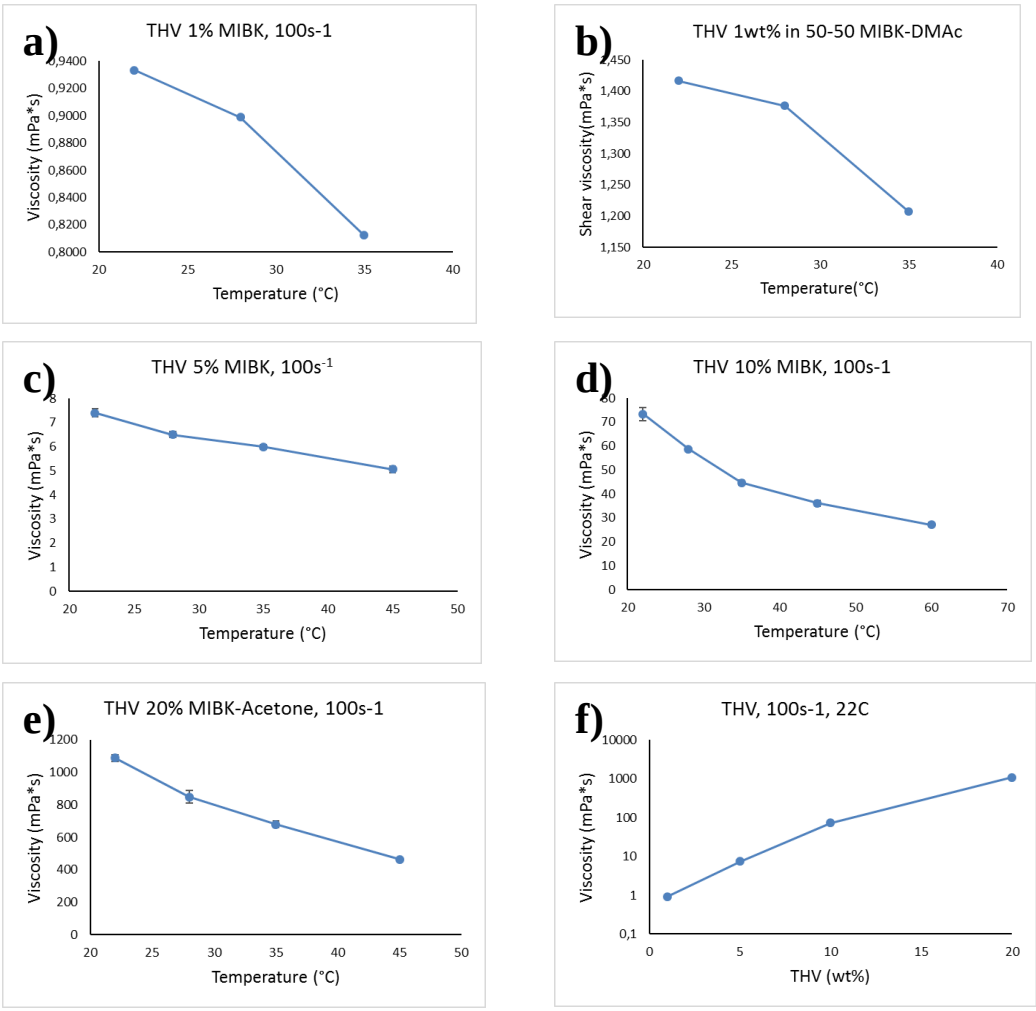


Figure 5.3 - Viscosity of several formulations at a shear rate of 100 s^{-1} (n = 3) with: (a-c-d) THV 1-5-10 wt% in MIBK, (b) THV 1 wt% in 50-50 v% MIBK-DMAc, (e) THV 20 wt% in 50-50 v% MIBK-acetone. (f) Viscosity trend at 22 °C for the different THV loadings reported in (a-c-d-e). The parallel plate geometry was used for all the measurements except for (e) where the cub and bobs geometry was used.

5.1.3 Gel permeation chromatography (GPC)

This section investigates the molecular weight of THV 221. The methodology can be found in section 3.3.16.

For THV 221, the measured Number Average Molecular Weight (Mn) was 2.145 x 10^5 g/mol, the Weight Average Molecular Weight (Mw) was 3.025 x 10^5 g/mol, and the polydispersity (PDI) was 1.411 (Figure 5.4). Labouriau et al. [242] analysed THV 220 and reported a Mn, Mw, and PDI of 0.928 x 10^5 g/mol, 1.95 x 10^5 g/mol and 2.10, respectively. The production of THV 220 was discontinued and substituted with THV 221. This could explain the small difference between the values found in this work and Labouriau et al. Another possibility was that the dn/dc used in this study was an estimate calculated with Equation 6 and might have led to slightly different results. The PDI reported in the Ullmann book [114] for a generic

THV grade was of ~ 1.7. Figure 5.4b show that a considerable portion of the polymer chains have an extremely high molecular weight, up to almost 1,000,000 g/mol.

In summary, the GPC results confirm that the THV had a high Mw of 3.025 x 10^5 g/mol and aPDI of 1.411. Similar values were found in the literature [242].

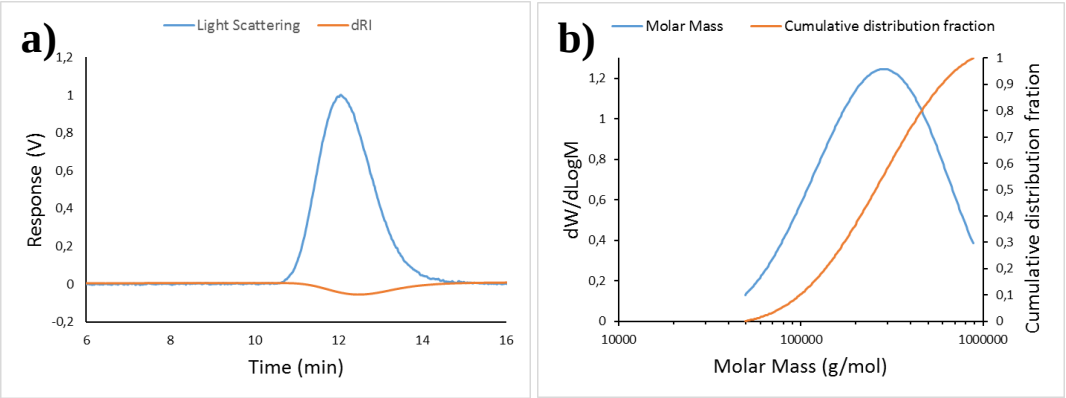


Figure 5.4 – (a) GPC graph and (b) molecular weight distribution of THV 221.

5.1.4 Discussion – ink characterisation

Material jetting requires the inks to have specific viscosities, surface energies, and evaporation rates. Because of that, several solvents and solutions were investigated for their use. MIBK was the chosen solvent because of its ideal evaporation rate, not too fast that it would clog the nozzles and not too slow that it would extend the printing times. Nonetheless, MIBK showed an unusual drying mechanism (wrinkle effect). When pure MIBK was deposited on top of a THV film, it deformed the surface forming wavy patterns. This behaviour was likely due to the relatively fast evaporation rate of MIBK and its being a modest solvent for THV. The wrinkle effect was in fact not visible when a good solvent or a slow evaporating solvent were used.

The viscosity of the inks roughly increased 10-100-1000 times by going from 1 to 5-10-20 wt%. The cup and bob geometry was initially used because it was a geometry ideal for solutions with high evaporation rates. However, this geometry was not accurate at high shear rates (> 100 s^{-1}) because of the formation of Taylor-vortices which caused the measured viscosity to increase [199]. Nonetheless, the parallel plate geometry measurements showed that the viscosity values obtained at a shear rate of 100 s^{-1} were comparable with those obtained with a cup and bob geometry. As expected, the viscosity decreased at higher temperatures.

The GPC results confirm that the THV had a high Mw of 3.025 x 10^5 g/mol and PDI of 1.411. It is believed that the viscosity, viscosity trends, surface energy, and wrinkle effect of THV 221 solutions have never been reported in literature before. Furthermore, only one source was available in the literature about the Mw of THV 220 [242] (a conference presentation). The

analyses and observations reported in this chapter are therefore an important initial step in the diffusion and better understanding of this material [163] (section 2.4.5) into more fields/applications.

The next sections discuss the use of THV in material jetting

5.2 Jetting with the Dimatix

5.2.1 Introduction

This section reports the experiments carried out to assess and optimise the jetting of low loading, low viscosity THV inks with the use of a Dimatix DMP-2830 system (section 3.3.2). The work carried out is summarised in the following flowchart:

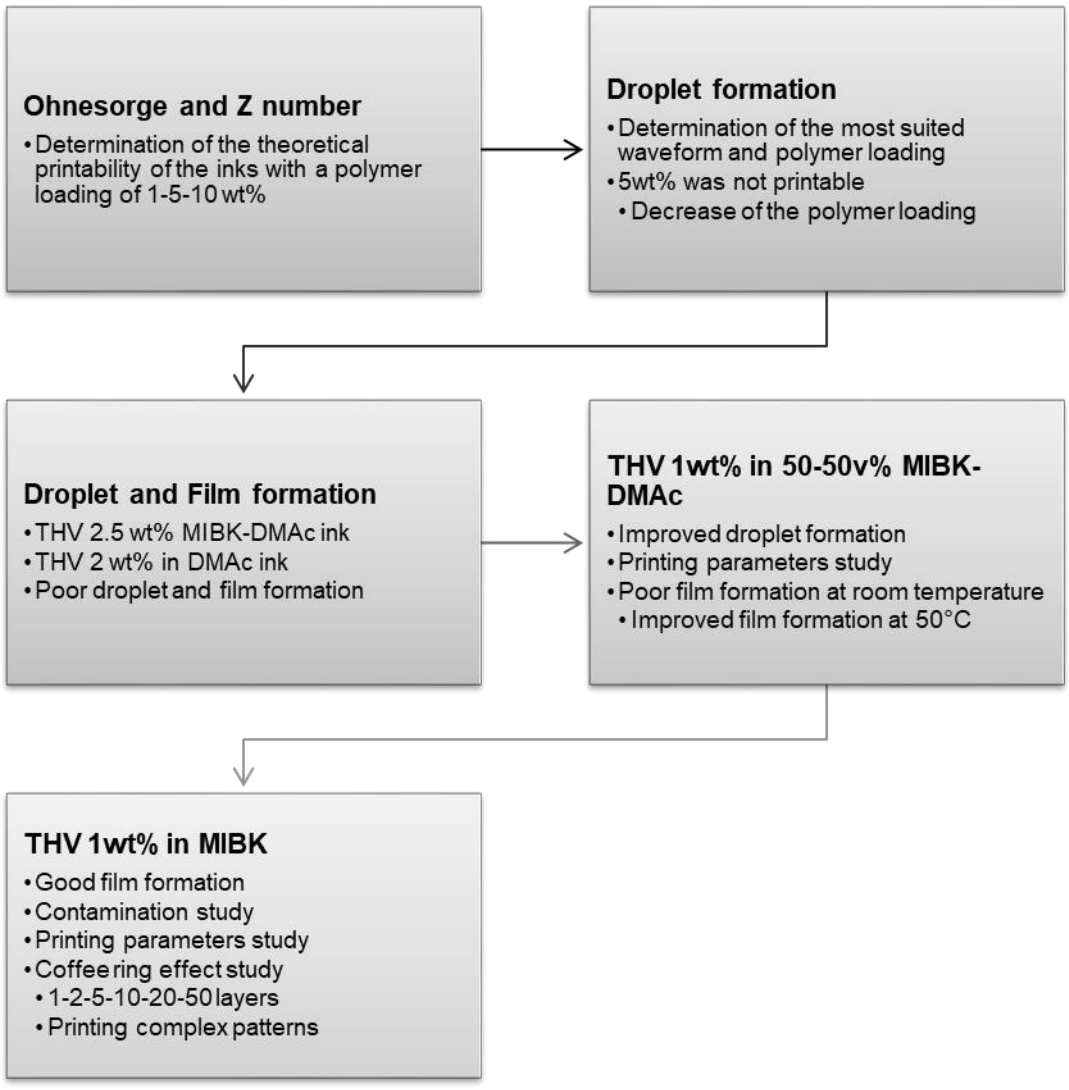


Figure 5.5 - Flow chart showing the development of the THV inks with the Dimatix

5.2.2 Ohnesorge and Z number

For information about the Ohnesorge and Z number see section 2.3.2.

From the information gathered in the previous section (surface energy, density, and viscosity), the Ohnesorge and Z number were calculated for three different formulations using Equation 3 (Table 5.5). Only the 5 wt% solution in MIBK had a Z number between 1 and 10 [82], [93], suggesting that the 1 wt% solution was too fluid and the 10 wt% was too viscous (section

2.3.2). Therefore, the 5 wt% ink was chosen as the first formulation to be printed with the Dimatix. Several parameters such as, waveform, frequency, jetting voltage, drop spacing, cartridge heating, and substrate heating were investigated to optimise the printing process.

Table 5.5 – Ohnesorge and Z number for several THV inks.

Ink	Oh number	Z number
THV 1 wt% in MIBK	0.0467	21.4
THV 5 wt% in MIBK	0.386	2.58
THV 10 wt% in MIBK	17.8	0.0562

5.2.3 Droplet formation

Judging from the Z numbers calculated in the previous section, THV 5 wt% in MIBK appeared to be a theoretically printable ink. Nonetheless, it was not possible to jet the ink despite the viscosity being slightly below the ideal range for the Dimatix (10-12 mPa.s [90]) which actually means that the ink should have had the opposite issue (dripping out of the nozzle). This deviation was due to the high molecular weight of the polymer (section 5.1.3) which made the ink a viscoelastic fluid [95], [96], [98], [99]. Haque et al. [98] calculated that with the typical strain rates encountered in material jetting ($> 5x10^{-4}$ s^{-1}), polymers with a Mw higher than 5×10^4 g/mol were going to experience coil-stretch transitions. The Mw of THV (3.025×10^5 g/mol) was above this threshold value.

The THV concentration was gradually reduced and two different solvents were employed to find the optimal printing conditions. With a THV 3 wt% solution in MIBK, only few nozzles were able to jet the ink (clogged nozzles). Furthermore, the jetting trajectories were not straight and the nozzles clogged in a few seconds. With a THV 2.5 wt% solution in 50-50 MIBK/DMAc, jetting was possible but only at 40 V and with a long tail which did not detach from the nozzle after having travelled for more than 1000 µm (Figure 5.6a). With a THV 2 wt% solution in DMAc, the tails were shorter but still relatively long. With a THV 1 wt% solution in MIBK the drop formation was very good and required a lower voltage (14 V), a short tail that recombined with the drop after ~ 300 µm was present (Figure 5.6b). The drop speed decreased from ~ 10 m/s to 1.5 m/s after the tail detached from the nozzle. The decrease in speed was due to the viscoelastic properties of the ink and similar results were observed by Haque et al. [98]. Overall, there was no visible difference in printability between the inks made with MIBK, DMAc and combination of the two except for the time required for the nozzles to clog. Having a lower vapour pressure than MIBK, DMAc did not clog the nozzles as quickly. 1 wt% was chosen as the optimal concentration but the initially used waveform (standard Dimatix waveform [243], Figure 5.6e) and voltage gave a process which was not

reliable. A small change in the voltage or waveform caused the nozzles to fail, thus a minimal change in the parameters or nozzle conditions during printing caused the print to fail.

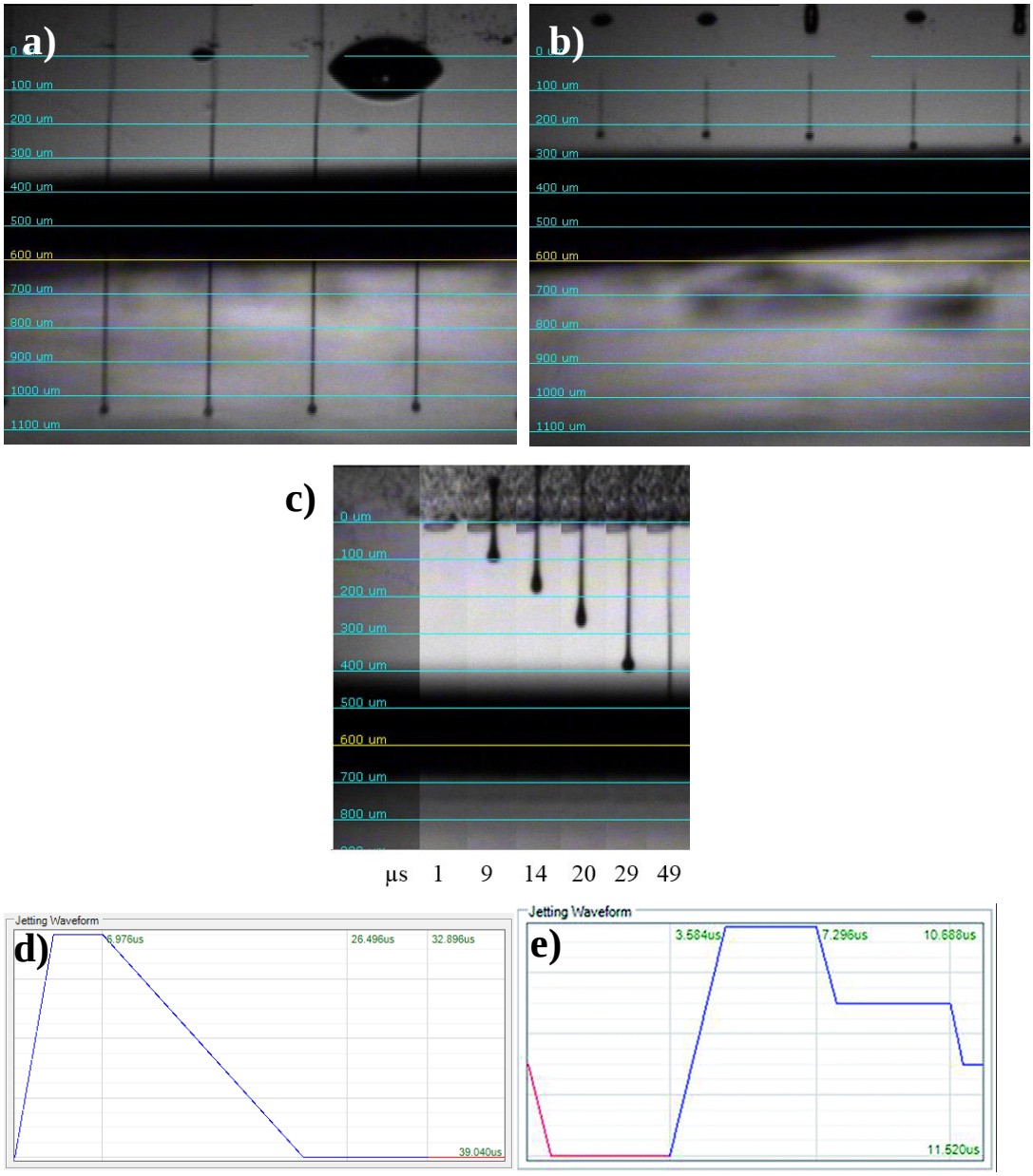


Figure 5.6 – Jetting of THV formulations with different concentrations, solvents, and waveforms. (a) THV 2.5 wt% in 50-50 v% MIBK-DMAc jetted with the standard Dimatix waveform. (b) THV 1wt% in MIBK jetted with the standard Dimatix waveform showed in (e). (c) THV 1wt% in MIBK drop at 1-9-14-20-29-49 µs after ejection. The drop was ejected with a custom-made waveform shown in (d).

A new waveform (Figure 5.6d) and a voltage of 40 V were used. The waveform was modified to maximise the strength of the "push" given from the piezoelectric system by maximising the voltage difference between the drop formation and ejection. This was done by removing the stand-by phase where the piezoelectric system is in resting position (the right side after the peak in Figure 5.6e). The slope of the peak was optimised empirically. The process was more robust and the drops were bigger, faster (~ 15 m/s constantly), and with a longer tail (Figure

5.6c). The nozzles were stable and the clogging time was relatively long (~ 60 seconds and 30 seconds at a nozzle temperature of 26.2 °C and 30 °C while not printing, respectively) and easy to fix (one cleaning cycle, where a cleaning cycle is a forced purging of the nozzles).

5.2.4 Film formation of the THV 2.5 wt% MIBK-DMAc ink

Figure 5.7 shows a 1-layer 3 x 3 mm film of THV 2.5 wt% in 50-50 v% MIBK-DMAc printed with a drop spacing (DS) of 30 µm, 16 nozzles, and nozzle and substrate temperature of 28 °C, on a polyethylene terephthalate (PET) substrate. The films were not uniform and stick-slip motions and coffee ring effect were observed (Figure 5.7). The coffee ring effect cause the solute to accumulate at the edge of a drying drop/film creating thicker/darker regions. In this case several thicker/darker horizontal lines are visible suggesting that the edge of the film receded several times during evaporation creating multiple coffee rings (stick-slip motion). Further information about the coffee ring effect can be found in section 2.3.3.

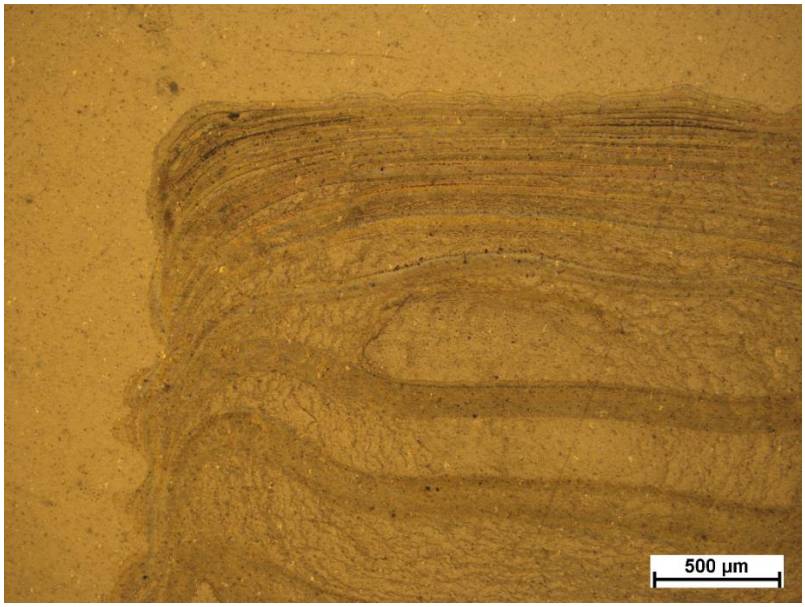


Figure 5.7 – Film produced by jetting THV 2.5 wt% in 50-50 v% MIBK-DMAc. The film was not uniform and stick-slip motions and coffee ring effect were present.

5.2.5 Film formation of the THV 2 wt% in DMAc ink

Figure 5.8 shows a 1-layer 3 x 3 mm film of THV 2wt% DMAc printed with a DS of 30 µm, 16 nozzles, and nozzle and substrate temperature of 28 °C, on PET. The nozzles had a lower tendency to clog because of the lower vapour pressure of DMAc. Despite showing a better film formation compared to the THV 2.5 wt% in 50-50 v% MIBK-DMAC ink, the coffee ring effect was still present (limited/lack of polymer in the centre in the film).

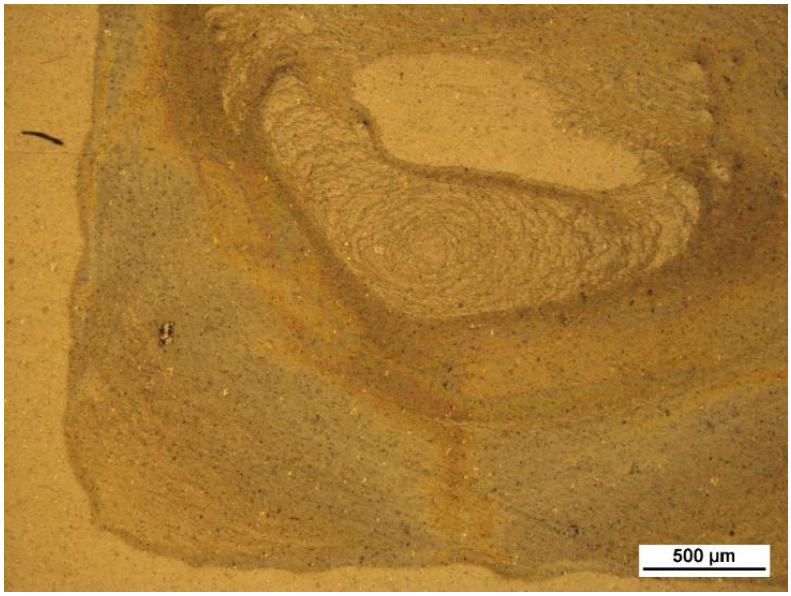


Figure 5.8 – Film produced by jetting THV 2 wt% in DMAC. The film was not uniform and coffee ring effect was present.

5.2.6 Drop, line, and film formation of the THV 1 wt% in 50-50 v% MIBK-DMAc ink

The film formation did not improve with THV 1 wt% in MIBK-DMAc but the ink showed improved nozzle stability and drop formation compared to the previous ink formulations. All of the following test were printed on glass slides using a nozzle and substrate temperature of 28 °C. A 1-layer 3 x 3 mm array of drops was printed with 1 nozzle and a DS of 200 µm so that each single drop would be isolated. The drops had a size of 78.54 ± 4.34 µm and showed a dot pattern (no uniform film) (Figure 5.9a). A single line printed with a DS of 50 µm was barely visible under the microscope. 5 layers of a single line were more visible and had a width of 120.73 ± 2.18 µm (Figure 5.9b). The line did not form a uniform film.

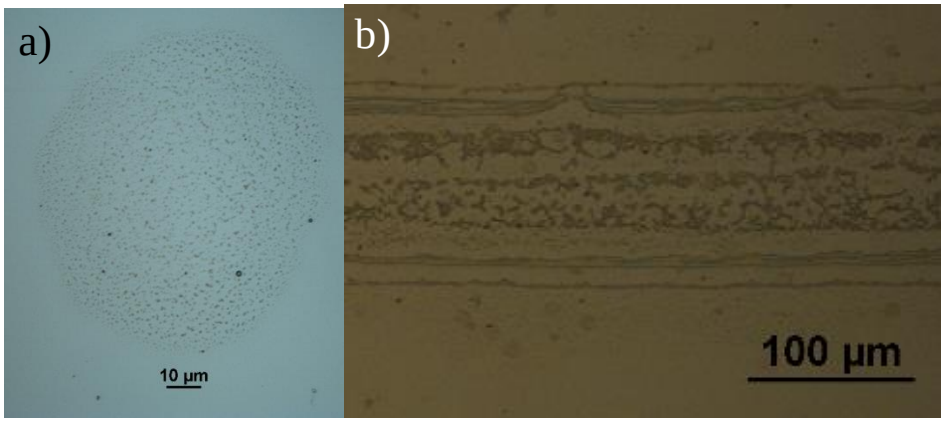


Figure 5.9 – THV 1 wt% in 50-50 v% MIBK-DMAc printed at a nozzle and substrate temperature of 28 °C. (a) Single drop. (b) 5 layers of a single line printed with a DS of 50 µm.

5-layer 3 x 3 mm films were printed with 1 nozzle and a DS of 10-20-35-50 µm. None of them formed a uniform film. Figure 5.10 shows the square printed with a drop spacing of 35 µm.

Similar looking films were obtained by He et al. [244] for a solvent based polycaprolactone ink.

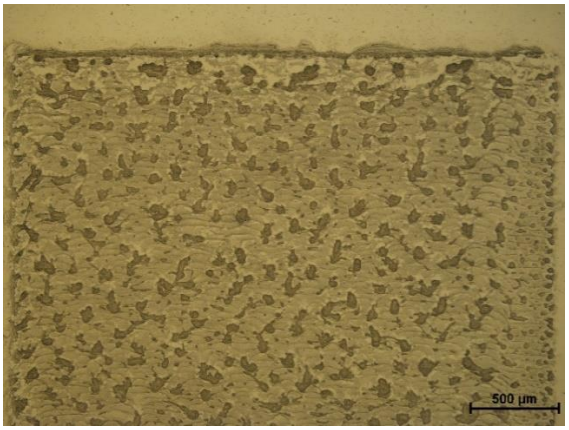


Figure 5.10 – THV 1 wt% in 50-50 v% MIBK-DMAc. 5 Layers of a 3 x 3 mm film printed with 1 nozzle with a DS of 35 µm at a nozzle and substrate temperature of 28 °C

Figure 5.11a shows a 99-layer 3 x 3 mm pattern printed with 16 nozzles and a DS of 10 µm. The small drop spacing (high density of drops) and absence of a delay time between layers did not allow the printed layers to dry before the subsequent layers were jetted. This caused the formation of a puddle of ink which only dried at the end of the printing process.

Several tests were carried out to assess the effect of a printing delay between layers. 20 layers were printed without a delay time and left to dry for 25 minutes. After that, 20 more layers were printed on top of the previously printed pattern (Figure 5.11b). While using the printer camera, it was observed in real time that the previously printed and dry pattern was floating and drifting on top of the newly printed 20 layers. This behaviour was due to the poor adhesion between the THV film and the glass substrate. Section 5.4.3 shows how this behaviour was exploited to detach the films from the glass slides without damaging them.

Figure 5.11c-d shows a pattern printed with a delay between layers of 0 and 20 seconds, respectively. With a 20 second delay the formation of a puddle of ink was avoided and the edges of the printed part were more defined and truer to the programmed pattern. Nonetheless, the coffee ring effect was still present. Overall, despite changing several printing parameters it was not possible to obtain a uniform film with the THV 1 wt% in 50-50 v% MIBK-DMAc ink. The only parameter that showed considerable improvements was the substrate temperature. For this experiment, substrate temperatures of 28 °C, 40 °C, and 50 °C were used while maintaining the nozzle temperature at 28 °C. It should be noted that while printing on a hot substrate for extended periods of time, the nozzles temperature gradually increased as the printhead was not equipped with a cooling system. This could cause undesired effects such as nozzle clogging and change in printability while printing for extended periods of time. 5-layer 3 x 3 mm patterns were printed with ~ 15 nozzles and a DS of 30 µm.

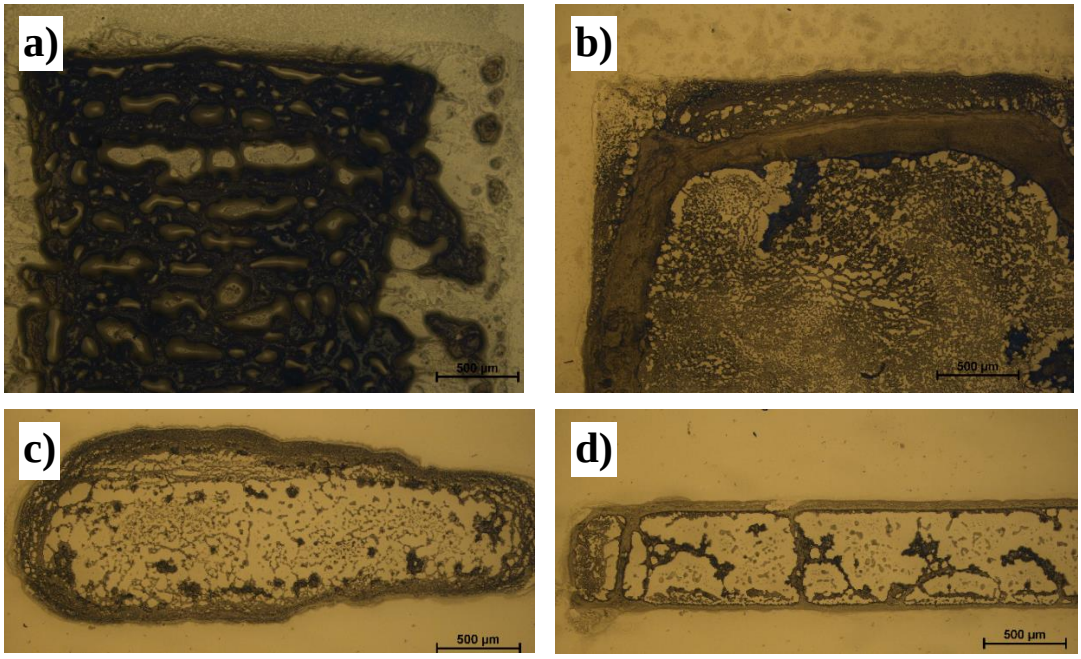


Figure 5.11 – THV 1 wt% in 50-50 v% MIBK-DMAc printed with 16 nozzles and a nozzle and substrate temperature of 28 °C. (a) 99 layers of a 3 x 3 mm pattern printed with a DS of 10 µm. (b) 40 layers of a 3 x 3 mm pattern printed with a DS of 30 µm and a pause of 25 minutes after the first 20 layers. (c-d) 5 layers of a 5 x 0.6 mm pattern printed with a DS of 40 µm with a delay between layers of 0 and 20 seconds, respectively.

At 28 °C, the film was not uniform and showed coffee ring patterns (Figure 5.12a). At 40 °C, the centre of the pattern was similar to that printed at 28 °C but the edges looked different, they were sharper and more uniform and with what looked like pores (Figure 5.12b). At 50 °C the film looked more uniform and the pore structure previously seen at the edges at 40 °C was now on the entire surface of the film (Figure 5.12c-d). The high temperature of the substrate likely minimised the coffee ring effect by not giving the polymer the time to migrate to the edges. It was also possible to distinguish the several swipes of the printhead as the ink had not the time to spread as much as at lower temperatures. At first, it was not clear if the pores exposed the underneath glass slide or if they were on top of a thin polymer film. By looking at the sample under an optical microscope, most of the pores had a slightly different colour compared to the glass slide suggesting that most of the pores were in fact on top of a thin polymer film. This was then confirmed by AFM analysis. By pulling the film with a needle tip, the "pore" structure stretched (Figure 5.12e-f). This highlighted the high elongation at break of THV even at small thicknesses (< 1 µm) and showed how some of the "pores" opened revealing the underlying glass slide. Further testing may show how to produce membranes with a narrow pore size distribution.

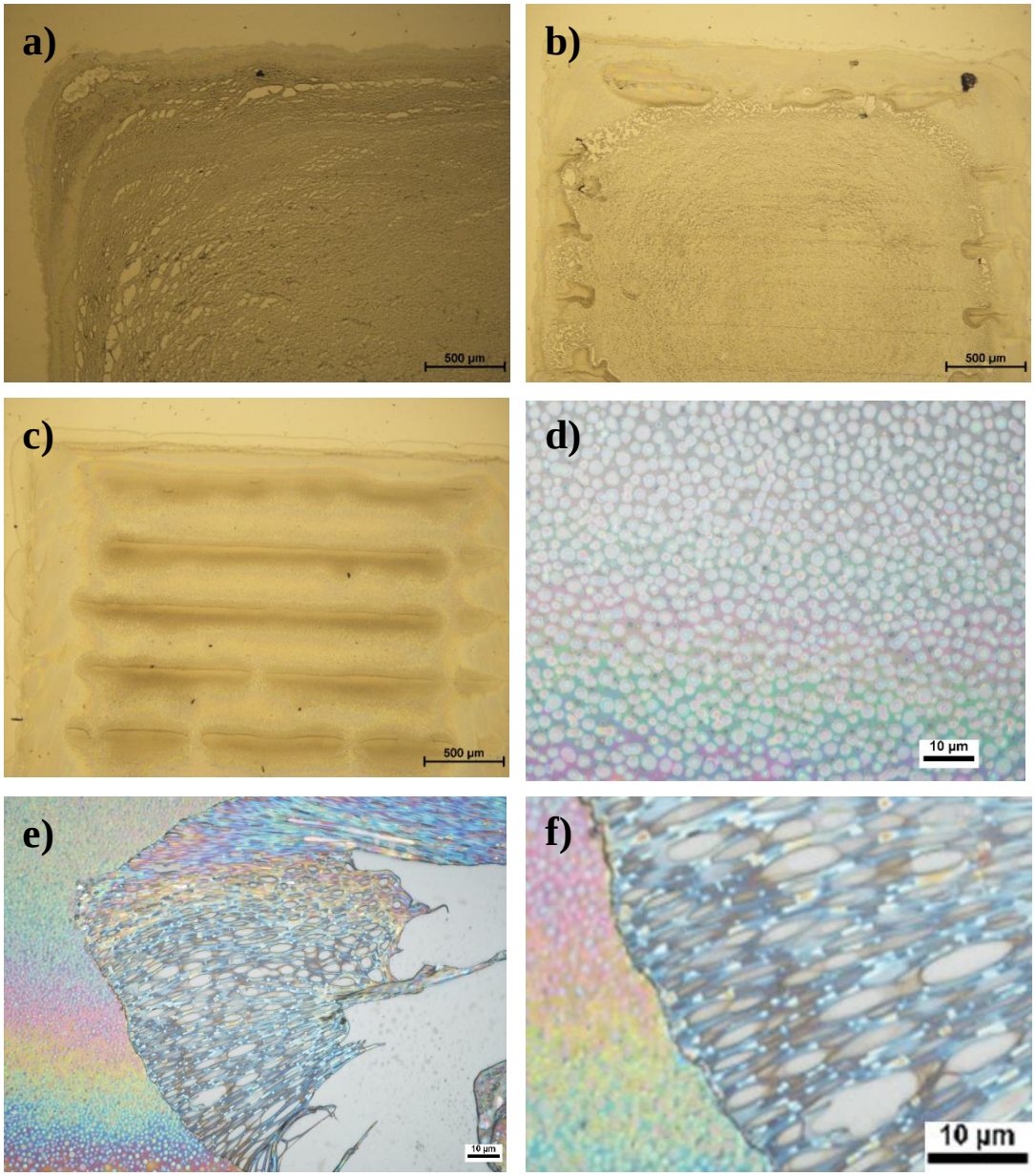


Figure 5.12 – THV 1 wt% in 50-50 MIBK-DMAc. Films of 5 layers with a drop spacing of 30 µm at (a) 28 °C, (b) 40 °C, (c-d-e-f) 50 °C. (d-e-f) Pore pattern of the film printed at 50 °C before and after being stretched with a needle tip.

A similar test was done using a syringe and a hot plate to assess the possibility of obtaining information on the film forming ability of a jetted ink in a cheaper and quicker way. A drop of the ink (Figure 5.13a) was deposited on a glass slide and dried at room temperature (Figure 5.13b) and at 50 °C (Figure 5.13c). The drop looked uniform while still wet (Figure 5.13a). When it dried at room T the coffee ring effect was evident (Figure 5.13b). When it dried at 50 °C the film was quite uniform with few pores (Figure 5.13c). This experiment showed that a formulation ability to form films could be tested in an easy, cheap, and fast way with just a syringe before using an inkjet printer, saving time and resources.

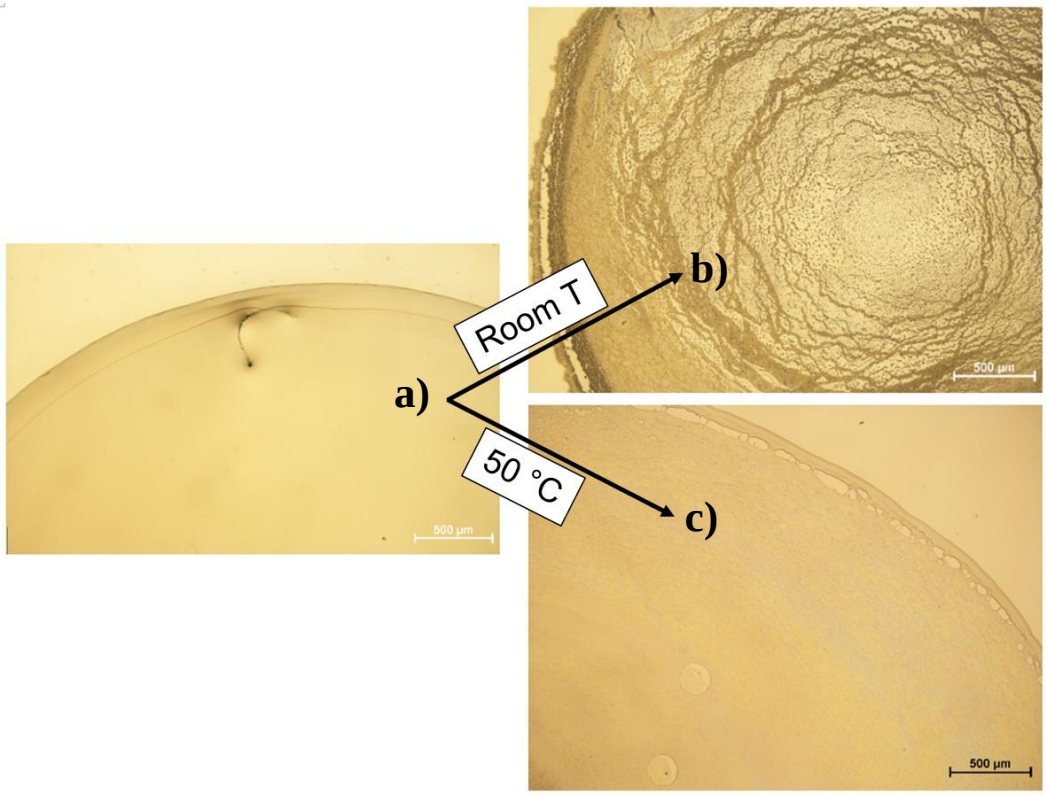


Figure 5.13 – (a) Syringe deposition of a drop of THV 1 wt% in 50-50 MIBK-DMAc and its drying at (b) room temperature and (c) at 50 °C. The drop showed a coffee ring effect when dried at room temperature and a more homogenous film when dried at 50 °C.

5.2.7 Drop, line, and film formation of the THV 1 wt% MIBK ink

THV 1 wt% in MIBK showed more potential than the other formulations as the film formation was mainly uniform. After printing two arrays of drops made of 1 and 2 layers, the drop size was measured to be 128 ± 16 µm for the first layer, and 114 ± 4 µm for the second layer (Figure 5.14 and Figure 5.15). The decrease in drop size while printing on a previous THV layer agreed with the higher contact angle of the ink on a THV substrate as shown in section 5.1.1. The drops formed extremely thin films which presented a coffee ring pattern with an edge and central height of roughly 8 and 3 nm, respectively. Two layers showed an edge and central height of roughly 43 and 7 nm. A second edge was also present as the second drop was smaller than the first one, thus the second edge corresponded to the edge of the first layer drop (Figure 5.15). In fact, the second edge measured ~ 9 nm.

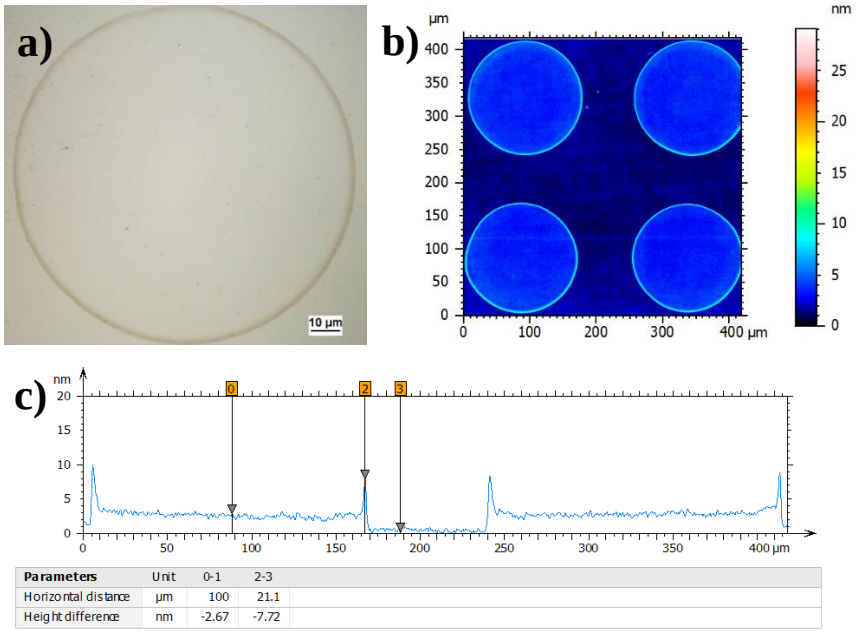


Figure 5.14 – Jetted drops of THV 1 wt% in MIBK on a glass slide. Drops seen by (a) an optical microscope and (b) CSI. (c) Profile of the drops generated from the data acquired with the CSI.

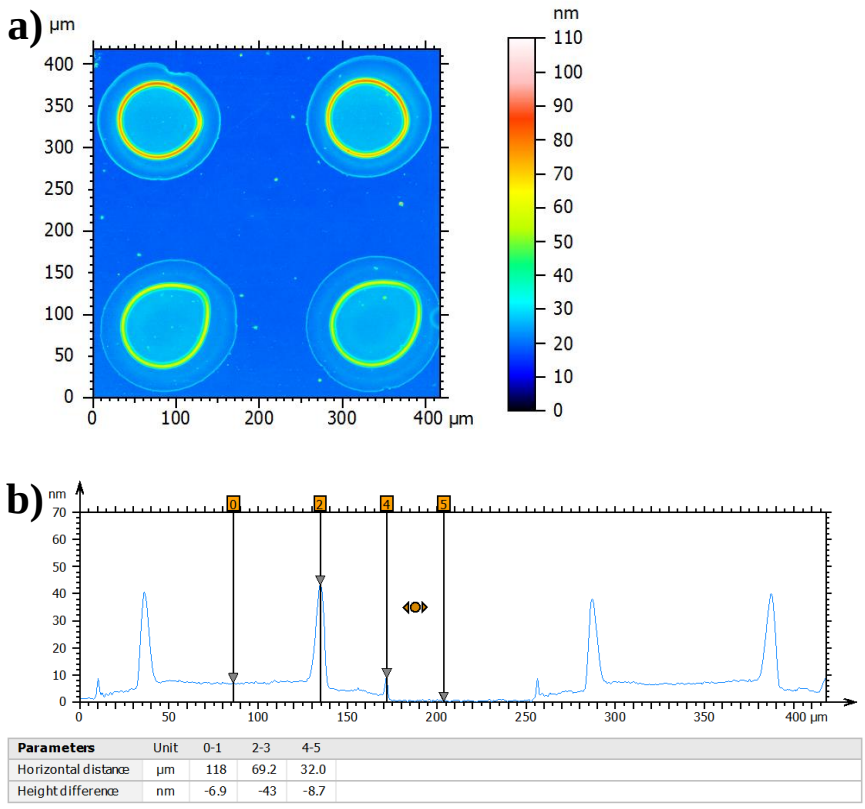


Figure 5.15 – (a) CSI image and (b) profile of two layers of drops of THV 1 wt% in MIBK on a glass slide.

It was observed that the size of the drops generated from the same nozzle of the Dimatix Cartridge (DMC) was very consistent. Nonetheless, the drop size changed from one nozzle to

the other. The change was likely due to imperfections in the DMC but the ink may also have had an influence on it. This behaviour was also observed in other experiments described later. It is important to keep this information in mind when planning experiments as a change in drop size could cause the formation of non-uniform films, gaps and decrease accuracy.

To assess the influence of the drop spacing, 3 mm lines were printed on a glass slide with a nozzle and substrate temperature of 22 °C and a DS of 60-80-100-120-140 µm. Each experiment was made of 4 sets (printed in sequence from left to right) of 5 lines printed simultaneously with five different adjacent nozzles (Figure 5.16e). The line widths are reported in Table 5.6, 3 measurements for each one of the 5 lines were taken (a total of 15 measurements). Figure 5.16a-b show the first and fourth set of lines printed with a DS of 60 µm. It was observed that the line width increased with each consecutive set of lines, so much that the lines merged together (Figure 5.16b). This may have been due to either changes in rheology of the ink inside the DMC or the nozzles needing some time to reach a stable printing regime. Another visible change was that the line width decreased with each consecutive nozzle (going down), this was even more evident with a drop spacing of 140 µm (Figure 5.16d). The drop size was so smaller that it could not form a line. This confirmed what was observed during the measurement of the drop size – each nozzle had its own drop size. This is a very important detail to know as often the drop size and line width are measured while using a single nozzle and assuming that all the nozzles are or behave the same. The lines started to have a wavy look at a drop spacing of 120 µm (Figure 5.16c) due to the fact that the average drop size was 128 µm (small overlap between drops). The ideal drop spacing (drop overlap) is usually determined empirically as it is often material specific [92]. Nonetheless, it is usually around 1/3 of the drop size. The correct drop spacing produces films with no gaps and no bulging.

Table 5.6 – Line width of THV 1 wt% in MIBK on glass (n = 15). The width min. was introduced when the lines assumed a wavy shape.

Drop spacing (µm)	Width max. (µm)	Stdev (µm)	Width min. (µm)	Stdev (µm)
60	168	17	/	/
80	138	18	/	/
100	124	9	/	/
120	125	9	99	17
140	132	11	80	12

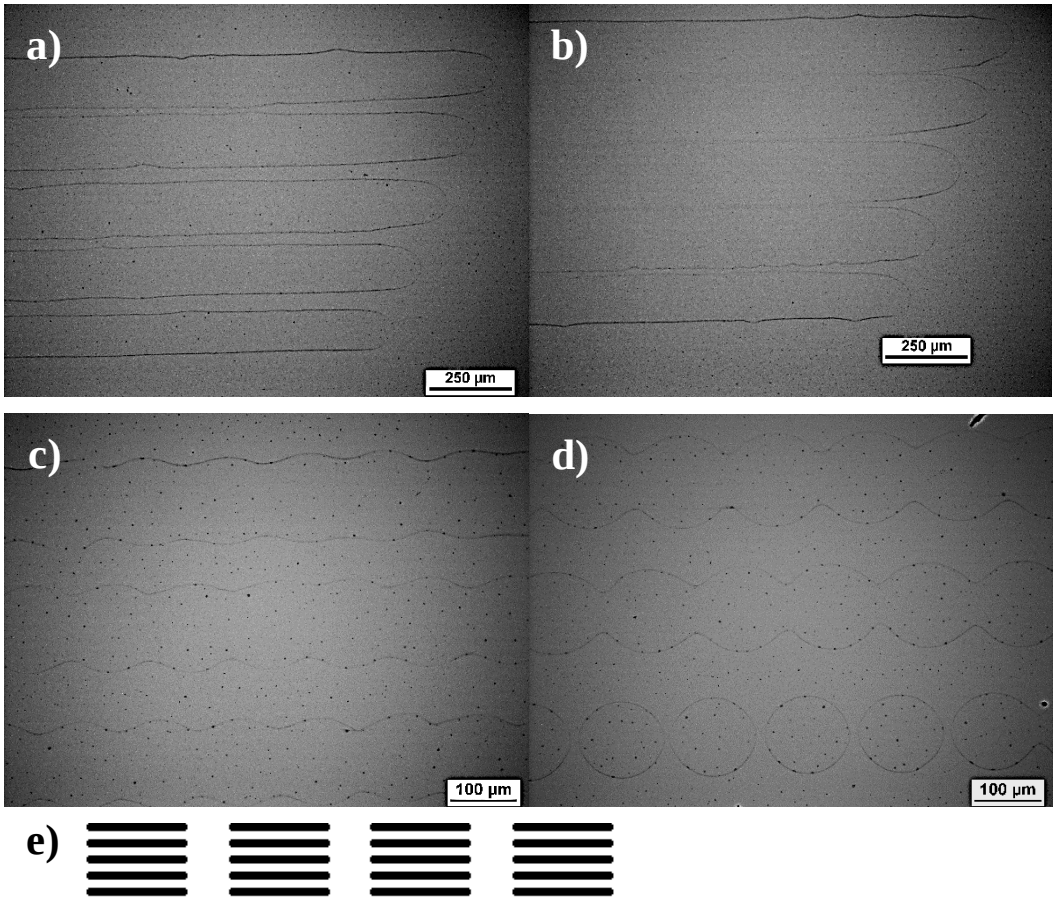


Figure 5.16 – THV 1% in MIBK. Lines printed on a glass slide with a nozzle and substrate temperature of 22 °C and a DS of (a-b) 60 µm, (c)120 µm, and (d) 140 µm. The pictures were corrected in saturation, contrast, brightness, and sharpness to increase visibility of the tracks. The printed pattern is shown in (e).

Next, several films were printed at different drop spacings. Defects and pores were present when a drop spacing smaller than 60 µm was used (Figure 5.17a-b). The best results were obtained with a drop spacing of 75 µm which generated what looked like a smooth and uniform layer (Figure 5.17c). The SEM/AFM/CSI imaging showed that despite looking uniform the film contained small pores of size roughly below 2 µm (Figure 5.17d-e-f). The size of the pores increased near the edges. The black and red spots visible in the SEM and CSI images were agglomerations of variable thickness (~ 50 - 500 nm) which are explained in depth in the section 5.2.7.1.

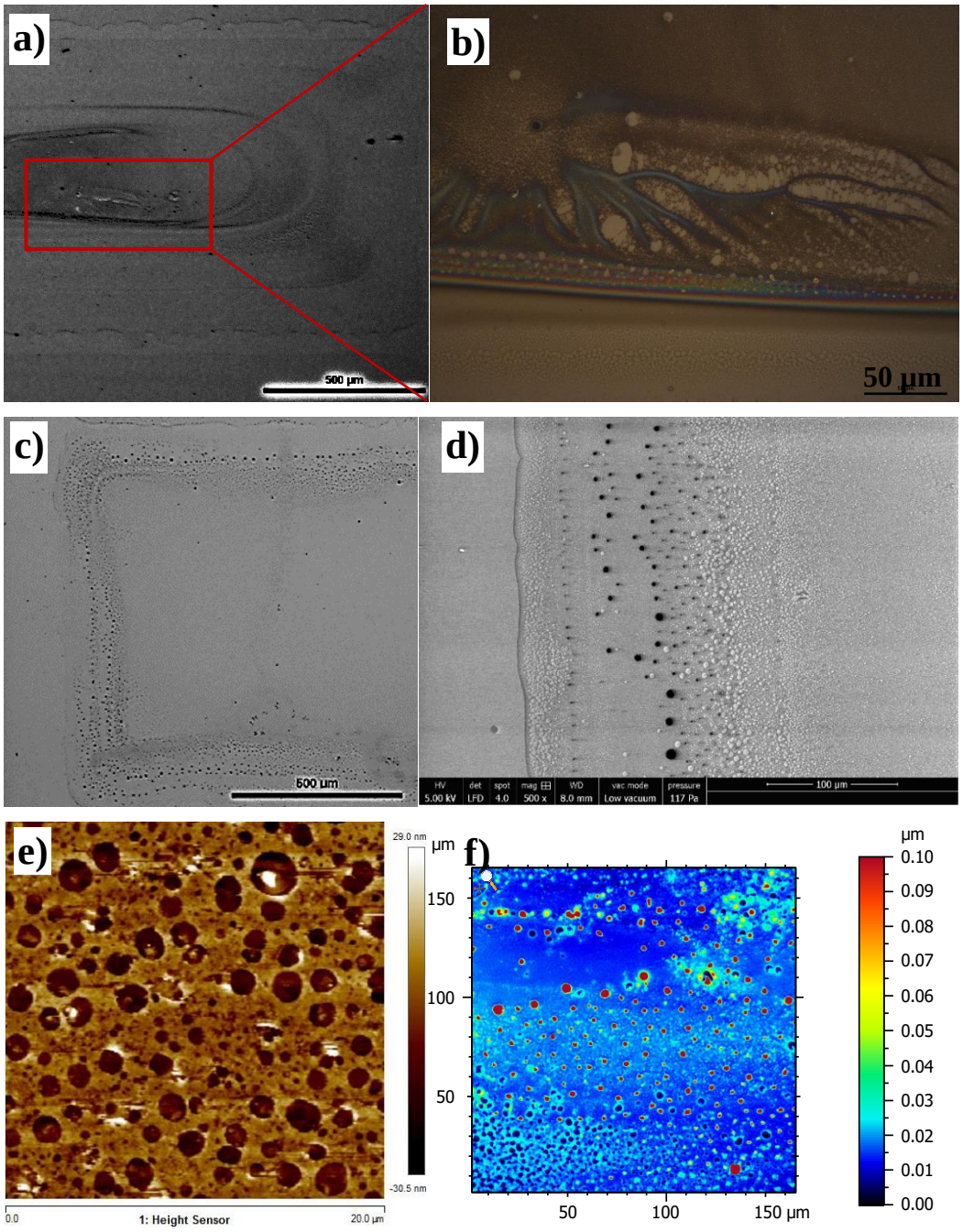


Figure 5.17 – Printed THV 1 wt% in MIBK, single layer. (a) Non-uniform film made with a DS of 60 µm. (b) Zoomed section of (a). (c) Uniform film made with a DS of 75 µm. (d) SEM of (c) showing pores and agglomerations. (e) AFM and (f) CSI of (c) showing pores. Pictures (a-c) were corrected in saturation, contrast, and sharpness. Image (e) was corrected with 1st order flattening.

When 5 layers were printed with a DS of 75 µm, an unusual pattern started to appear (Figure 5.18a). The CSI showed a film of ~ 45 nm in thickness with bumps of ~ 200 nm in thickness (Figure 5.18b-c-d). The position of the bumps was counterintuitive as it was not in the centre of the printed drops but in the gaps between drops. The position of the drops was identified by looking at the wavy pattern of the contour. This effect was likely caused by the coffee ring effect and is explained in more depth in section 5.2.7.2. The outer contour (after the wavy

contour) was the first layer that had spread more on glass. The SEM imaging showed an increase in the number of agglomerations and no porosity compared to the 1-layer films seen earlier (Figure 5.19). When 30 layers were printed, bigger agglomerations were visible and the film lost uniformity (Figure 5.20). It was evident that the size of the agglomerations increases with the number of layers. A discussion on these agglomerations will be given in the next section.

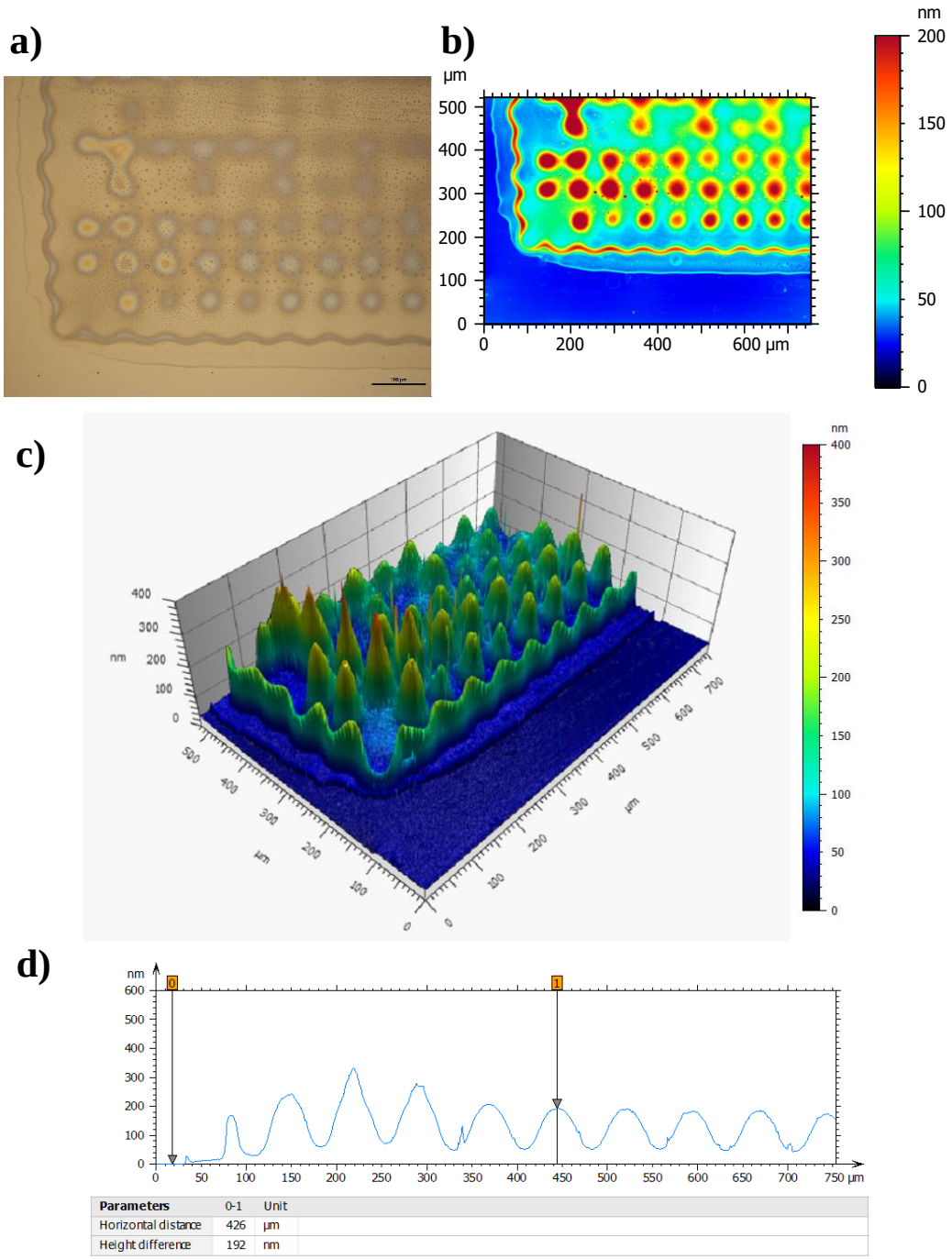


Figure 5.18 – Printed THV 1 wt% in MIBK, 5 layers with a DS of 75 µm. (a) Optical microscope image. (b) CSI 2D map. (c) CSI 3D map. (d) Horizontal CSI profile of the second line of "bumps" from the bottom.

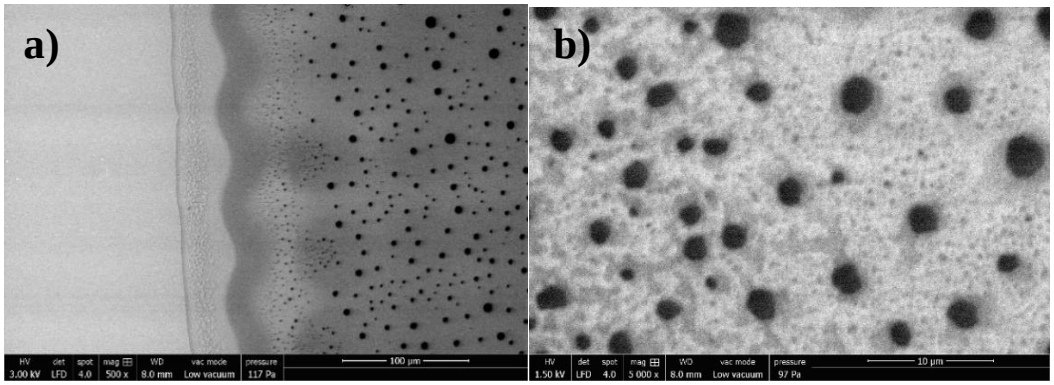


Figure 5.19 – SEM images of printed THV 1 wt% in MIBK, 5 layers with a DS of 75 µm. Scale bars (a) 100 µm, (b) 10 µm. The film presents no porosity and more agglomerations compared to the 1-layer film in Figure 5.17c-d.

5.2.7.1 Agglomerations investigation

The agglomerations present on the printed films seen in the previous section were initially thought to be due a phenomenon called dewetting. Dewetting happens when films are not stable, holes appears at random locations in the films and keep growing over time. When two or more holes touch they form a thin line of liquid which becomes a droplet by Plateau-Rayleigh instability (Figure 5.20c). The density of nucleated holes depends on the presence of contaminants and internal stresses. Internal stresses increase with increasing polymer molecular weight. Dewetting is more prone to happen for thin film, low viscosities, and when the drying temperature is above the glass transition of the polymer [104], [245]–[247]. In this case, THV had a Tg of 5 °C [195], the printed films were few tens of nanometres thick, and the viscosity was low (~ 0.9 mPa.s). Therefore, many of the requirements for dewetting were present.

Figure 5.20a-b compares the agglomeration seen in a 30 layers THV 1 wt% in MIBK film (Figure 5.20a) to the drops formed by the dewetting of a poly(4-vynylpyridine) film from the literature (Figure 5.20b) [245]. The agglomerations on THV looked very similar to the drops formed by the dewetting of the film. Furthermore, what looked like the growth phase was observed in some of the printed films (Figure 5.20d).

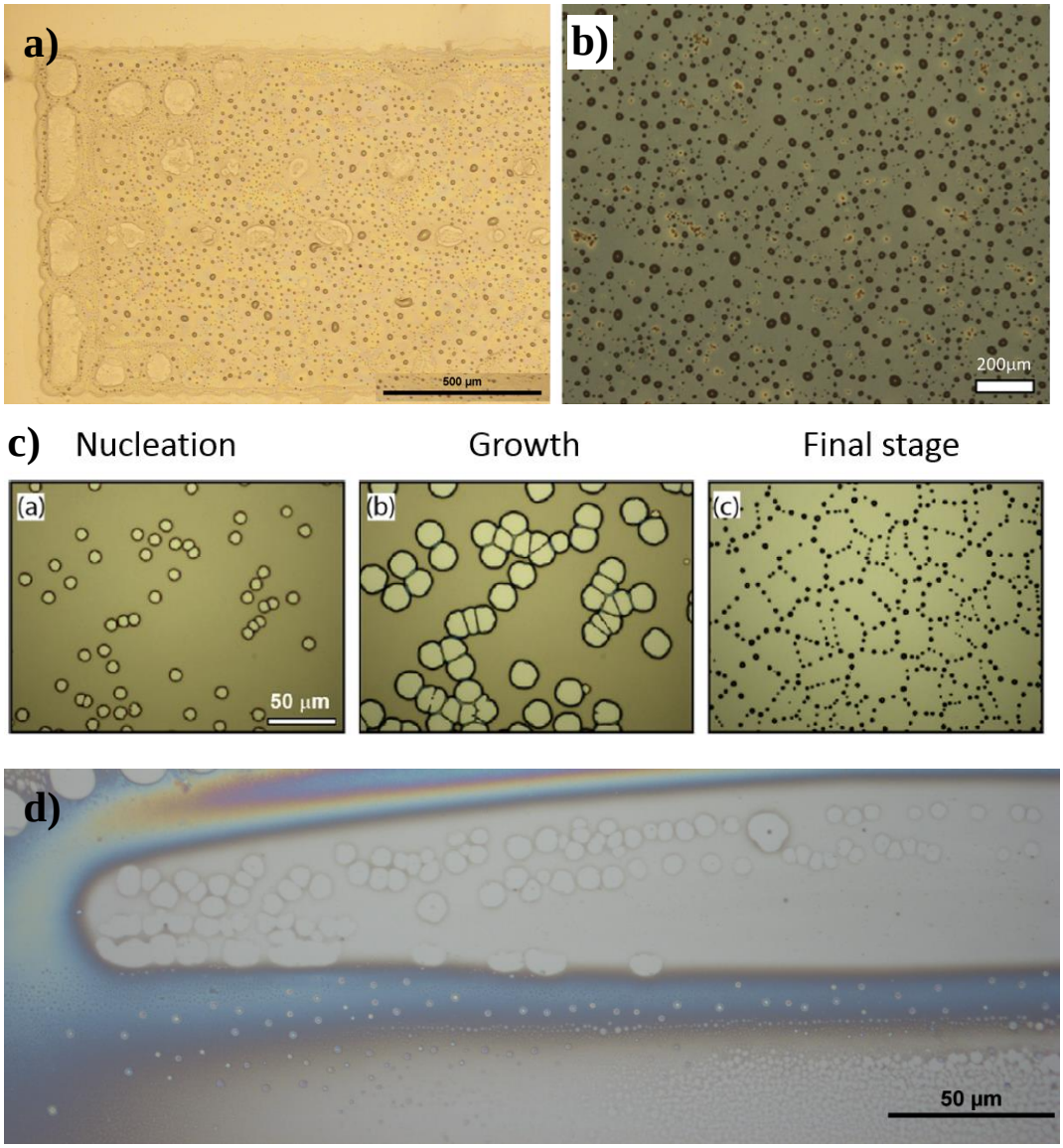


Figure 5.20 – (a) Agglomerations present on a 30-layer THV 1 wt% in MIBK film compared to (b) the drops formed by the dewetting of a film from the literature [245]. *(c) Dewetting mechanism* [245] *and (d) possible growth stage observed in some of the printed THV films.*

Despite these similarities and the presence of the requirements for dewetting, further experiments showed that the agglomerations were not caused by dewetting. After printing 100 layers and taking pictures after each layer it was observed that the size of the agglomerations grew with the number of layers and often slightly changed position. In other tests, the substrate temperature was changed to 26-30-35-40-50 °C while printing 20 layers of THV 1 wt% in MIBK on both a glass slide and a THV coated glass slide. The drop spacing used was 50 µm and the nozzle temperature was set to 28 °C. The prints on THV showed an increase in agglomeration size as the temperature increased. The prints on glass slide showed a tendency for the films to detach from the substrate and migrate to the centre of the printed pattern, a behaviour similar to what seen in Figure 5.11b or when the film was exposed to water (water detaches the film from the glass slide as will be discussed in section 5.4.3). Furthermore, the

agglomerations were still fluid after weeks and/or after 20 minutes in oven at 170 °C. The agglomerations that had an elongated or irregular shape became spherical after been exposed to high temperatures in the oven. This suggested that the agglomerations were not the solvent as it should have evaporated nor THV as it should have been solid. During the SEM imaging, the electron beam caused the agglomerations to move/spread in the direction of the beam and to become white (Figure 5.21) (the SEM image is acquired by scanning from top to bottom the sample with an electron beam).

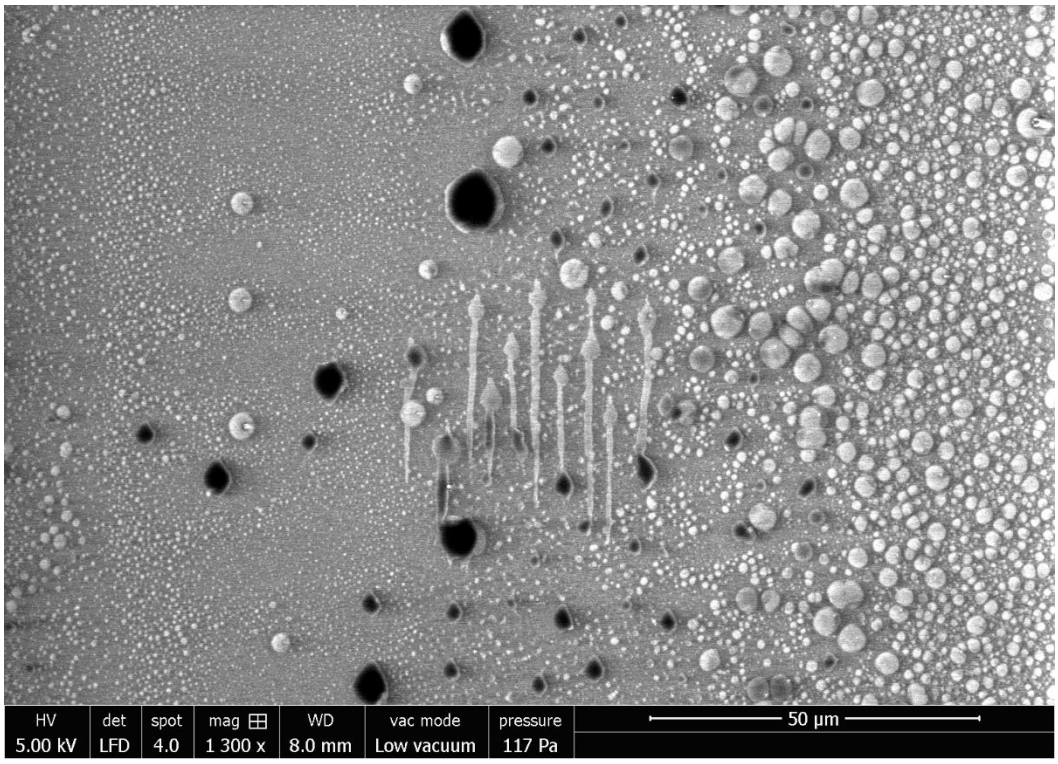


Figure 5.21 – SEM image showing the (black) agglomerations present in the jetted THV film (1 layer). The SEM image is acquired by scanning (from top to bottom) the sample with an electron beam. The black agglomerations were being moved (to the bottom) and discoloured over time by the scanning electron beam (white lines in the centre of the image). The other white elements were pores.

The next hypothesis was that a contaminant was present. The possible origins of the contamination were determined to be either the solvent, syringes, or DMC. The solvent (MIBK) had a purity of 99.5% and that 0.5% of impurity was comparable in amount to the 1 wt% of THV. The solvent was tested by evaporating 1 mL of solvent one drop at a time on the same spot on a glass slide with a glass pipette, green syringe (Braun Injekt), and white syringe (BD Plastipak). The glass pipette and green syringe gave similar results, a small amount of contamination with a grainy appearance was left behind (Figure 5.22a). The white syringe showed a great amount of an oily contaminations which was clearly visible even with just one single drop of solvent (Figure 5.22b). The white syringes in fact contained medical grade silicone oil which was likely to be the source of the oily contamination.

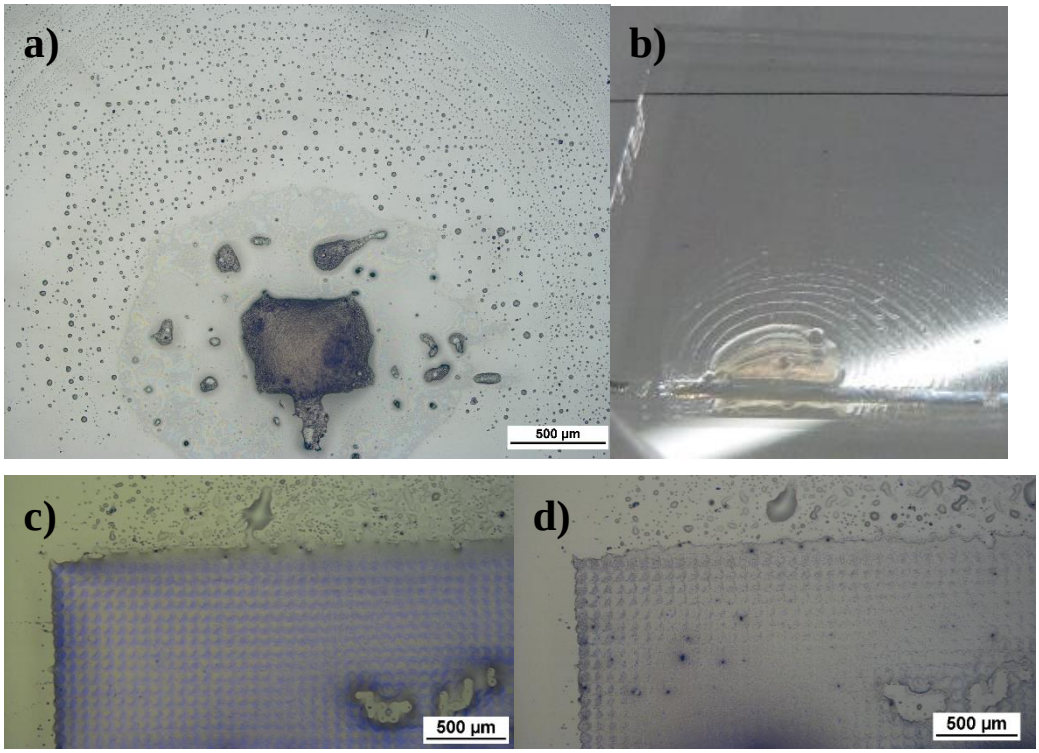


Figure 5.22 – Contaminations present when MIBK was deposited through a (a) green syringe, (b) white syringe, (c) standard Dimatix cartridge (DMC-11610) as printed and (d) after 20 min at 170 °C.

Therefore, the first conclusion was that the solvent was not the origin of the contamination and that white syringes should be avoided. To test the Dimatix cartridges, the MIBK solvent was jetted without any THV in it. If no contamination was seen to originate from the DMC, similar results to the green and glass pipette test done before should have been observed. After jetting single drops and square patterns of pure solvent, a fluid substance was observed (Figure 5.22c). The fluid only partially decreased in volume after 20 minutes at 170 °C in an oven (Figure 5.22d), and almost disappeared after 20 minutes at 250 °C. The plastic bag that contained the ink inside the DMC was in fact made of polypropylene which has a poor compatibility with MIBK [248]. It was then clear that the contamination was coming from the DMC. This was further confirmed by the fact that the agglomerations were not seen in films produced by drop casting with a green syringe, or jetted with the PICO Pµlse printer (section 5.3). Finally, the more chemically resistant cartridge (DMCLCP-11610) was used to print the same pattern with a THV 1 wt% in MIBK ink and no agglomerations/contaminations were visible (Figure 5.23). Finally, the detaching of the THV films from the glass substrate, observed in Figure 5.11b when multiple layers were printed, was also due to the presence of this oily contamination.

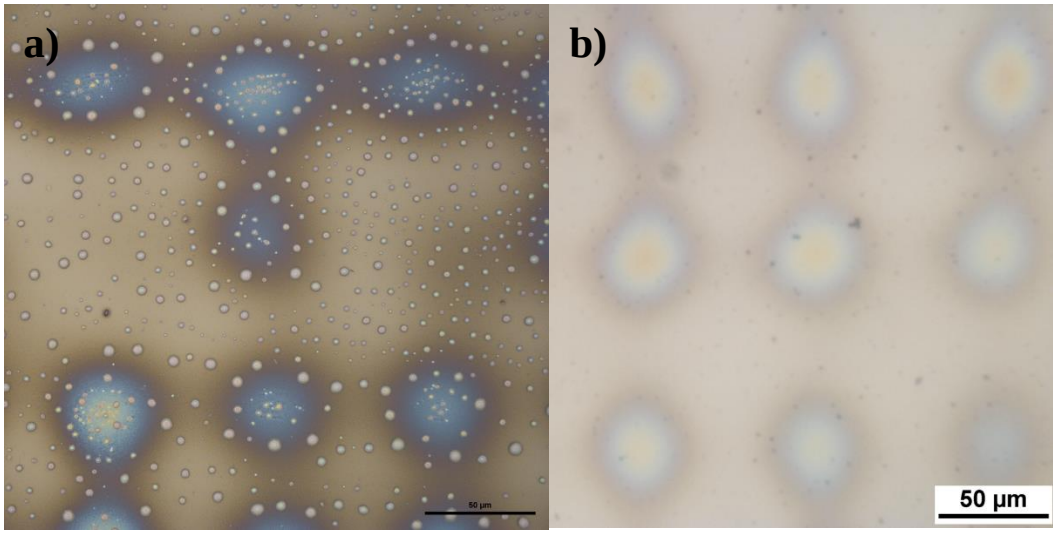


Figure 5.23 – 5-layer THV 1 wt% in MIBK film produced with (a) DMC-11610 (b) DMCLCP-11610. Because of the higher chemical resistance of the DMCLCP-11610, no agglomeration/contamination was visible.

5.2.7.2 Print strategies and complex patterns

The previous sections studied the behaviour of the ink when drops, lines and films were printed with different printing parameters and number of layers. The presence and source of contaminations were also identified. This section investigates the profiles and appearances of several complex patterns.

Figure 5.24 shows the CSI and AFM of a 1-layer THV 1wt% in MIBK film printed with a DS of 75 µm without the contaminations coming from the DMC. The coffee ring was still present and created a thick contour of variable thickness between 40 and 200 nm. The thickness in the centre of the film was ~10 nm. The AFM showed that, when the film was printed without contamination, the previously seen pore structure was absent (Figure 5.17e). Nonetheless, small pores were present due to small artefacts/particles of size inferior to 50 nm present on the glass slide. The presence of these artefact was confirmed by the fact that they were taller than the THV film, had a lower adhesion, and were observed also in parts of the glass slide without the THV film (Figure 5.24b-c). These artefacts suggest that the use of a mould with small pillars (e.g. produced via two-photon polymerisation) may be used to impart a specific pore size, shape, and distribution to the printed THV films. The film could be then removed from the mould with water as explained in section 5.4.3. A trend in modern manufacturing is to miniaturise as much as possible and this also includes films [249]–[252]. As explained by Xue et al. [247], the demand of nanometre-thick films is in constant rise; MJ (and THV) could play an important role in it, especially in multi-material applications.

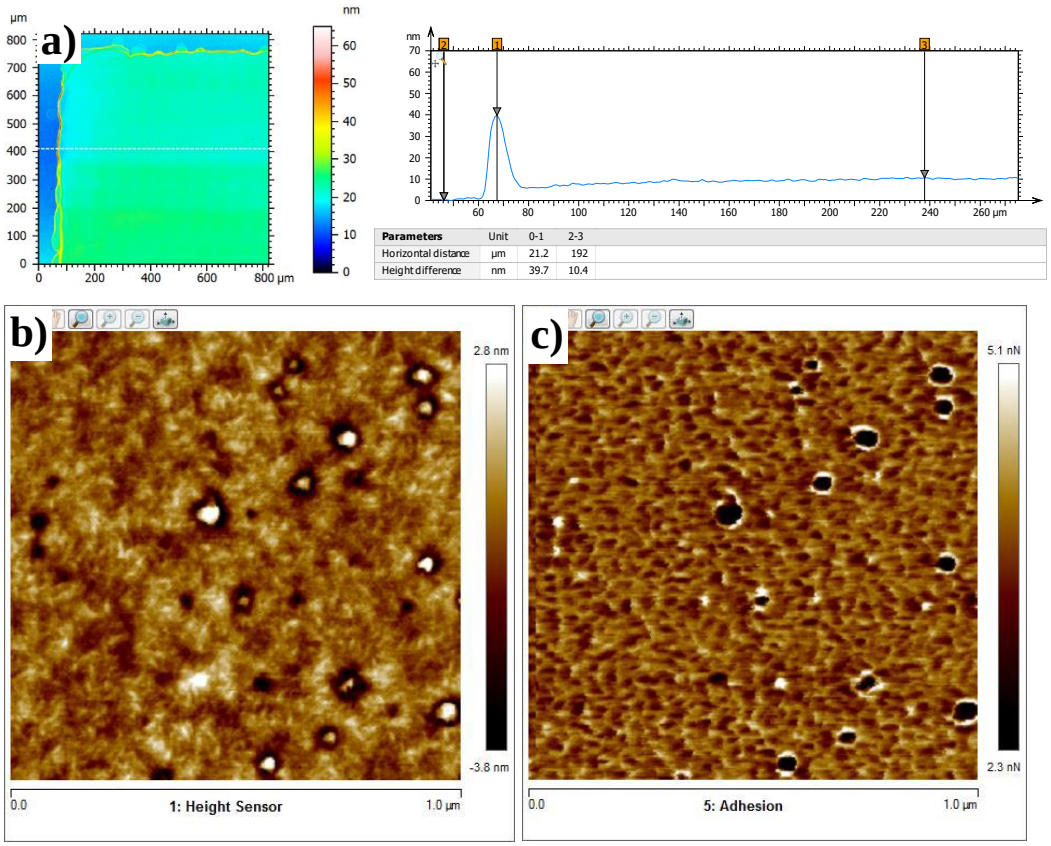


Figure 5.24 – (a) CSI with height profile and (b-c) AFM (height and adhesion map) of a 1-layer THV 1 wt% in MIBK film printed with a DS of 75 µm without the contaminations coming from the DMC. The AFM images were corrected with a 1st order flattening. The film was uniform and had a thickness of roughly 10 nm with few defects in the nanometre range due to artefacts present on the glass slide.

In section 5.2.7 it was shown that when multiple layers were printed with a DS of 75 µm unusual patterns started to appear. To further investigate the nature and origin of those unusual patterns, DS of 100-120-140-250 µm were used to print 1-2-5-10-20-50 layers (Figure 5.25). With a DS pf 100 µm (Figure 5.25a-e), at the second layer, bumps appeared between the positions of the jetted drops (Figure 5.25a). After 5 layers, the bumps increased in size (Figure 5.25b). After 10 layers they became smoother and "craters" with the shape of the drops started to appear (Figure 5.25c). After 20 layers, the bumps joined together forming a network and the craters became well defined (Figure 5.25d). After 50 layers, the pattern reversed, the craters were now higher than the space between the drops (Figure 5.25e).

With a DS of 120 µm (Figure 5.25f-l), a similar trend was observed but this time the drops were slightly further apart from each other and did not touch as much. Because of the increase in distance, after 5 layers there was no bump between the drops, instead, 4 smaller peaks/bumps appeared where the four neighbouring drops were touching (Figure 5.25g). This meant that the peaks/bumps were formed by the overlapping areas of the thicker contours (of each neighbouring drops) caused by the coffee ring effect. With a smaller drop spacing the four peaks would join in the exact centre between the four neighbouring drops, explaining the

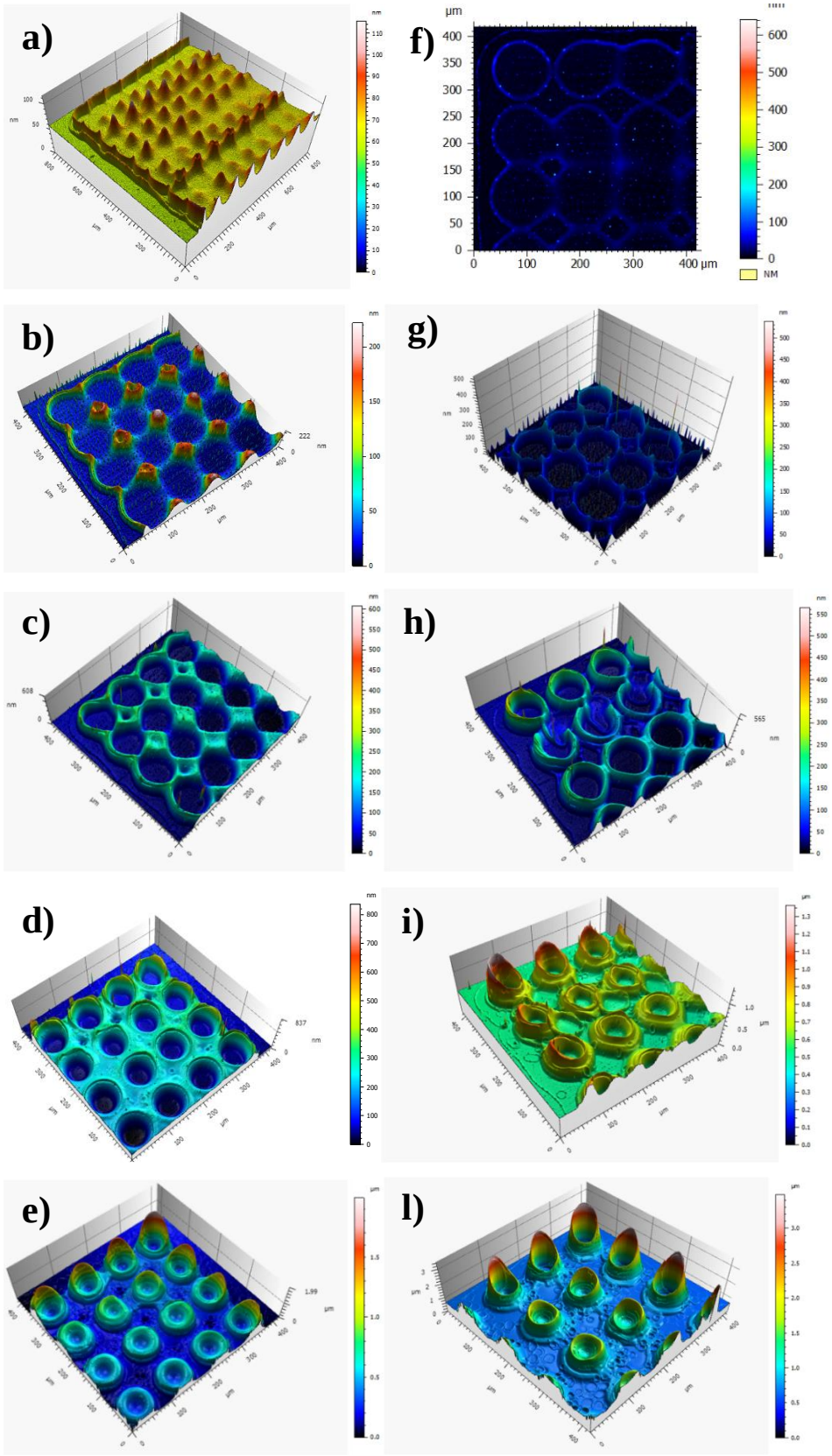


Figure 5.25 - CSI of printed THV 1 wt% in MIBK. DS of 100 µm on the left column and 120 µm on the right column. From top to bottom, the number of layers printed were 2-5-10-20-50.

formation of the bumps observed in previous experiments. After 10 layers with the DS of 120 µm, barely connected craters started to form (Figure 5.25h). The image suggested that, for at least one layer, the second nozzle/row did not jet properly and the drops were deposited in the wrong position. Nonetheless, this was an interesting observation as it showed that the craters could be modified and "open" afterwards, allowing for more complex patterns to be printed. After 20 and 50 layers, the craters were filled with more material (Figure 5.25i-l).

The 20 and 50 layers for both the 100 and 120 µm DS also showed that the first and second line of drops did not have a uniform contour thickness, instead a thicker contour was present in the side facing the outside of the print (Figure 5.25e-l). Namely, where there were no neighbouring drops. The lack of neighbouring drops caused the evaporation rate to be higher, intensifying the coffee ring effect in that direction. This effect is very noticeable in the first line of drops, both vertically and horizontally, and it is less pronounced on the second line of drops.

Figure 5.26 shows how big uniform patterns could be printed with this technique and how the patterns/topographies changed considerably by going from 5 layers (Figure 5.26a) to 20 layers (Figure 5.26b).

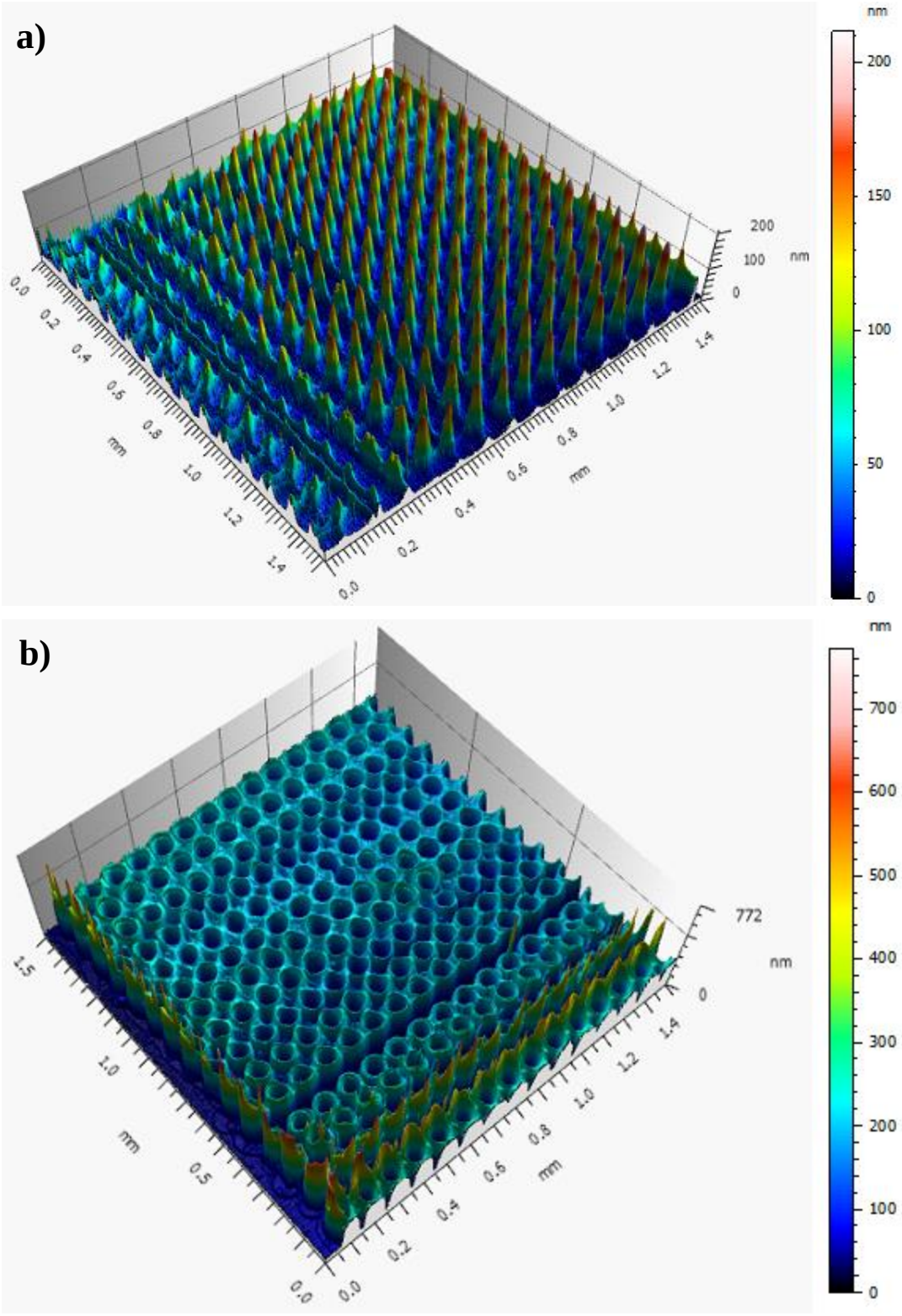


Figure 5.26 –CSI of printed THV 1 wt% in MIBK with a DS of 100 µm. The topography of the film mutated by going from (a) 5 layers to (b) 20 layers.

When drops were printed with a DS of 250 µm they were far enough from each other to be considered isolated drops. Figure 5.27a shows the thickness trend at the centre and edge/contour of the drops. The centre had a variable thickness but never went above 10 nm. It

seemed that each consecutive layer partially dissolved the THV present in the centre and "pushed" it to the edge (due to the coffee ring effect). The contour got exponentially thicker with each layer (Figure 5.27a). Figure 5.27b-c show the CSI for 10 and 50 layers printed with a DS of 250 µm.

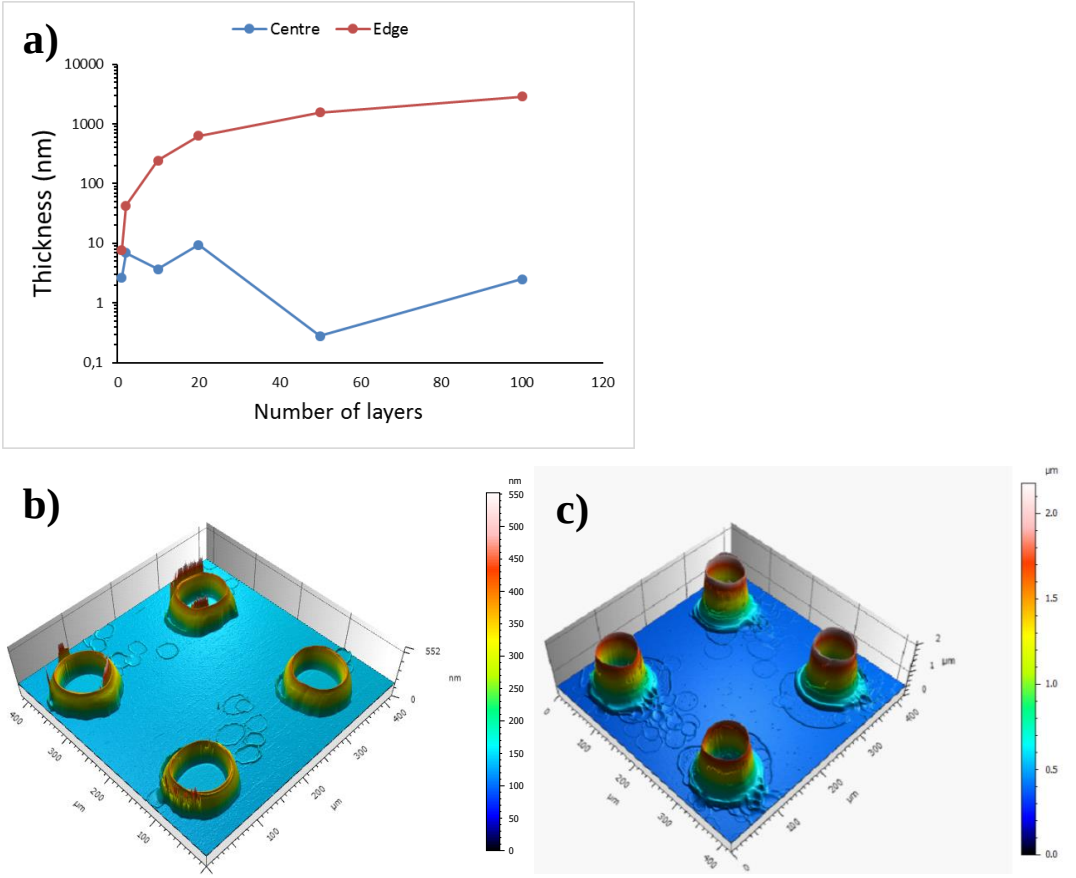


Figure 5.27 – (a) Plotted thickness of the centre and edge of isolated drops of THV 1 wt% in MIBK. (b) CSI of 10 layers and (c) 50 layers of isolated drops of THV 1 wt% in MIBK.

To further test the capabilities of this technique other patterns were printed on a THV coated glass slide. Nonetheless, the Dimatix software showed a limitation. The software was only capable of printing drops in a predetermined grid. For example, while printing with a DS of 90 µm with a print origin at the coordinates x = 0 µm and y = 0 µm, it was not possible to print the next layer in the gaps between the drops of the previous layer (Figure 5.28a). In fact, when the print origin was changed to x = 50 µm and y = 50 µm the actual print origin was shifted the closest multiple of the DS used (x = 90 µm and y = 90 µm in this case). This function is useful when the drops are required to overlap every time, but it does not allow for drops to be printed between previously printed drops. To by-pass this limitation two complementing patterns with empty gaps and twice the resolution (DS of 45 µm) were designed (Figure 5.28b). Because of the empty spaces, the actual distance between two drops was of 90 µm. The black and red patterns were printed at alternating layers. Figure 5.28b

shows 4 layers printed with this technique. After 100 layers, a uniform grid-like pattern was obtained (Figure 5.28c).

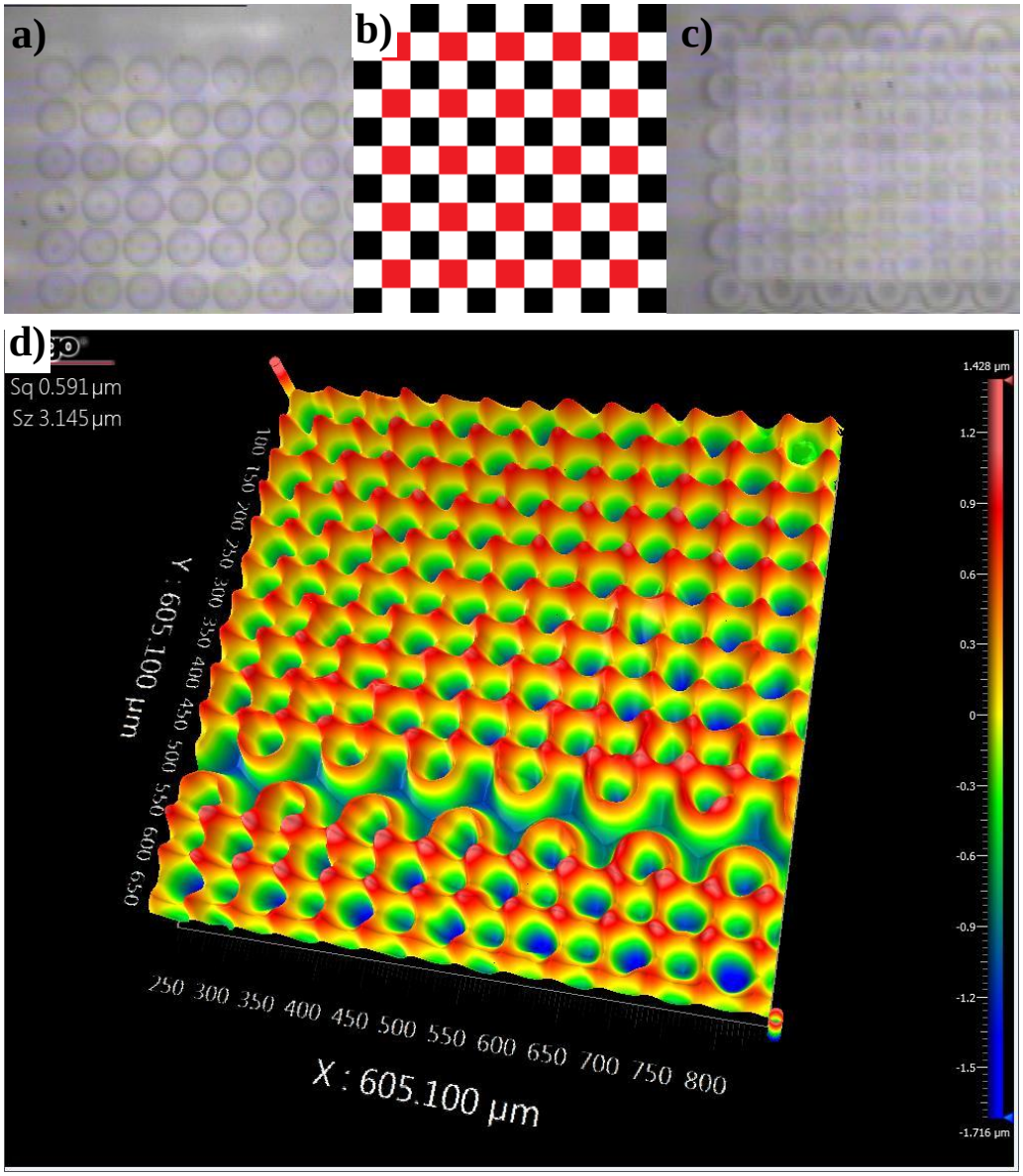


Figure 5.28 – Printed THV 1 wt% in MIBK on top of a THV coated glass slide. (a) Arrays of drops printed with a DS of 90 µm. (b) Checkboard design done by alternatively printing black and red patterns. The resolution was of 45 µm but because of the white gaps the actual DS was of 90 µm. (c) 4 layers printed with pattern (b). (d) CSI of two adjacent 100-layer parts printed with pattern (b).

Finally, a different design, a one-drop thick grid pattern was printed with a DS of 75 µm and with 1-2-5-10-20-50 layers (Figure 5.29). As previously seen, the first layer had spread more compared to the second layer (Figure 5.29a). The coffee ring effect caused the formation of long thick walls/edges. With each additional layer the thickness of the wall increased. 1-2-5-10-20-50 layers had a wall thickness of ~ 50-150-260-450-600 nm.

In summary, the coffee ring effect was likely responsible for the unusual patterns, suggesting that it may be avoided by countering the coffee ring effect (which could be done with several

techniques (section 2.3.3)). Nonetheless, different drop spacings and number of layers gave quite different repeatable patterns/topographies which may be useful for specific applications (e.g. increase or decrease contact angle, micro-reactors, composite materials). Even though the coffee ring effect has been exploited in several publications (to increase the resolution of the prints by allowing the formation of thinner tracks/features) [253]–[256], this might be the first time that these type of patterns are printed and reported in such detail.

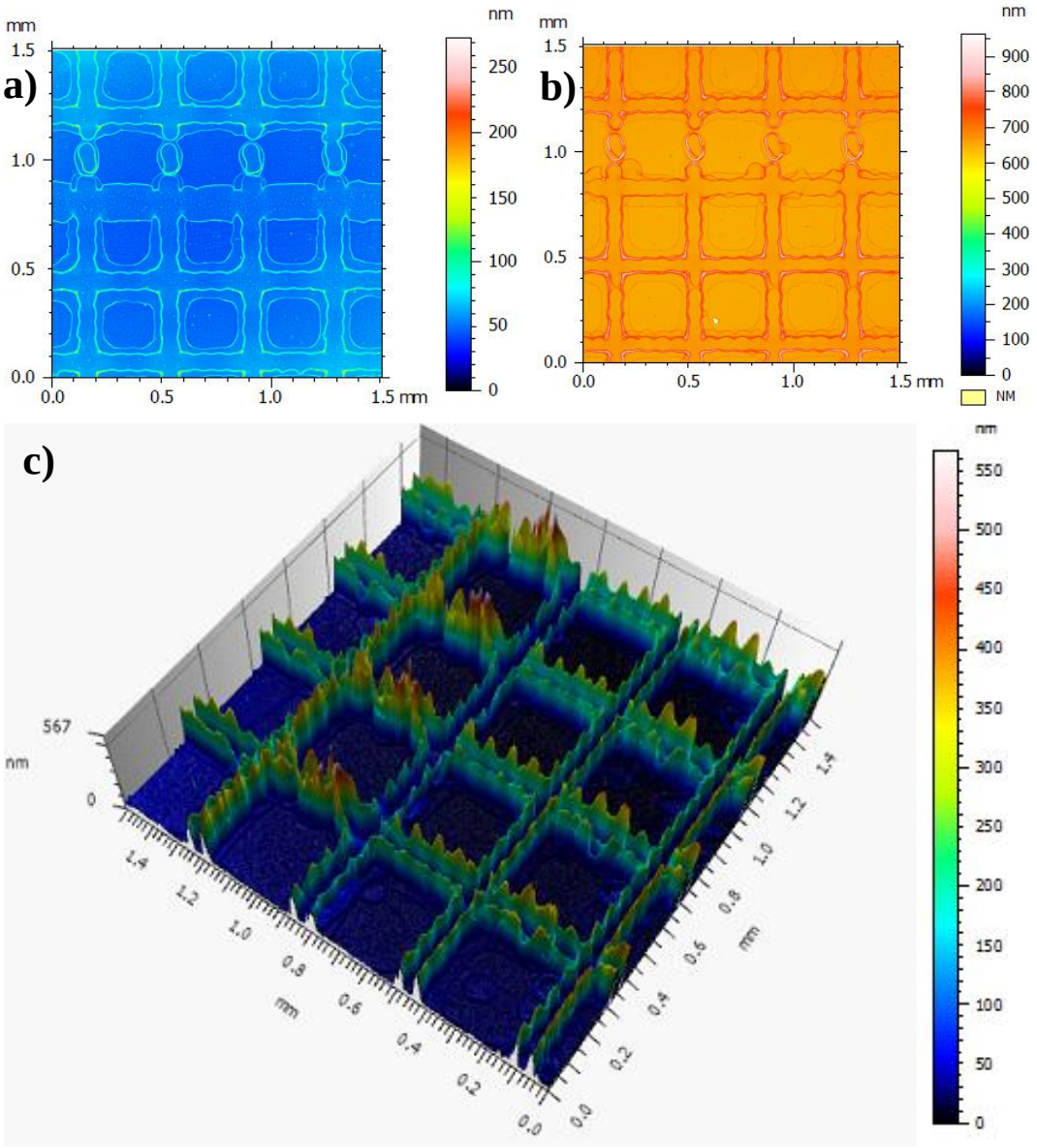


Figure 5.29 – CSI of one-drop-thick grid patterns printed with a DS of 75 µm with (a) 2 layers, (b) 5 layers, and (c) 10 layers.

5.2.8 Discussion – Jetting with the Dimatix

Six different low viscosity inks were tested: THV 1-3-5 wt% in MIBK, THV 1-2.5 wt% in 50-50 v% MIBK-DMAc, and THV 2 wt% in DMAc. It was not possible to form uniform films with all of the inks containing DMAc. MIBK showed a uniform film formation. DMAc had a

lower evaporation rate and higher surface tension than MIBK, which meant that, when mixed together, the Marangoni flow was not inwards but outwards, amplifying the coffee ring effect [100]. Nonetheless the DMAc-MIBK solution gave relatively satisfactory results at high substrate temperatures (50 °C) likely because of the quick evaporation of the solvents [102]. The solvent type did not affect the jetting behaviour, except for the clogging of the nozzles. Solvents with a high evaporation rate are more prone to form polymeric films at the nozzles surface which clog the nozzles [98].

Despite being in the printable region, THV 5 wt% in MIBK could not be jetted. This was due to the high molecular weight of the polymer (3.025×10^5 g/mol) which caused the ink to behave as a viscoelastic fluid. In fact, As calculated by Haque et al. [98], with the typical strain rates encountered in material jetting ($> 5x10^{-4}$ s^{-1}), polymers with a Mw higher than 5×10^4 g/mol were going to experience coil-stretch transitions. The printable concentration was found to be 1 wt%. THV 1 wt% in MIBK showed the formation of uniform single layer films with a strong coffee ring effect. The thickness of a 1-layer film was 10 nm (Figure 5.24a). As explained by Xue et al. [247], the demand of nanometre-thick films is in constant rise; MJ (and THV) could play an important role in it, especially in multi-material parts.

Multiple layers formed unusual patterns likely caused by the coffee ring effect (Figure 5.25). These patterns were studied at different drop spacings and number of layers. Unique, repeatable patterns, which may be useful for specific applications (e.g. increase or decrease contact angle, micro-reactors, composite materials) were possible. Even though the coffee ring effect has been exploited in several publications (to increase the resolution of the prints by allowing the formation of thinner tracks/features) [253]–[256], this might be the first time that these type of patterns are printed and reported in such detail.

Several issues and limitations of the Dimatix/ink such as different drop size for different nozzles and increase in drop size with printing time were also exposed. The DMC-11610 was proven to be non-compatible with the MIBK solvent and to produce a contamination which made the 1-layer films porous and caused the detachment of the films from the glass slide. The more chemically resistant DMCLCP-11610 did not produce any visible contamination.

Overall, uniform films of thickness down to 10 nm were produced. Porous films were also produced when the ink was contaminated or when the glass slide had superficial artefacts. Thicker films were more difficult to produce due to the coffee ring effect but the latter could be exploited to produce patterns/topographies that could be tailored by changing drop spacing and/or number of layers.

5.3 Jetting with the PICO Pµlse

5.3.1 Introduction

This section reports the experiments carried out to assess and optimise the jetting of high loading, high viscosity THV inks with the use of a Nordson EFD PICO Pµlse jet dispensing system (section 3.3.2). The work carried out is summarised in the following flowchart:

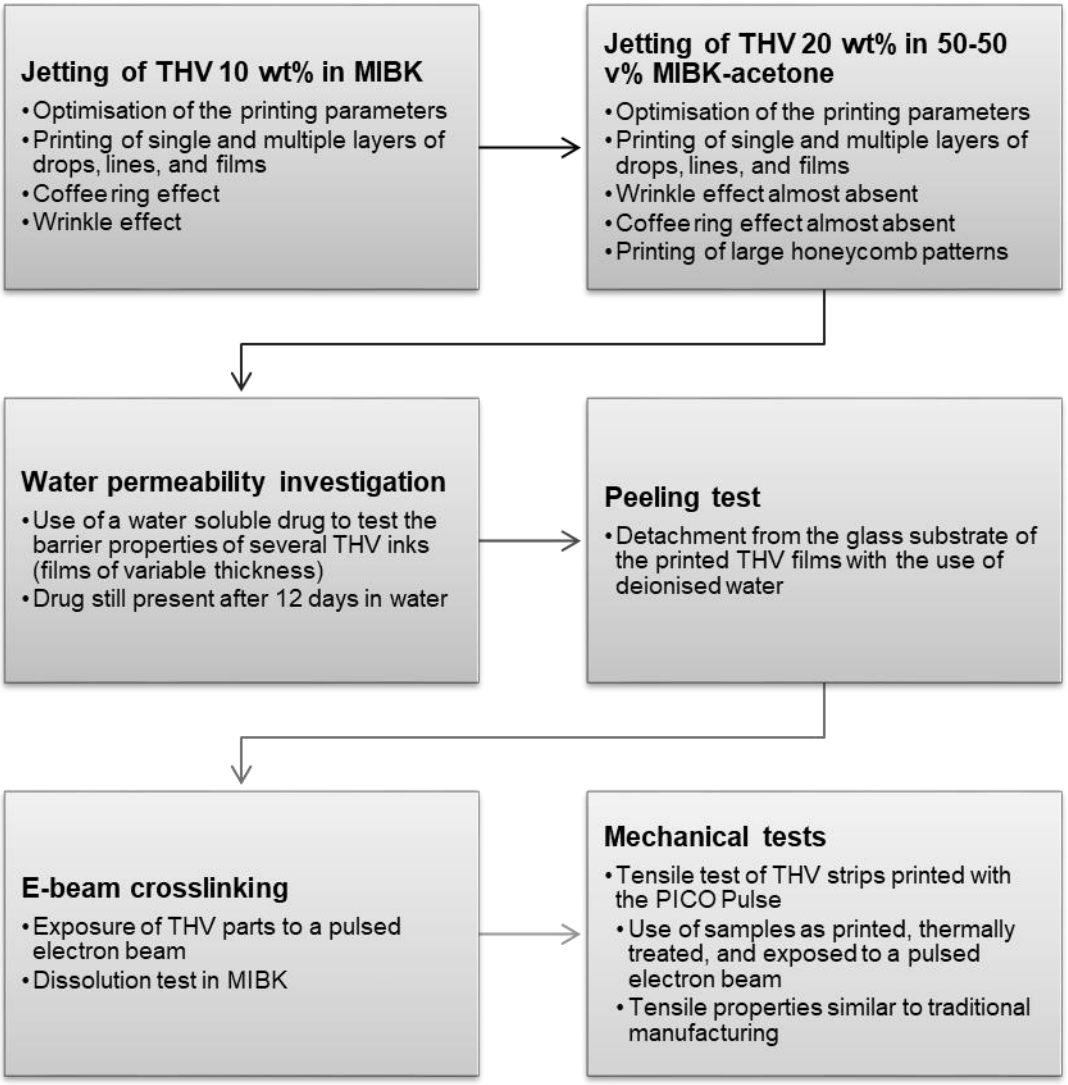


Figure 5.30 - Flow chart showing the development of the THV inks with the PICO Pulse

5.3.2 THV 10% MIBK

The THV 10 wt% in MIBK ink was printed with the PICO Pµlse because of its high viscosity. Several temperatures and pressures were tested to find the optimal printing parameters. At high temperatures and pressures (60 °C and 1-0.5 bar) splashing was observed (Figure 5.31). The drop size and line width were roughly 2404 µm and 2244 µm for pressures of 1 bar

(sometimes the drops were bigger than the microscope field of view) and 1968 ± 311 µm and 2085 ± 220 µm for pressures of 0.5 bar (Table 5.7).

Table 5.7 – Drop size and line width of printed THV 10 wt% in MIBK at different DS, pressure and nozzle temperature.

Pressure (bar)	Temperature (°C)	Drops Size (µm)	Stdev (µm)	Line width (µm)	Stdev (µm)
1	60	~2404	/	2244 (1000DS)	/
0.5	60	1968	311	2085 (1000DS)	220
0.25	45	763 (unstable size)	128	697 (1000DS)	210
0.25	30	568 (unstable print)	75	/	/
1	30	653 (1st layer)	27	620 (500DS)	49
		506 (2nd layer)	75	660 (400DS)	30
2	30	723	29	/	/

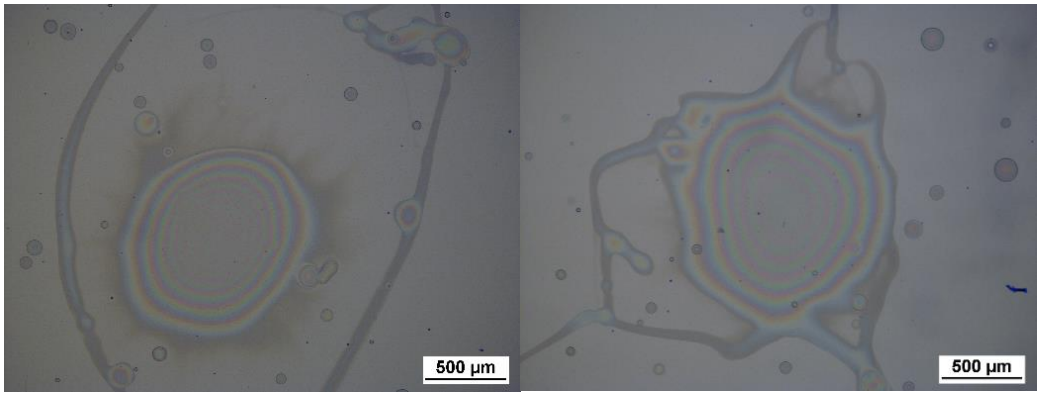


Figure 5.31 – Printed THV 10 wt% in MIBK with a nozzle temperature of 60 °C and a pressure of 0.5 bar

By decreasing the temperature and pressure to 45 °C and 0.25 bar the splashing was eliminated: the drops were smaller but also quite unstable (high standard deviation) (Figure 5.32). The drop size and line width were 763 ± 311 µm and 697 ± 210 µm. Films printed with a drop spacing of 500 µm were uniform (Figure 5.32c) with occasional holes because of the size instability of the drops (Figure 5.32d).

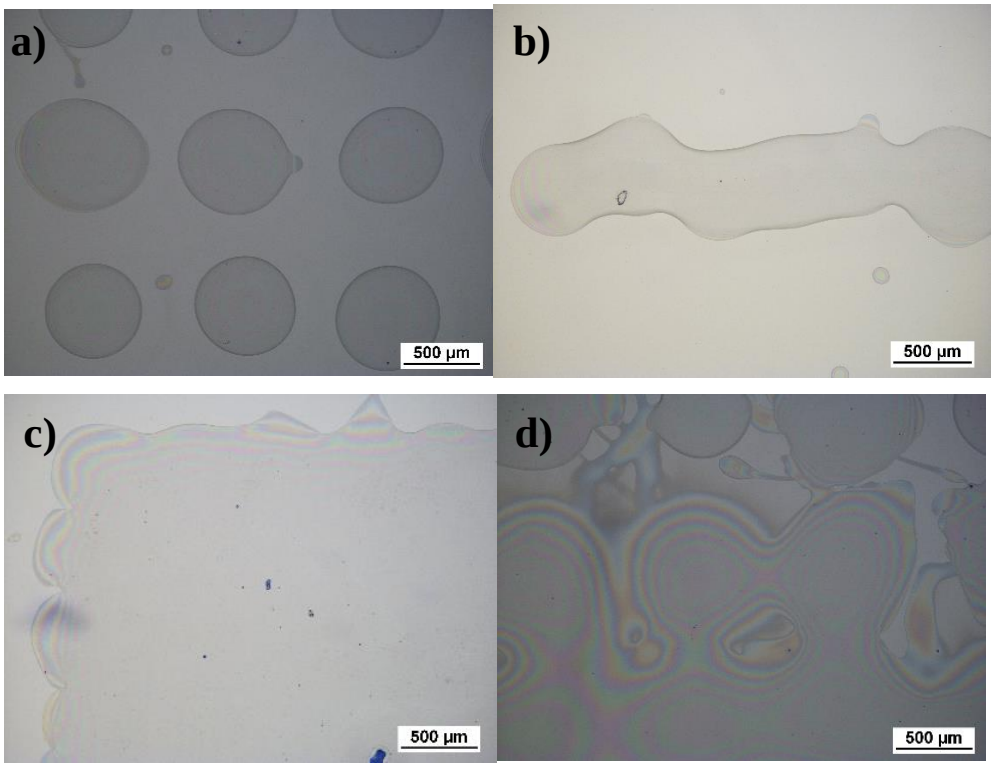


Figure 5.32 – Printed THV 10 wt% in MIBK with a nozzle temperature of 45 °C and pressure of 0.25 bar. (a) Array of drops. (b) Line printed with a DS of 500. (c-d) Film printed with a DS of 500. (d) Due to the unstable drop size the films had gaps in some positions.

By further decreasing the temperature to 30 °C while keeping the pressure at 0.25 bar, the printing became unstable and many drops were not jetted.

By increasing the pressure to 1 bar and keeping the temperature at 30 °C the printing became more consistent. Figure 5.33a and Figure 5.34 show the 1-2-3-layer drop. The drop size was 653 ± 27 µm for 1 layer and 506 ± 75 for 2 layers. The decrease in drop size on the second layer was consistent with what observed with the Dimatix and THV 1 wt% in MIBK (section 5.2.7). The 3-layer drop showed the presence of the wrinkle effect (Figure 5.34c). The coffee ring effect was still present but not as strongly as in THV 1 wt%. The thickness of the edge and centre of the drops is reported in Table 5.8. The edge of the drops was thicker due to coffee ring effect while the "shoulder" was the edge of the first drop as it had spread more and was still visible in the next layers. With the SEM none of the drops showed the presence of pores.

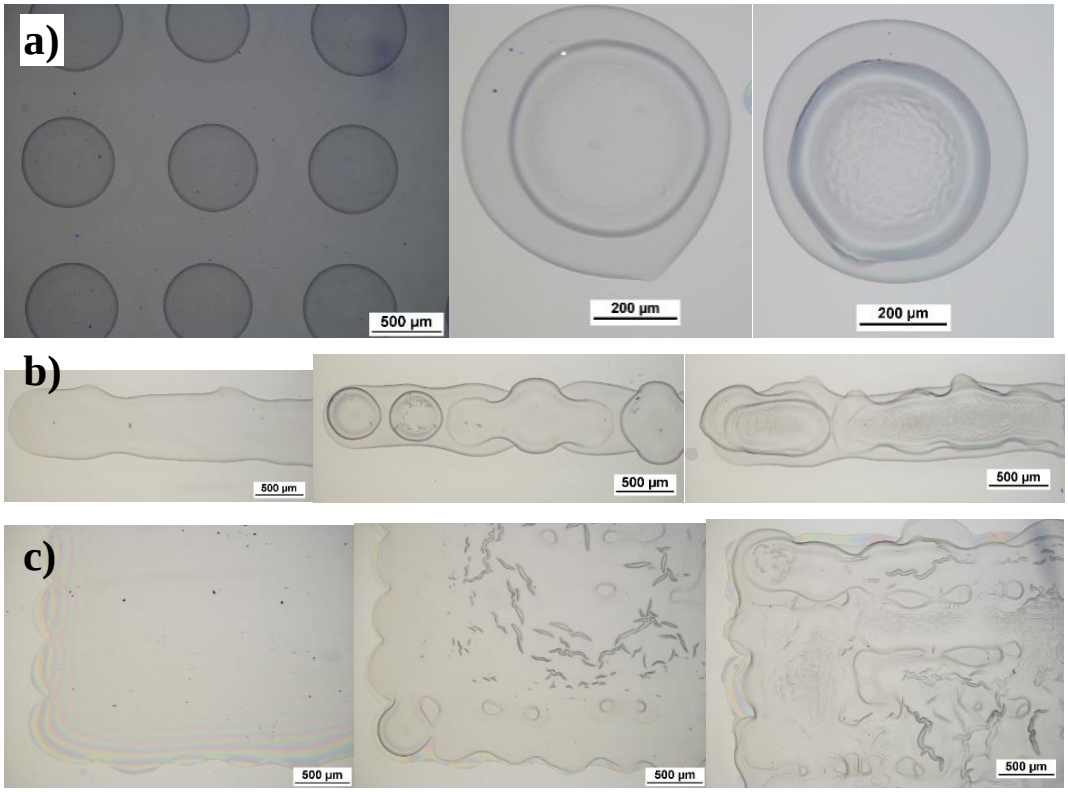


Figure 5.33 - Printed THV 10 wt% in MIBK with a nozzle temperature of 30 °C, pressure of 1 bar, and DS of 500 µm. 1-2-3-layer (from left to right) of (a) drops, (b) lines, (c) films done with.

Table 5.8 – Thickness of printed THV 10 wt% in MIBK with a nozzle temperature of 30 °C, pressure of 1 bar, and DS of 500 µm. The higher edge was due to the coffee ring effect while the "shoulder" was the edge of the first layer drop as it spreads more.

	Drop (µm)			Line (µm)		Film (µm)	
layers	**shoulder**	**edge**	**centre**	**edge**	**centre**	**edge**	**centre**
1	/	2.19	1.39	2.06	1.38	/	4
2	2.17	6.44	1.88	6.4	3	/	7.5
3	2.62	10.5	2.91	9.1	4	/	/

Figure 5.33b and Figure 5.35 show the 1-2-3-layer lines printed with a DS of 500 µm. The line width was 620 ± 49 µm. Because of the decrease in drop size when printing on top of THV, the second layer did not form properly, but it improved on the third layer (Figure 5.35). The wrinkle effect also appeared on the third layer. The thickness of the edge and centre of the lines are reported in Table 5.8. The use of a DS of 400 µm gave better results with more straight lines (Figure 5.36). The SEM analysis showed that no pore was present in the prints.

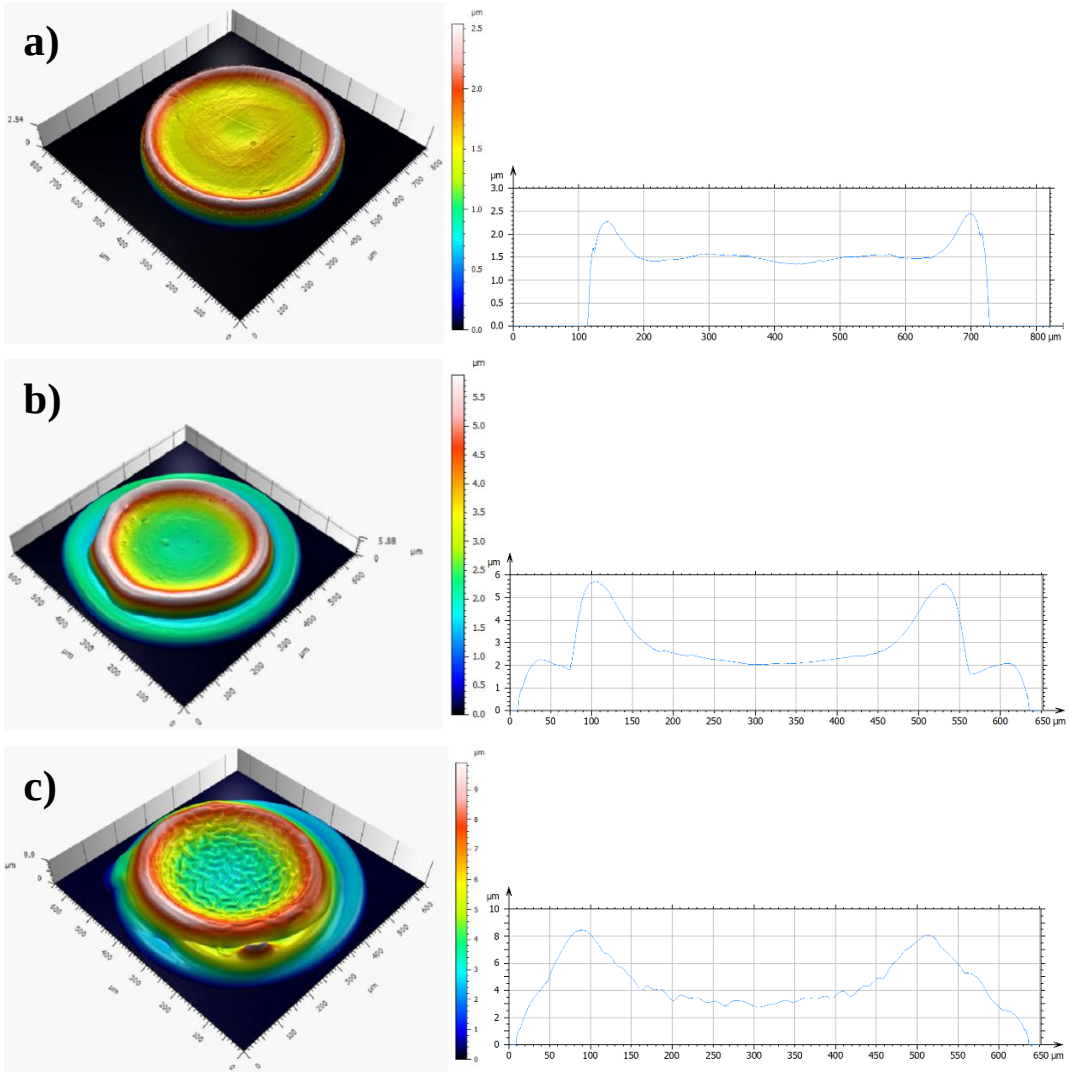


Figure 5.34 - Printed THV 10 wt% in MIBK with a nozzle temperature of 30 °C and pressure of 1 bar. CSI and profile of (a) 1-layer, (b) 2-layer, (c) 3-layer drop.

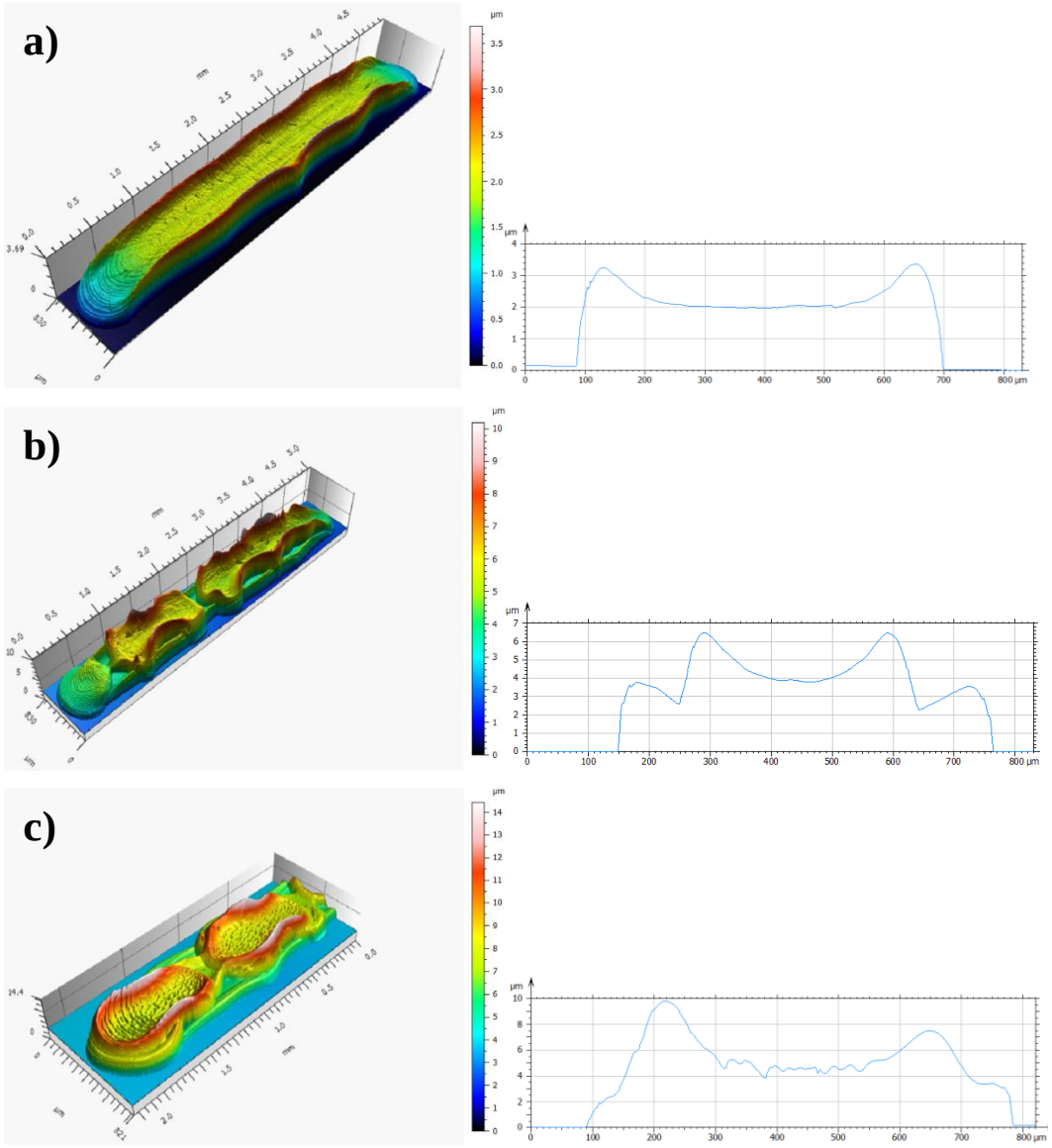


Figure 5.35 - Printed THV 10 wt% in MIBK with a nozzle temperature of 30 °C, pressure of 1 bar, and DS of 500 µm. CSI and profile of (a) 1-layer, (b) 2-layer, (c) 3-layer line.

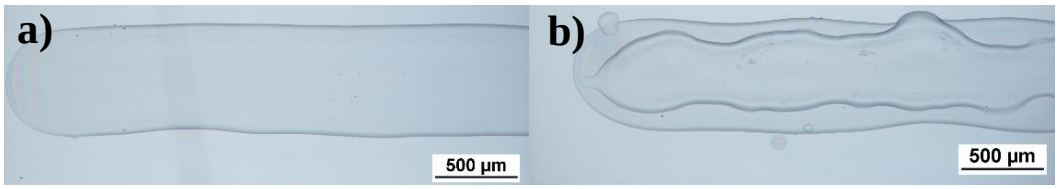


Figure 5.36 – (a) 1-layer and (b) 2-layer lines printed with THV 10 wt% in MIBK at a nozzle temperature of 30 °C, pressure of 1 bar, and DS of 400 µm.

Figure 5.33c and Figure 5.37 show the 1-2-3-layer films done with a DS of 500 µm. Because of the decrease in drop size when printing on top of THV, the second and third layer had gaps. The wrinkle effect also appeared on the second and third layer. The CSI showed the presence of receding lines (Figure 5.37a) suggesting that during evaporation the film edge did not pin

on the glass slide and kept slipping, thus avoiding the formation of the coffee ring. The thickness at the centre of the film roughly doubled with 2 layers (Table 5.8)

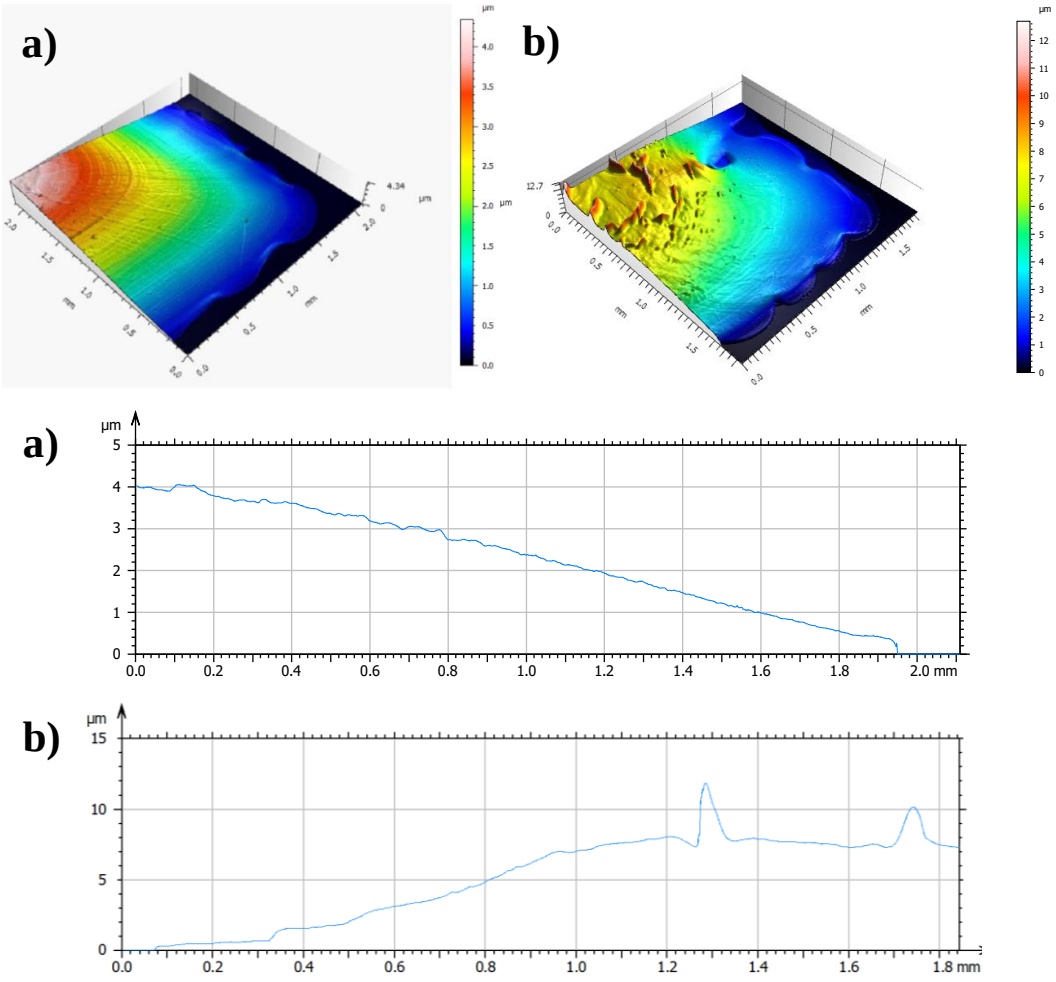


Figure 5.37 - Printed THV 10 wt% in MIBK with a nozzle temperature of 30 °C, pressure of 1 bar, and DS of 500 µm. CSI and profile of (a) 1- and (b) 2-layer films.

By increasing the pressure to 2 bar and keeping the temperature at 30 °C no significant change was observed, except for a bigger drop size (Table 5.7).

5.3.3 THV 20% MIBK-Acetone

To decrease the viscosity of the ink and increase the drying speed of the 20 wt% THV ink, 50-50 v% MIBK-acetone was used as solvent. Because of the high viscosity of the ink the Nordson EFD HPx High-Pressure Dispensing Tool was employed. This tool increases the used pressure by roughly seven times. For example, when a pressure of 2 bar was used, the actual pressure was 14 bar. The high pressure and fast evaporation rate caused the prints to have occasional bubbles of air trapped in it. The wrinkle effect was absent likely due to the presence of acetone in the ink formulation and high polymer loading (section 5.1.1.1). Nonetheless, it did appear on sporadic occasions.

Table 5.9 – Drop size and line width of printed THV 20% in 50-50 v% MIBK-Acetone at several pressures, temperatures and drop spacings (n = 15). The samples were printed with the Nordson EFD HPx High-Pressure Dispensing Tool.

Pressure (bar)	Temperature (°C)	Drops Size (µm)	Stdev (µm)	Line width (µm)	Stdev (µm)	Drop spacing (µm)
3	60	1142	59	/	/	500
2	60	910	98	/	/	500
2	50	1194	121	1329	30	800
2	50	1037	56	1153	45	1000

Several temperatures and pressures were investigated to pinpoint the optimal printing parameters. Higher temperatures and pressures make the ink easier to jet but can cause splashing. Lower temperatures and pressures decrease splashing but can make the jetting process less reliable (no drop ejection, lower drop accuracy). An increase in pressure can be compensated by a decrease in temperature and vice versa. Higher temperatures also lead to faster drying rates and possible nozzle clogging.

Printing at a nozzle temperature and pressure of 60 °C and 3 bar gave smooth drops, lines, and films but the edge definition was poor as a small degree of splashing was present (Figure 5.38b-c). The drop size was 1142 ± 59 µm (Table 5.9). Decreasing the pressure to 2 bar while keeping the temperature at 60 °C did not show any significant change but, as expected, the drop size slightly decreased to 910 ± 98 µm.

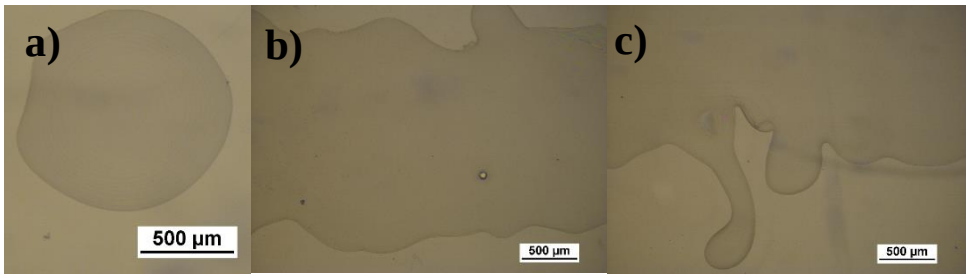


Figure 5.38 – Printed THV 20 wt% in 50-50 v% MIBK-acetone with a DS of 500 µm, nozzle temperature of 60 °C, and pressure of 2 bar. (a) Drop, (b) line, (c) film edge showing splashing.

By decreasing the temperature to 50 °C while using the same pressure (2 bar), the splashing decreased, the printing process was stable, and the edges of the printed patterns were well defined (Figure 5.39). The drop size was of 1037 ± 56 µm. Figure 5.39 shows drops, lines, and film printed with a DS of 1000 and 800 µm. A DS of 1000 µm was too big and gaps were seen while printing films (Figure 5.39a). Nonetheless, this could be useful if pores are desired. Further optimisation of the printing parameters may allow for a narrow pore size distribution to be produced. Figure 5.40 shows the 1-2-layer drops, lines, and film printed with a DS of 600 µm. The latter were also analysed with the CSI (Figure 5.41). The 1-2-layer drops and lines showed almost no coffee ring effect and visible slipping lines (Figure 5.41a-b). Figure

5.41c shows a film made of 1 and 2 layers with a smooth transition between the 1 layer and 2 layers side. The thicknesses of the drops, lines, and films are reported in Table 5.10. The thickness roughly increased linearly with the number of layers. SEM analysis showed that no pore was present in the prints.

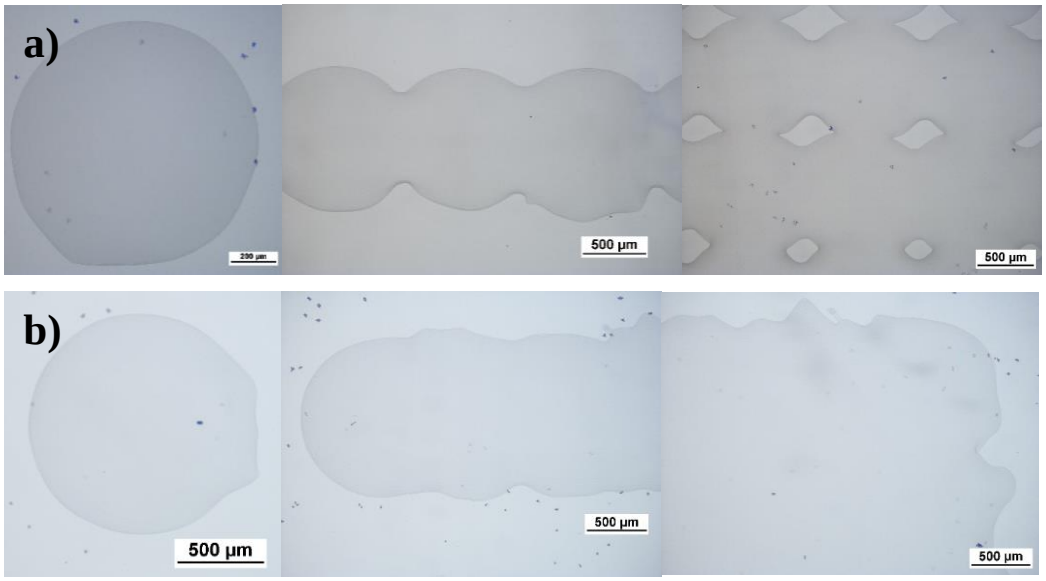


Figure 5.39 – Drops, lines, and films made with THV 20 wt% in 50-50 v% MIBK-acetone printed with a nozzle temperature of 50 °C, pressure of 2 bar, and DS of (a) 1000, (b) 800 µm. The scale bar is 500 µm except in the drop in (a) where it is 200 µm.

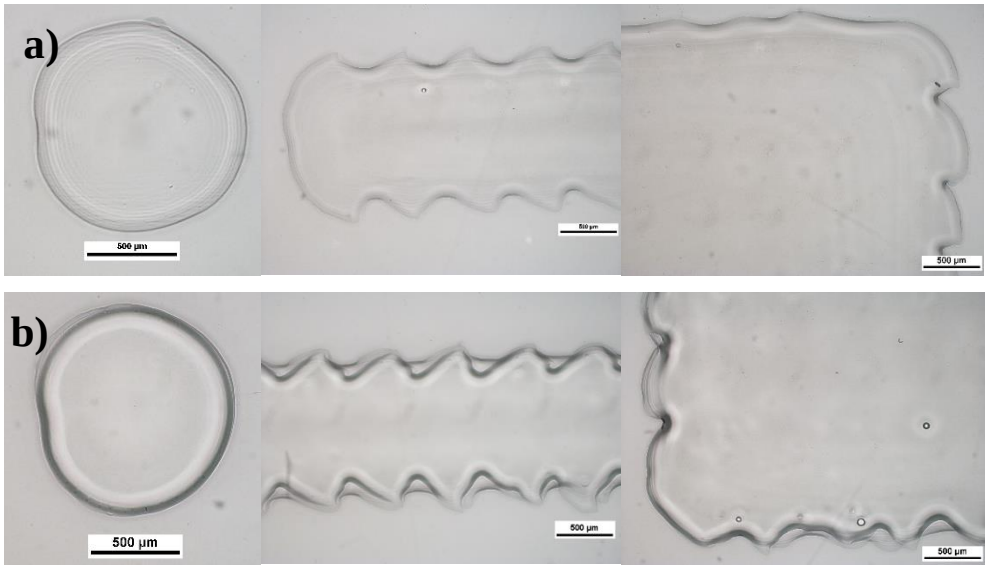


Figure 5.40 - Drops, lines, and films made with THV 20 wt% in 50-50 v% MIBK-acetone printed with a DS of 600 µm, nozzle temperature of 50 °C, and pressure of 2 bar. (a) 1 layer, (b) 2 layers. The scale bar is 500 µm.

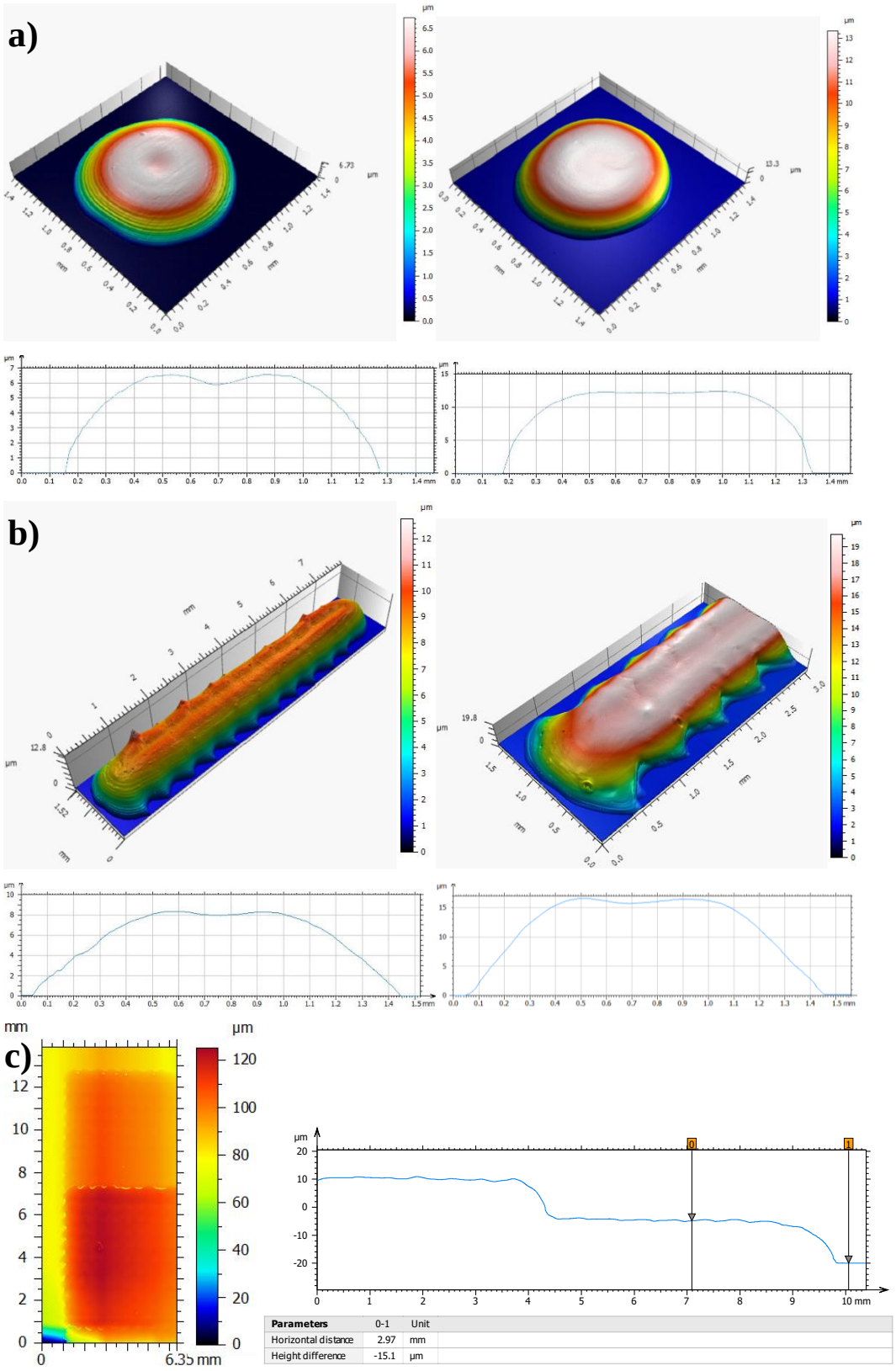


Figure 5.41 - Printed THV 20 wt% in 50-50 v% MIBK-acetone with a DS of 600 µm, nozzle temperature of 50 °C, and pressure of 2 bar. CSI and profile of 1-2-layer (a) drops, (b) lines, (c) films.

Table 5.10 - Thickness of printed THV 20 wt% in 50-50 v% MIBK-acetone with a nozzle temperature of 50 °C, pressure of 2 bar, and DS of 600 µm. The coffee ring effect was practically absent. The shoulder was also absent as the drop size seemed to not change on the second layer.

	Drop (µm)			Line (µm)		Film (µm)	
layers	**shoulder**	**edge**	**centre**	**edge**	**centre**	**edge**	**centre**
1	/	6.56	5.94	8.37	8.05	/	15.1
2	/	/	12.1	16.4	15.9	/	30.5
3	/	/	/	/	/	/	43
10	/	/	/	/	/	/	158

Nozzle temperatures down to 30 °C (at 2 bar) were also utilised but the printing process was not completely repeatable. It was later discovered that the ink/printhead needed a "conditioning" at the start of the day to be able to print at low temperatures. The conditioning consisted of printing few films at high temperatures and pressures such as 60 °C and 3 bar. This was probably necessary to properly fill the printhead with ink during the first use.

To test the capabilities of the printer and ink to produce complex patterns, glass slides were fully covered with honeycomb patterns (Figure 5.42). The parameters used were: DS of 600 µm, nozzle temperature of 50 °C, and pressure of 2 bar. The 1-layer honeycomb had an edge and central thickness of 15 and 14.2 µm, respectively. The 4-layer honeycomb had an edge and central thickness of 64 and 41.8 µm, respectively. The coffee ring was more pronounced after 4 layers. Overall, the prints showed good stability and accuracy.

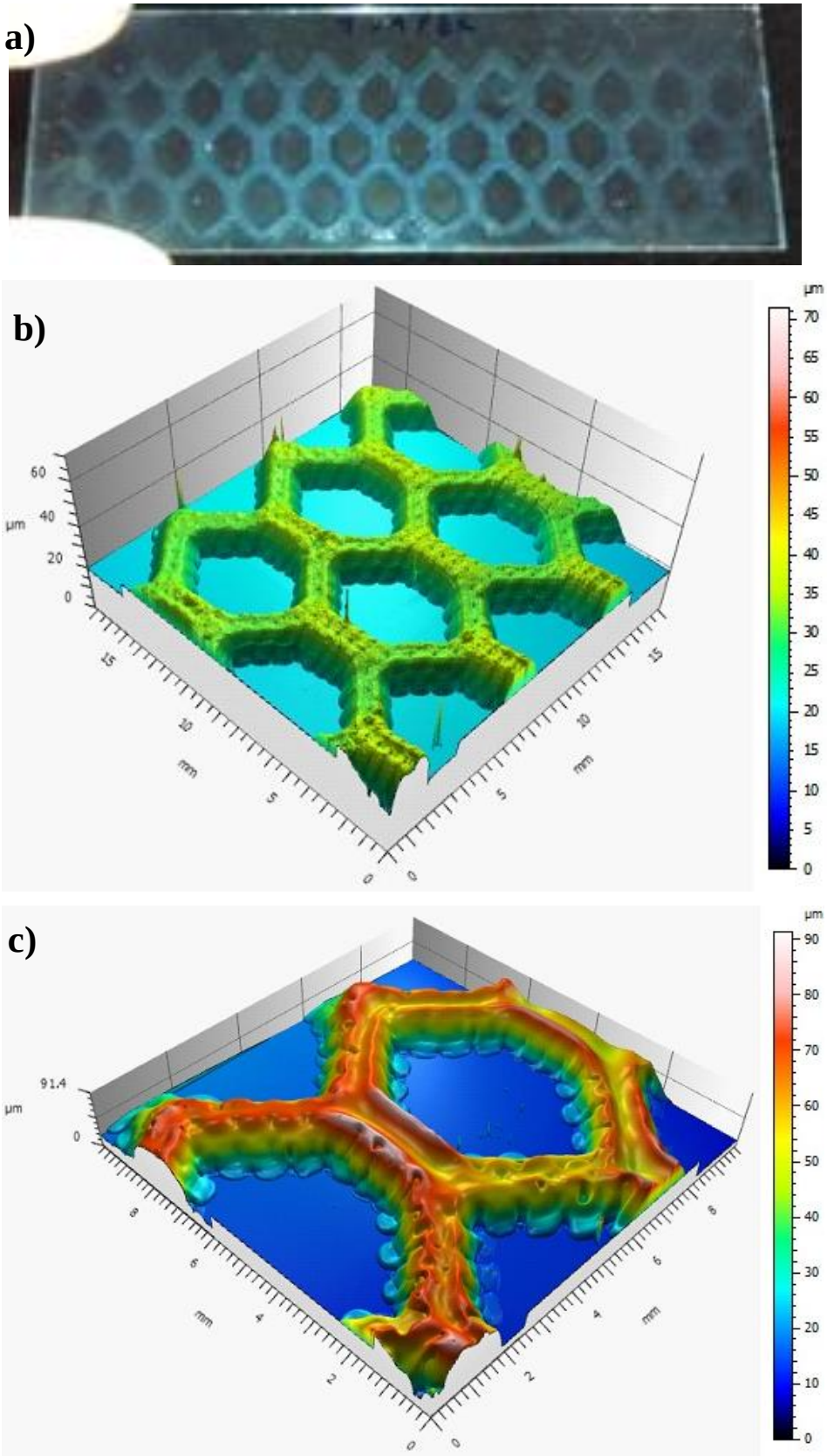


Figure 5.42 - Printed honeycomb made of THV 20 wt% in 50-50 v% MIBK-acetone with a DS of 600 µm, nozzle temperature of 50 °C, and pressure of 2 bar. (a) Picture and (b) CSI of a 1-layer honeycomb and (b) CSI of a 4-layer honeycomb.

5.3.4 Discussion – Jetting with the PICO Pµlse

THV 10 wt% in MIBK was jetted with a PICO Pµlse at several nozzle temperatures, pressures, and drop spacings. The parameters were optimised to decrease splashing and obtain drops of consistent shape and dimensions [81]. The best results, among the experiments carried out, were given by a nozzle temperature of 30 °C, pressure of 1 bar, and drop spacings < 500 µm. The coffee ring effect was still present for drops and lines but not as badly as in the THV 1 wt% in MIBK. The films did not show the coffee ring effect, instead, the CSI showed a clear slipping pattern likely due to the non-pinning of the film on the glass slide [107]. The wrinkle effect was also often present for the 2- and 3-layer prints. Overall, the prints showed good uniformity, accuracy, and no porosity. The thickness of a 1-layer film was 4 µm (Table 5.8).
THV 20 wt% in 50-50 v% MIBK-acetone was jetted with a PICO Pµlse at several nozzle temperatures, pressures, and drop spacings. The parameters were optimised to decrease splashing and obtain drops of consistent shape and dimensions. The best results, among the experiments carried out, were given by a nozzle temperature of 50 °C, pressure of 2 bar (while using the HPx High-Pressure Dispensing Tool), and drop spacing of 600 µm. The coffee ring effect was mostly absent and the CSI showed a clear slipping pattern likely due to the non-pinning of the film on glass slide. The wrinkle effect was also mostly absent. Complex big patterns such as honeycombs were printed successfully. Overall, the prints showed good uniformity, accuracy and no porosity. The thickness of a 1-layer film was 15.1 µm (Table 5.10).
Overall THV was successfully printed with the PICO Pµlse at different concentration and processing parameters. High level of complexity and accuracy were achieved. THV showed to be very versatile with the option to be printed at low and high polymer loadings with different solvents. This demonstrated that further tailoring and optimisations would be possible if desired, opening the use of THV into several applications such as nanometre thick protective layer [162], [166], [167], porous membrane, drug delivery system [168], and microfluidic device [169]–[172].

5.4 Water permeability investigation

5.4.1 Introduction

THV is usually used as a barrier layer and because of its biocompatibility it could also be used in medical implants. US20080118541A1 patent [168] stated that fluoropolymers are widely used in medical applications thanks to their outstanding biocompatibility and low drug permeability. Unlike most fluoropolymers, THV has a low crystallinity which allows for a faster drug release and higher elongation at break (lower tendency for the film to crack) [168]. Because of these properties, Pacetti [168] patented the use of THV in medical devices such as coronary stents. This section investigates the uniformity, barrier properties and water permeability of the ink jetted THV films.

5.4.2 Results

To assess the barrier proprieties and water permeability of the printed THV, layers of THV were printed with both Dimatix and PICO Pµlse on top of a water-soluble drug (thiamine HCl, also known as vitamin B1) already used in another project in our lab by Hatim Cader.

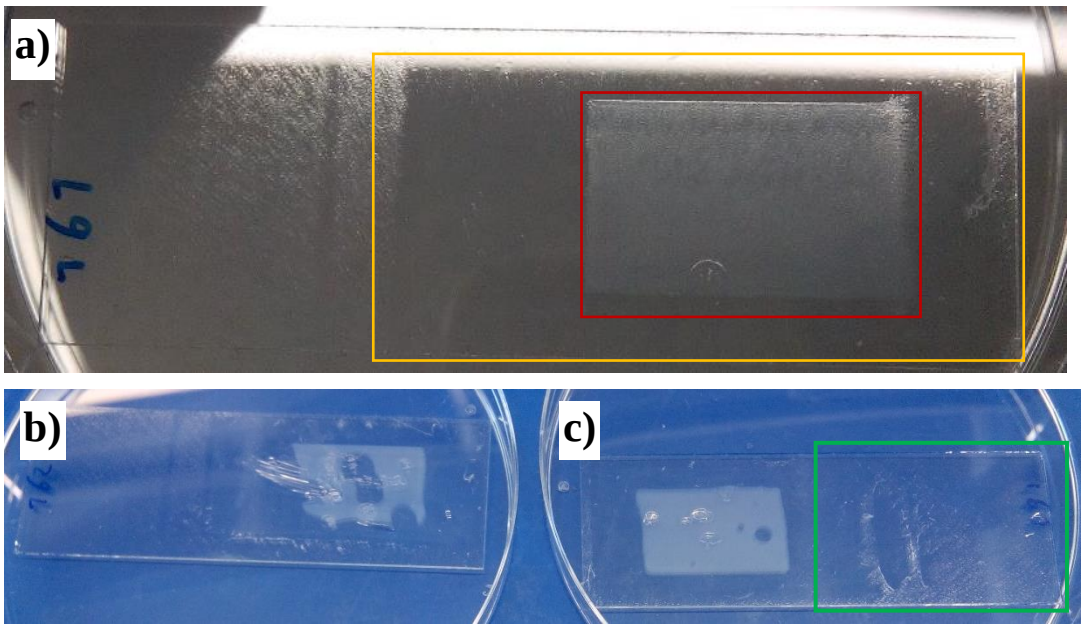


Figure 5.43 – THV 10 wt% in MIBK was used to coat a water-soluble drug (opaque area) printed on a glass slide. Sample (a) before and (b) after being submerged in deionised water. The red box in (a) shows the drug while the orange box shows the protective THV layer. (c) Sample that was only partially submerged in water, the green box shows the part submerged in water.

In a first step, the Dimatix was used to print a single layer of a 15 x 25 mm pattern of water-soluble drug on top of a glass slide. In a second step, the PICO Pµlse was used to print a single layer of the THV 10 wt% ink in MIBK with a nozzle temperature of 90 °C and pressure of 0.5 bar (Figure 5.43). The high nozzle temperature was chosen to decrease the drying time of the

jetted layer and minimise possible interactions with the drug. To compensate for the increase in temperature and reduce splashing, the pressure was decreased to 0.5 bar. Two samples were produced. The first sample was submerged in deionised water for 3 hours (Figure 5.43b). The second sample was partially submerged in deionised water for 3 hours in a sealed glass jar (Figure 5.43c, the green box delimitate area submerged in water).

Without a protective layer/coating the drug would dissolve in water in few seconds. In the first sample the majority of the drug was still present after 3 hours in water (Figure 5.43b). The dissolution mainly happened on the left side of the sample suggesting that the water was reaching the drug by infiltrating between the THV film and glass slide and not by diffusing through the THV film. The drug also dissolved in the centre of the film with circular patterns suggesting that the film had defects that allowed the access of water. On the second sample, similar dissolution patterns were observed (Figure 5.43c and Figure 5.44). The edges presented a smaller degree of dissolution and circular dissolution patterns were present in the centre of the film in correspondence of few film defects. Figure 5.44a was taken with an optical microscope with cross polarised light and shows the edge of the drug pattern below the protective THV film. The crystal structure of the drug was visible. Right after dissolution (Figure 5.44b) the edge was less defined and the crystal grains were smaller near the edge. After few days the sample was fully dry and "spikes" of crystal drug appeared at the edges (were the drug was dissolved) (Figure 5.44c). Figure 5.44d-e show a circular dissolved pattern at the centre of the drug pattern showing an artefact at the exact centre. After few days spikes of crystal drug appeared where the drug was dissolved (Figure 5.44f). These results suggested that the protective THV film (< 10 µm in thickness) was mainly uniform, devoid of pores but with occasional defects. Furthermore, water seemed to infiltrate between the glass slide-THV interface due to the poor bonding between the two interfaces.

To avoid the glass-THV interface issue the drug was printed on a THV coated glass slide to form a sandwich structure. However, this solution came with another issue – the drug did not wet the polymer and the formation of a film was not possible (Figure 5.45). The drug formed several agglomerations whose size depended on the drop spacing utilised during the printing of the drug. Smaller drop spacing formed fewer but bigger agglomerations. The drop spacings used were 20-10-5 µm with a nozzle temperature of 28 °C. A single layer of an array of 12 x 3 squares of 3 x 3 mm each was printed on each glass slide. The advantage of having many isolated agglomerations of drug was that each glass slide had over 1000 agglomerates which were independent from each other, meaning that a defect in the protective film would only affect one agglomeration and not the entire sample. The overlying protective films were printed with inks made of 1-10-20 wt% THV.

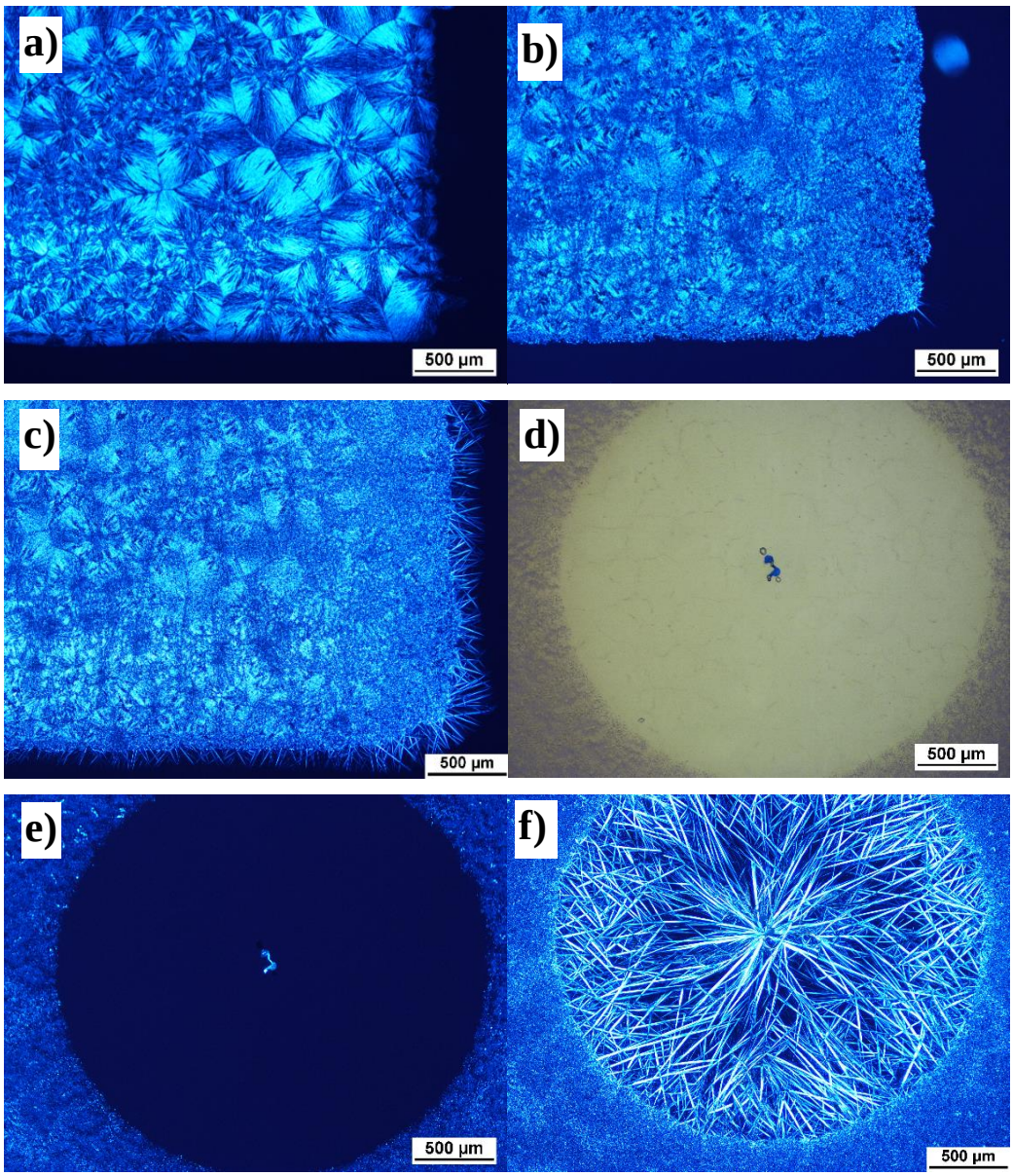


Figure 5.44 – Optical microscope images with cross polarised light of the sample partially submerged in water. Edge of the drug (below a THV coating) showing the crystal structure of the drug (a) before and (b) right after being partially submerged in water, and (c) few days after being left to dry. (d) Dissolved drug due to a defect in the protective THV coating in the centre of the film (e-f) right after being partially submerged in water, and (c) few days after being left to dry.

1-2-10-20-50 layers of protective film were printed with the Dimatix with a THV 1 wt% in MIBK ink. The samples were left in deionised water for 3 hours and all of the agglomeration dissolved. Figure 5.45a-b and Figure 5.45c-d show the polarised and non-polarised light images of the samples with 50 layers of THV 1 wt% in MIBK ink before and after dissolution. The failure of the film could be due its low thickness (< 500 nm) and presence of contaminations from the Dimatix cartridge (section 5.2.7.1) which caused the formation of a porous layer. Figure 5.45e shows the presence of several holes in the THV coating in the location of what was a drug agglomeration.

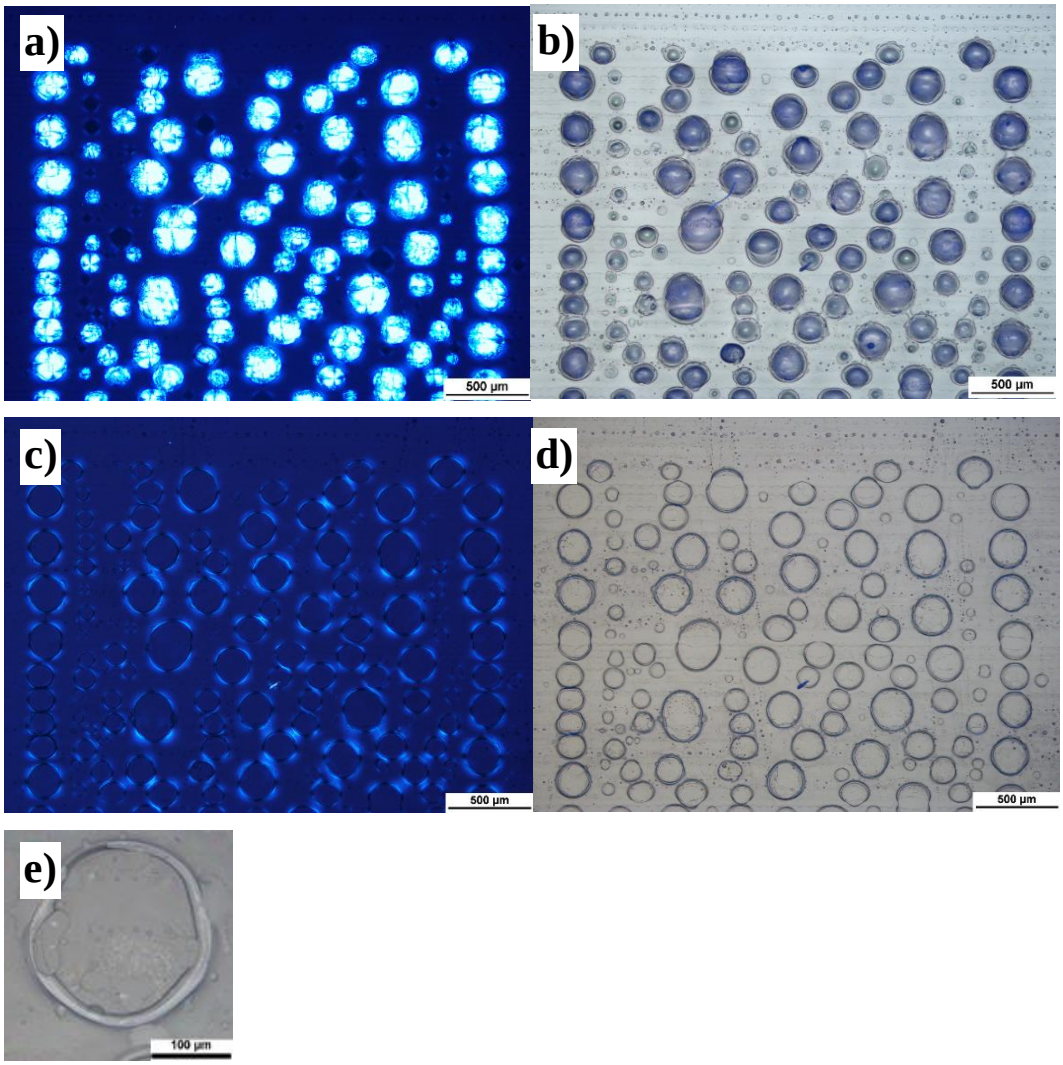


Figure 5.45 – Optical microscope images of a water-soluble drug printed with the Dimatix on top of a THV coated glass slide and covered with 50 layers of a protective THV film. The layers were printed with a THV 1 wt% in MIBK ink. Sample (a-b) before and (b-c-e) after dissolution in water, the bright/blue spheres are drug crystals. (e) Visible holes in the protective THV layer. The drug was dissolved away to a non-uniform protective THV layer.

Next, 1-2-3 layers of protective film were printed with the PICO Pµlse with a 10 wt% THV solution in MIBK with a nozzle temperature of 40 °C, a pressure of 2 bar and a DS of 350 µm. A quite strong wrinkle effect was visible. All of the protective films (1-2-3 layers) were effective in protecting the drug for 3 hours in deionised water except in the area affected by the wrinkle effect as showed in Figure 5.47. Nonetheless, some of the drug that seemed gone started to reappear after some time. Figure 5.46 show the drug crystallisation process after 35-40-48-75 minutes from being removed from water. The drug should have been confined in the bubbles/pockets of agglomerations but the image after 75 minutes shows how the drug crystals diffused inside of the wrinkle effect (still below the THV protective layer) (Figure 5.46d).

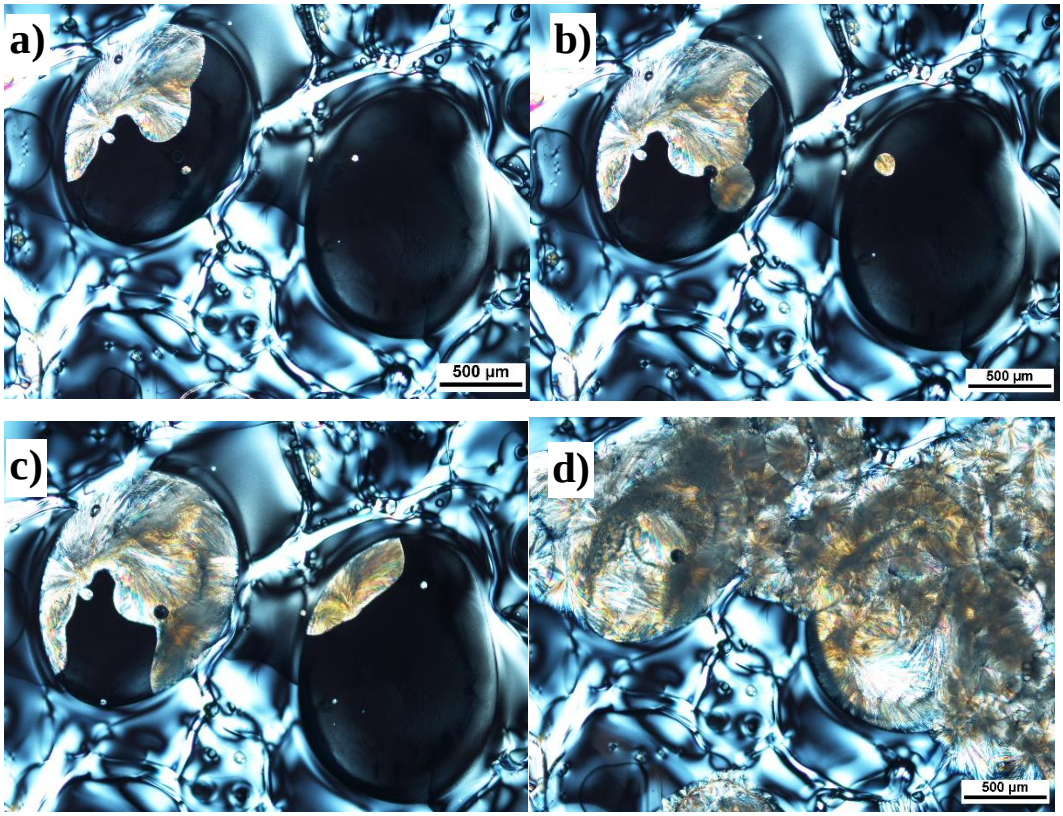


Figure 5.46 - Crystallisation process of the drug after (a) 35, (b) 40, (c) 48, and (d) 75 minutes from being removed from the water. The protective layer was made with 2 layers of THV 10 wt%.

1-2-3 layers of protective film were printed with the PICO Pµlse with a 20 wt% THV solution in 50-50 v% MIBK-acetone with a nozzle temperature of 50 °C, a pressure of 2 bar (using the Nordson EFD HPx High-Pressure Dispensing Tool) and a DS of 600 µm. Similarly to the previous test, a less intense but still present wrinkle effect was observed. All of the protective films (1-2-3 layers) were effective in protecting the drug for 6 hours in deionised water despite the presence of the wrinkle effect (Figure 5.47d). The wrinkle effect was quite unusual as at that time it had never been observed for films printed with the 20 wt% solution. Its presence in this test was traced back to the fact that the underlying THV film was completely dry at the time the ink was jetted to form the protective layer. Further experiments showed that the wrinkle effect was in fact more prone to happen when the previous THV layer was completely dry and less often observed when printing with no delay or few minutes of delay between layers. The thickness of the underlying THV layer may also have had an effect. Thicker coatings were more prone to wrinkle.

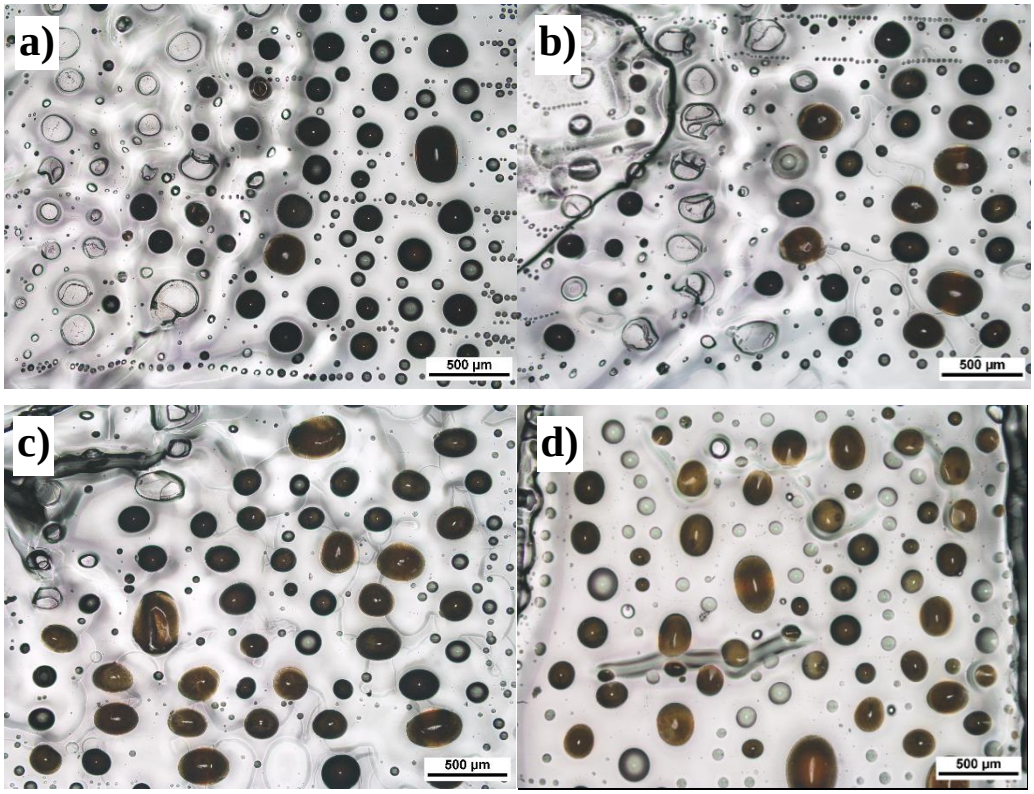


Figure 5.47 – Optical microscope images of a water soluble drug printed with the Dimatix on top of a THV coated glass slide and covered with (a) 1, (b) 2, (c) 3 layers of protective THV film (THV 10 wt% in MIBK ink). After 3 hours in deionised water, the drug only dissolved in the portions of film disturbed by the wrinkle effect (left side). (d) Protective layer made of 1 layer of THV 20 wt% in 50-50 v% MIBK-acetone, the wrinkle effect was present but no visible dissolution happened after 6 hours in water.

Finally, the sample coated with 1-2-3 layers of THV 20 wt% were left in deionised water for 12 days in a sealed glass jar. The entire glass slide was covered in drug drops and protective layers and only half of the glass slide was submerged in water. After 12 days all the drug agglomerations seemed gone, even those not submerged in water. When several "bubbles" of drug were punctured with the tip of a needle, a fluid spilled out (Figure 5.48a). After drying, crystals were visible, demonstrating that water got inside the bubble and that a degree of drug was still present (Figure 5.48b-c). It took roughly 22 days for the film to be dry enough for the drug to reappear/crystallise (Figure 5.49). A time much longer than that was seen for a thinner protective THV layer done with 2 layers of THV 10 wt% (Figure 5.46). The time release of drug in water was not measured in these tests. Nonetheless, it was likely that the drug was being released in water very slowly. Further studies are necessary to assess the drug release capabilities of THV.

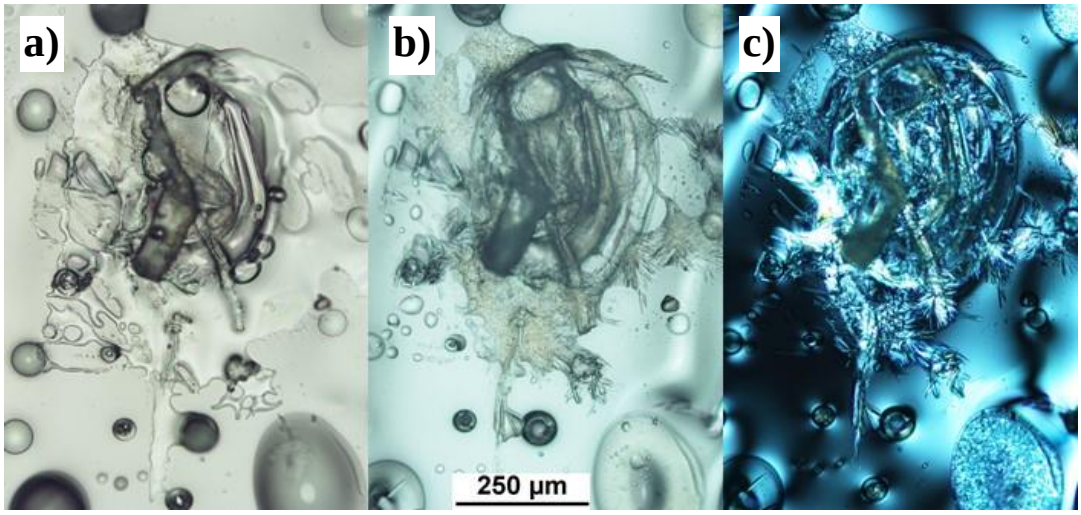


Figure 5.48 – Popped agglomeration/bubble of drug after being submerged in deionised water for 12 days. After popping the bubble, (a) a fluid came out of it and after the fluid dried (b-c) crystals were visible. This demonstrated that water got inside the bubble and that a degree of drug was still present.

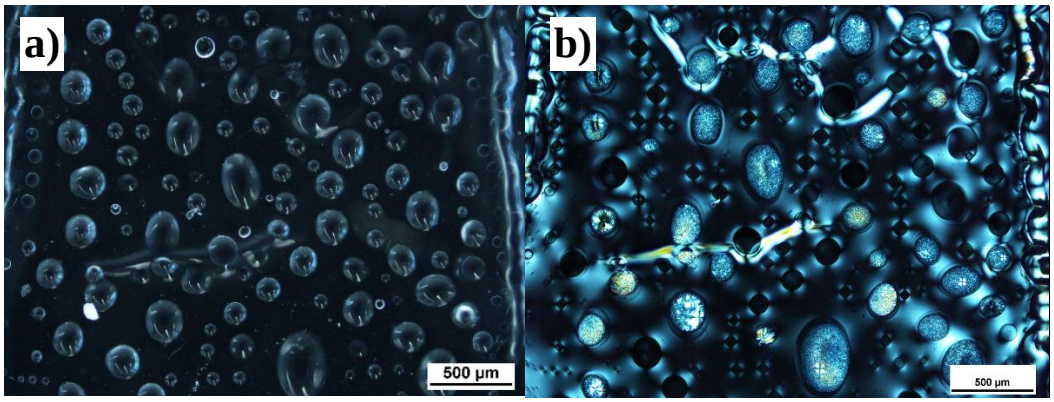


Figure 5.49- Drug covered with 1 layer of THV 20 wt% in 50-50 v% MIBK-acetone. (a) Sample after being submerged in water for 12 days, no drug crystals were visible. (b) After 22 days from being removed from the water, the majority of the drug agglomeration crystallised.

5.4.3 Discussion

The THV films also showed promising results in encapsulating a water-soluble drug. Unlike most fluoropolymers, THV has a low crystallinity which allows for a faster drug release and higher elongation at break (lower tendency for the film to crack). Because of these properties, Pacetti [168] patented the use of THV in medical devices such as coronary stents. In this section, a water-soluble drug was used to demonstrate the uniformity and lack of pores in the THV films. The drug was initially jetted on a glass slide and then covered with a THV layer. The drug only partially dissolved due to sporadic defects in the film and infiltration of water between the glass-THV interface. To avoid this interface issue, the drug was sandwiched between two THV layers. When submerged in water, the drug seemed to dissolve away and

water was found inside of the agglomeration "bubbles" of drug. Nonetheless, when the samples dried, the drug crystallised. This confirmed that the films did not have pores as the drug was still trapped inside the THV films after 12 days in water but also that water was able to slowly infiltrate the THV sandwich. A slow release of drug may also have been possible. Further studies are necessary to assess the drug release capabilities of THV.

5.5 Peeling test

5.5.1 Introduction

The experiments discussed in section 5.2.5 and 5.2.7.1 showed how the presence of an oily contamination or water could detach the polymer film from the glass slide. This behaviour, while undesirable when printing thick films with the Dimatix, it was useful to detach the printed part from the substrate without damaging them. This section investigates how to safely and easily detach films of different thickness (down to a few nanometres) produced with different parameters and printers.

5.5.2 Results and discussion

After exposing THV films printed with both Dimatix and PICO Pµlse to water it was observed that the films detached from the glass slide and floated on top of the water almost immediately. However, the time required for the film to detach depended on the printing temperature. When the films (THV 10 wt% in MIBK) were printed at temperatures below 50 °C they quickly detached, while when printed at 90 °C they did not fully detach after 3 hours in water (but they were peeled easily with a pair of tweezers). Because the films floated in water, it was possible to transport the films without touching or damaging them just by moving the water underneath them. The technique worked for both thick and thin films (down to a few nanometres) (Figure 5.50). While trying to pick up a nanometre thick film with a pair of tweezers the film wrapped around the tweezers. This could be a way to apply a thin coating layer or porous membrane to a complex surface/object (similarly to hydrographics printing where specific paint patterns are applied to three-dimensional surfaces by dipping said surfaces in a water tank having the specific paint pattern on the surface of the water [257]).
Figure 5.50a shows a glass slide coated with 1 mL of THV 10% in MIBK with a syringe by drop casting. The left edge of the film was easily detached with few drops of water, the drops then moved across the glass slide to stay at the glass-THV interface while the film was being lifted/peeled.
Figure 5.50b shows a detached and floating film printed with the PICO Pµlse (THV 20 wt%, 1 layer, nozzle temperature of 50 °C, pressure of 2 bar, and DS of 600 µm). Figure 5.50c shows a detached and floating film printed with the PICO Pµlse (THV 10 wt%, 2 layers,

nozzle temperature of 40 °C, pressure of 2 bar, and DS of 350 µm). Drops of water were deposited on the floating film. A dye may be used to observe the permeability of the film. Figure 5.50d shows three films of few tens of nanometres in thickness printed with the Dimatix (THV 1 wt% in MIBK, 10 layers, nozzle and substrate temperature of 22 °C, DS of 75 µm). The first film on the left was floating on water while the second (in the centre of the glass slide) was partially covered in water but still attached to the glass slide. The films were completely detached only when the entirety of the film was submerged in water (at least for short time scales). Films that were thick/strong enough could also be detached with a sharp tip (e.g. syringe needle, tweezers) without the use of water and without damaging them. The use of water could not be avoided in the case of nanometre-thick films.

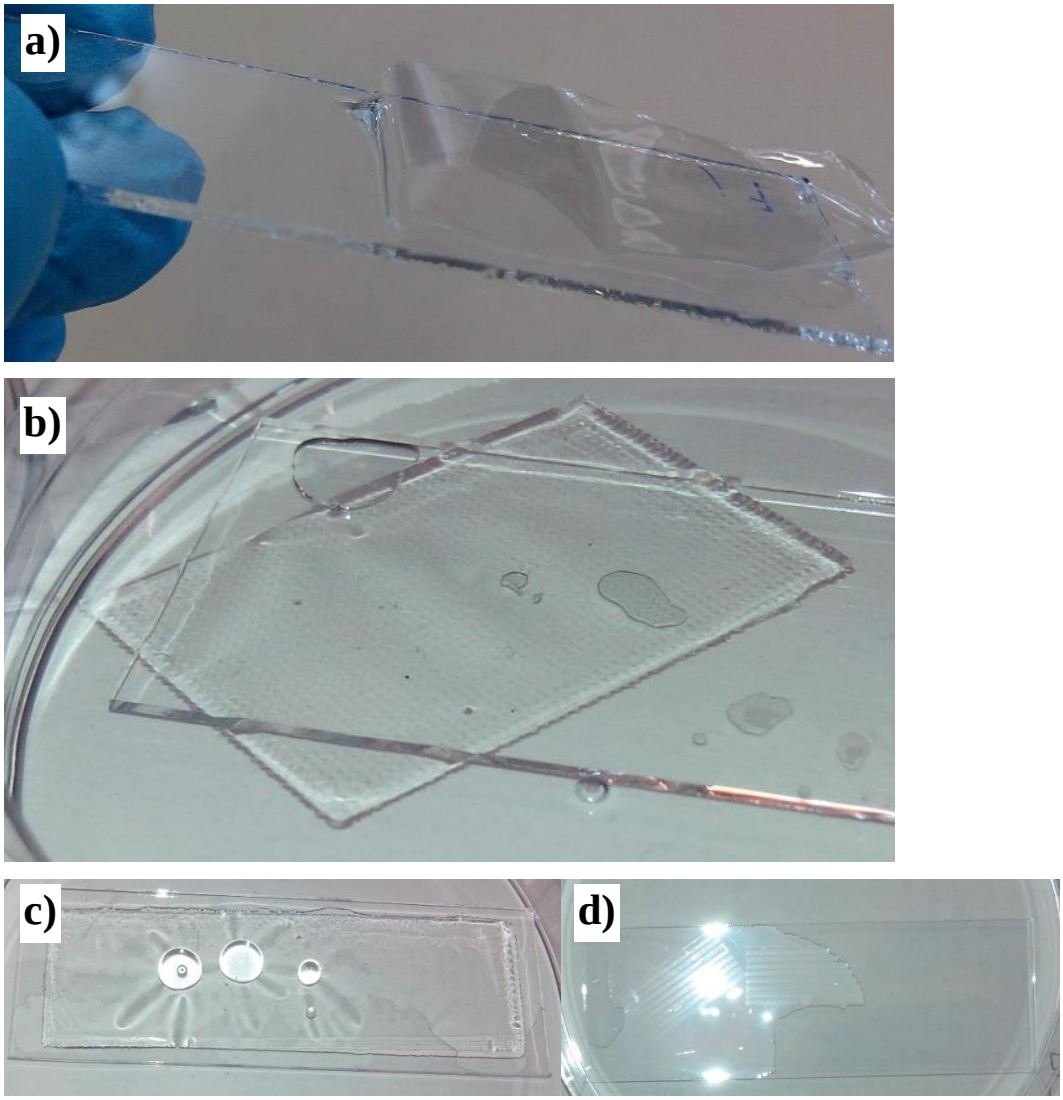


Figure 5.50 – THV films detached with the use of water. (a) Glass slide coated with 1 mL of THV 10% in MIBK with a syringe by drop casting. (b) 1-layer film of THV 20 wt% in 50-50 v% MIBK-acetone. (c) 2-layer film of THV 10 wt% in MIBK. (d) 10-layer film of THV 1 wt% in MIBK with a thickness of few tens of nanometres.

5.5.3 Summary

Water was successfully used to detach THV films of different thickness (down to a few nanometres) produced with different parameters and printers. The printing temperature had an influence on how strong the bonding between the glass slide and THV film was. This technique could also be used to transport very thin films/membranes without damaging them.

5.6 E-beam crosslinking

5.6.1 Introduction

It is well known that THV undergoes crosslinking when exposed to an electron beam [114], [242] but very little information is available about the process or properties of the irradiated parts. E-beam cross-linking improves the mechanical properties, chemical resistance and increases the temperature resistance of the polymer to temperatures >150 °C [114] (the melting temperature of non-crosslinked THV 221 is 115 °C [162], [164]). This section investigates the effect of a pulsed electron beam on THV films. The methodology can be found in section 3.3.18.

5.6.2 Results and discussion

It was observed that the amount of energy and number of the shots affected the surface appearance of the THV coated glass slides. 1 shot at 35 kV (Figure 5.51c) showed a slightly smoother surface than 1 shot at 30 kV but 3 shots at 35kV (Figure 5.51b) showed a visibly rougher surface. This suggested that 3 shots were transferring too much energy and heat to the sample. Compared to a reference sample (Figure 5.51d), 1 shot at 35 kV showed a more even surfaces without the presence of superficial defects/artefacts. SEM and EDX analyses suggested that the reflective particles on top of the films (Figure 5.51b-c), which increased in density with the number of shots, were glass fragments generated due to the thermal stress caused by the E-beam process (known to have extremely high heating and cooling rates). The part of the glass slide not coated in THV cracked when exposed to the electron beam (Figure 5.51a).

A portion of the central part of the films was peeled and left in MIBK for 10 months. The films swelled but none of them showed significant dissolution, proving that a degree of crosslinking had happened [113], even at the lowest energies (1 shot, 30 kV).

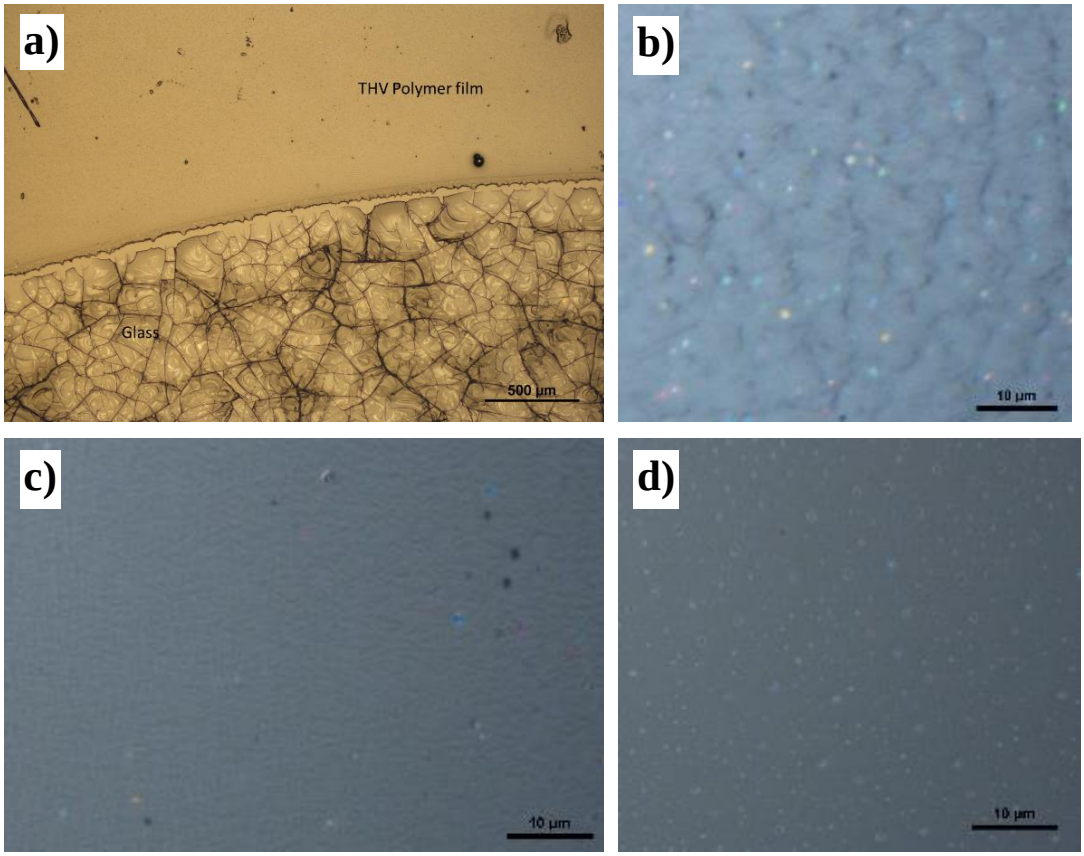


Figure 5.51 – Electron beam irradiated THV coated glass slides. (a) 3 shots at 35 kV, the top side shows the THV film while the bottom shows the cracked glass slide surface. (b) 3 shots at 35 kV. (c) 1 shot 35kV. (d) Reference non-irradiated THV film.

Next, a glass slide with 4 samples of roughly 30 x 5 x 0.155 mm were exposed to the electron beam and two samples were subsequently submerged in MIBK. This time the samples had a thickness of ~ 155 µm, almost six times thicker than that in the previous experiment. After few minutes in MIBK the THV strips separated in 2 parts, a superficial skin and the remaining lower part. The lower part dissolved in the next hour while the skin appeared to be insoluble, even after 4 months. This suggested that the penetration (and crosslinking) of the electron beam was limited to the surface giving the possibility of increasing the chemical and thermal resistance of specific layers such as the layers/channels in contact with aggressive fluids in microfluidic devices.

5.6.3 Summary

The electron beam successfully crosslinked the THV but only on its surface. The crosslinked samples were left in MIBK for 10 months and no complete dissolution happened, suggesting that a degree of crosslinking had happened [113]. Evidence suggested that the penetration (and crosslinking) of the electron beam was limited to the surface. This gives the possibility of increasing the chemical and thermal resistance of specific layers such as the layers/channels in contact with aggressive fluids in microfluidic devices.

5.7 Mechanical tests

5.7.1 Introduction

This section investigates the mechanical properties of THV films printed with a DS of 600 and 800, as printed, after a thermal treatment, and after exposure to a pulsed electron beam. The methodology can be found in section 3.3.21.

5.7.2 Results and discussion

The tensile tests showed values similar to those reported by the manufacturer in their material data sheet (Elongation at break = 600 - 700%, Tensile at break = 20 MPa, Flexural modulus = 80 MPa, Shore D hardness = 44) [195], [258]. The results of the tensile tests are shown in Figure 5.52 and Table 5.11. The elongation at break (EaB) was higher in the untreated samples and the highest elongation of 782% was achieved by the samples printed with a DS of 600 µm. The EaB decreased to roughly 500% for the heat treated and crosslinked samples. The tensile at break was higher in the heat-treated samples and the highest value of 22.8 MPa was achieved by the samples printed with a DS of 800 µm. The UTS was around 16 MPa and 9.4 MPa for the untreated and crosslinked samples, respectively. The untreated samples printed with a DS of 800 and 600 µm showed similar values of UTS even though the samples printed at 600 µm were 20 - 40 µm (20 - 50%) thicker. The approximate Young's modulus was higher for the untreated samples and decreased in heat treated samples (the stress-strain curve did not show Hookean (linear) behaviour therefore the Young's modulus could not be calculated with precision, see section 3.3.21).

The untreated samples were white/opaque when they reached their breaking point, which was due to the alignment of the amorphous chains into crystalline regions. Only half of the heat-treated samples became white/opaque, suggesting the presence of defects in the films and explaining the large standard deviation. The heat-treated samples that performed particularly poorly were exhibiting the wrinkle effect (section 5.1.1.1) and were much thicker than other samples printed with the same number of layers, suggesting that there were pockets of air inside of those samples.

Figure 5.52d shows the stress-strain curves of samples 221_1 (untreated), 222_1 (oven), and 219 (E-Beam). Overall, the heat treatment decreased the elongation at break and increased the tensile at break suggesting a higher degree of crystallinity [45]. The exposure to the electron beam did not improve any of the measured properties likely because the crosslinking only happened at the surface of the samples as explained in section 5.6. The E-beam samples had, in fact, a similar stress-strain curve to that of the untreated samples but with a lower elongation

at break (Figure 5.52d). The early break may have been caused by the superficial crosslinked layer that had a lower EaB [45] and acted as a stress concertation point.

As explained in the methodology the samples were printed two at a time and this was reflected in the mechanical properties listed in Table 5.11. Each couple gave very similar mechanical properties, especially for the elongation at break and thickness.

The thickness of the samples did not show any significant change after thermal treatment, even the samples that showed the wrinkle effect. On the other hand, the weight of the samples decreases of 1.5 - 2.0 mg (~ 1 - 2 %) after thermal treatment.

Table 5.11 – Tensile properties of THV samples printed with a DS of 600 and 800 µm. The samples were tested as printed, after a thermal treatment in oven, and after being exposed to and E-beam.

Test	DS and Treatment	Max Load (N)	Young mod. max (MPa)	Young mod. min (MPa)	Yield stress (MPa)	UTS (MPa)	EaB (%)	Thick. (mm)	Numb. Of Layers
221_1	800 µm	12.9	98.6	78.6	6.2	16.6	689	0.097	10
221_2		13.6	95.5	78.4	6.4	17.6	686	0.097	10
224_1		10.9	104.1	82.5	5.4	11.5	561	0.118	10
224_2		14.3	104.6	81.1	5.3	15.2	667	0.118	10
227_1	600 µm	20.1	79.4	72.0	5.4	17.0	782	0.148	8
227_2		17.1	83.5	70.2	5.2	14.9	713	0.144	8
228_1		19.5	84.2	68.8	5.5	17.1	775	0.142	7
228_2		18.4	86.4	73.9	5.5	16.5	769	0.139	7
222_1	800 µm, Oven	14.2	80.8	67.0	6.1	22.8	483	0.078	9
222_2		12.8	81.0	65.6	5.9	20.9	449	0.076	9
223_1		8.5	53.0	43.5	3.6	7.6	339	0.139	10
223_2		10.5	46.3	38.6	3.5	9.5	411	0.139	10
225_1	600 µm, Oven	21.4	54.2	47.3	4.4	19.7	526	0.136	8
225_2		18.5	54.4	49.0	4.3	17.0	512	0.136	8
226_1		14.2	48.3	43.3	3.9	12.6	457	0.141	8
226_2		11.8	49.0	41.3	3.8	10.4	426	0.141	8
219	800 µm, E-Beam	14.0	69.3	61.4	4.7	9.2	588	0.190	10
220_1		4.9	84.3	67.0	5.4	9.9	421	0.063	4
220_2		4.3	70.0	55.7	4.5	8.7	423	0.063	4

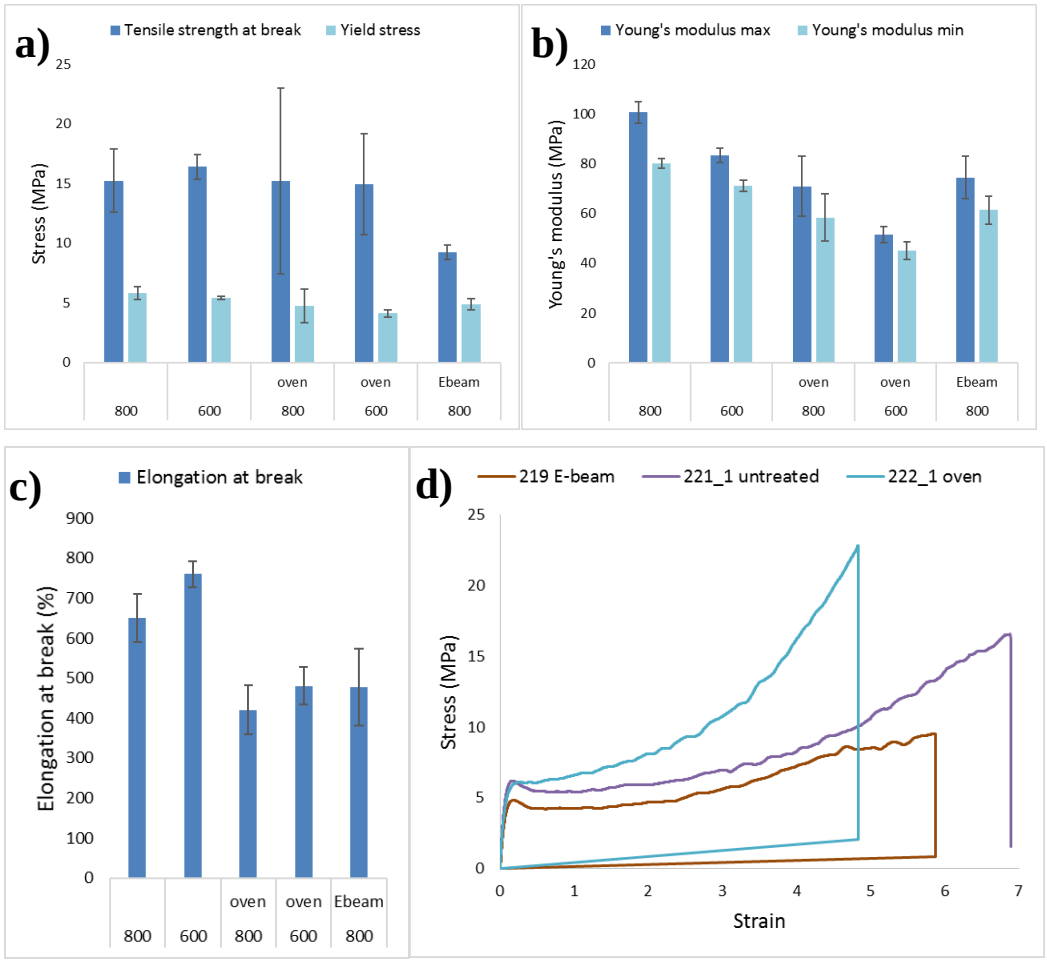


Figure 5.52 - Tensile properties of THV samples printed with a DS of 600 and 800 µm. The samples were used as printed, after a thermal treatment in oven, and after being exposed to and E-beam. (a)Tensile strength at break and Yield stress. (b) Young's modulus maximum and minimum. (c) Elongation at break. (d) Stress strain curve of samples 221_1 (untreated), 222_1 (oven), and 219 (E-Beam).

5.7.3 Summary

The tensile test of the THV samples printed with a PICO Pµlse showed values similar to those reported by the manufacturer in their material data sheet (Elongation at break = 600 - 700%, Tensile at break = 20 MPa, Flexural modulus = 80 MPa, Shore D hardness = 44) [195], [258]. These were excellent results proving that material jetting had the potential to print parts with the same quality of traditional manufacturing but with a far greater freedom of design.

6 Discussion

6.1 Introduction

In chapters 4 and 5 the results of the investigation of polymer powder bed fusion and material jetting were presented, involving firstly the PCTFE and PFA powders and secondly the THV inks. These three fluoropolymers were chosen for their outstanding properties such as wide service temperature, excellent chemical resistance, low gas permeability, low dielectric constant, low surface energy, resistance to flames and sunlight, and different processability (low/medium/high melting temperature and soluble/insoluble in common solvents) (section 2.4) [117] [118]. Because of these properties, fluoropolymers have been widely used in all facets of human life from household to automotive, electrical and chemical industries, as well in medical devices and aircraft [112][113]. Their addition to the currently limited AM material portfolio would be a great step forward for the technology [15], [36]. It is believed that no work has been published on the use of PCTFE, PFA, and THV in AM.

In the following sections several analytical analyses on the raw materials are firstly discussed, followed by the critical process of improving the powder flowability, and concluded by the laser sintering of the PCTFE and PFA powders and jetting of the THV inks.

6.2 Characterisation of the polymers and improvement of the powder flow

The thermal characterization of the PCTFE and PFA powder showed how the presence of carbon black (CB) increased the crystallization temperature, and consequently the crystallization speed from the melt polymers. Therefore, increasing the minimum powder bed temperature required to avoid warping. This aspect is often overlooked in the literature for pPBF and only a few papers investigated it [52], [206]–[208]. It is believed that the isothermal crystallisation and activation energy of crystallisation of PFA and PCTFE, with and without CB, have never been published before.

This PhD showed that PCTFE likely required a powder bed temperature above 190 °C as, at that temperature, the 1/2t crystallisation was 6.92 and 11.47 minutes when PCTFE was used with and without 1 wt% CB (Table 4.2). Similarly, PFA likely required a powder bed temperature above 288 °C: at that temperature, the 1/2t crystallisation was less than 10 minutes for both neat PFA and PFA with 0.2 wt% CB (Table 4.2). The activation energy of crystallisation for PCTFE and PFA was 394.9 and 630.9 kJ/mol, respectively (Figure 4.2e-f). After the addition of CB, the activation energy of crystallisation was almost unchanged for PCTFE and slightly increased for PFA.

A similar study was conducted by Drummer et al. [208]. They used isothermal crystallisation analyses to determine the activation energy of polyamide 12 (PA12), polyoxymethylene (POM), high density polyethylene (PE-HD), polypropylene (PP) and polyetherketone (PEEK HP-3, EOS GmbH). They showed that PA12 and PP had the lowest slope and activation energy meaning that fluctuations in powder bed temperature would have a lower impact on the crystallisation speed.

The TGA analyses showed that no significant decomposition took place after 5 hours at 201.55 °C for PCTFE (Figure 4.3). Several sources in the literature confirmed the thermal stability of PCTFE which did not show any significant decomposition after 3 hours at 250 °C [149]. PCTFE decomposition started slowly at 300 °C and accelerate at 400°C (Figure 4.3). These values were confirmed by the literature [120], [149], [150]. The main decomposition products of PCTFE are CTFE monomers with traces of $C_2F_2Cl_2$, C_3F_5Cl, and $C_2F_3Cl_3$ [149]. The PFA decomposition started slowly at 400 °C (Figure 4.3) and was confirmed by the literature [210]. After 2 years at 285 °C PFA showed no sign of decomposition [145]. These results confirmed that PCTFE and PFA could be processed safely (without the production of harmful decomposition product and decrease in Mw), at the powder bed temperatures used in pPBF (~182 °C). Furthermore, thermal degradation is actually expected to happen during extrusion and compression moulding of PCTFE, inducing the Zero Strength Time (of a generic PCTFE grade) to drop from 350 to roughly 200 and 300 seconds [211], respectively. Hence, pPBF could allow the production of parts with higher ZST (molecular weight) with potentially higher mechanical properties compared to traditional manufacturing. Nonetheless, using high molecular weight and high viscosity polymers is also challenging in pPBF (high porosity [25], [51], [63], [64]).

The pPBF system used in this PhD was equipped with a CO_2 laser (heating source) and it was important that the processed polymers absorbed at the wavelength of the CO_2 laser. Generally, this is not a problem for most polymers as the C-H and C-C bonds have an acceptable absorption in the CO_2 laser wavelength [32], [33]. The PCTFE IR spectrum showed high absorbance at the CO_2 laser wavelength due to the C-Cl stretching at 937 and 972 cm^{-1} [149], [214] (Figure 4.9). Carbon black had a great absorbance in the entire IR range measured (Figure 4.8). The addition of 1 wt% CB to the PCTFE powder shifted the entire PCTFE spectrum to a lower transmittance (higher absorbance). Because of its broad absorption range, CB is often used to increase the absorption in several systems that use different heating sources such as lamps (High Speed Sintering) [215] and laser diode (Sintratec) [216], [217]. PFA showed a low absorbance in the wavelength of the CO_2 laser. Similarly to PCTFE, the addition of CB increased the overall absorbance. Compared to PFA, THV showed a slightly higher absorbance in the wavelength of the CO_2 laser because of the presence of C-H bonds [143], [218].

The PCTFE had a particularly small particle size distribution (<1 µm) and required a flowing agent to spread correctly in the EOS P100. This particle size was much smaller than the current standard of ~45-90 µm [22]. Nonetheless, there are examples in the literature where powders with a particle size smaller than 1 µm were used [142], [143] and printed successfully. However, these publications did not investigate or explain the flowability characteristics of the powder. In this PhD an in-depth study of the flowability of the powders that showed how a sub-optimal powder size could be made acceptable with the use of flowing agents [73]–[75] and thermal treatments was conducted. The effect of two additives and two thermal treatments were assessed with the FT4 powder rheometer [221]. By way of comparison, Ziegelmeier et al. [193], [194] tested the quality of the data obtained with the FT4 to a Revolution Powder Analyzer and the Hausner Ratio and showed that all the methods gave similar results. Carbon black was the additive that showed the best improvement in flowability. Even though 2 wt% CB showed the best flowability in the FT4 study (Table 4.4), 1 wt% CB was used to minimize possible negative effects on the properties of the final parts [142]. Another flowing agent utilized was fumed nano-silica (NS) but it did not perform as well as CB. When mixed with the PCTFE powder, NS gave a lower CBD and higher SE (lower flowability) compared to CB. CB performed better than NS possibly because CB is a conductive material and could also decrease the cohesion between particles caused by static charges [75]. NS is usually the principal material of reference when flowability issues are encountered in pPBF [191], [222], [223] and other fields [74], [75]. The results of this PhD showed that CB may provide a better solution to the flowability issues in powders for pPBF. Despite the larger particle size distribution, the PFA powder still required the use of CB to have good flowability but in a smaller amount compared to PCTFE: just 0.5 wt% instead of 1 wt%. Moreover, loadings as low as 0.2 wt% showed satisfactory flowing properties.

The effect of two thermal treatments were also assessed with the FT4 powder rheometer. The first heat treatment method consisted of heating the PCTFE powder at temperatures above 200 °C for several hours. The longer the residence time and the higher the temperature, the greater the improvement in flowability (Table 4.4). This was likely due to an increasing number of particles sintered together which increased the particle size and decreased cohesion (Figure 4.5 and Figure 4.6). A similar process to increase the bulk density of PEEK powder up to 17% by reducing the specific surface of the particles (smoother particles) was patented by EOS [190]. Schmidt et al. [191] used a heated downer reactor to smooth polymeric particles that were injected in the reactor as an aerosol to minimise contacts between particles and reactor walls. The residence time in the reactor necessary to achieve smooth particles depended on the viscosity of the polymer. The second heat treatment method consisted of using the CO_2 laser of the EOS P100 to sinter a layer of powder and subsequently grind the produced parts. The newly obtained powder showed an increase in particle size and a remarkable increase in

conditioned bulk density to 0.82 g/mL from the 0.51 g/mL of the virgin powder, 37.3% and 23.8% of the absolute density, respectively. It is believed that this is the first time that a CO_2 laser was used to increase the particle size and improve the flowability of a polymeric powder. With a tailor-made system, this may become a suitable and scalable process to optimise particle size and flow. The PFA powder had a larger particle size distribution and, under the SEM, the powder particles looked similar to the thermally-treated PCTFE particles (Figure 4.6). This suggested that the PFA powder might have been produced in a similar way: with a thermal treatment step. Finally, no visible changes were observed between the virgin and used (17 uses/cycles) PFA powder (Figure 4.15), suggesting that no sintering was happening between the particles of the powder at the used powder bed temperatures (182 °C). This fact, added to the high thermal resistance of fluoropolymer, would mean that the PCTFE and PFA powder could be recycled numerous times without incurring in issues such as changes in viscosity and particle size [55], [62].

6.3 Powder bed fusion of PCTFE and PFA

It is well-known that additive manufacturing (AM), has great potential but several limitations, one of which is the narrow material portfolio [15], [36]. This is especially true for pPBF where polyamide and few other polymers are the main materials used (PA12, PA11, PA612, PA6, PS, PAEK, PEBA, PP, PPS, TPU [37]–[41]). Furthermore, PA12 made up ~ 95 % of the market in 2009 [9]. None of these polymers possess the outstanding combination of properties that fluoropolymers hold (section 2.4).

Today, the use of fluoropolymers in pPBF is limited to PVDF [138], [141]–[143]. All the research done on this material was conducted by the same group of people and focused on the biological properties of small scaffolds (~ 1.5 x 1.5 x 1 cm). Little to no consideration was given to the pPBF process and many essential process parameters, necessary for the reproduction of the studies, were missing. In this PhD, several parameters and techniques used to print PCTFE and PFA were investigated and described in depth. These observations will also be useful in the development of other challenging polymers in AM.

The sintered PCTFE parts showed a tendency to warp after 10-20 layers depending on the parameters and scan strategies utilized (Table 4.6). This was caused by the powder bed temperature (~182 °C) being too close to the crystallization temperature of the polymer (170 °C) and low powder bulk density [22], [61]. The presence of CB increased the absorbance of the CO_2 laser as evidenced by how the powder started smoking at lower energy densities (0.008 J/mm^2). No smoke was observed at 0.008 J/mm^2 without CB. Optimized scanning strategy led to a marked increase in printable layers before parts would warp enough to touch the recoating blade. The reduced warping was likely due a lower degree of sintering when a delay was introduced between scans on the same layer and due a support effect from the

surrounding powder when the part and surrounding powder were exposed to a low energy scan before scanning the actual part. The printed parts were brittle but a 30 minutes post sintering step at 250 °C increased the strength of the parts and density from ~35% to ~60% (Figure 4.23). Higher densities may be achieved with longer residence time and/or higher temperatures in the oven.

Neat PFA was used in the initial screening of the process parameters. It was observed that the amount of warping was proportional to the degree of sintering and energy density except when the polymer layer was fully melted (Figure 4.26). This tendency to instantly warp was due to the wide thermal jump between the crystallization temperature (271.93 °C) and powder bed temperature (182 °C). 0.4 wt% CB was then added to the powder and the same process parameters were used to have a comparison with the neat PFA (Figure 4.27). The strength of the samples increased with the addition of CB confirming the increase in absorbance in the wavelength of the CO_2 laser (section 4.1.5). Different warping behaviours, likely to a different heating/cooling mechanism, were also observed when PFA was laser sintered with and without CB (Figure 4.27). The samples were found to produce smoke when an ED of 0.040 J/mm^2 was used. Several printing parameters were investigated to produce two process maps showing the degree of warping for several sets of parameters (Table 4.7 and Table 4.8). The test showed that a hatch spacing of 0.1 had a narrower processing window (range of parameters that leads to a successful print) compared to a hatch spacing of 0.2 mm, meaning that small changes in the parameters would cause the printing process to fail. The orientation of the parts was found to have an effect on the final properties of the parts [227], [228]. When two scans were used, 1 in X direction and 1 in Y direction, a hotspot on the top right corner was created. This effect could be partially countered by rotating the samples by 45° or by scanning twice only in the X (or Y) direction (Figure 4.29).

The EOS P100 software allowed the use of two special scan strategies, “Skincore” and “Mesh 2D” [224]. The Mesh 2D scan was used to create grids inside of a 20 x 20 mm square having a contour 2 mm thick and showed a flaw in its design as one section of it was scanned twice, leading to possible polymer degradation (Figure 4.30). The Skincore scan was used to study the effect of a low ED contour with a high ED core (Figure 4.31). It was found that the warping at the contour of the sample was stronger (with a low ED contour) because the now weaker (more porous [138]) contour was more prone to be deformed by the residual thermal stresses. The vector length also had an effect on the part properties. Lower vector lengths showed the production of smoke and hence decomposition as the parts were reaching higher local temperatures (Figure 4.32). This was caused by the laser coming back to the same spot more quickly during the scan of short samples/vectors, which gives the part less time to cool down. Wegner et al. [71] observed similar results with PA powders. Furthermore, these observations were also confirmed by the fact that while using the same parameters to print two parts of

different size, only the smaller part showed detectible sintering. Consecutive scans of a part on the same layer could be used to increase the sintering and strength of the parts to the detriment of geometrical accuracy due to warping and shrinking (Figure 4.34). The sorted scan strategy caused discontinuities in samples with complex geometries due to the laser jumping from one section to the other (Figure 4.36).

It is believed that these implications have never been discussed in the literature of pPBF. Furthermore, there is a tendency in the literature for pPBF to only use very basic scanning strategies such 1 or 2 X-Y scans without exploring other solutions [22][234]. This might be due to the software limitation of commercial pPBF systems, usually designed and optimised to print a limited number of commercial polymers and not for research purposes. On this note, another diffuse issue with commercial pPBF system is the big building chambers [31], designed to increase throughput but inconvenient when testing new powders and formulations (as high quantities of powder are required, often more than 10 kg per formulation). Warping was absent when grid structures with a hatch spacing above 0.75 mm were produced (Figure 4.37). The grids shrank uniformly in all directions. The Y track width increased with decreasing hatch spacing as the local powder temperature was being increased by the previous X scan. The track width was also increased by a low ED pre-scan or by scanning the grid twice (Figure 4.38).

Thin, flexible, porous, hydrophobic PFA membranes were produced. Water droplets did not go through the membrane but isopropanol droplets (because of their lower surface tension) went through. The membranes did warp after printing but a heat treatment at 260 °C flattened them (Figure 4.40). This suggested that a powder bed temperature of 260 °C could avoid warping. By looking through the thin membranes, carbon black agglomerations were visible, hence this could also be a method to assess the quality/performance of different mixing methods. The density, porosity and pore size of the membranes may be tuned by changing the laser parameters or with a post-sintering step in an oven. In the literature, researchers just started to assess the quality of laser sintered polyamide membranes [230], [231].

Multiple layer parts were possible but the produced parts were very brittle. Slightly stronger parts of 50 layers were produced by pre-scanning a wider area of the powder bed (Figure 4.43). The warping was also mitigated by using masking tape on a build plate [232]. 13 layers were printed before running out of powder which meant that more layers could have been printed (Figure 4.44). With the same parameters and without the use of a build plate, the parts warped at the first layer. PFA and ETFE sheets were also used as build platform but with poor results due to several technical issues (section 4.4.3). A similar approach was reported by Niino et al. [233] when they processed PEEK at 200 °C instead of the recommended > 350 °C. To avoid warping they anchored the parts to a rigid 12 mm thick PEEK build plate and obtained densities up to 96%.

Most of results observed in these experiments were possible because of the difficulties in processing PCTFE and PFA and their narrow processing window. Small changes in parameters that would go unnoticed in commercial pPBF powder grade like PA 12 (because of PA 12 wide and robust processing window [235]) become very noticeable in PCTFE and PFA. Nonetheless, these effects still happen in powders like PA 12 and may have an influence on the final properties of the parts. Therefore, challenging polymers have the advantage of being sensitive to any small changes in processing parameters and highlighting all the effects that the parameters have on the polymer powder and final parts. This makes challenging polymers interesting case studies.

Overall, PCTFE and PFA showed potential for pPBF and can already be used to produce thin membranes and small parts. The high viscosity of the grades used in this PhD (section 3.2) and fast heating/cooling rates characteristic of the pPBF process made the produced parts porous. Nonetheless, the high viscosity also improved the recyclability of the powders by avoiding the caking of the powder particles at high temperatures. A process that uses a low powder bed temperature can bring considerable economic advantages both on equipment investment [236] and power consumption. In fact, 35% of the consumed energy is used by the chamber heaters [237]. Nonetheless, systems with higher powder bed temperatures (expensive [236]) and/or build platforms might be required to print stronger, bigger and more complex parts made of PCTFE and PFA.

6.4 Material Jetting of THV

Similarly to pPBF, one of the major limitation of MJ is its narrow material portfolio due the specific material requirements such as solubility, viscosity, surface tension, molecular weight, and evaporation rate (section 2.3.2) [83]. Because of their chemical resistance, only a few grades of fluoropolymer are soluble in common solvents at room temperature, including THV, PVDF, Teflon AF, and CYTOP. One of the advantages of MJ over pPBF and several other AM techniques is its ability to produce multi-material parts [83]. THV could be useful in many applications where a protective/inert, flexible, and transparent material is required.

Today, the use of fluoropolymers in MJ is limited to P(VDF–TrFE). Furthermore, P(VDF–TrFE) was used only at low concentrations (< 3 wt%) and, because of the high boiling temperature of the solvents used, often required a time and energy consuming oven drying step which limited the throughput of the process [96], [98], [135]–[137].

In this PhD several solvents and solutions were investigated for the jetting of THV. MIBK was the chosen solvent because of its ideal evaporation rate, not too fast that it would clog the nozzles and not too slow that it would extend the printing times. Nonetheless, MIBK showed an unusual drying mechanism (wrinkle effect, section 5.1.1.1). When pure MIBK was deposited on top of a THV film, it deformed the surface forming wavy patterns. This behaviour

was likely due to the relatively fast evaporation rate of MIBK and its being a modest solvent for THV. The wrinkle effect was in fact not visible when a good solvent or a slow evaporating solvent were used.

The viscosity of the inks increased roughly 10-100-1000 times by going from 1 to 5-10-20 wt%. The cup and bob geometry was initially used to measure the viscosity because it is a geometry ideal for solutions with high evaporation rates. However, this geometry was not accurate at high shear rates (> 100 s^{-1}) because of the formation of Taylor-vortices which caused the measured viscosity to increase [199]. Nonetheless, the parallel plate geometry measurements showed that the viscosity values obtained at a shear rate of 100 s^{-1} were comparable with those obtained with a cup and bob geometry. As expected, the viscosity of the inks decreased at higher temperatures.

The GPC results confirmed that the THV had a high Mw of 3.025 x 10^5 g/mol and PDI of 1.411.

It is believed that the viscosity, viscosity trends, surface energy, and wrinkle effect of THV 221 solutions have never been reported in literature before. Furthermore, only one source was available in the literature about the Mw of THV 220 (a conference presentation [242]). The analyses and observations reported in this PhD are therefore an important initial step in the diffusion and better understanding of this material [163] (section 2.4.5) into more fields/applications.

This PhD showed that THV could be printed at low and high loadings, from 1 wt% to 20 wt% while using solvents with an evaporation time at room temperature lower than one minute. The Dimatix was used to print low viscosity inks while the PICO Pµlse was used to print high viscosity inks.

Six different low viscosity inks were tested, THV 1-3-5 wt% in MIBK, THV 1-2.5 wt% in 50-50 v% MIBK-DMAc, and THV 2 wt% in DMAc. It was not possible to form uniform films with all of the inks containing DMAc. MIBK showed a uniform film formation. DMAc had a lower evaporation rate and higher surface tension than MIBK which meant that, when mixed together, the Marangoni flow was not inwards but outwards, amplifying the coffee ring effect [100]. Nonetheless the DMAc-MIBK solution gave relatively satisfactory results at high substrate temperatures (50 °C) likely because of the quick evaporation of the solvents [102]. The solvent type did not affect the jetting behaviour, except for the clogging of the nozzles. Solvents with a high evaporation rate are more prone to form polymeric films at the nozzles surface which clog the nozzles [98]. Despite being in the printable region (section 5.2.2), THV 5 wt% in MIBK could not be jetted. This was due to the high molecular weight of the polymer (3.025 x 10^5 g/mol) which caused the ink to behave like a viscoelastic fluid. In fact, As calculated by Haque et al. [98], with the typical strain rates encountered in material jetting (> $5x10^{-4}$ s^{-1}), polymers with a Mw higher than 5 x 10^4 g/mol were going to experience coil-

stretch transitions. The printable concentration was found to be 1 wt%. THV 1 wt% in MIBK showed the formation of uniform single layer films with a strong coffee ring effect. The thickness of a 1-layer film was 10 nm (Figure 5.24a). As explained by Xue et al. [247], the demand of nanometre-thick films is in constant rise; MJ (and THV) could play an important role in it, especially in multi-material parts. Multiple layers of THV 1 wt% in MIBK formed unusual patterns likely caused by the coffee ring effect (Figure 5.25). These patterns were studied at different drop spacings and number of layers. Unique, repeatable patterns, which may be useful for specific applications (e.g. increase or decrease contact angle, micro-reactors, composite materials) were possible. Even though the coffee ring effect has been exploited in several publications (to increase the resolution of the prints by allowing the formation of thinner tracks/features) [253]–[256], this may be the first time that these type of patterns are printed and reported in such detail. Several issues and limitations of the Dimatix/ink such as different drop size for different nozzles and increase in drop size with printing time were also exposed. The DMC-11610 was proven to be non-compatible with the MIBK solvent and to produce a contamination which made the 1-layer films porous and caused the detachment of the films from the glass slide. The more chemically resistant DMCLCP-11610 did not produce any visible contamination.

Overall, uniform films of thickness down to 10 nm were produced. Porous films were also produced when the ink was contaminated or when the glass slide had superficial artefacts. Thicker films were more difficult to be produced due to the coffee ring effect but the latter could be exploited to produce patterns/topographies that could be tailored by changing drop spacings and/or number of layers.

The PICO Pµlse, used to print the 10 wt% and 20 wt% inks, had a much lower resolution (bigger drop size) compared to the Dimatix but also a much higher throughput.

THV 10 wt% in MIBK was jetted with a PICO Pµlse at several nozzle temperatures, pressures, and drop spacings. The parameters were optimised to decrease splashing and obtain drops of consistent shape and dimensions [81]. The best results, among the experiments carried out, were given by a nozzle temperature of 30 °C, pressure of 1 bar, and drop spacings < 500 µm. The coffee ring effect was still present for drops and lines but not as strongly as in the THV 1 wt% in MIBK ink. The films did not show the coffee ring effect, instead, the CSI showed a clear slipping pattern likely due to the non-pinning of the film on the glass slide [107]. The wrinkle effect was also often present for the 2- and 3-layer prints. Overall, the prints showed good uniformity, accuracy, and no porosity. The thickness of a 1-layer film was 4 µm (Table 5.8).

THV 20 wt% in 50-50 v% MIBK-acetone was jetted with a PICO Pµlse at several nozzle temperatures, pressures, and drop spacings. The parameters were optimised to decrease splashing and obtain drops of consistent shape and dimensions. The best results, among the

experiments carried out, were given by a nozzle temperature of 50 °C, pressure of 2 bar (while using the HPx High-Pressure Dispensing Tool), and drop spacing of 600 µm. The coffee ring effect was mostly absent and the CSI showed a clear slipping pattern likely due to the non-pinning of the film on glass slide. The wrinkle effect was also mostly absent. Complex large patterns such as honeycombs were printed successfully. Overall, the prints showed good uniformity, accuracy and no porosity. The thickness of a 1-layer film was 15.1 µm (Table 5.10).

The combination of the two printers would allow to quickly print big patterns (PICO Pµlse) with superficial fine details (Dimatix) (Figure 5.28). The mechanical properties of the printed films were excellent and comparable to those obtained with traditional manufacturing [195], [258], with elongation at breaks and ultimate tensile strengths up to 782% and 22.8 MPa.

It is well known that THV undergoes crosslinking when exposed to an electron beam [114], [242] but very little information is available about the process or properties of the irradiated parts. E-beam cross-linking improves the mechanical properties, chemical resistance and increases the temperature resistance of the polymer to temperatures >150 °C [114] (the melting temperature of non-crosslinked THV 221 is 115 °C [162], [164]). The use of a pulsed electron beam system [200] showed to only crosslink the surface of the film, giving the possibility of increasing the chemical and thermal resistance of specific layers such as the layers/channels in contact with aggressive fluids in microfluidic devices. The crosslinked samples were left in MIBK for 10 months and no complete dissolution was observed, indicating that a degree of crosslinking happened [113].

The THV films also showed promising results in encapsulating a water-soluble drug. Unlike most fluoropolymers, THV has a low crystallinity which allows for a faster drug release and higher elongation at break (lower tendency for the film to crack). Because of these properties, Pacetti [168] patented the use of THV in medical devices such as coronary stents. In this PhD, a water-soluble drug was used to demonstrate the uniformity and lack of pores in the THV films. The drug was initially jetted on a glass slide and then covered with a THV layer. The drug only partially dissolved due to sporadic defects in the film and infiltration of water between the glass-THV interface. To avoid this interface issue, the drug was sandwiched between two THV layers. When submerged in water, the drug seemed to dissolve away and water was found inside of the agglomeration/pockets of drug. Nonetheless, when the samples dried, the drug crystallised. This confirmed that the films did not have pores as the drug was still trapped inside the THV films after 12 days in water but also that water was able to slowly infiltrate the THV sandwich. A slow release of drug may also have been possible. Further studies are necessary to assess the drug release capabilities of THV.

Finally, films of all the thicknesses (even of few nanometres) could be detached from a glass slide (without receiving any damage) with just water. The films could also be transported on a layer of water (as they floated).

Overall, THV was a very versatile polymer that could be printed with different solvents and loadings, by itself or in multi-material applications, with the potential to be used as a nanometre thick protective layer [162], [166], [167], porous membrane, drug delivery system [168], and microfluidic device [169]–[172].

7 Conclusions

7.1 Introduction

The following points are taken from the total of this work, they are the conclusions of the characterisation and improvement of the PCTFE and PFA powders, the specific conclusions of the laser sintering of PCTFE and PFA, and finally the conclusions from the work involving the THV printing.

7.2 Conclusions: powder bed fusion of PCTFE and PFA

- This is the first time it has been proven that PCTFE parts can be manufactured using pPBF:
    - Multiple layers were printed with and without the use of additives.
    - Warping and porosity were the major limitation of the process.
        - Optimised parameters and post sintering steps were suggested as possible solutions to the warping and porosity issues.
- This is the first time it has been proven that PFA parts can be manufactured using pPBF:
    - Single layer membranes were produced. They had a thickness of ~ 150 µm and porosity of ~ 60 %. Water droplets were unable to infiltrate the membrane while IPA droplets wet and went thought the membrane. The membranes showed good strength and flexibility.
    - Grids with accurate dimension and no warping were printed.
    - Multiple layers were possible with optimised parameters. Nonetheless, the printed parts were very brittle. Stronger parts were obtained with the use of a build platform as support structure.
    - The effect of several conditions such as the addition of carbon black, printing parameters, part orientation, scan strategies, vector length, and pre-heating of the powder bed with a pre-scan were investigated.
- Thermal analyses showed several interesting results:
    - The addition of carbon black to the PCTFE and PFA powders, increased the crystallisation temperature and speed. This aspect is often overlooked in the literature for pPBF.
    - First suggestions on possible ideal powder bed temperatures to minimise warping during print.
    - The powders were stable at the used powder bed temperatures.

- Several methods were used to improve the flowability of the powders:
    - Carbon black gave the highest improvements in flowability and bulk density, likely because of its conductivity and ability to decrease the cohesion forces due to static electricity.
    - The use of a static eliminator did not bring any discernible improvement.
    - Heat treatments were conducted with an oven and CO_2 laser. In both cases, the powder saw an increase in particle size, flowability, and bulk density.

7.3 Conclusions: material jetting of THV

- This is the first time THV inks were used in material jetting.
    - Reported for the first time in the literature the viscosity, viscosity trends, surface energy, wrinkle effect, and Mw of THV 221 solutions.
    - Low loading/viscosity inks were printed with the Dimatix:
        - Several solvents were tested but MIBK gave the best results. An unusual drying mechanism referred to as "wrinkle effect" was observed and studied. This effect was caused by the solvent being a fair solvent for MIBK and having a quite high evaporation rate. Furthermore, the thickness and dryness of the underlying THV also had an influence on the wrinkle effect.
        - A strong coffee ring effect was present. Nonetheless, it was used to advantage to make precise and repeatable structures with high resolutions. An extensive investigation with the CSI showed the origin and evolution of these structures.
        - The presence of a contamination was detected, investigated, and solved. This study suggests that the presence of the contamination led to the formation of porous membranes. When the source of the contamination was removed the printed film appeared uniform, with few imperfections due to artefacts present on the glass slide.
    - High loading/viscosity inks were printed with the PICO Pµlse.
        - Two inks were used, THV 10 wt% in MIBK, and THV 20 wt% in 50-50 v% MIBK-acetone. At high polymer loadings the coffee ring effect was almost absent.
        - Thick films and complex patterns such as honeycombs were printed with relative high throughputs.
- The combination of the two printers could allow for both high throughputs and resolutions.

- Mechanical tests showed that the printed parts had mechanical properties comparable to those obtained in traditional manufacturing.
- Preliminary tests with a pulsed electron beam showed that it was possible to crosslink THV. Nonetheless, the crosslinking only happened at the surface of the parts.
- THV films showed promising results in encapsulating a water-soluble drug.

8 Recommendations for future work

8.1 Introduction

This PhD is the first work to investigate the use of PCTFE, PFA, and THV in AM in the robust manner required, not only determining printability but starting to interrogate the printed parts. During this PhD many issues were discussed and solved, bringing these polymers one step closer to their adoption in AM. As such there is a lot of investigation still required.

8.2 Improvement of the raw materials

Both PCTFE and PFA showed potential in pPBF but one of the limitations encountered was due the commercial powder grades not being optimised for AM. Powder suppliers should design a powder grade tailored for AM applications, with a particle size in the ideal range for AM and a lower melt viscosity to minimise porosity, and enhanced particle coalescence and formation of homogenous melt films [22]. This is often difficult as it can be a risky investment for the suppliers when no research has been done in the field. Ideally, this PhD has given enough evidence to support the idea that fluoropolymers have a promising future in AM.

8.3 Improvement of the pPBF systems

It was argued in this study that the warping could be minimised or eliminated with the use of higher powder bed temperatures and use of build plates. Therefore, high temperature pPBF systems should be tested with these polymers. Printers designed to hold build plates of different nature would also contribute to the reduction of warping by the use of support structures. Similar technologies such as high-speed sintering (HSS) could also bring improvements as they showed less warping compared to laser systems [215].

8.4 Membrane applications

In this study pPBF was used to print porous membranes [230], [231]. Due to time limitations, the mechanical properties and the pore size and distribution were not investigated. A design of experiment could be conducted to determine the influence of the parameters on pore size and distribution. As PFA can be easily spread for the first layer even without the use of CB, the same experiments could be conducted on membranes made of neat PFA. Other additives could also be used. Glass bubbles are known to reduce warpage. Membranes made of PCTFE and THV could also be investigated.

Porous membranes could also be printed with THV with the use of moulds, specific process parameters, or addition of a second component (like in the case of the contamination coming from the Dimatix cartridge).

8.5 Heat treatments

It was argued in this study that the particle size distribution could be increased and controlled through heat treatments. Further investigations could make this a viable way to improve particle size distribution and flowability. Conductive additives could also be added before and/or after thermal treatment to discover if the flowability could be improved even further.
Because of the high viscosity of the raw polymers, the laser sintered parts were porous but post sintering steps showed the possibility to increase their densities. Optimised post sintering steps may allow for the printing of functional parts despite the low initial densities.
The use of the CO_2 laser showed promise as a method to increase the particle size distribution. Further studies, optimisations, and even the prototyping of a machine build for this purpose could give access to a new way to modify the particle size distribution and flowability. The laser could be used to sinter small particles together or smooth the surface of bigger particles similarly to what has already done in the literature but with an oven/reactor [190], [191].

8.6 Use of THV in powder bed fusion

In this PhD THV was used in material jetting; nonetheless, its low melting temperature could make it a good candidate for pPBF. However, THV is supplied as an agglomerate, meaning it has a very wide particle size distribution, from a few microns to a few millimetres. This would require either a great amount of powder to be bought and sieved or to be cryogenically-ground.

8.7 Counter coffee ring effect

THV showed a strong coffee ring effect at low concentrations. Many strategies could be applied to decrease or completely remove the coffee ring effect as reported in section 2.3.3. The removal of the coffee ring effect should allow the production of film with a uniform thickness from a few nanometres to a few microns.

8.8 Wrinkle effect

It was argued in this study that the wrinkle effect was connected to the quality of the solvent (poor, fair, good), solvent evaporation rate, polymer loading, thickness and dryness of the underlying THV layer. Nonetheless, a more in-depth study of the wrinkle effect is required to improve the robustness and reproducibility of the printing process by expanding on what was found in this PhD.

8.9 E-Beam crosslinking

Further studies on the crosslinking of THV with an electron beam could help understanding the beam penetration and parameters necessary to fully crosslink the entireties of the printed samples. Parts properties could be greatly improved with this technique [114].

8.10 Drug release

THV showed the ability to encapsulate and protect a water-soluble drug. Further tests could be carried out to measure the drug release of THV for medical applications/implants [168]. It would also be interesting to study the effects of the electron beam crosslinking on the drug release and water permeability of THV.

8.11 Microfluidic devices

The body of microfluidic devices could be printed with the PICO Pμlse, taking advantages of its high throughput and higher polymer loading compatibility, while small details could be printed with the Dimatix thanks to its high resolution [169]–[172]. An electron beam could be used to increase the chemical and thermal resistance of the device during or at the end of the print.

Bibliography

[1] I. Gibson, D. W. Rosen, and B. Stucker, “Additive Manufacturing Technologies: Rapid Prototyping to Direct Digital Manufacturing,” 2nd ed., New York: Springer, 2015, pp. 128–145.

[2] American Society for Testing and Materials International, “Standard Terminology for Additive Manufacturing Technologies, designation: F2792–12a.” [Online]. Available: http://www.astm.org/FULL_TEXT/F2792/HTML/F2792.htm. [Accessed: 18-Apr-2016].

[3] R. Hague, S. Mansour, and N. Saleh, “Material and design considerations for rapid manufacturing,” *Int. J. Prod. Res.*, vol. 42, no. 22, pp. 4691–4708, 2004.

[4] B. G. Compton and J. A. Lewis, “3D-printing of lightweight cellular composites,” *Adv. Mater.*, vol. 26, no. 34, pp. 5930–5935, 2014.

[5] C. L. Ventola, “Medical applications for 3D printing: current and projected uses,” *Pharm. Ther.*, vol. 39, no. 10, pp. 704–711, 2014.

[6] D. Bourell, B. Stucker, J. T. Montgomery, M. R. Vaughan, and R. H. Crawford, “Design of an actively actuated prosthetic socket,” *Rapid Prototyp. J.*, vol. 16, no. 3, pp. 194–201, 2010.

[7] J. M. Williams *et al.*, “Bone tissue engineering using polycaprolactone scaffolds fabricated via selective laser sintering.,” *Biomaterials*, vol. 26, no. 23, pp. 4817–27, Aug. 2005.

[8] GE Aviation, “Fuel Nozzle.” [Online]. Available: http://www.ge.com/stories/advanced-manufacturing. [Accessed: 15-Apr-2016].

[9] Wohlers Associates, “Wohlers Report, https://wohlersassociates.com/2009report.htm,” 2009.

[10] N. Hopkinson and P. Dickens, “Analysis of rapid manufacturing—using layer manufacturing processes for production,” *Proc. Inst. Mech. Eng. Part C, J. Mech. Eng. Sci.*, vol. 217, no. 1, pp. 31–39, 2003.

[11] N. Hopkinson and P. Dickens, “Rapid prototyping for direct manufacture,” *Rapid Prototyp. J.*, vol. 7, no. 4, pp. 197–202, 2001.

[12] GE Aviation, “GE9X.” [Online]. Available: http://www.geaviation.com/newengine/. [Accessed: 25-Apr-2016].

[13] R. Hague, I. Campbell, and P. Dickens, “Implications on design of rapid manufacturing,” *Proc. Inst. Mech. Eng. Part C, J. Mech. Eng. Sci.*, vol. 217, no. 1, pp. 25–30, 2003.

[14] R. I. Campbell, R. J. Hague, B. Sener, and P. W. Wormald, “The potential for the bespoke industrial designer,” *Des. J.*, vol. 6, no. 3, pp. 24–34, 2003.

[15] R. S. Evans, D. L. Bourell, J. J. Beaman, and M. I. Campbell, “SLS materials development method for rapid manufacturing,” in *Proceedings SFF Symposium, Austin (TX), USA*, 2005, pp. 184–196.

[16] P. F. Jacobs, *Rapid prototyping & manufacturing: fundamentals of stereolithography*. Society of Manufacturing Engineers, 1992.

[17] D. N. Silva, M. Gerhardt de Oliveira, E. Meurer, M. I. Meurer, J. V. Lopes da Silva, and A. Santa-Bárbara, "Dimensional error in selective laser sintering and 3D-printing of models for craniomaxillary anatomy reconstruction.," *J. Craniomaxillofac. Surg.*, vol. 36, no. 8, pp. 443–9, Dec. 2008.

[18] M. D. B. S. Tam, S. D. Laycock, D. G. Bell, and A. Chojnowski, "3-D printout of a DICOM file to aid surgical planning in a 6 year old patient with a large scapular osteochondroma complicating congenital diaphyseal aclasia," *J. Radiol. Case Rep.*, vol. 6, no. 1, pp. 31–37, 2012.

[19] M. Masters and M. Mathey, "Direct manufacturing of custom-made hearing instruments," in *SME Rapid Prototyping Conference and Exhibition*, 2002.

[20] GE Global Research, "3D Printing Creates New Parts for Aircraft Engines." [Online]. Available: http://www.geglobalresearch.com/innovation/3d-printing-creates-new-parts-aircraft-engines. [Accessed: 25-Apr-2016].

[21] HRS Flow, "SLM inserts - Selective Laser Melting, SLM inserts- Selective Laser Melting, Products HRSflow." [Online]. Available: https://www.hrsflow.com/eng/prodotti/slm-inserts-selective-laser-melting/slm-inserts-selective-laser-melting.php. [Accessed: 18-Nov-2018].

[22] R. D. Goodridge, C. J. Tuck, and R. J. M. Hague, "Laser sintering of polyamides and other polymers," *Prog. Mater. Sci.*, vol. 57, no. 2, pp. 229–267, Feb. 2012.

[23] D. L. Bourell, T. J. Watt, D. K. Leigh, and B. Fulcher, "Performance Limitations in Polymer Laser Sintering," *Phys. Procedia*, vol. 56, pp. 147–156, 2014.

[24] M. Vasquez, "Analysis and development of new materials for polymer laser sintering, PhD Thesis," © Mike Vasquez, 2012.

[25] S. Ziegelmeier, "Process analysis and material behavior of thermoplastic elastomers throughout the laser sintering processing chain, PhD Thesis," University of Nottingham, 2016.

[26] Y. Wang, E. James, and O. R. Ghita, "Glass bead filled Polyetherketone (PEK) composite by High Temperature Laser Sintering (HT-LS)," *Mater. Des.*, vol. 83, 2015.

[27] Oxford Dictionaries, "sinter: definition." [Online]. Available: http://www.oxforddictionaries.com/it/definizione/inglese_americano/sinter. [Accessed: 27-Apr-2016].

[28] J.-P. Kruth, G. Levy, F. Klocke, and T. H. C. Childs, "Consolidation phenomena in laser and powder-bed based layered manufacturing," *CIRP Ann. - Manuf. Technol.*, vol. 56, no. 2, pp. 730–759, Jan. 2007.

[29] E. Moeskops, N. Kamperman, B. van de Vorst, and R. Knopppers, "Creep behaviour of polyamide in selective laser sintering," in *Proceedings SFF Symposium, Austin (TX), USA*, 2004, pp. 60–7.

[30] G. N. Levy, R. Schindel, and J. P. Kruth, "Rapid manufacturing and rapid tooling with layer manufacturing (LM) technologies, state of the art and future perspectives," *CIRP Ann. - Manuf. Technol.*, vol. 52, no. 2, pp. 589–609, Jan. 2003.

[31] EOS, "FORMIGA P100 manual." .

[32] J. Workman Jr, *The Handbook of Organic Compounds, Three-Volume Set: NIR, IR, R, and UV-Vis Spectra Featuring Polymers and Surfactants*. Elsevier, 2000.

[33] Michigan State University, “Infrared Spectroscopy.” [Online]. Available: https://www2.chemistry.msu.edu/faculty/reusch/virttxtjml/Spectrpy/InfraRed/infrared.htm. [Accessed: 21-Apr-2016].

[34] H. Zarringhalam, N. Hopkinson, N. F. Kamperman, and J. J. de Vlieger, “Effects of processing on microstructure and properties of SLS Nylon 12,” *Mater. Sci. Eng. A*, vol. 435–436, pp. 172–180, Nov. 2006.

[35] N. Hopkinson, R. Hague, and P. Dickens, *Rapid manufacturing: an industrial revolution for the digital age*. John Wiley & Sons, 2006.

[36] Wohlers Associates, “Wohlers Report, https://wohlersassociates.com/2014report.htm,” 2014.

[37] Materialise, “3D Printing Materials, Additive Manufacturing at Materialise.” [Online]. Available: https://www.materialise.com/en/manufacturing/materials. [Accessed: 15-Dec-2018].

[38] Prodways, “Plastic powders for laser sintering 3D printing.” [Online]. Available: https://www.prodways.com/en/type/plastic-powders/. [Accessed: 15-Dec-2018].

[39] EOS, “High-end Plastic Materials for Additive Manufacturing.” [Online]. Available: https://www.eos.info/material-p. [Accessed: 15-Dec-2018].

[40] Arkema, “PEKK Polyetherketoneketone – Arkema.com.” [Online]. Available: https://www.arkema.com/en/products/product-families/pekk-kepstan/. [Accessed: 15-Dec-2018].

[41] Toray, “Toraymill™PPS.” [Online]. Available: https://www.toray.jp/chemical/en/polymer/pol_004h.html. [Accessed: 15-Dec-2018].

[42] S. Sinha Ray and M. Okamoto, “Polymer/layered silicate nanocomposites: a review from preparation to processing,” *Prog. Polym. Sci.*, vol. 28, no. 11, pp. 1539–1641, 2003.

[43] J. H. Koo *et al.*, “Innovative selective laser sintering rapid manufacturing using nanotechnology,” in *Proceedings SFF Symposium, Austin (TX), USA*, 2005, pp. 98–108.

[44] H. C. H. Ho, W. L. Cheung, and I. Gibson, “Effects of graphite powder on the laser sintering behaviour of polycarbonate,” *Rapid Prototyp. J.*, vol. 8, no. 4, pp. 233–242, 2002.

[45] C. E. Carraher, *Seymour/Carraher’s Polymer Chemistry*, 7th ed. Boca Raton: CRC Press, Taylor & Francis Group, 2007.

[46] J. P. Kruth, X. Wang, T. Laoui, and L. Froyen, “Lasers and materials in selective laser sintering,” *Assem. Autom.*, vol. 23, no. 4, pp. 357–371, 2003.

[47] E. D. Dickens *et al.*, “Sinterable semi-crystalline powder and near-fully dense article formed therewith,” US 6136948, 24-Oct-2000.

[48] University of Cambridge, “Engineering tripos part IIa: module 3C1 manufacturing engineering tripos part IIa: module 3P1 2012-13 polymer processing.” [Online]. Available: www.wrap.org.uk. [Accessed: 28-Jul-2019].

[49] M. H. E. van der Beek, “Specific volume of polymers: Influence of the thermomechanical history. PhD Thesis,” Eindhoven University of Technology, 2005.

[50] J.-P. Kruth, G. Levy, R. Schindel, T. Craeghs, and E. Yasa, “Consolidation of polymer powders by selective laser sintering,” in *Proceedings of the 3rd International Conference on Polymers and Moulds Innovations*, 2008, pp. 15–30.

[51] O. R. Ghita, E. James, R. Trimble, and K. E. Evans, “Physico-chemical behaviour of Poly (Ether Ketone) (PEK) in High Temperature Laser Sintering (HT-LS),” *J. Mater. Process. Technol.*, vol. 214, no. 4, pp. 969–978, Apr. 2014.

[52] F. Neugebauer, V. Ploshikhin, J. Ambrosy, and G. Witt, “Isothermal and non-isothermal crystallization kinetics of polyamide 12 used in laser sintering,” *J. Therm. Anal. Calorim.*, vol. 124, no. 2, pp. 925–933, 2016.

[53] K. Senthilkumaran, P. M. Pandey, and P. V. M. Rao, “Influence of building strategies on the accuracy of parts in selective laser sintering,” *Mater. Des.*, vol. 30, no. 8, pp. 2946–2954, 2009.

[54] R. D. Goodridge, R. J. M. Hague, and C. J. Tuck, “An empirical study into laser sintering of ultra-high molecular weight polyethylene (UHMWPE),” *J. Mater. Process. Technol.*, vol. 210, no. 1, pp. 72–80, Jan. 2010.

[55] M. Schmid, A. Amado, and K. Wegener, “Materials perspective of polymers for additive manufacturing with selective laser sintering,” *J. Mater. Res.*, vol. 29, no. 17, pp. 1824–1832, Jul. 2014.

[56] B. Partee, S. J. Hollister, and S. Das, “Selective laser sintering process optimization for layered manufacturing of CAPA® 6501 polycaprolactone bone tissue engineering scaffolds,” *J. Manuf. Sci. Eng.*, vol. 128, no. 2, pp. 531–540, 2006.

[57] S. Berretta, Y. Wang, R. Davies, and O. R. Ghita, “Polymer viscosity, particle coalescence and mechanical performance in high-temperature laser sintering,” *J. Mater. Sci.*, vol. 51, no. 10, pp. 4778–4794, Feb. 2016.

[58] A. Wegner, “New Polymer Materials for the Laser Sintering Process: Polypropylene and Others,” *Phys. Procedia*, vol. 83, pp. 1003–1012, 2016.

[59] A. Almabrouk Mousa, “Experimental investigations of curling phenomenon in selective laser sintering process,” *Rapid Prototyp. J.*, vol. 22, no. 2, pp. 405–415, Mar. 2016.

[60] A. E. Tontowi and T. H. C. Childs, “Density prediction of crystalline polymer sintered parts at various powder bed temperatures,” *Rapid Prototyp. J.*, vol. 7, no. 3, pp. 180–184, 2001.

[61] I. Gibson and D. Shi, “Material properties and fabrication parameters in selective laser sintering process,” *Rapid Prototyp. J.*, vol. 3, no. 4, pp. 129–136, 1997.

[62] G. M. Vasquez, C. E. Majewski, B. Haworth, and N. Hopkinson, “A targeted material selection process for polymers in laser sintering,” *Addit. Manuf.*, vol. 1, pp. 127–138, 2014.

[63] K. Dotchev and W. Yusoff, “Recycling of polyamide 12 based powders in the laser sintering process,” *Rapid Prototyp. J.*, vol. 15, no. 3, pp. 192–203, May 2009.

[64] K. Plummer, M. Vasquez, C. Majewski, and N. Hopkinson, “Study into the recyclability of a thermoplastic polyurethane powder for use in laser sintering,” *Proc. Inst. Mech. Eng. Part B J. Eng. Manuf.*, vol. 226, no. 7, pp. 1127–1135, Apr. 2012.

[65] U. Ajoku, N. Saleh, N. Hopkinson, R. Hague, and P. Erasenthiran, “Investigating

mechanical anisotropy and end-of-vector effect in laser-sintered nylon parts," *Proc. Inst. Mech. Eng. Part B, J. Eng. Manuf.*, vol. 220, no. 7, pp. 1077–1086, 2006.

[66] N. K. Tolochko, Y. V Khlopkov, S. E. Mozzharov, M. B. Ignatiev, T. Laoui, and V. I. Titov, "Absorptance of powder materials suitable for laser sintering," *Rapid Prototyp. J.*, vol. 6, no. 3, pp. 155–161, 2000.

[67] M. M. Savalani, L. Hao, and R. A. Harris, "Evaluation of CO2 and Nd: YAG lasers for the selective laser sintering of HAPEX®," *Proc. Inst. Mech. Eng. Part B J. Eng. Manuf.*, vol. 220, no. 2, pp. 171–182, 2006.

[68] A. Simchi, "The role of particle size on the laser sintering of iron powder," *Metall. Mater. Trans. B*, vol. 35, no. 5, pp. 937–948, 2004.

[69] P. Hesse, T. Paul, and R. Weiss, "Powder for layerwise manufacturing of objects," US8710144B2, 29-Apr-2014.

[70] M. Vyroubalova, "Fracture surface analysis of selective laser sintered polyamide," *Chem. List.*, vol. 105, pp. s589–s590, 2011.

[71] A. Wegner and G. Witt, "Understanding the decisive thermal processes in laser sintering of polyamide 12," in *The 30th International Conference of the Polymer Processing Society*, 2015.

[72] G. V Barbosa-Cánovas, *Food Engineering - Volume I*. EOLSS Publications, 2009.

[73] B. Bhandari, N. Bansal, M. Zhang, and P. Schuck, *Handbook of food powders*. Woodhead Publishing, 2013.

[74] M. S. Rahman, *Handbook of food preservation*. CRC press, 2007.

[75] M. M. Lexow and D. Drummer, "New Materials for SLS: The Use of Antistatic and Flow Agents," *J. Powder Technol.*, vol. 2016, 2016.

[76] K. L. Mittal and R. Jaiswal, *Particle adhesion and removal*. John Wiley & Sons, 2015.

[77] A. Castellanos, "The relationship between attractive interparticle forces and bulk behaviour in dry and uncharged fine powders," *Adv. Phys.*, vol. 54, no. 4, pp. 263–376, 2005.

[78] EXAIR, "Static Eliminators: Eliminate Static and Blowoff Dust with Ionized Compressed Air." [Online]. Available: http://www.exair.com/en-US/Primary Navigation/Products/Static Eliminators/Pages/Static Eliminators.aspx. [Accessed: 15-Jun-2017].

[79] M. Krantz, H. Zhang, and J. Zhu, "Characterization of powder flow: Static and dynamic testing," *Powder Technol.*, vol. 194, no. 3, pp. 239–245, 2009.

[80] Y. Guo, H. S. Patanwala, B. Bognet, and A. W. K. Ma, "Inkjet and inkjet-based 3D printing: connecting fluid properties and printing performance," *Rapid Prototyp. J.*, vol. 23, no. 3, pp. 562–576, 2017.

[81] B. Derby, "Inkjet Printing of Functional and Structural Materials: Fluid Property Requirements, Feature Stability, and Resolution," *Annu. Rev. Mater. Res.*, vol. 40, no. 1, pp. 395–414, Jun. 2010.

[82] S. D. Hoath, *Fundamentals of inkjet printing: the science of inkjet and droplets*. John Wiley & Sons, 2016.

[83] M. Vaezi, S. Chianrabutra, B. Mellor, and S. Yang, "Multiple material additive manufacturing–Part 1: a review," *Virtual Phys. Prototyp.*, vol. 8, no. 1, pp. 19–50, 2013.

[84] D. Kim, S. H. Lee, S. Jeong, and J. Moon, "All-ink-jet printed flexible organic thin-film transistors on plastic substrates," *Electrochem. Solid-State Lett.*, vol. 12, no. 6, pp. H195–H197, 2009.

[85] S. Jung, A. Sou, E. Gili, and H. Sirringhaus, "Inkjet-printed resistors with a wide resistance range for printed read-only memory applications," *Org. Electron.*, vol. 14, no. 3, pp. 699–702, 2013.

[86] G. L. Goh, J. Ma, K. L. F. Chua, A. Shweta, W. Y. Yeong, and Y. P. Zhang, "Inkjet-printed patch antenna emitter for wireless communication application," *Virtual Phys. Prototyp.*, vol. 11, no. 4, pp. 289–294, 2016.

[87] Y. L. Kong *et al.*, "3D printed quantum dot light-emitting diodes," *Nano Lett.*, vol. 14, no. 12, pp. 7017–7023, 2014.

[88] D. Radulescu, N. Schwade, and D. Wawro, "Uniform paclitaxel-loaded biodegradable microspheres manufactured by ink-jet technology," in *Proc Winter Symp and 11th Int Symp On Adv Drug Del Sys., Salt Lake City*, 2003.

[89] M. J. Uddin, N. Scoutaris, P. Klepetsanis, B. Chowdhry, M. R. Prausnitz, and D. Douroumis, "Inkjet printing of transdermal microneedles for the delivery of anticancer agents," *Int. J. Pharm.*, vol. 494, no. 2, pp. 593–602, 2015.

[90] Fujifilm, "Jettable Fluid Formulation Guidelines," *may 16, 2013*. [Online]. Available: https://www.fujifilmusa.com/shared/bin/Dimatix_Materials_Printer_Jettable_Fluid_Formulation_Guidelines_05-13.pdf. [Accessed: 15-Feb-2018].

[91] Nordson EFD, "PICO Pµlse Series Valves - Operating Manual." .

[92] J. Ledesma Fernandez, "Jetting of multiple functional materials by additive manufacturing, PhD Thesis," University of Nottingham, 2018.

[93] D. Jang, D. Kim, and J. Moon, "Influence of Fluid Physical Properties on Ink-Jet Printability," *Langmuir*, vol. 25, no. 5, pp. 2629–2635, Mar. 2009.

[94] C. Clasen, P. M. Phillips, L. Palangetic, and and J. Vermant, "Dispensing of rheologically complex fluids: The map of misery," *AIChE J.*, vol. 58, no. 10, pp. 3242–3255, Oct. 2012.

[95] S. D. Hoath *et al.*, "Inkjet printing of weakly elastic polymer solutions," *J. Nonnewton. Fluid Mech.*, vol. 205, pp. 1–10, Mar. 2014.

[96] U. S. Bhansali, M. A. Khan, and H. N. Alshareef, "Organic ferroelectric memory devices with inkjet-printed polymer electrodes on flexible substrates," *Microelectron. Eng.*, vol. 105, pp. 68–73, May 2013.

[97] D. Xu *et al.*, "Inkjet printing of polymer solutions and the role of chain entanglement," *J. Mater. Chem.*, vol. 17, no. 46, pp. 4902–4907, 2007.

[98] R. I. Haque, R. Vié, M. Germainy, L. Valbin, P. Benaben, and X. Boddaert, "Inkjet printing of high molecular weight PVDF-TrFE for flexible electronics," *Flex. Print. Electron.*, vol. 1, no. 1, p. 15001, 2015.

[99] D. C. Vadillo, S. D. Hoath, W.-K. Hsiao, and M. R. Mackley, "The effect of inkjet ink

composition on rheology and jetting behaviour," in *NIP & Digital Fabrication Conference*, 2011, vol. 2011, no. 2, pp. 568–572.

[100] M. Kuang, L. Wang, and Y. Song, "Controllable Printing Droplets for High-Resolution Patterns," *Adv. Mater.*, vol. 26, no. 40, pp. 6950–6958, Oct. 2014.

[101] C. Seo, D. Jang, J. Chae, and S. Shin, "Altering the coffee-ring effect by adding a surfactant-like viscous polymer solution," *Sci. Rep.*, vol. 7, no. 1, p. 500, 2017.

[102] Y. Li, Q. Yang, M. Li, and Y. Song, "Rate-dependent interface capture beyond the coffee-ring effect," *Sci. Rep.*, vol. 6, p. 24628, Apr. 2016.

[103] D. Soltman and V. Subramanian, "Inkjet-Printed Line Morphologies and Temperature Control of the Coffee Ring Effect," *Langmuir*, vol. 24, no. 5, pp. 2224–2231, Mar. 2008.

[104] A. M. J. Edwards, R. Ledesma-Aguilar, M. I. Newton, C. V Brown, and G. McHale, "Not spreading in reverse: The dewetting of a liquid film into a single drop," *Sci. Adv.*, vol. 2, no. 9, Sep. 2016.

[105] Y. Li, C. Lv, Z. Li, D. Quéré, and Q. Zheng, "From coffee rings to coffee eyes," *Soft Matter*, vol. 11, no. 23, pp. 4669–4673, 2015.

[106] R. D. Deegan, "Pattern formation in drying drops," *Phys. Rev. E*, vol. 61, no. 1, pp. 475–485, 2000.

[107] Z. Lin and S. Granick, "Patterns Formed by Droplet Evaporation from a Restricted Geometry," *J. Am. Chem. Soc.*, vol. 127, no. 9, pp. 2816–2817, Mar. 2005.

[108] P. J. Yunker, T. Still, M. A. Lohr, and A. G. Yodh, "Suppression of the coffee-ring effect by shape-dependent capillary interactions," *Nature*, vol. 476, no. 7360, p. 308, 2011.

[109] D. J. Harris, H. Hu, J. C. Conrad, and J. A. Lewis, "Patterning colloidal films via evaporative lithography," *Phys. Rev. Lett.*, vol. 98, no. 14, p. 148301, 2007.

[110] T. Kajiya*, D. Kaneko, and M. Doi, "Dynamical Visualization of 'Coffee Stain Phenomenon' in Droplets of Polymer Solution via Fluorescent Microscopy," *Langmuir*, vol. 24, no. 21, pp. 12369–12374, Nov. 2008.

[111] D. W. Smith, S. T. Iacono, and S. S. Iyer, *Handbook of fluoropolymer science and technology*. John Wiley & Sons, 2014.

[112] J. G. Drobny, *Technology of Fluoropolymers*, 2nd ed. Boca Raton: CRC Press Taylor & Francis Group, 2009.

[113] S. Ebnesajiad and P. R. Khaladkar, "Fluoropolymer Applications in Chemical Processing Industries, The Definitive User's Guide and Databook; William Andrew, Inc.: Norwich, NY, 2004;(c) B. Ameduri; B. Boutevin, Well-Architectured Fluoropolymers: Synthesis, Properties and Applications." Elsevier: Amsterdam, 2004.

[114] Wiley-VCH, *Ullmann's Polymers and Plastics: Products and Processes*. Wiley, 2016.

[115] D. O'Hagan, "Understanding organofluorine chemistry. An introduction to the C–F bond," *Chem. Soc. Rev.*, vol. 37, no. 2, pp. 308–319, 2008.

[116] D. A. Dixon, B. E. Smart, P. J. Krusic, and N. Matsuzawa, "Bond energies in organofluorine systems: applications to Teflon® and fullerenes," *J. Fluor. Chem.*, vol. 72, no. 2, pp. 209–214, Jun. 1995.

[117] Savillex, "PTFE 3D Chemical structure." [Online]. Available:

http://www.savillex.com/UserFiles/Images/PTFE 3D Chemical Structure.jpg. [Accessed: 18-Apr-2016].

[118] E. N. Brown, D. M. Dattelbaum, D. W. Brown, P. J. Rae, and B. Clausen, "A new strain path to inducing phase transitions in semi-crystalline polymers," *Polymer (Guildf).*, vol. 48, no. 9, pp. 2531–2536, Apr. 2007.

[119] D. L. Kerbow and J. Scheirs, *Modern Fluoropolymers*. John Wiley and Sons, 1997.

[120] S. Ebnesajjad, *Fluoroplastics Volume 1: Non-Melt Processible Fluoropolymers - The Definitive User ' s Guide and Data Book*, 2nd ed. Waltham, USA: Elsevier Inc., 2015.

[121] "Ethylene, Material Safety Data Sheet." [Online]. Available: http://www.sigmaaldrich.com/. [Accessed: 26-Feb-2015].

[122] Matheson, "Tetrafluoroethylene (TFE), Material Safety Data Sheet." [Online]. Available: http://www.mathesongas.com/pdfs/msds/MAT22980.pdf. [Accessed: 18-Apr-2016].

[123] Synquest Laboratories, "Chlorotrifluoroethylene (CTFE), MSDS." [Online]. Available: http://synquestlabs.com/product/id/6734.html. [Accessed: 18-Apr-2016].

[124] Synquest Laboratories, "1,1-Difluoroethylene (VDF), MSDS." [Online]. Available: http://synquestlabs.com/product/id/52401.html. [Accessed: 18-Apr-2016].

[125] Synquest Laboratories, "Vinyl fluoride (VF), MSDS." [Online]. Available: http://synquestlabs.com/product/id/28129.html. [Accessed: 18-Apr-2016].

[126] Sigma Aldrich, "Propene, MSDS." [Online]. Available: http://www.sigmaaldrich.com/. [Accessed: 18-Apr-2016].

[127] DuPont, "Fluorointermediates." [Online]. Available: http://www2.dupont.com/FluoroIntermediates/en_US/products/index.html. [Accessed: 16-Feb-2015].

[128] T. A. Osswald, E. Baur, S. Brinkmann, K. Oberbach, and E. Schmachtenberg, *International Plastics Handbook - The Resource for Plastics Engineers (4th Edition)*. Hanser Publishers, 2006.

[129] PlasticEurope, "Guide for the Safe Handling of Fluoropolymer Resins." 2012.

[130] M. Kutz, *Applied plastics engineering handbook: processing and materials*. William Andrew, 2011.

[131] F. Dos Santos, "Formulation of an electroactive ink jet printing ink," FR3066495A1.

[132] C. Lee and J. A. Tarbutton, "Electric poling-assisted additive manufacturing process for PVDF polymer-based piezoelectric device applications," *Smart Mater. Struct.*, vol. 23, no. 9, p. 95044, 2014.

[133] D. A. Porter, T. V. T. Hoang, and T. A. Berfield, "Effects of in-situ poling and process parameters on fused filament fabrication printed PVDF sheet mechanical and electrical properties," *Addit. Manuf.*, vol. 13, pp. 81–92, 2017.

[134] S. Zhang, Z. Liang, Q. Wang, and Q. M. Zhang, "Ink-jet printing of ferroelectric poly(vinylidene fluoride-trifluoroethylene) copolymers," *MRS Proc.*, vol. 889, pp. 0889-W05-02, Jan. 2005.

[135] D. Thuau, K. Kallitsis, F. D. Dos Santos, and G. Hadziioannou, "All inkjet-printed

piezoelectric electronic devices: energy generators, sensors and actuators," *J. Mater. Chem. C*, vol. 5, no. 38, pp. 9963–9966, 2017.

[136] O. Pabst, J. Perelaer, E. Beckert, U. S. Schubert, R. Eberhardt, and A. Tünnermann, "All inkjet-printed piezoelectric polymer actuators: Characterization and applications for micropumps in lab-on-a-chip systems," *Org. Electron.*, vol. 14, no. 12, pp. 3423–3429, Dec. 2013.

[137] O. Pabst *et al.*, "Inkjet printed micropump actuator based on piezoelectric polymers: Device performance and morphology studies," *Org. Electron.*, vol. 15, no. 11, pp. 3306–3315, 2014.

[138] W. Huang *et al.*, "Microstructure , Mechanical , and Biological Properties of Porous Poly (vinylidene fluoride) Scaffolds Fabricated by Selective Laser Sintering," *Int. J. Polym. Sci.*, vol. 2015, pp. 1–9, 2015.

[139] MakeItFrom, "Polyvinylidene Fluoride (PVDF) Material Properties." [Online]. Available: http://www.makeitfrom.com/material-properties/Polyvinylidene-Fluoride-PVDF/. [Accessed: 27-Apr-2016].

[140] S. Ebnesajjad, *Fluoroplastics, Volume 2: Melt Processible Fluoropolymers-The Definitive User's Guide and Data Book*, 2nd ed. Elsevier Inc., 2015.

[141] C. Shuai *et al.*, "Tailoring properties of porous Poly (vinylidene fluoride) scaffold through nano-sized 58s bioactive glass," *J. Biomater. Sci. Polym. Ed.*, vol. 27, no. 1, pp. 97–109, 2016.

[142] C. Shuai *et al.*, "Nanodiamond reinforced polyvinylidene fluoride/bioglass scaffolds for bone tissue engineering," *J. Porous Mater.*, vol. 24, no. 1, pp. 249–255, 2017.

[143] W. Huang *et al.*, "MgO whiskers reinforced poly(vinylidene fluoride) scaffolds," *RSC Adv.*, vol. 6, no. 110, pp. 108196–108202, 2016.

[144] "3M pioneers 3D printing with PTFE." [Online]. Available: https://www.3m.co.uk/3M/en_GB/design-and-specialty-materials-uk/products/full-story/?storyid=238bb6ed-2857-4929-93c5-a1c9cc684776. [Accessed: 27-Jun-2018].

[145] Wiley-VCH, *Ullmann's Encyclopedia of Industrial Chemistry*, 7th ed. Weinheim: Wiley-VCH Verlag GmbH & Co. KGaA: Weinheim, Germany, 2011.

[146] S. Ebnesajjad, *Introduction to Fluoropolymers: Materials, Technology and Applications*. William Andrew, 2013.

[147] E. S. Clark, "The molecular conformations of polytetrafluoroethylene: forms II and IV," *Polymer (Guildf).*, vol. 40, no. 16, pp. 4659–4665, Jul. 1999.

[148] MatWeb, "Daikin NEOFLON M-400H PCTFE Granular Molding Powder." [Online]. Available: http://www.matweb.com/search/datasheet.aspx?matguid=c8a9d395a25249e59833a60eb558fbbb. [Accessed: 19-Apr-2016].

[149] F. Boschet and B. Ameduri, "(Co)polymers of Chlorotrifluoroethylene: Synthesis, Properties, and Applications," *Chem. Rev.*, vol. 114, no. 2, pp. 927–980, Jan. 2014.

[150] Daikin, "NEOFLON PCTFE Molding Powder," 2003. [Online]. Available: http://www.daikinchem.de/downloads/PCTFE.pdf. [Accessed: 05-Feb-2016].

[151] S. C. Lin, B. Kent, C. A. Wilkie, A. B. Morgan, and G. L. Nelson, "In Fire and Polymers V:

Materials and Concepts for Fire Retardancy," in *CA Wilkie, AB Morgan, GL Nelson, Eds*, 2009, pp. 288–297.

[152] G. J. Samuels, G. J. Shafer, T. Li, C. A. Threlfall, N. Iwamoto, and E. J. Rainal, "Copolymers for barriers," WO2008079986A1, 03-Jul-2008.

[153] J. D. Hoffman and J. J. Weeks, "Specific volume and degree of crystallinity of semicrystalline polychlorotrifluoroethylene, and estimated specific volumes of the pure amorphous and crystalline phases," *J. Res. Natl. Bur. Stand.*, vol. 60, p. 465, 1958.

[154] H. H. Luther, P. Hickman, and A. V. Astin, "Research Highlights of the National Bureau of Standards," 1961.

[155] C. P. Carpenter, H. F. Smyth Jr, and U. C. Pozzani, "The assay of acute vapor toxicity, and the grading and interpretation of results on 96 chemical compounds.," *J. Ind. Hyg. Toxicol.*, vol. 31, no. 6, pp. 343–346, 1949.

[156] J. J. M. Hamilton, "Polymerization of trifluorochloroethylene in the presence of silver ion, bisulfite ion and persulfate," US 2569524 A, 02-Oct-1951.

[157] G. F. Roedel, "Method for polymerizing chlorotrifluoroethylene," US 2613202 A, 07-Oct-1952.

[158] T. Bruce and D. M. Young, "Process for polymerizing chlorotrifluoroethylene with bis-heptafluorobutyryl peroxide," US 2700662 A, 25-Jan-1955.

[159] W. T. Miller, A. L. Dittman, and S. K. Reed, "Halogen-substituted acetyl peroxide catalyst for halo-olefin polymerization," US 2586550, 19-Feb-1952.

[160] R. L. Myers, "Reaction of Chlorotrifluoroethylene with Oxygen," *Ind. Eng. Chem.*, vol. 45, no. 8, pp. 1783–1785, Aug. 1953.

[161] W. T. Miller, "Method of making halocarbon polymers," US 2564024, 14-Aug-1951.

[162] S. Ok, S. Sadaf, and L. Walder, "Basic characterization and investigation of a fluorinated terpolymer in pure state and in mixtures with kaolinite at solid interphases of thin films prepared by facile solution cast and nonsolvent methods," *High Perform. Polym.*, vol. 26, no. 7, pp. 779–789, 2014.

[163] J. Gardiner, "Fluoropolymers: origin, production, and industrial and commercial applications," *Aust. J. Chem.*, vol. 68, no. 1, pp. 13–22, 2015.

[164] J. Drobny, *Fluoroplastics*, vol. 16. iSmithers Rapra Publishing, 2006.

[165] Zeus, "THV 221 Tubing properties." [Online]. Available: http://static6.arrow.com/aropdfconversion/70e9b97fe3ab281c2a45c13add27be814cdfad47/39399604475797896thv_zeus.pdf. [Accessed: 20-Jul-2019].

[166] S. Ok, J. Sheets, S. Welch, S. Kaya, A. Jalilov, and D. R. Cole, "Tuning hydrophobicity of a fluorinated terpolymer in differently assembled thin films," *J. Polym. Sci. Part B Polym. Phys.*, vol. 55, no. 8, pp. 643–657, Apr. 2017.

[167] S. Ok, S. A. Furquan, Z. Khan, and A. U. Dogan, "Near superhydrophobic-fluorinated THV fiber-like structures and fibers prepared by electrospinning," *High Perform. Polym.*, vol. 28, no. 2, pp. 206–214, 2016.

[168] S. Pacetti, "Use of a terpolymer of tetrafluoroethylene, hexafluoropropylene, and vinylidene fluoride in drug eluting coatings on medical devices," US20080118541A1,

22-May-2008.

[169] P. H. King, J. C. Corsi, B.-H. Pan, H. Morgan, M. R. R. de Planque, and K.-P. Zauner, "Towards molecular computing: Co-development of microfluidic devices and chemical reaction media," *Biosystems*, vol. 109, no. 1, pp. 18–23, Jul. 2012.

[170] S. Begolo, G. Colas, J.-L. Viovy, and L. Malaquin, "New family of fluorinated polymer chips for droplet and organic solvent microfluidics," *Lab Chip*, vol. 11, no. 3, pp. 508–512, 2011.

[171] C. Slim *et al.*, "Two-step local functionalization of fluoropolymer Dyneon THV microfluidic materials by scanning electrochemical microscopy combined to click reaction," *Electrochem. commun.*, vol. 60, pp. 5–8, Nov. 2015.

[172] C. Perreard *et al.*, "Electrochemically assisted micro localized grafting of aptamers in a microchannel engraved in fluorinated thermoplastic polymer Dyneon THV," *RSC Adv.*, vol. 5, no. 15, pp. 11128–11131, 2015.

[173] I. M. Hutchings and G. D. Martin, *Inkjet technology for digital fabrication*. John Wiley & Sons, 2012.

[174] pro-K Fluoropolymergroup, "pro-K Fluoropolymergroup Product information Polychlorotrifluoroethylene (PCTFE)." [Online]. Available: www.pro-kunststoff.de. [Accessed: 02-Mar-2019].

[175] Braun, "Injekt®-F Solo." [Online]. Available: https://www.bbraun.com/en/products/b/injekt-f-solo.html. [Accessed: 02-Oct-2018].

[176] Becton Dickinson and Company, "Plastipak syringes," 2016. [Online]. Available: http://downloads.consumables.com/doc/tds/100-0953_TDS.pdf. [Accessed: 02-Oct-2018].

[177] Fujifilm, "Dimatix Materials Printer DMP-2850 Data Sheet," 2016.

[178] Fujifilm, "Materials Printer, Cartridge DMP-2800, DMC-11600." [Online]. Available: https://www.fujifilmusa.com/shared/bin/FAQs_DMP-2800_Series_Printer_DMC-11600+Series+Cartridge.pdf. [Accessed: 26-Sep-2018].

[179] Nordson EFD, "PICO® Toμch™ Controller Operating Manual." .

[180] Hitachi, "Tabletop Microscope TM3030." [Online]. Available: http://www.hitachi-hightech.com/eu/product_detail/?pn=em-tm3030. [Accessed: 17-May-2016].

[181] Nikon, "Eclipse LV100 Polarizing Microscopes." [Online]. Available: https://www.nikoninstruments.com/en_GB/Products/Upright-Microscopes/Research/Eclipse-LV100-POL. [Accessed: 17-May-2016].

[182] R. L. Blaine and S. M. Marcus, "Bias in isothermal time-to-event studies due to approach to test temperature," *J. Therm. Anal.*, vol. 49, no. 3, pp. 1485–1492, Aug. 1997.

[183] R. L. Blaine, "Isothermal Crystallization Using the Q Series™ DSC and Liquid Nitrogen Cooling System," *TA Appl Notes*, 2008.

[184] ASTM International, "ASTM E2070-13, Standard Test Methods for Kinetic Parameters by Differential Scanning Calorimetry Using Isothermal Methods." West Conshohocken, PA, 2018.

[185] J. Šesták and G. Berggren, “Study of the kinetics of the mechanism of solid-state reactions at increasing temperatures,” *Thermochim. Acta*, vol. 3, no. 1, pp. 1–12, 1971.

[186] V. M. Gorbachev, “Some aspects of Šestak’s generalized kinetic equation in thermal analysis,” *J. Therm. Anal. Calorim.*, vol. 18, no. 1, pp. 193–197, 1980.

[187] Conservation and Art Materials Encyclopedia Online (CAMEO), “Polychlorotrifluoroethylene.” [Online]. Available: http://cameo.mfa.org/wiki/Polychlorotrifluoroethylene. [Accessed: 12-Feb-2016].

[188] AZO Materials, “Polychlorotrifluoroethylene (PCTFE) - Supplier Data by Goodfellow.” [Online]. Available: https://www.azom.com/article.aspx?ArticleID=2342. [Accessed: 28-Jun-2018].

[189] S. Anton and F. Otto, “Solutions and swollen masses of polymerized trifluorochlorethylene,” US2851462 A, 09-Sep-1958.

[190] F. Muller, A. Pfister, and M. Leuterer, “Paek powder, in particular for the use in a method for a layer-wise manufacturing of a three-dimensional object, as well as method for producing it,” US20120114848A1, 10-May-2012.

[191] J. Schmidt *et al.*, “A novel process route for the production of spherical LBM polymer powders with small size and good flowability,” *Powder Technol.*, vol. 261, pp. 78–86, 2014.

[192] Freeman Technology, “FT4 Powder Rheometer manual.” .

[193] S. Ziegelmeier, F. Wöllecke, C. Tuck, R. D. Goodridge, and R. Hague, “Characterizing the bulk & flow behaviour of LS polymer powders,” in *Proceedings SFF Symposium, Austin (TX), USA*, 2013.

[194] S. Ziegelmeier *et al.*, “An experimental study into the effects of bulk and flow behaviour of laser sintering polymer powders on resulting part properties,” *J. Mater. Process. Technol.*, vol. 215, no. 1, pp. 239–250, 2015.

[195] 3M, “3M™ Dyneon™ Fluoroplastic THV 221AZ Product Description.” [Online]. Available: http://multimedia.3m.com/mws/media/688837O/td-thv-221az-eng.pdf. [Accessed: 09-Feb-2018].

[196] J. W. Johnson, “Safety assessment of MIBK (methyl isobutyl ketone),” *Int. J. Toxicol.*, vol. 23, pp. 29–57, 2004.

[197] Louisiana State University, “Common solvent properties.” [Online]. Available: http://macro.lsu.edu/HowTo/solvents.htm. [Accessed: 05-Feb-2018].

[198] Taminco, “TDS - Dimethylacetamide (DMAc), Eastman Chemical Company.” [Online]. Available: http://ws.eastman.com/ProductCatalogApps/PageControllers/ProdDatasheet_PC.aspx?product=71103648. [Accessed: 05-Feb-2018].

[199] A. Heritage, *A basic introduction to rheology*. Bohlin Instruments Ltd., 1994.

[200] J. W. Murray, J. C. Walker, and A. T. Clare, “Nanostructures in austenitic steel after EDM and pulsed electron beam irradiation,” *Surf. Coatings Technol.*, vol. 259, pp. 465–472, Nov. 2014.

[201] Y. Uno, A. Okada, K. Uemura, P. Raharjo, T. Furukawa, and K. Karato, “High-efficiency

finishing process for metal mold by large-area electron beam irradiation," *Precis. Eng.*, vol. 29, no. 4, pp. 449–455, Oct. 2005.

[202] D. I. Proskurovsky, V. P. Rotshtein, G. E. Ozur, Y. F. Ivanov, and A. B. Markov, "Physical foundations for surface treatment of materials with low energy, high current electron beams," *Surf. Coatings Technol.*, vol. 125, no. 1–3, pp. 49–56, Mar. 2000.

[203] A. V Batrakov, A. B. Markov, G. E. Ozur, D. I. Proskurovsky, and V. P. Rotshtein, "Surface alloying of metallic substrates with pre-deposited films through a pulsed electron-beam mixing," *Eur. Phys. Journal-Applied Phys.*, vol. 43, no. 3, pp. 283–288, 2008.

[204] C. A. Gómez, R. Su, A. Thompson, J. DiSciacca, S. Lawes, and R. K. Leach, "Optimisation of surface topography characterisation for metal additive manufacturing using coherence scanning interferometry," in *Proc. euspen/ASPE Dimensional Accuracy & Surface Finish in AM*, 2017.

[205] ASTM International, "ASTM D638-14 Standard Test Method for Tensile Properties of Plastics." West Conshohocken, PA, 2014.

[206] T. Silverman, M. Naffakh, C. Marco, and G. Ellis, "Effect of WS2 Inorganic Nanotubes on Isothermal Crystallization Behavior and Kinetics of Poly(3-Hydroxybutyrate-co-3-hydroxyvalerate)," *Polymers* , vol. 10, no. 2. 2018.

[207] K. Wudy, L. Lanzl, and D. Drummer, "Selective Laser Sintering of Filled Polymer Systems: Bulk Properties and Laser Beam Material Interaction," *Phys. Procedia*, vol. 83, pp. 991–1002, 2016.

[208] D. Drummer, D. Rietzel, and F. Kühnlein, "Development of a characterization approach for the sintering behavior of new thermoplastics for selective laser sintering," *Phys. Procedia*, vol. 5, pp. 533–542, 2010.

[209] THASS - Thermal Analysis & Surface Science, "Buoyancy Phenomenon in TGA Systems." [Online]. Available: http://thass.net. [Accessed: 17-Sep-2018].

[210] Q. Lei, C. E. J. Dancer, C. R. M. Grovenor, and P. S. Grant, "Preparation, microstructure and microwave dielectric properties of sprayed PFA/barium titanate composite films," *Compos. Sci. Technol.*, vol. 129, pp. 198–204, Jun. 2016.

[211] M. Bromley, "Personal communication." 2015.

[212] S. C. De Araujo and Y. Kawano, "Near-infrared spectra of polyamide 6, poly(vinyl chloride), and polychlorotrifluoroethylene," *J. Appl. Polym. Sci.*, vol. 85, no. 1, pp. 199–208, Jul. 2002.

[213] SciFinder, "PCTFE IR spectra, Spectral data were obtained from Wiley Subscription Services, Inc. (US), Spectrum ID: HIP-1_HU-04-IRSPC-1615." .

[214] C. Y. Liang and S. Krimm, "Infrared Spectra of High Polymers. III. Polytetrafluoroethylene and Polychlorotrifluoroethylene," *J. Chem. Phys.*, vol. 25, no. 3, p. 563, 1956.

[215] N. Hopkinson and P. Erasenthiran, "High speed sintering-early research into a new rapid manufacturing process," in *Proceedings SFF Symposium, Austin (TX), USA*, 2004, pp. 312–320.

[216] C. Von Burg, "Additive manufacturing device with a heating device," US20180085998A1, 29-Mar-2018.

[217] I. P. F. Richards, T. M. N. Garabet, I. S. Bitar, and F. M. Salmon, “Optimising thermoplastic polyurethane for desktop laser sintering.”

[218] Y. Ji, J. Liu, Y. Jiang, and Y. Liu, “Analysis of Raman and infrared spectra of poly(vinylidene fluoride) irradiated by KrF excimer laser,” *Spectrochim. Acta Part A Mol. Biomol. Spectrosc.*, vol. 70, no. 2, pp. 297–300, Jul. 2008.

[219] M. Lessel, P. Loskill, F. Hausen, N. N. Gosvami, R. Bennewitz, and K. Jacobs, “Impact of van der Waals Interactions on Single Asperity Friction,” *Phys. Rev. Lett.*, vol. 111, no. 3, p. 035502, Jul. 2013.

[220] F. E. Baumann and N. Wilczok, “Preparation of precipitated polyamide powders of narrow particle size distribution and low porosity.” Google Patents, 03-Aug-1999.

[221] Freeman Technology, “FT4 Powder Rheometer System.” [Online]. Available: http://www.freemantech.co.uk/_powders/?pt=About the FT4 Page&p=MQ==. [Accessed: 04-May-2016].

[222] C. H. Clausen, D. J. Mickish, W. J. Nebe, and S. R. Vaidya, “Laser sinterable thermoplastic powder,” US 6110411 A, 29-Aug-2000.

[223] H. Chung and S. Das, “Functionally graded Nylon-11/silica nanocomposites produced by selective laser sintering,” *Mater. Sci. Eng. A*, vol. 487, no. 1–2, pp. 251–257, 2008.

[224] EOS, “Formiga P100 Software manual.” 2017.

[225] M. Drexler, M. Lexow, and D. Drummer, “Selective Laser Melting of Polymer Powder – Part Mechanics as Function of Exposure Speed,” *Phys. Procedia*, vol. 78, pp. 328–336, 2015.

[226] M. Vasquez, B. Haworth, and N. Hopkinson, “Optimum sintering region for laser sintered nylon-12,” *Proc. Inst. Mech. Eng. Part B J. Eng. Manuf.*, vol. 225, no. 12, pp. 2240–2248, Oct. 2011.

[227] K. Dai and L. Shaw, “Distortion minimization of laser-processed components through control of laser scanning patterns,” *Rapid Prototyp. J.*, vol. 8, no. 5, pp. 270–276, 2002.

[228] W. S. Land, B. Zhang, J. Ziegert, and A. Davies, “In-Situ Metrology System for Laser Powder Bed Fusion Additive Process,” *Procedia Manuf.*, vol. 1, pp. 393–403, 2015.

[229] S. Catchpole-Smith, N. Aboulkhair, L. Parry, C. Tuck, I. A. Ashcroft, and A. Clare, “Fractal scan strategies for selective laser melting of ‘unweldable’nickel superalloys,” *Addit. Manuf.*, vol. 15, pp. 113–122, 2017.

[230] A. Jayakumar, S. Singamneni, M. Ramos, A. M. Al-Jumaily, and S. S. Pethaiah, “Manufacturing the Gas Diffusion Layer for PEM Fuel Cell Using a Novel 3D Printing Technique and Critical Assessment of the Challenges Encountered,” *Materials (Basel).*, vol. 10, no. 7, p. 796, 2017.

[231] Z.-X. Low, Y. T. Chua, B. M. Ray, D. Mattia, I. S. Metcalfe, and D. A. Patterson, “Perspective on 3D printing of separation membranes and comparison to related unconventional fabrication techniques,” *J. Memb. Sci.*, vol. 523, pp. 596–613, 2017.

[232] T. Niino, H. Haraguchi, Y. Itagaki, S. Iguchi, and M. Hagiwara, “Feasibility study on plastic laser sintering without powder bed preheating,” in *Proceedings SFF Symposium, Austin (TX), USA*, 2011, vol. 20, pp. 0–5.

[233] T. Niino and T. Uehara, “Low temperature selective laser melting of high tempertaure

plastic powder," in *Proceedings SFF Symposium, Austin (TX), USA*, 2015, pp. 866–877.

[234] J. Bai, B. Zhang, J. Song, G. Bi, P. Wang, and J. Wei, "The effect of processing conditions on the mechanical properties of polyethylene produced by selective laser sintering," *Polym. Test.*, vol. 52, pp. 89–93, 2016.

[235] E. C. Hofland, I. Baran, and D. A. Wismeijer, "Correlation of Process Parameters with Mechanical Properties of Laser Sintered PA12 Parts," *Adv. Mater. Sci. Eng.*, vol. 2017, 2017.

[236] J.-Y. Lee, J. An, and C. K. Chua, "Fundamentals and applications of 3D printing for novel materials," *Appl. Mater. Today*, vol. 7, pp. 120–133, 2017.

[237] A. Franco, M. Lanzetta, and L. Romoli, "Experimental analysis of selective laser sintering of polyamide powders: an energy perspective," *J. Clean. Prod.*, vol. 18, no. 16–17, pp. 1722–1730, Nov. 2010.

[238] K. A. Baldwin and D. J. Fairhurst, "The effects of molecular weight, evaporation rate and polymer concentration on pillar formation in drying poly(ethylene oxide) droplets," *Colloids Surfaces A Physicochem. Eng. Asp.*, vol. 441, pp. 867–871, Jan. 2014.

[239] T. Okuzono, K. Ozawa, and M. Doi, "Simple Model of Skin Formation Caused by Solvent Evaporation in Polymer Solutions," *Phys. Rev. Lett.*, vol. 97, no. 13, p. 136103, Sep. 2006.

[240] U. W. Gedde, *Polymer physics*. Springer Science & Business Media, 2013.

[241] L. L. Spangler, J. M. Torkelson, and J. S. Royal, "Influence of solvent and molecular weight on thickness and surface topography of spin-coated polymer films," *Polym. Eng. Sci.*, vol. 30, no. 11, pp. 644–653, 1990.

[242] A. Labouriau, D. Wrobleski, G. M. Kestell, S. C. Tornga, S. Pattillo, and B. Orler, "Probing gamma-irradiation damage of polymers," in *29th Compatibility, Aging and Stockpile Stewardship Conference*, 2011.

[243] Fujifilm, "FUJIFILM Dimatix Materials Printer DMP-2800 Series User Manual." 2010.

[244] Y. He, R. D. Wildman, C. J. Tuck, S. D. R. Christie, and S. Edmondson, "An Investigation of the Behavior of Solvent based Polycaprolactone ink for Material Jetting," *Sci. Rep.*, vol. 6, p. 20852, Feb. 2016.

[245] A. M. Telford, S. C. Thickett, and C. Neto, "Functional patterned coatings by thin polymer film dewetting," *J. Colloid Interface Sci.*, vol. 507, pp. 453–469, Dec. 2017.

[246] T. Kerle, J. Klein, and R. Yerushalmi-Rozen, "Accelerated rupture at the liquid/liquid interface," *Langmuir*, vol. 18, no. 26, pp. 10146–10154, 2002.

[247] L. Xue and Y. Han, "Inhibition of dewetting of thin polymer films," *Prog. Mater. Sci.*, vol. 57, no. 6, pp. 947–979, Jul. 2012.

[248] Celltreat scientific products, "Polypropylene Chemical Compatibility Guide." [Online]. Available: https://www.celltreat.com/wp-content/uploads/Polypropylene-Chemical-Compatibility-Guide-2018.pdf. [Accessed: 28-Sep-2018].

[249] R. R. Schaller, "Moore's law: past, present and future," *IEEE Spectr.*, vol. 34, no. 6, pp. 52–59, 1997.

[250] B. Gompf, J. Beister, T. Brandt, J. Pflaum, and M. Dressel, “Nanometer-thick Au-films as antireflection coating for infrared light,” *Opt. Lett.*, vol. 32, no. 11, pp. 1578–1580, 2007.

[251] M. Bernardi, M. Palummo, and J. C. Grossman, “Extraordinary sunlight absorption and one nanometer thick photovoltaics using two-dimensional monolayer materials,” *Nano Lett.*, vol. 13, no. 8, pp. 3664–3670, 2013.

[252] P. C. Yashar and W. D. Sproul, “Nanometer scale multilayered hard coatings,” *Vacuum*, vol. 55, no. 3–4, pp. 179–190, 1999.

[253] Z. Zhang, X. Zhang, Z. Xin, M. Deng, Y. Wen, and Y. Song, “Controlled inkjetting of a conductive pattern of silver nanoparticles based on the coffee-ring effect,” *Adv. Mater.*, vol. 25, no. 46, pp. 6714–6718, 2013.

[254] K.-H. Lee, S.-M. Kim, H. Jeong, and G.-Y. Jung, “Spontaneous nanoscale polymer solution patterning using solvent evaporation driven double-dewetting edge lithography,” *Soft Matter*, vol. 8, no. 2, pp. 465–471, 2012.

[255] L. Zhang *et al.*, “Inkjet printing high-resolution, large-area graphene patterns by coffee-ring lithography,” *Adv. Mater.*, vol. 24, no. 3, pp. 436–440, 2012.

[256] V. Bromberg, S. Ma, and T. J. Singler, “High-resolution inkjet printing of electrically conducting lines of silver nanoparticles by edge-enhanced twin-line deposition,” *Appl. Phys. Lett.*, vol. 102, no. 21, p. 214101, 2013.

[257] L. Print, “Water Transfer Printing Process.” [Online]. Available: https://www.liquidprintone.com/hydrographic-water-transfer-printing/. [Accessed: 16-May-2018].

[258] 3M, “Dyneon ™ Fluorothermoplastic Product Comparison Guide Options More More Answers.” [Online]. Available: http://multimedia.3m.com/mws/media/227519O/dyneontm-fluorothermoplastic-product-comparison-guide.pdf. [Accessed: 23-Jul-2018].

[259] MakeItFrom, “Polychlorotrifluoroethylene (PCTFE) Material Properties :: MakeItFrom.com.” [Online]. Available: http://www.makeitfrom.com/material-properties/Polychlorotrifluoroethylene-PCTFE/. [Accessed: 15-Feb-2016].

[260] E. N. Brown, P. J. Rae, and E. B. Orler, “The influence of temperature and strain rate on the constitutive and damage responses of polychlorotrifluoroethylene (PCTFE, Kel-F 81),” *Polymer (Guildf).*, vol. 47, no. 21, pp. 7506–7518, Oct. 2006.

[261] J. Brandrup and E. H. Immergut, *Polymer handbook*. Wiley New York, 1975.

[262] A. M. Bueche, “Melting Temperature and Polymer—Solvent Interaction: Polychlorotrifluoroethylene,” *J. Am. Chem. Soc.*, vol. 74, no. 1, pp. 65–67, Jan. 1952.

[263] Isoflon, “Fluoropolymer Material Specifications.” [Online]. Available: http://isoflon.com/images/pdf/PROPRIETES-PHYSIQUES-FLUORO-POLYMERES-ANGLAIS.pdf. [Accessed: 15-Feb-2016].

[264] C. Maier and T. Calafut, *Polypropylene: the definitive user’s guide and databook*. William Andrew, 1998.

Appendix

Table 0.1- Thermal properties of PCTFE

Property	**Test method (ASTM)**	**Units**	**Typical value**	**Ref.**
Specific heat, Cp		J/Kg·K	$0.9x10^{3}$	[150]Daikin
Melting point		°C	210-216	[150] [149]
Crystallisation T		°C	178.5	[120]
Tg (depending on crystallinity)		°C	44-77	[149]
α relaxations		°C	150	[149]
β relaxations		°C	90	[149]
γ relaxations		°C	-37	[149]
Heat deflection temperature	D-648	°C	126	[150]
Thermal conductivity, k	C-177	W/m·K	0.21	[150]
Thermal expansion +30~–30°C –30~–100°C –100~–190°C T Not specified	D-696	cm/cm/°C 130µm/(m·K)	 $7.0X10^{-5}$ $5.1X10^{-5}$ $3.6X10^{-5}$ 130	[150] [259]
Flammability	D-635		Non-flammable	[150]
Heat of fusion, ΔHf^{0}*		J/g	41.9-43.5	[260][261][262]
Onset decomposition		°C	364	[140]
Peak mass loss rate		°C	405	[140]
Ignition		°C	580	[140]
α_t**		K	$60x10^{6}$	[128]
Poisson's ratio			0.39	[260] Kel-F 81

*ΔHf^{0} for 100% crystalline. 46% crystalline is roughly 19.9 J/g [260].

Table 0.2- Typical Physical Properties of PCTFE

Property	**Test method (ASTM)**	**Units**	**M-300H**	**M-400H**	**Ref.**
Specific gravity	D-792		2.11~2.16	2.11~2.16	[150]
Zero strength time	D-1430	s	200~300	350~450	[150]
Tensile strength, σ_B	D-638	MPa	31.4~37.2	33.3~39.2	[150]
Elongation, ε_B	D-638	%	50~200	100~250	[150]
Tensile modulus of elasticity	D-638	MPa	$(1.3\sim1.5)\times10^4$	$(1.2\sim1.4)\times10^4$	[150]
Compression strength	D-695 0.2% off set 1% strain	 MPa MPa	 39~44 12~14	 36~41 11~13	[150]
Compression modulus of elasticity	D-695	MPa	$(1.4\sim1.6)\times10^3$	$(1.2\sim1.4)\times10^3$	[150]
Flexural strength	D-790	MPa	68~73	66~71	[150]
Flexural modulus elasticity	D-790	MPa	$(1.6\sim1.9)\times10^3$	$(1.4\sim1.7)\times10^3$	[150]
Impact strength	D-256	J/m	133~144	133~144	[150]
Hardness(Shore:durometer)		ShoreD	D80	D80	[150]
Deformation under load 24 h/686N	D-621 25°C 80°C 100°C	%	 ≤0.2 1.7~1.9 7.0~9.0	 ≤0.2 1.4~1.6 4.5~6.5	[150]
Ball hardness	DIN 53 495	N/mm^2	65-70		[263]
Bulk modulus, K		GPa	5.80		[260]
Shear modulus, G		GPa	1.31		[260]
Young modulus, E		GPa	3.66		[260]
Shear wave speed, C_s		m/s	780		[260]
Longitudinal wave speed, C_1		m/s	1870		[260]
Refractive index			1.43		[187]
Density fully amorphous fully crystalline		g/cm3	 2.187 2.077		[149]
Melt flow rate		cc/s	39.4×10^{-3}		[120]

Melt viscosity	By capillary rheometer at 230°C	Pa·s	$1x10^{8}$	[148]
Limiting Oxygen Index (LOI)		%	100	[140]
Coefficient of dynamic friction on steel			0.35	[263]

Table 0.3- Flow, apparent density, and ZST of NEOFLON (PCTFE)

Product no.	**Test method (ASTM)**	**Units**	**Typical value**	**Ref.**
Flow value M-300 M-300H M-300P-M-300PL M-400H	Measured by flow tester at 230°C, 100MPa load	mL/s	 $1\sim3 \times 10^{-3}$ $1\sim3 \times 10^{-3}$ $1\sim3 \times 10^{-3}$ $0.5\sim0.8 \times 10^{-3}$	[150]
Apparent Density M-300 M-300H M-300P-M-300PL M-400H	Recognized by Underwriters' Laboratories	g/mL	 0.60 1.00 1.20 1.00	[150]
ZST M-300 M-300H M-300P-M-300PL M-400H	ASTM D 1430, zero strength time at 250°C	s	 200~300 200~300 200~300 301~450	[150]

Table 0.4- Electrical Properties of PCTFE

Property	**Test method (ASTM)**	**Units**	**Typical Value**	**Reference**
Dielectric constant 10^3HZ	D-150		2.6	[150]
Dielectric dissipation factor 10^3HZ	D-150		0.02	[150]
Dielectric strength Short time 4 mils thickness 68 mils thickness	D-149	Volt/Mil	 3000 500	[150]
Arc resistance	D-495	s	360	[150] [149]
Volume resistivity 50% R.H. Short time	D-257	Ω-cm	$2X10^{17}$ 10	[150] [149]
Surface resistivity 100% R.H. 50% relative humidity 25°C	D-257	Ω-cm	$1X10^{15}$ 10	[150] [149]
Dielectric strength	D-149	V/µm	20	[149]

Table 0.5- Gas permeability of PCTFE and FEP

	Gas	**Unit**	**PCTFE**	**FEP**	**Reference**
Gas permeability constant	N2	cm^3, cm/cm^2, s, atm	$1.8X10^{-11}$	$1.2X10^{-8}$	[150]
	O2		$1.5X10^{-10}$	$3.7X10^{-8}$	[150]
	H2		$5.6X10^{-9}$	$1.1X10^{-7}$	[150]
	CO2		$2.9X10^{-10}$	$9.7X10^{-8}$	[150]
	CH4			$6.6X10^{-9}$	[150]
Moisture permeability constant Water absorption		g/m, 24 h %, 24 h % by weight, 168 h	0.2 0.00 0.0	1.6 <0.01	[150]

Table 0.6- 7 Days immersion test of PCTFE [150]

Substance	Conc. (%)	Temp. (°C)	Weight change (%)
Hydrochloric acid	10	25	0.0
Sulfuric acid	96	70	0.0
Nitric acid	70	70	0.0
Fluoric acid	50	25	0.0
Acetic acid	50	175	0.1
Chromic acid	50	175	0.0
Acetic acid anhydride		70	+0.1
Caustic soda	50	b.p.	+0.1
Caustic soda		25	0.0
Caustic soda	Saturation	175	0.0
Sodium chloride	Saturation	175	0.0
Methyl alcohol		25	0.0
Ethyl alcohol		80	+0.2
Acetone		25	+0.1
Carbon tetrachloride		70	+9.7
Chloroform		90	+8.5
Trichloethylene		80	+9.2
Toluene		110	+5.0
Xylene		90	+6.5
Benzene		90	+7.0
n-Hexane		90	+4.5
Methylethylketone		90	+4.6
Aniline		70	0.0
Ethyl acetate		70	+6.5
Ether		25	+3.8
Dioxan		90	+5.7
Diethylamine		25	+1.9
Formaldehyde		135	+0.7
Phenol		70	0.0

Table 0.7- Temperature necessary to solubilise PCTFE in different solvents

Solvent	**Temperature required (°C)**	**Boling T. (°C)**	**Conc. (%)**	**Ref**
1,2-dichloro and 2,5-dinitrotrifluorobenzene	130	/	/	[149]
2,5-dichlorotrifluoromethylbenzene	130-150	/	/	[149]
benzene	200	80	/	[149]
cyclohexane	>235	80	/	[149]
Toluene	142	110	/	[149]
carbon tetrachloride	114	76	/	[149]
1,1,1-trichloroethane	120	74	/	[149]
1,2,3-trifluoropentachloropropane	/	~148	/	[149]
Camphor	175	204	12	[189]
Fenchone	160	193	12	[189]
Cineol (Eucalyptol)	130	176	12	[189]
Solubility parameter, δ*	14.7 MPa			[264]

*square root of the cohesive energy density